A Surface Science Approach Towards Understanding and Mitigating Fouling and Corrosion in Crude Oil Refinery Units

by

Douglas Hazelton

A thesis submitted in partial fulfillment of the requirements for the degree of

Master of Science

In

Materials Engineering

Department of Chemical and Materials Engineering
University of Alberta

ABSTRACT

This research presents a detailed investigation of corrosion and organic fouling on several important metallurgies in a broad range of crude oils. Throughout a refinery, fouling of metallic heat-transfer surfaces is a ubiquitous, costly, and complex phenomena, made increasingly challenging by largely variable oil feedstock, chemical and physical properties of the metallic surface, and their interrelation. Inorganically driven fouling is a mechanistic description that introduces a concept wherein corrosive processes influence subsequent organic fouling. Corrosion alters physical and chemical properties of a fouling surface, which increases wetting behavior of problematic species, introduces alternate reaction pathways, and generally catalyzes the growth of mixed inorganic-organic foulants.

The research goal was to acquire a deeper understanding of the mechanisms that drive fouling and corrosion in refinery units, to document the controlled manipulation of fouling propensity using additive chemistry, and initial development of thin-film coatings to resist corrosion and fouling. Several key findings were delivered. First, a systematic elucidation of the time-dependent interrelation between sulfidic corrosion and carbonaceous fouling. Second, broad similarities amongst fouling deposition across multiple crude oils and temperatures. Third, the essential role of surface metallurgy in establishing fouling rates. An iron-naphthenate additive was used to manipulate crude oil fouling tendency, which imparted different behaviors under high and low temperature experimental conditions. Thin-film metallic surface coatings were applied to wires with little mitigative effect, but key trends were observed that will be applied to subsequent design.

Experiments were conducted in a batch, stirred, high-pressure, high-temperature reactor vessel with custom electrical feedthroughs facilitated resistive heating of metallic wire or ribbon while immersed in a bath of hot crude oil. This system allowed control of wire temperature, oil temperature, flow, and pressure under repeatable experimental conditions. Several combinations of metallurgy, crude oil, and temperature were employed. Metallurgies were selected as carbon steel,

P91 (9wt% Cr, 1wt% Mo) alloy steel, and 347SS (347 stainless-steel), and were employed as hot-drawn, 200 μm diameter wire. They were immersed in oil blends of varying, understood fouling propensity (Blend HI - high fouling, Blend BC - medium fouling, and Blend BDH - high fouling). A low fouling oil, Crude G, was used for tests with iron-naphthenate additive, and medium fouling Crude A for experiments with coated wires. Temperature combinations explored were wire and oil bath values of 490 °C wire/290 °C bath and 350 °C wire/250 °C bath. This served to demonstrate fouling behavior both above and below the commonly accepted threshold for thermal cracking.

Evaluation of corroded and fouled wires was accomplished by applying complimentary bulk and surface characterization techniques, to the three select metallurgies, after exposure to multiple combinations of crude oil, temperature, and fouling time. Analytical techniques including transmission electron microscopy (TEM), focused ion beam (FIB), scanning electron microscopy (SEM), and energy dispersive X-ray analysis (EDX) were employed to detail the fouling phenomenology of several industrially relevant metallurgies. A key microstructural with 347SS, at high temperature, included the transformation of near-surface, textured, austenitic grain structure into a micron scale, highly porous inner-sulfide/chromium-oxide bilayer composite.

In the high-temperature fouling scenarios, all wires experienced substantial sulfidic corrosion and catalytic growth and adhesion of organic fouling. An iron sulfide (pyrrhotite $Fe_{(1-x)}S$) formed almost instantaneously at the metal surface, followed by coke around its periphery at longer times. This temporal sequence, combined with observation of thicker foulant associated with detached plumes of the sulfide, leads to a hypothesis of inorganically driven, organic fouling. Chemically, the sulfide functions as a potent dehydrogenation catalyst that drives the transformation of pitch to coke. Physically, the textured, corroded surfaces promote wetting and trapping of important fouling precursors. Below thermal cracking temperature, similar characteristics are observed, but take longer to occur. The 347SS wire is nearly immune to sulfidic corrosion at these conditions.

PREFACE

Chapter 1 of this thesis provides a general summary of fouling and corrosion in oil and gas refining

Chapter 2 is a literature survey, covering fouling and corrosion and introduces a focused concept that drove this research – inorganics driven fouling

Chapter 3 provides a summary of experimental conditions and equipment that was utilized in this research

Chapter 4 of this thesis has been published in the manuscript entitled; Sulfide promoted chronic fouling in a refinery: A broad phenomenon, Fuel, 2015, 160, 479-489. I was the first author of this publication and was responsible for the laboratory work and composition.

Chapter 5 is an extension of the work conducted in Chapter 4 and includes contrasting fouling experiments conducted at lower temperature with identical metallurgy.

Chapter 6 includes an initial survey of high and low temperature fouling behavior of carbon steel and P91 metallurgies, in the presence of an iron-naphthenate additive.

Chapter 7 introduces initial design aspects and fouling experiments with carbon steel and P91 metallurgies with anti-fouling, thin-film, metallic coatings.

Chapter 8 is a summary and conclusion from the research conducted.

ACKNOWLEDGEMENTS

I would like to thank my supervisors, Dr. David Mitlin and Dr. Weixing Chen for their support and guidance throughout my graduate program and research. As well, Dr. Alireza Kohandehghan and Dr. Beniamin Zahiri have my full gratitude for their incredible assistance with the transmission electron microscopy work conducted for this study.

I am thankful to Paul Concepcion, Kai Cui, Martin Kupsta and the rest of the technical staff at the National Institute for Nanotechnology for their assistance during my Master of Science program. Also, for the time spent maintaining the instruments needed for much this research.

Finally, my group mates; I would like to thank Tyler Stephenson, Justin Lepore, Chris Holt, Zhi, Li, Brian Olsen, Xuehai Tan, Peter Kalisvaart and the many students within Dr Mitlin's research group for always being helpful and inciteful.

TABLE OF CONTENTS

LIST OF FIGURES

LIST OF TABLES

LIST OF EQUATIONS

$$\text{Fouling} = \frac{dm}{dt} = \phi_d(\ Deposition\ Rate) \ - \phi_r(Removal\ Rate)$$

$$\mathrm{Q}_{clean} \ = \ \mathrm{U}_{clean}\,\mathrm{A}_{clean}\,(T_S - \mathrm{T}_{oil})_{clean}$$

$$\mathrm{FF} = \frac{1}{U_{fouled}} - \frac{1}{U_{clean}} = \frac{\mathrm{A}(\mathrm{T}_{wire} - \mathrm{T}_{oil})}{\mathrm{Q}_{fouled}} - \frac{A(T_{wire} - T_{oil})_{clean}}{Q_{clean}}$$

$$\frac{dR_f}{dt} = \ \alpha Re^{-0.66} Pr^{-0.33} e^{-\frac{E}{RT_f}} - \gamma\tau$$

$$CII = \frac{Asphaltene + Saturates}{Resins + Aromatics}$$

$$FF = A_c\left[\left(\frac{\Delta T}{P}\right)_{fouled} - \left(\frac{\Delta T}{P}\right)_{clean}\right]$$

$$FFF = \left[A_f\left(\frac{\Delta T}{P}\right)_{fouled} - A_c\left(\frac{\Delta T}{P}\right)_{clean}\right]$$

$$Fe + 2RCOOH \ \rightarrow Fe(RCOO)_2 + H_2$$

$$Fe + H_2S \ \rightarrow FeS + H_2$$

$$Fe(RCOO)_2 + H_2S \underset{rev}{\longleftrightarrow} FeS + 2RCOOH$$

$$Fe(RCOO)_2 \rightarrow FeO + \mathrm{RCOR}$$

$$4FeO \rightarrow Fe_3O_4(magnetite) + \alpha Fe$$

CHAPTER 1

Introduction and Research Objectives: Refinery Pre-Heat Train Fouling

1.1 Consequences of Fouling and Corrosion

Petroleum hydrocarbons are a ubiquitous source of energy, largely running our modern world. In 2016 the global demand for crude oil was > 97 million barrels per day.[1] Generating usable goods from crude oils and natural gas requires a complex series of extraction, separation, transportation, and refining processes. Each step is plagued by some form of corrosion and fouling, with costly significance. It is estimated that corrosion and fouling costs the petroleum industry more than $25bil per year, individually.[2,3]

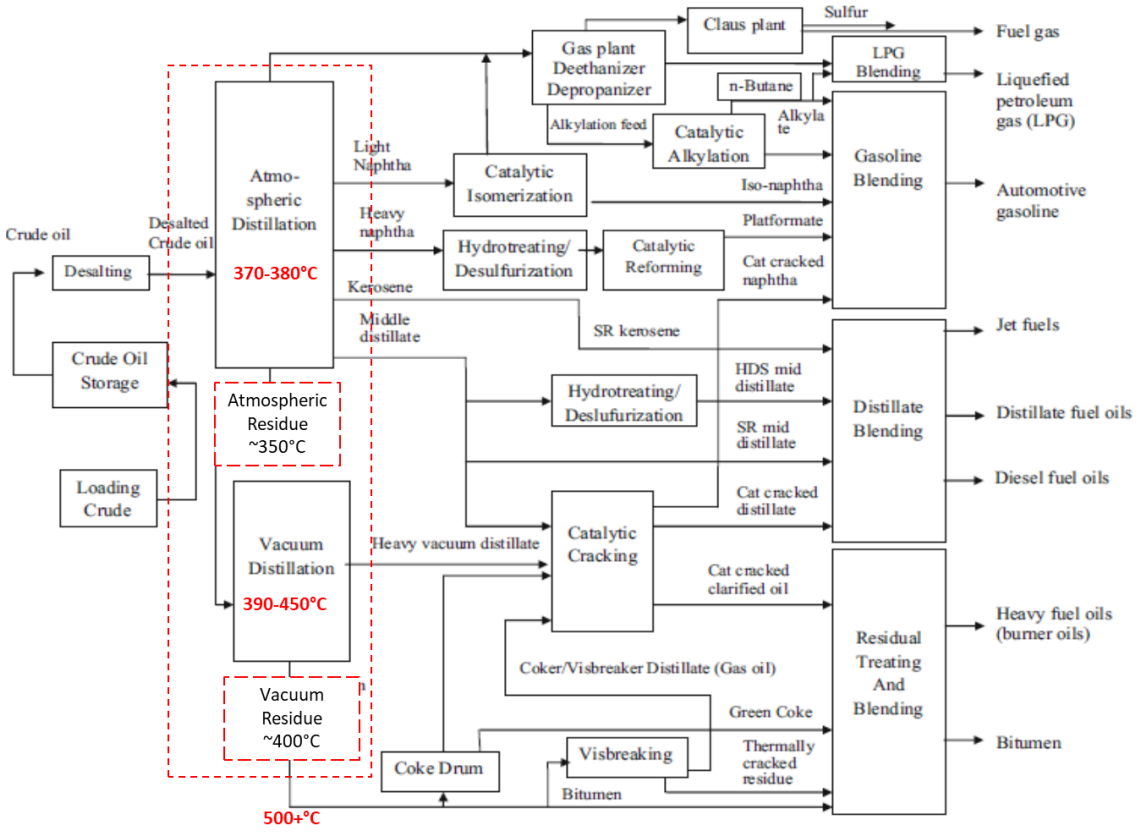

Figure 1.1 A refinery process diagram with operations of interest, atmospheric and vacuum distillation, highlighted by a dashed, red line. Several process temperatures have been overlaid, including: Atmospheric distillation inlet, 370-380°C; Atmospheric residue (bottoms), ~350°C; Vacuum distillation inlet, ~390-450°C; Vacuum residue (bottoms), ~400°C; Coker furnace outlet (drum inlet), 500+°C. Image sourced from Corrosion Problems and Solutions in Oil Refining and Petrochemical Industry, pg. 291, ISBN: 978-3-319-45254-8.

Amongst the final stages in creating value-added products from raw crude oils is refining. A hydrocarbon refinery is a complex series of separation and conversion processes, engineered to create high value product pools from a low value natural resource. It performs to fractionate, reject impurity elements, and alter molecular structure of a crude oil feedstock. Oil refineries typically process

between 100,000 and 2,000,000 barrels of crude oil per day into saleable petroleum products.[4,5] In the United States, over 18 million barrels of oil are refined, per day.[6] Figure 1.1 depicts the process layout of a complex refinery. Figure 1.2 shows various manifestations of fouling and corrosion throughout a refinery, linked with causation.

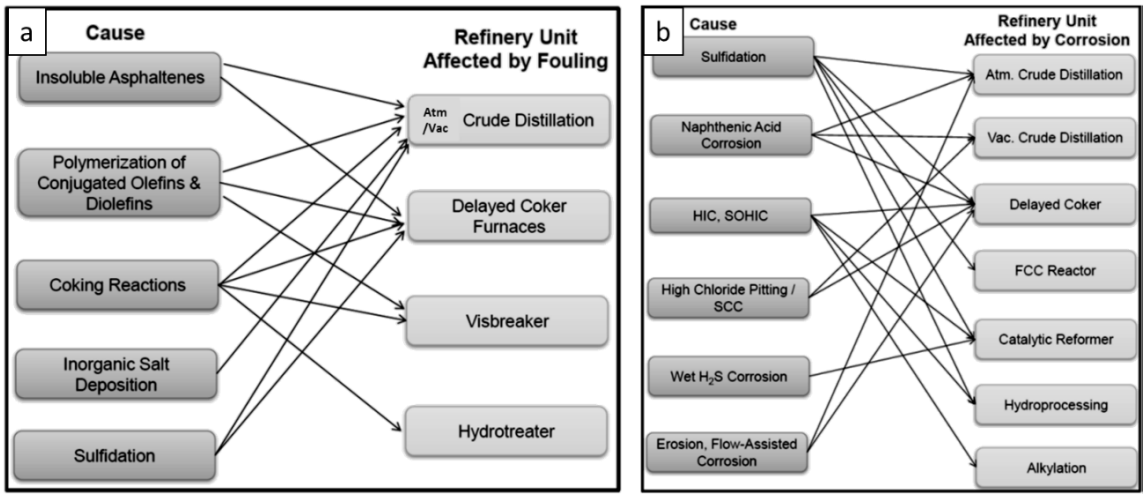

Figure 1.2 An overview of (a)fouling and (b)corrosion in refining, linking causation to the afflicted refinery processes.

Refining necessitates elevated temperatures, spanning ambient to above 500°C, and significant demand is put onto an intricate network of heat exchangers and fired furnaces. A pervasive scenario throughout a refinery is a flowing crude oil, or crude fraction, in contact with a heated metal surface that is prone to foul and corrode. For example, the preheat train (PHT) and fired furnace for atmospheric and vacuum distillation will bring the bulk temperature of a whole crude oil to ~350°C, while in delayed coking a residual feedstock fraction is brought to temperatures exceeding 500°C, to facilitate thermal cracking.[7] In both cases, thermally insulating layers of mixed organic and inorganic material accumulate and foul vessel surfaces, with tremendous cost associated to material loss/replacement, increased hydraulic horsepower demand, reduced heat transfer, safety, and increased greenhouse gas emissions. Figure 1.3 shows a PHT for atmospheric distillation, including a heat exchanger network and fired-furnace, and a shell-and-tube heat exchange unit in a clean and fouled state.

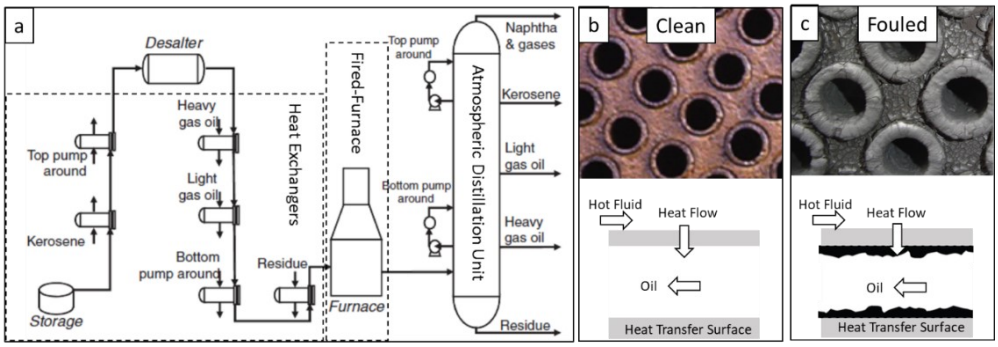

Figure 1.3 A refinery preheat train (PHT), leading into an atmospheric distillation unit, and heat exchanger tubulars in clean and fouled states. (a)The PHT, comprised of a heat exchanger network and a fired-furnace. (b) Heat exchange tubulars in a clean state. (c) Heat exchange tubes in a fouled state. Images (b), (c) sourced from Crude Oil Fouling, pgs 11,27 ISBN: 9780128012567.

The annual profit loss in refineries across the US due to fouling has been estimated on the order of $ 10 billion USD per year - approximately $4 billion in the United States, alone.[8] Much of this economic loss in a refinery occurs within the PHT. One article,[9] states that a 1ºC drop in crude oil temperature at the entrance of the PHT, due to fouling, costs a refiner over to 250 000 pounds per year, where typical temperature losses are in the range 8-10°C per year. Furthermore, it is estimated fouling in the PHT costs 0.25% of world oil production, due to incremental energy consumption. A large collection of data associating fiscal damages and fouling is provided by Coletti and Macchietto.[10] These numbers reveal the severe fiscal consequences of fouling, in a crude oil refinery.

Refiners experience additional economic penalty when fouling concerns limit crude purchasing flexibility. With increasing frequency, *difficult* crudes are coming to market, and *easily refined* feedstocks are diminishing. Low viscosity, light (low density, high API) crude oils with low sulfur, organic acid and asphaltene content are higher cost inputs, by easier to refine. These light, sweet oils are becoming less available and progressively refineries must manage lower quality, sour, high density, high viscosity crude, with significant asphaltene content. These are *opportunity* crudes, as they can be purchased at a discount, but require complex, *deep* refining processes and intensify challenges related to fouling and corrosion. Lower quality crudes become attractive inputs for a refinery when accurate knowledge of fouling propensity and management strategies are made available. Improving the quality and knowledge depth of feedstock chemistry is becoming increasingly essential.[11,12]

1.2 Fouling and Corrosion

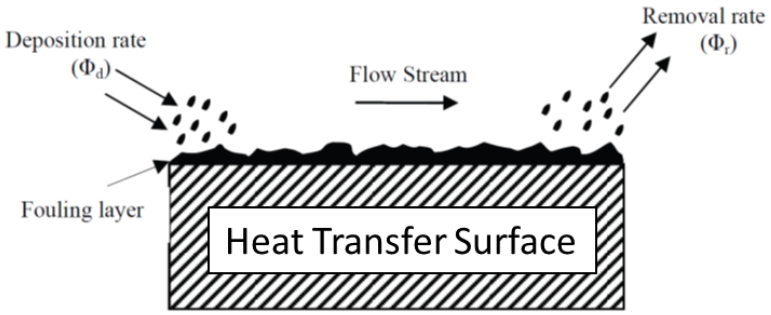

Figure 1.4 A fouling heat transfer surface. Here, fouling is simplified to the summation of deposition and removal rates. Image source: www.intechopen.com.

$$\text{Fouling} = \frac{dm}{dt} = \phi_d(\,Deposition\ Rate) \; - \phi_r(Removal\ Rate) \qquad \textbf{Equation 1.1}$$

Fouling is the undesirable accumulation of material on the surface of process equipment. Corrosion is the deterioration of a material due to chemical reaction with the process environment. Consistently, the two phenomena do not manifest with distinction in real systems and will be referenced as fouling. Figure 1.4 is a simplified depiction of fouling and Equation 1.1 is a simple mathematical representation of fouling, as mass accumulation, and removal from a surface. More intricately, it is a multi-staged phenomenon, initiating after an induction period, then controlled by material diffusion/transport to an interface, adhesion/ removal, and thermal ageing. Fouling has been described using mechanistic scenarios: chemical reaction fouling, particulate fouling, corrosion fouling, crystallization fouling and biological fouling, where interaction amongst the scenarios is typical.[13] Experimentally and in real systems fouling is correlated to incremental heat transfer resistance, termed fouling factor (FF), or fouling resistance (Rf). Figure 1.5 depicts the fouling phenomenon. Figure 1.5a represents a sequential fouling process and crude oil precursors Figure 1.5b is a graphical representation of fouling, as fouling factor with time, showing linear, slowing, and asymptotic deposition. Figure 1.5C is a matrix containing the fouling scenarios, after Epstein.[14]

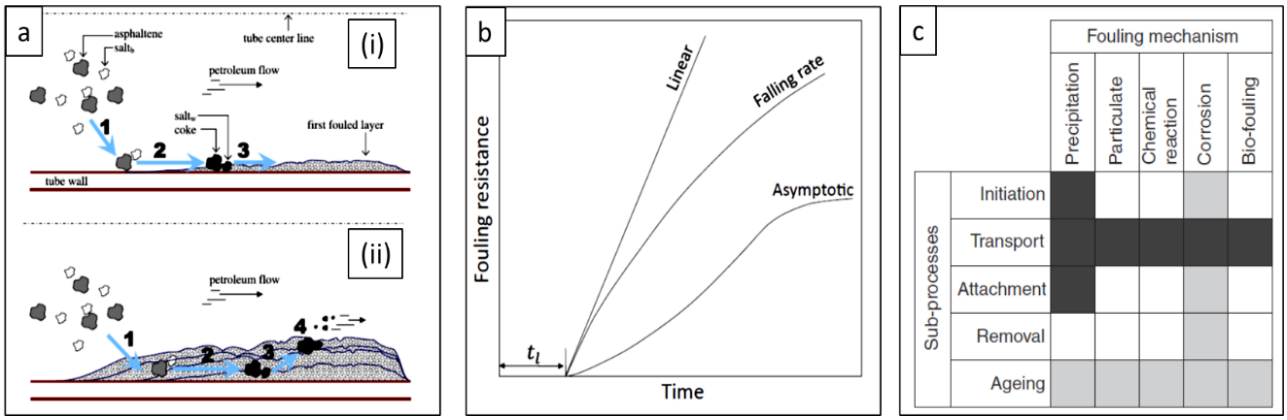

Figure 1.5 An overview of the fouling phenomenon. (a) The process of fouling from petroleum in (i) an induction/initiation period and (ii) in a developing period. CFD modeling of fouling in crude oil pre-heaters, (b) a graphical representation of fouling using a plot of fouling resistance with time. Fouling follows linear, falling rate and asymptotic behavior, after an induction period t_l. A matrix showing the stages and mechanistic scenarios of fouling. Darker coloring indicates areas that have been more significantly researched. Images (a) sourced from M. Bayat et al. / Energy Conversion and Management 64 (2012) 344–350. and (b), (c) sourced from Crude Oil Fouling, pgs 23,36 ISBN: 9780128012567.

Separately, organic, carbonaceous fouling and sour corrosion in oil refining are well documented phenomenon. Synergies between these highly deleterious processes are observed experimentally and in real systems. However, a full understanding of their interaction remains elusive, especially their variability, with feedstock selection. Figure 1.4C is a 5x5 fouling matrix highlighting research focus: Darker areas have obtained the most attention. Notably, corrosion fouling and synergies with chemical reaction fouling have received much less attention than other areas.

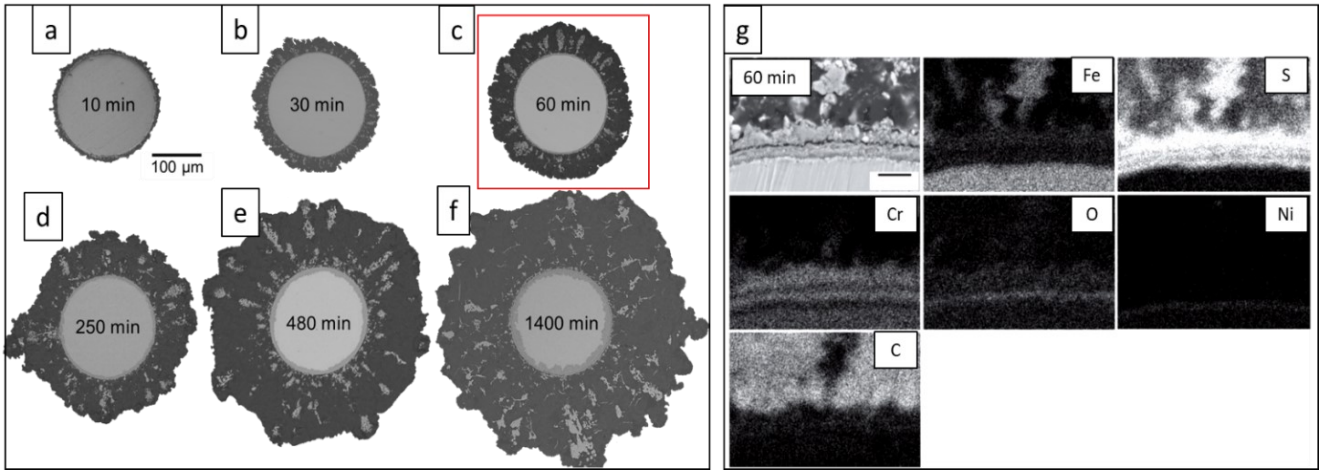

Figure 1.6 Evolution of corrosion and fouling with time on 316-stainless steel at 550°C, after (a-f) 10 minutes through 1400 minutes in an atmospheric bottoms oil fraction. (g) Is SEM and EDX elemental data of the corroded and fouled wire surface after 60 minutes.

Researchers Wiehe,[15] and Wang and Watkinson,[16] have put forth theoretical framework for synergy between sour corrosion and carbonaceous fouling. Parker and Macfarlane observed iron sulfides and coke combined within foulants removed from a delayed coking furnace, suggesting a mechanism of organic induced fouling because of corrosion. Stephenson et al.[17,18] explored this interrelation experimentally and propose a well-documented link between corrosion and the rate of foulant adhesion, onto a heated metal surface. Their critical observation was that significant organic fouling did not initiate until the metal surface was fully covered by a microscopic layer of sulfide. Also observed was that the presence of a stable oxide layer reduces the rate of fouling, especially in high Cr-containing alloys, such as 316 stainless-steel. Figure 1.6a through 1.6f shows the time evolution of fouling for a specific combination of variables: oil – an atmospheric reduced crude, surface temperature - 550°C, and metallurgy – 316 stainless-steel. Figure 1.6g presents an associated elemental survey that correlates with the 60-minute fouled wire. It shows a corroded surface (iron and sulfur) and carbonaceous material intermingled with corrosion product. Scenarios of corrosion-then-fouling can be inferred.

The numerous, complex, and interrelated processes occurring in a bulk oil at elevated temperature and at a heated metal surface facilitate fouling and are not well understood. A thorough understanding of the interaction between the substrate surface and chemical species responsible for fouling and corrosion could help in developing suitable mitigation methods and facilitate more efficient refining of "difficult" feedstocks creating competitive advantage. At present, the general strategies employed to reduce fouling and corrosion include feedstock selection/blending, optimized process conditions, chemical additives, materials selection, and anti-fouling / anti-corrosive coatings. Were the limited observations, presented above, to become more generally applicable, covering various oil types and refining conditions, it would have significant implications in formulating long-term anti-fouling strategies. At this point, however, the *corrosion-then-fouling* sequence is yet to be broadly documented. Specifically, very little is known regarding how the oil feedstock properties

(e.g. TAN, sulfur speciation, asphaltene stability, Cl- content) and surface properties and metallurgy interact to affect this phenomenon.

1.3 Research Objectives

Corrosion, fouling and their interrelation in crude oil refining has been well documented in real systems and experimentally. Although significant understanding and experience exists, no broad strategy has been established for mitigation, especially when variances in crude oil are considered. A central mitigation strategy is missing an in-depth understanding of the interaction between oil constituents and a high temperature metallic surface. This is especially true in the cases of organic fouling that is influenced by iron sulfide, corrosion product. Recent studies have provided preliminary evidence for this interaction, but a broad understanding remains elusive. Specifically, there is missing an account for the function of variable surface chemistry (i.e. the role of metallurgy, corrosion product, and texture) and the influence specific crude oil properties (oil type).

In this work corrosion and fouling are documented throughout a series of experiments where metallurgy, temperature (wire and oil), and time are employed as key variables. This detailed study will accomplish three critical and interrelated learning objectives: 1) Establish the extent of the general correlation between surface condition and overall fouling, documenting the time-dependent phenomenology of the process; (2) investigate the mechanistic role of underlying base metallurgy, especially in relation to increasing Cr-chromium and Mo-molybdenum (as carbon steel, versus Cr-Mo, versus stainless steels) in determining fouling severity; and (3) establish the role of oil properties in determining 1) and 2), and towards making this learning more broadly applicable for various oil types. In the final part of this research, an iron naphthenate additive is introduced to Crude G and an initial survey of several thin films coatings are introduced as a potential mitigation methodology

Details of experimentation and results follow a survey of literature, presented in the next chapter, Chapter 2. Chapter 3 introduces an overview of the experimental conditions and processes utilized in this research. Chapter 4 are detailed results of the fouling and corrosion phenomenon, at

high temperature. Chapter 5 is a collection of results from fouling experiments completed with the wire surface temperature below thermal cracking temperature. Chapter 6 employs the use of an iron-naphthenate additive and the influence it imparts on fouling and corrosion, above and below thermal cracking conditions, in low fouling Crude G. Chapter 7 introduces the use of thin-film metallic coatings as an anti-fouling, anti-corrosion measure in a medium-fouling oil, Blend A.

1.4 References

(1) Petroleum, B. *BP Stat. Rev. World Energy* **2016**, No. June, 1–48.

(2) Papavinasam, S. *Corrosion Control in the Oil and Gas Industry*; 2014.

(3) Bott, T. R. *Fouling of Heat Exchangers*; Elsevier B.V.: Amsterdam, The Netherlands, 2005.

(4) Coletti, F.; Hewitt, G. F. *Crude Oil Fouling*; 2015.

(5) Diaz-Bejarano, E.; Behranvand, E.; Coletti, F.; Mozdianfard, M. R.; Macchietto, S. *Appl. Energy* **2017**, *206* (September), 1250–1266.

(6) Statista 2017. https://www.statista.com/statistics/273579/countries-with-the-largest-oil-refinery-capacity/.

(7) Gary, J. H.; Handwerk, G. E.; Kaiser, M. J. *Petroleum Refining: Technology and Economics*, 5th ed.; CRC Press/Taylor and Francis: New York, NY, 2005.

(8) Deshannavar, U. B.; Rafeen, M. S.; Ramasamy, M.; Subbarao, D. *Journal of Applied Sciences*. 2010, pp 3167–3174.

(9) Macchietto, S.; Hewitt, G. F.; Coletti, F.; Crittenden, B. D.; Dugwell, D. R.; Galindo, A.; Jackson, G.; Kandiyoti, R.; Kazarian, S. G.; Luckham, P. F.; Matar, O. K.; Millan-Agorio, M.; Müller, E. A.; Paterson, W.; Pugh, S. J.; Richardson, S. M.; Wilson, D. I. *Heat Transf. Eng.* **2011**, *32* (3–4), 197–215.

(10) Coletti, F.; MacChietto, S. *Ind. Eng. Chem. Res.* **2011**, *50* (8), 4515–4533.

(11) Kekäläinen, T.; Pakarinen, J. M. H.; Wickström, K.; Lobodin, V. V.; McKenna, A. M.; Jänis, J. *Energy & Fuels* **2013**, *27* (4), 2002–2009.

(12) Ho, T. C. *Int. J. Heat Mass Transf.* **2016**, *95*, 62–68.

(13) Coletti, F.; Hewitt, G. *Crude Oil Fouling: Deposit Characterization, Measurements, and Modeling*; Elsevier Science, 2014.

(14) Epstein, N. *Heat Transf. Eng.* **1983**, *4* (1), 43–56.

(15) Wiehe, I. A. *Process Chemistry of Petroleum Macro Molecules*, Vol. 121.; CRC Press: Boca Raton, FL, 2008.

(16) Wang, W.; Watkinson, A. P. *Proc. Int. Conf. Heat Exch. Fouling Clean. IX* **2011**, 23–30.

(17) Stephenson, T.; Kubis, A.; Derakhshesh, M.; Hazelton, M.; Holt, C.; Eaton, P.; Newman, B.; Hoff, A.; Gray, M.; Mitlin, D. *Energy and Fuels* **2011**, *25* (10).

(18) Stephenson, T.; Hazelton, M.; Kupsta, M.; Lepore, J.; Andreassen, E. J.; Hoff, A.; Newman, B. Eaton, P.; Gray, M.; Mitlin, D. *Fuel* **2015**, 139.

CHAPTER 2

Background and Literature Survey

2.1 Fouling in a Refinery Preheat Train (PHT)

Complex deposits[1–3] of organic and inorganic material build up and *foul* the surface of refinery heat exchange equipment. Deposited materials and corrosion product (collectively ***foulants***) are often comprised of precipitated asphaltenes, pyrolytic coke, iron-based corrosion products, and inorganic salts. Corrosion is the deterioration of processing equipment because of reaction with impurities such as naphthenic acids, organic sulfur compounds, chlorides, and H_2S, all present in varying quantity in crude oils. Corrosion may accompany and/or promote fouling and is often included as an associated mechanism. Wholly described as crude oil fouling,[4] the encompassed phenomena distress operations by encumbering efficient heat transfer, raising greenhouse gas emissions, increasing hydraulic resistance, and compromising safety.

Fouling depends heavily on the chemistry of feedstock oil and inorganic contaminants, temperature of the fouling surface and bulk fluid, fluid velocity and shear stress, and chemical and physical condition of the fouling surface. The literature cited in this chapter explores corrosion and fouling in the PHT and distillation units of a crude oil refinery. The environmental conditions for this type of fouling are presented, followed by an examination of deposits from real systems, then various test systems and scenarios are described in an overview of experimental crude oil fouling. Important physical and chemical influencers leading to crude oil fouling are explored, detailing constituents important to this study, then an overview of mitigation practices is presented. The concluding section of this chapter explores synergies amongst various contributors to fouling, especially recent studies that observe and explore links between sour corrosion and organic, carbonaceous (organic) fouling.

2.2 Refinery Distillation and the PHT

Atmospheric and vacuum distillation are initial separation processes in a refinery and are immediately downstream of the desalting unit (see Figure 1.1). A desalter functions to remove impurities from a feedstock oil, including emulsified water and suspended solids. Distillation units

fractionate a crude by boiling. Before being discharged into the atmospheric distillation unit, a whole crude oil passes through a series of heat exchangers and fired furnaces – the PHT, bringing the bulk fluid temperature to 370-380 °C. Furnace outlet temperatures, leading into vacuum distillation can be in the range 390C-450 °C.[5] Localized temperature of the steel heat exchange surfaces can exceed 500 °C, although it is desirable to limit operating temperatures to below ~380 °C, to avoid carbonaceous fouling, related to thermal cracking.[6] The dominant fouling processes change throughout the preheat train, mainly due to temperature. Low(er) temperature foulants include mineral salts, sands, clays, and iron-based corrosion products. Asphaltene deposition typically increases with rising process temperature unless extreme instability exists within the oil feedstock. Coking occurs in the fired heater section, where temperatures are the most severe. [2–9] Corrosion occurs throughout the preheat train, on all susceptible surfaces, and is a strong function of crude oil chemistry, temperature, and surface metallurgy. Construction materials range from simple carbon steels (containing elements Fe, Mn, C) to low-alloy, chromium-molybdenum (Fe, Cr, Mo) steels, to stainless steels, especially austenitic types (Fe, Cr, Ni).

2.3 Fouling in Real Systems

Several researchers have studied actual refinery foulants in detail. Tay and Kazarian[3] examined fouling deposits on carbon steel heat exchanger tubes, using ATR-FTIR imaging. They removed samples from a section in the PHT of an atmospheric distillation unit, operated between 150 ºC and 170 ºC. Organic material including asphaltene, as well as inorganic calcium carbonates and sulfates, sulfoxide corrosion products, and oxalates, were identified. Another study analyzed foulant from a refinery pre-heat train and found a similar mixture of organic and inorganic materials, including asphaltene, iron-based corrosion products, and mineral salts.[2] They point out that at lower temperatures the inorganic fraction of the foulant is higher than the organic fraction, and this trend flips as temperature increases to 350 °C, at the outlet. Here, significantly more organic material, with higher asphaltene content was identified. In a pioneering work, Parker and McFarlane[7] completed a microscopy and elemental survey of fouling deposits taken from the furnace of delayed coking unit.

The considered heterogeneous masses were comprised, at large, by carbonaceous material (semi-coke and pyrolytic carbon), lesser fractions of iron and sulfur, and minor amounts of other mineral matter, such as sands and clays. The operating temperature of the coker furnace exceeded 550 °C. In these studies, the influence of corrosion was not addressed. The process of fouling is significantly influenced by operating conditions and crude oil chemistry.[10]

2.4 Fouling in Experimental Systems

$$Q_{clean} = U_{clean} A_{clean} (T_s - T_{oil})_{clean} \quad \textbf{Equation 2.1}$$

$$FF = \frac{1}{U_{fouled}} - \frac{1}{U_{clean}} = \frac{A(T_{wire} - T_{oil})}{Q_{fouled}} - \frac{A(T_{wire} - T_{oil})_{clean}}{Q_{clean}} \quad \textbf{Equation 2.2}$$

$$\frac{dR_f}{dt} = \alpha Re^{-0.66} Pr^{-0.33} e^{-\frac{E}{RT_f}} - \gamma\tau \quad \textbf{Equation 2.3}$$

In a clean, unfouled state, heat transferred from a hot surface to a cool fluid follows Equation 2.1. Deposited materials cause discernable impedance to heat transfer, allowing fouling to be measured experimentally and in real systems. Considering Equation 2.1, thermal energy transfer Q is proportional to surface area A and the temperature difference ΔT (T_s-T_{oil}) between the bulk liquid and hot surface. The overall heat transfer coefficient U, considers conductive, convective and radiative energy transfer and has units W/mK. A *fouling factor (FF)* or fouling resistance (R_f) represents a change in overall heat transfer, from a previous clean / reference state. Mathematically, it is the inverse heat transfer coefficient. To equate the fouling factor, one must have accurate knowledge of: power input (Q), surface area (A), surface temperature (Ts), and bulk fluid temperature (Toil). Equation 2.2 is the fouling factor calculation, referenced to a clean state. Initial rate of change of the fouling factor, dR_f/dt, is also important, and Equation 2.3 is a well-accepted model for systems undergoing chemical reaction fouling, significant in refining, originally proposed by Ebert and Panchel.[11] It is an extension from fouling as the generalized summation of adhesion and removal processes. It states the time rate of change in heat transfer ability depends on fluid flow and system

geometry (i.e. Reynolds number - Re) and interfacial shear stress (τ), a film temperature (T_f), and an activation energy (E_A). It suggests a threshold condition, where material removal can balance deposition processes and low, or even negative, fouling rates may be achieved.

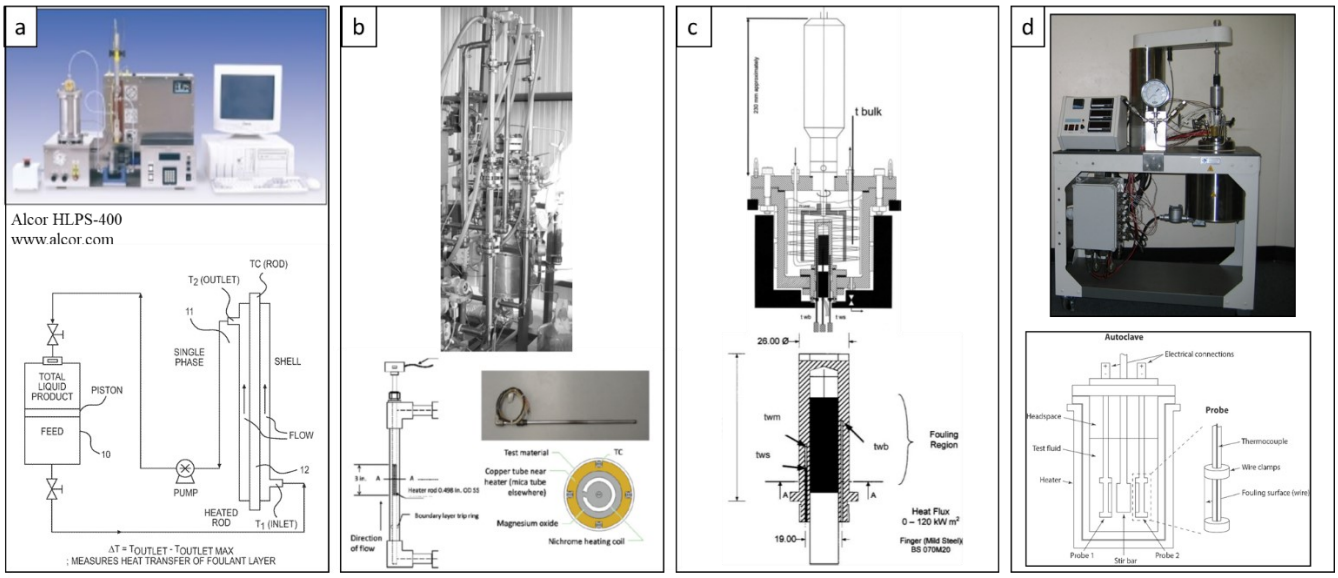

Figure 2.1 Fouling units used in experimentation. (a) Alcor HLPS, (b) HTRI system, (c) Batch-type, stirred system, (d) Batch-type, stirred system using resistively heated wires.

Figure 2.1 presents several experimental systems that are actively utilized in the study of crude oil fouling. They detect thermally insulating foulants through a change in power input, if the surface temperature is constant, or changes in surface temperature, if the power input is constant. A test unit must allow precise control of the principal variables that influence fouling. Most important is chemistry of the crude oil feedstock, then temperatures (bulk and interfacial), pressure, and flow, especially as it relates to shearing stresses at a fouling interface. Geometrically, the systems differ, affecting fluid dynamics and shape of the heat transfer surface. Broadly, fouling test units are categorized into batch-type systems and flow-through systems of tubular or annular geometry.

Fan et al.[12] examined the fouling tendency of a light crude oil, on a 1018 carbon steel surface, and the effect of various system properties using an Alcor HLPS test unit (show in Figure 2.1a). In this system, a hot crude oil flows through the annular space between two concentric tubulars. The inner surface is heated. A single, high fouling oil, linked to asphaltene instability and suspended solids content, was used. Results from SARA fractionation and the calculated colloidal instability

index (CII) were included. Fouling experiments lasting 4.5 hours were completed at three interface temperatures: 250 °C, 300 °C and 400 °C, and at two different flow velocities, both in a laminar regime. An advantage of the annular geometry is that accurate knowledge of the flow fields are easily determined. Increasing surface temperature and decreasing hydrodynamic shear increased fouling rates. The researchers identify a strong similarity between asphaltene and foulant composition. They also noted high concentrations of iron and sulfur in the fouling deposit, but a corrosion mechanism was not explored.

Figure 2.1b shows an annular system used by Bennet et al.,[9] designed by the HTRI (Heat-Transfer-Research-Institute), described by Lestina and Zettler.[13] They studied derivative fouling rates (dR_f/dt) of four crude oils. Initial surface temperatures were between 375 ºC and 445 ºC, with bulk oil temperature at 315 °C. A 304 stainless-steel heat transfer surface was employed. Flow rates produced Reynolds numbers exceeding 100,000, ensuring a turbulent system and initial shear stress at the fouling interface was 13 Pa. Their sample, Crude C, was the highest fouling: It contained the highest sulfur content of 5.33 wt%, the highest total acid number of 0.92, and 9.7 wt% asphaltene. Chemical characterization of the fouling deposit suggested that the dominant fouling mechanism was coking, with significant contributions from particulate fouling (iron sulfide) and corrosion of the 304 stainless-steel surface. Interestingly, these researchers noted an isokinetic temperature near 407 °C, where the four crudes oils fouled at identical rates.

Shearing stress, dependent on fluid velocity and system geometry, can have dramatic effect on foulant accumulation. Watkinson,[14] compared two annular fouling systems and the effect of shear stress. A Hot Liquid Process Simulator (HLPS) was operated in parallel to a Portable Fouling Research Unit (PFRU). Re-circulating flow over 48 hours, at Reynolds numbers of 1500-6000, was used in the PFRU, whereas single-pass, creeping flow (Re ~1) was used in the HLPS over 4 hours. At similar film temperatures, fouling rates were roughly a factor of 250 –500 higher in the HLPS, where velocity was about 250 times lower. It was noted that heat transfer appeared to be dominated by natural convection in the HLPS system, consistent with chemical reaction fouling in laminar flow.

Experimentally, the role of flow regime, principally a turbulent regime, has been demonstrated, by Yang et al.,[15] to reduce fouling on a carbon steel surface. They produced system turbulence by the addition of thin wires and compared to a baseline case without inserts, at surface temperatures near 400ºC. Models describing threshold fouling conditions are important design parameters to consider in reals systems.[16,17]

Petkovic and Watkinson[18]have demonstrated fouling, in a batch, stirred system using a heated, carbon steel rod, shown in Figure 2.1c. They investigated two atmospheric bottoms, at bulk temperature of 320 ºC, surface temperatures up to 500 ºC, and the effects of suspended iron oxides. Foulants at 386 °C surface temperature were 35% organic material and 65% inorganic ash. At 448 °C, the trend flipped, and the deposit was 84% organic and 14% inorganic. Deposition rates for the first oil increased from 42 to 135 mg/day, with temperature, and from 16.5 to 23 mg/day, for the second sample, which highlights both the strong dependence on temperature and crude oil chemistry. They later added various size, micron-scale iron oxide (Fe_2O_3), at two concentrations and an unexpected relationship was observed. With increasing iron oxide additive concentration and size, fouling rates dropped initially before peaking and finally falling to very low levels. The vivid decrease at higher dopant concentration was attributed, in part to an erosion mechanism.

Figure 2.1d was utilized by Derakhshesh et al.[19,20] and Stephenson et al.[21,22] It is a 2000mL, stirred batch reactor, designed to investigate crude oil fouling on resistively heated wires. Both researchers explored fouling at delayed coking conditions with an atmospheric residue, high in asphaltene and sulfur. An initial study by Stephenson et al.,[21] used wires of pure iron and of 316 stainless-steel, heated to temperatures exceeding 500 °C, while immersed in 250°C oil. Significant amounts of pyrolytic coke and crude oil pitch were generated. The researchers noted significant corrosion of the wire surface, and a detailed microscopy study elucidated a likely synergy between sulfidic corrosion and carbonaceous fouling. Radially, from the wire surface, they observed, iron sulfide, a coke layer interspersed with iron sulfides, and an outermost layer of toluene insoluble *pitch*. A second study by Stephenson et al.[22] examined the time evolution of a fouling wire, under similar

experimental conditions, which revealed the formation of iron sulfide was nearly instantaneous and preceded carbonaceous fouling. They also demonstrated an inhibitory effect of Thiophene, highlighting the importance of sulfur speciation, not total sulfur content, towards sour corrosion induced fouling.

Derakhshesh et al.[19] compellingly demonstrated catastrophic chemical reaction fouling due to unstable asphaltenes, under delayed coker furnace conditions. They used 316 stainless-steel wires, heated to above 500 °C. Instability of the asphaltene fraction was driven by additions of an aliphatic oil. The foulant observed on their 316 stainless steel wires was comprised of iron sulfides and thermal coke, a similar foulant morphology to that of Stephenson. Derakhshesh[20] also explored the role of sulfide additives on fouling. Their results showed chemicals with higher sulfur content produced more coke and iron sulfide. This contrasts with the inhibitory effect of Thiophene demonstrated by Stephenson et al.,[22] and further exposes a strong dependence on sulfur speciation, towards overall fouling.

2.5 Crude Oil

Table 2.1 Crude assays comparing a heavy, sour crude oil and a light sweet oil. Data source: www.exxonmobil.com/en/company/worldwide-operations/crude-oils/assays

Property	Heavy, Sour Crude	Light, Sweet Crude
API Gravity,	19.2	52.5
Specific Gravity (60/60F),	0.939	0.769
Carbon, wt %	84.3	85.7
Hydrogen, wt %	12.1	14.2
Pour point, F	(16.6)	(85.1)
Neutralization number (TAN), MG/GM	1.103	0.020
Sulfur, wt%	3.950	0.113
Viscosity at 20C/68F, cSt	579.9	1.4
Viscosity at 40C/104F, cSt	125.5	1.0
Viscosity at 50C/122F, cSt	69.1	0.9
Mercaptan sulfur, ppm	59.3	3.0
Nitrogen, ppm	3,709.3	177.3
CCR, wt%	11.3	0.4
N-Heptane Insolubles (C7 Asphaltenes), wt%	9.0	0.02
Nickel, ppm	59.9	0.1

Vanadium, ppm	157.0	0.8
Calcium, ppm	1.2	N/A
Reid Vapor Pressure (RVP) Whole Crude, psi	4.9	10.5
Hydrogen Sulfide (dissolved), ppm	-	N/A
Salt content, ptb	8.8	8.1
Paraffins, vol %	20.0	53.9
Naphthenes, vol %	23.7	30.5
Aromatics (FIA), vol %	55.7	15.6

Physical and chemical properties of a crude oil, refinery feedstock are essential factors to consider in fouling research. Terms *light/heavy*, *sweet/sour* are broad indicators of an oils quality, providing generality to density and sulfur content, while minimal insight into fouling. A heavy, sour crude is one having API° between 22° and 10° and sulfur content greater than 0.5wt%. Increased density implies a likely relation to higher asphaltene content.[23] It is typical of a heavy, sour oil to have a greater fouling and corrosion tendency than a light, sweet crude. However, total sulfur content reveals little about corrosivity,[24] and it is not solely the existence of asphaltenes which indicate a problematic crude oil, but rather the stability of their dispersion.[25] A crude oil assay is more detailed and will convey properties such as density, viscosity, pour point, sulfur content, acid number, asphaltene content, carbon residue, among others. Incremental, but still limited insight into fouling propensity is provided. Two crude oil assays are present in Table 2.1, comparing properties of a light, sweet and a heavier, sour material. Notably, the higher density oil has increased viscosity, sulfur and asphaltene content, and acid number. Improving the quality and knowledge depth of feedstock chemistry is essential for fouling research and management, and new techniques are emerging.[26–28]

SARA[29] is a fractionation technique, generalizing the colloidal nature of crude oils, and provides a useful framework to understand deposition, especially due to asphaltene stability. Here, crude oils are considered as a colloidal system made up of the following solubility fractions.

- Maltene fraction – heptane soluble
    - (S) saturates: a precipitant or non-solvent for asphaltenes;[30]
    - (Ar)aromatics: a solvent for asphaltenes;[31]

- (R) resins: a dispersant for asphaltenes;[32]

- (A) asphaltenes – toluene soluble, heptane insoluble.

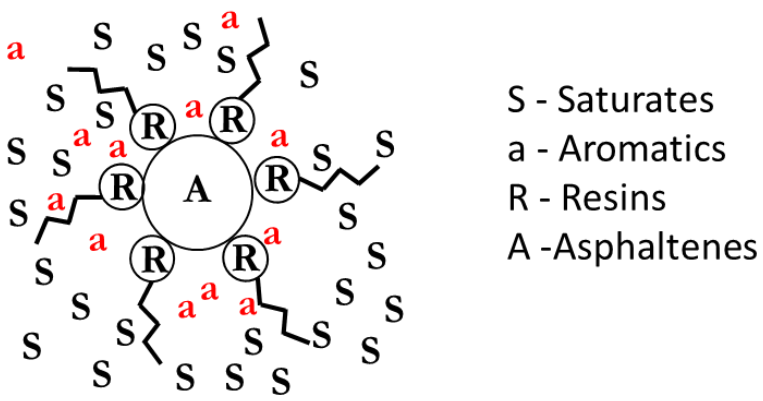

Figure 2.2 The colloidal structure of crude oils. Image sourced from Stephenson, T. Corrosion – Fouling on Heat Transfer Surfaces. University of Alberta, 2015.

$$CII = \frac{Asphaltene + Saturates}{Resins + Aromatics} \qquad \textbf{Equation 2.4}$$

Figure 2.2 is a general diagram of the colloidal nature of crude and Equation 2.4 is a colloidal stability index that can be calculated for a given crude oil, when the SARA fractions are known. If oil has a CII value below 0.7, it is defined as stable and if the CII is higher than 0.9 is considered as unstable.[33] The colloidal stability of the asphaltene phase in a crude oil or blend will have significant effect on fouling tendency.

2.6 Refinery Fouling, Categorically

Fouling has been described by distinct mechanistic scenarios, where three dominate in refinery heat exchangers and furnaces. Those are organic chemical reaction-fouling, corrosion-fouling, and particulate-fouling, typically not manifest as exclusive processes.[34–36] Fouling from crude oil is linked to heteroatom species and distinct, separate phases – water and solids. Organic fouling from crude oils is caused by gums, asphaltenes, and waxes. Below thermal cracking temperature, asphaltene content and stability is a prime driver for chemical reaction fouling.[37–40] Particulate fouling is a dominant mechanism at temperatures below ~180°C, but will occur

throughout a refinery. Suspended solids can be linked to emulsified water and upstream processing, ultimately to the effectiveness of a refinery desalter. These foulants include mineral salts, chlorides, iron-based corrosion products, sands, and clays. Corrosion and chemical reaction fouling intensify above ~220 °C.[41] Beyond ~350 °C thermal, pyrolytic cracking results in the formation of carbonaceous, organic rich deposits of semi-solid crude oil pitch and petroleum coke, also linked to asphaltenes.[6,42–44] Corrosion fouling is driven by sulfur containing compounds, especially H_2S, naphthenic acids, and chlorides.[45,46] Notable synergies amongst the described fouling mechanisms are prolific, especially between sulfidic corrosion and organic fouling,[8,21] and between sulfidic and naphthenic acid corrosion.[47,48].

2.6.1 Chemical Reaction Fouling: Asphaltenes and Thermal Coke

Asphaltenes are associated, almost ubiquitously, with organic, chemical reaction fouling and encumber all stages of crude oil processing.[49,50] Precipitation occurs when changes in composition, temperature, or pressure destabilize the colloidal crude oil system. They are a complex associated species and tend to aggregate and deposit when their dispersion and solubility is disturbed.[51] Once asphaltenes precipitate they will tend to adsorb, especially to heat exchange surfaces, often with such extreme force that the adhered material will resist significant fluid dynamic shear.[52] Asphaltenes,[53] their phase behaviour,[38] and adsorption properities,[54] have been studied in detail. They contain high heteroatom concentration, are the heaviest, most polar and aromatic fraction of a crude oil, and are traditionally classified by solubility in aromatic hydrocarbons (toluene) and insolubility in a linear n-alkane, often heptane.[30,55] Gabrienko et al.[56] provide insight into the phase behavior of asphaltenes by inducing oil instability with n-heptane and analyzing aggregate formation and composition, using in-situ ATR-FTIR spectroscopy.

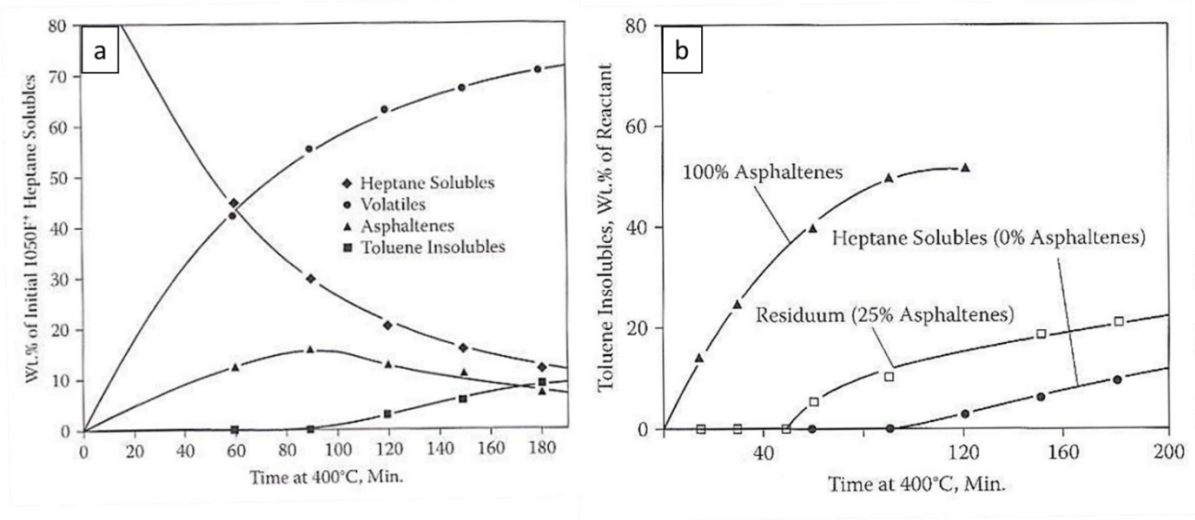

Figure 2.3 An overview of the coking process. (A) Demonstrates the production of toluene insoluble with concomitant reduction in asphaltene. (B) Show the generation of toluene insoluble from fractions containing various percentage of asphaltene. Images sourced from Wiehe, I.A. Process chemistry of petroleum macromolecules. CRC Press, 2008.

Hydrocarbon materials, subject to high temperature processing, thermally crack and produce coke.[57] Treatment above ~350 ºC,[6] leads to the pyrolysis and the production of toluene insoluble pitch and pyrolytic carbon. Pyrolysis is a thermo-chemical decomposition of organic material at elevated temperatures in the absence of oxygen. When a crude oil or residue is subjected to pyrolysis, there is an induction period before coke formation begins. Coke formation is sensitive to asphaltene concentration and phase stability. A successful kinetic model, which describes coke formation from reacted asphaltenes, during thermal treatment at 400 ºC, has been presented by Wiehe.[44] He demonstrated experimentally, an induction period prior to coke formation, and relation to asphaltene solubility. His research showed a period of increasing asphaltene (toluene soluble) concentration followed by coke (toluene insoluble) production and a parallel reduction in asphaltene concentration. This process is presented graphically in Figure 2.3. Conclusively, coke production should be proportional to asphaltene content. Trejo et al.,[58] demonstrated coking from each of the SARA fraction of an atmospheric residue. Their results: 43.1wt% from the asphaltene fraction, 4.4.6wt% from resins, 3.8wt% from aromatics and 0.3wt% from saturates. It is clear the asphaltene fraction is a prime contributor to organic fouling even at temperatures above a cracking threshold. Coke formation tendency of crude oil has also been examined by Schabron et al.[42]

2.6.2 Corrosion-Fouling: Sulfur and Organic Acids

Generally, the constituents in a crude oil feedstock linked to corrosion are sulfur compounds, saltwater, inorganic and organic chlorides, inorganic and organic acids, and organic nitrogen compounds. Corrosive naphthenic acids and sulfur compounds are especially problematic for refinery distillation units and the PHT. Oxygen and sulfur are heteroatoms in a hydrocarbon feedstock and exist in reactive sulfur species and naphthenic acids. Acidic crudes are those with total acid number(TAN) above 0.5 mg,KOH/mg, and high sulfur, sour crudes contain greater than 0.5wt% sulfur.[59,60] Sulfidic corrosion in refining, heavily derived from H2S, has been reviewed by Rebak.[45] Slavcheva[46] presents an analogous review of naphthenic acid corrosion. Synergies between sulfidic and naphthenic acid corrosion are prolific.[61–63]

Naphthenic acid corrosion (NAC), occurs in a number of high temperature refining processes, especially in the range 220 ºC to 400 ºC, which principally includes the PHT, atmospheric and vacuum distillation units.[46,64] NAC depends heavily on temperature, fluid velocity and acid structure. Oxygen is a prime constituent of naphthenic/organic acids, which are a broad and chemically complex species, having the general formula $C_nH_{2n+Z}O_2$.[65] Notably, no direct links have been established between corrosivity and TAN. Modern predictors, using techniques such as ATR-FTIR, Raman, IR and LC-MS have evolved to study the role and evolution of naphthenic acids during high temperature corrosion.[66,67] Flego et al.[68] have evaluated the distribution of naphthenic acids in a crude oil before and after corrosion tests to elucidate which were involved in the observed corrosion processes. It was found that acids with 1-3 naphthenic rings and 14-17 carbon atoms were the most reactive and underwent more significant structural changes. Naphthenic acids that thermally decompose have been shown to react and produce pseudo-passivating oxide corrosion scales. Jin et al.[69] examined the protectiveness of oxide layers formed on carbon steel from a pure, model acid (palmitic acid) and a commercial naphthenic acid. Molecular structure of the acid was a principal factor in the formation and protectiveness of resultant iron oxide corrosion products. Importantly, the two acids reacted differently in the presence of sulfur compounds. Furthermore, in a corrosion study using a mixed

environment of naphthenic acids and reactive sulfur species, magnetite was identified on a 5% Cr steel, and noted as an important aspect for surface passivation.[70] Naphthenic acids are notorious for their role in deteriorating pseudo-passivating iron sulfide scales.[61] Below 230 °C, carbon steels suffer only mildly in the presence of naphthenic acids and when flow rates are low. 5wt% Cr, 0.5wt% Mo and 9wt% Cr, 1wt% Mo are more resistant than carbon steels and can be used above 230 °C and at moderate flow rates. Austenitic stainless steels, especially with molybdenum additions are significantly resistant to NAC.[71]

Sulfidation, sour / sulfidic corrosion may be defined as the corrosive attack experienced by metals and alloys when exposed to *sulfur-bearing* atmospheres, especially those containing H_2S, leading to formation of metallic sulfide(s) as corrosion product(s). Zheng et al.[72] have studied the diverse nature of corrosion products, formed on steels by H_2S in an aqueous environment, which included mackinawite, cubic FeS, troilite, and pyrite. Wet, sour corrosion processes are important upstream of a refinery PHT, below ~200 °C, in systems containing a significant aqueous fraction. Here, sulfidic/sour corrosion of refinery steels is due to reactive sulfur compounds, including H_2S, throughout the range 230–550+ °C.[73] Some sulfur compounds found in petroleum may react directly with a steel surface, while some decompose to form hydrogen sulfide. Collectively, these reaction pathways, of S-bearing species with iron in steels, is simply referenced as sulfidation.

It is important to consider sulfur speciation and their ability to react to the aggressive H_2S species. Resultant iron sulfide corrosion scales are most commonly pyrrhotite(s), which is an identifier for all sub-stoichiometric, iron mono-sulfides, with the general formula $Fe_{1-x}S$, and NiAs substructure[74] This type of attack is pervasive throughout the higher temperature portion of the PHT and in atmospheric and vacuum distillation units.[45] In some cases, iron sulfide scales offer a level of protectiveness to the underlying steel, but the predictability of this behavior is low. It is complicated by the presence of naphthenic acids, sulfur speciation and growth conditions affecting inherent scale porosity and material stresses that lead to delamination. Although total sulfur content is a driver for

anticipating corrosive tendency, the principal factors influencing sour corrosion are temperature, metallurgy, and sulfur speciation.

Total sulfur content in an oil is not a sufficient predictor for sour corrosion, and speciation of sulfur compounds must be considered. Reactive sulfur species include H_2S, organic sulfides, and disulfides,[61] while thiophenes have been shown to have inhibiting effects on corrosion and fouling.[22] Furthermore, at temperatures over 350 ˚C, hydrogen sulfide forms from the thermal decomposition of thermally labile sulfur compounds in crude oils.[75] Lepore,[76] completed a detailed study comparing the high temperature decomposition and corrosion tendency of 8 model sulfur compounds. He used: carbon steel; low alloy 5wt% Cr and 9wt% Cr, 1wt% Mo steels; 410 and 316 stainless-steels. Figure 2.4 shows the iron sulfide corrosion products on the exposed metallurgies. Delamination is observed on the steels with thicker films, and the 316-stainless steel was most corrosion resistant in all scenarios.

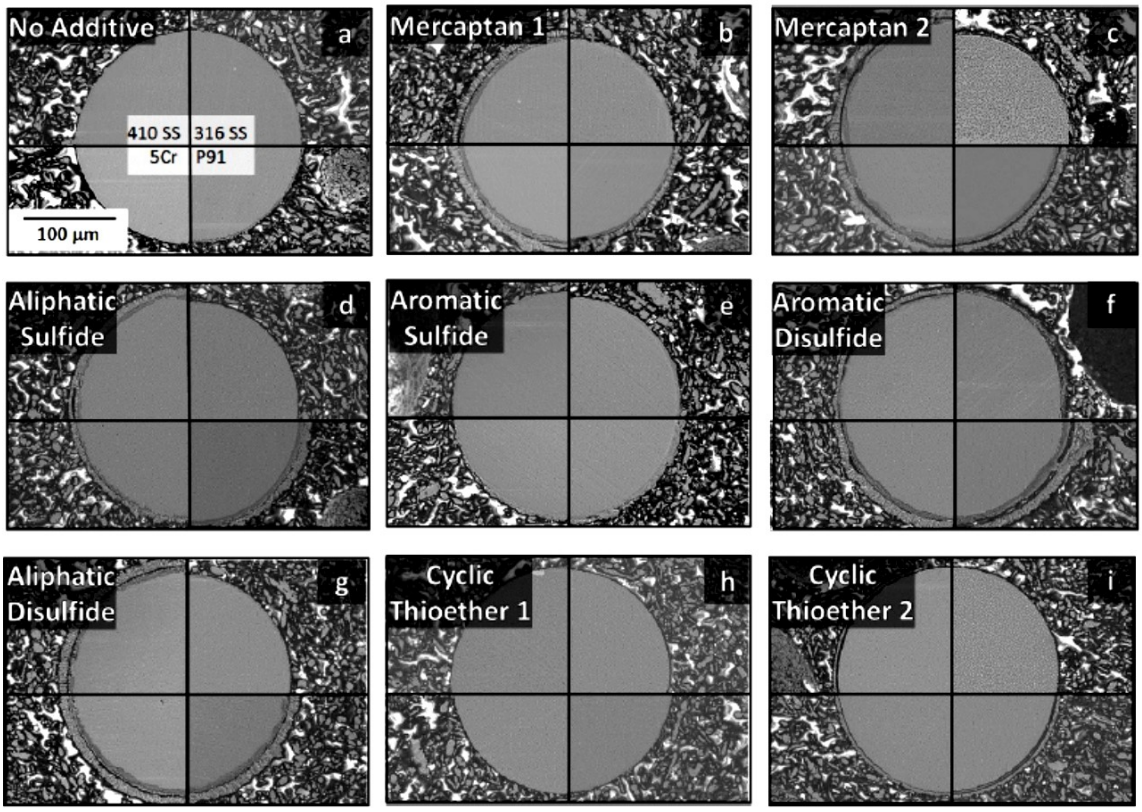

Figure 2.4 SEM cross-sections of corroded wires. In each sub-figure, the metallurgies 410 stainless-steel, 316 stainless-steel, 9%Cr-1%Mo, and 5%Cr are presented in a clockwise pattern starting with 316 stainless-steel in the top-right. The sulfide reactants are indicated in each image.

Carbon steels are the most common refinery metals, used in about 80% of components, but possess little resistance to sour corrosion in hostile environments, especially above ~230C. [5,45] As the aggressive nature of the system intensifies, steels with increased chromium content, up to and including stainless steels, are employed.[77] In one study,[78] sulfidation resistance of three common refinery steels was assessed. Materials, XC18 carbon steel (Fe, 0.18%C), P5 alloy steel (Fe, 5%wt Cr, 0.5wt% Mo) and 304L stainless-steel (Fe, 18wt% Cr, 8wt% Ni), were exposed to a high sulfur oil at 300 °C for up to 98 hours. Corrosion rates were 304L less than P5, less than XC18. Detailed analysis of the corrosion product revealed iron sulfides, as sub-stoichiometric pyrrhotite(s). Stephenson et al.[21,22] also observed a pyrrhotite phase when pure iron and 316SS wires were immersed in an atmospheric reduced crude with high sulfur content and heated to above 500 °C. Lepore also identified pyrrhotite on his wires of carbon steel, low alloy 5wt%Cr steel, 9wt%Cr-1wt%Mo steel, 410 stainless-steel, and 316 stainless-steel.

2.6.3 Particulate-Fouling

Suspended solids are present as contaminants in crude oils and influence fouling tendencies. Not only detrimental to the fouling process, but also increase corrosion of heat exchangers and poison catalysts.[41] These materials include corrosion products (iron oxides and sulfides), mineral salts (chlorides, carbonates, sulfates), clays and sands.[2,3,7]. Water soluble components may enter a refinery system via tightly emulsified water in the crude oil feedstock. Chemical inhibitors, added in upstream processing, such as corrosion, mineral scale and paraffin inhibitors, may also negatively influence corrosion and fouling in the refinery.[41] The efficiency of a refinery desalting unit will dictate how much of these material gets to the PHT, but small amounts are always expected.[79,80] That is, particulate fouling in the PHT is primarily mitigated by efficient operation of the desalting unit. Experimentally, Watkinson doped a crude oil with iron and aluminum oxide particles and noted intensified fouling propensity.[35] Fan et al.[12] identified suspended iron sulfides and oxides as a causation for fouling in their examination of deposits from an Australian light crude. Petkovic and Watkinson[18] investigated particulate fouling by adding micron-scale iron oxide(Fe_2O_3), of different

size, and at different concentrations. With increasing additive concentration, fouling rates dropped initially before peaking and finally falling to very low levels. The vivid drop in deposition at higher dopant concentration was attributed, in part, to an erosion mechanism.

2.7 Mitigation

2.7.1 Blending

Blending high quality, easily *refinable* crudes with opportunity feedstocks is a driver for a balanced refining economy. Blending can mitigate corrosion-related fouling by dilution of sulfur content and acidity, and chemical reaction fouling by reducing asphaltene concentration. Furthermore, mixing a heavy, viscous crude with a lighter oil will reduce viscosity and minimize the hydraulic power requirements. Properly managed, blending can be an effective tool for refining low-cost, high fouling crudes. Improper management will result in catastrophic fouling rates, primarily from unstable asphaltene, at significant cost. Wiehe[38] describes incompatible, self-incompatible and nearly incompatible oil mixtures, in a recent review of the field. Alvarez et al.[81] utilized ellipsometry to measure instability in crudes and blended feedstock. Viscosity and density data has been used to model compatibility.[82] Fan et al.[12] demonstrated fouling from a self-incompatible, light Australian crude oil, due to unstable, albeit low, asphaltene concentration. Derakhshesh[19] showed catastrophic fouling when an aliphatic oil and an atmospheric residue, high in asphaltene, were mixed. An opposite trend was demonstrated by Hong and Watkinson,[83] when an aromatic diluent, an asphaltene solvent, was added to a crude oil, reducing fouling tendency. Stratiev et al.[28] investigated blends of 22 crude oils, characterized by 67 physical and chemical properties.

2.7.2 Chemical Additives

Chemical inhibitors have been used to stabilize asphaltenes, reduce coking and mitigate corrosion. Additives, derived from multifunctional polyisobutenyl oxazolidines, have been studied with some success for their ability to stabilize asphaltenes.[84] Phthalocyanines of tin and silicon have also been established as asphaltene stabilizers.[85] Rogel [86]presents a theoretical framework for the development and mechanism of asphaltene inhibitors. Sulfur compounds are added to a feedstock to

reduce coking.[87] Additives containing sulfur and silicon have demonstrated effectiveness at reducing coking during steam cracking.[88] Stephenson et al.[22] demonstrated a dramatic reduction in corrosion induced fouling, at 550 °C using additions of thiophene.[22] Seed particles can be added to a fouling system to redirect the deposition of pyrolytic coke from the surface of process equipment to the particles.[89] A recent work provides insights for fouling potential prediction and also provided a unique method to evaluate the performance of antifoulants.[90]

Coking reactions can be minimized in the presence of *available* hydrogen. Hydrogen terminates free radical intermediates, ensuring their reactivity is removed before polymerisation/condensation/coking can occur. Without sufficient hydrogen to stabilize free radicals, conversion continues to produce toluene insoluble material until coke is finally formed. Habib et al.[91] used an iron sulfide to catalyze olefin hydrogenation, in an atmosphere of hydrogen and in the presence of hydrogen donor solvents. The choice of an iron sulfide catalyst is significant; it has low activity for hydrogenation and it was expected to limit hydrogen addition to aromatics. They found a significant reduction to addition reactions and good control over selective thermal cracking versus aromatic hydrogenation. A study by Zachariah et al.[92] investigated several donor solvents, based upon hydrogen transfer characteristics, namely donation and shuttling, for their efficacy towards suppressing coke formation during pyrolysis of a bitumen feedstock. Tetralin functioned best at suppressing coke formation. Additionally, the role of system pressure was investigated, and it was shown that increasing pressure, kept light solvent material in the liquid phase, which also served to suppress coke formation. Overall, results from this study point towards hydrogen availability being a dominant factor for controlling coke formation.

2.7.3 Materials Selection

Material selection has significant impact on corrosion, especially when refining sour crudes with naphthenic acids. Chromium is the fundamental alloying element added to steels to impart corrosion resistance. As corrosivity increases, carbon steels are replaced by low alloy, chromium(Cr) - molybdenum(Mo) steels and stainless-steels. Modified McConomy curves show increasing

resistance to sour corrosion with chromium levels, from mild carbon steel, through 5wt%Cr, up to 18wt% Cr-8wt% Ni stainless-steel.[45] In the presence of high TAN crude oils, molybdenum-bearing alloy steels, also with increased chromium content, and stainless steels are used.[64] Steels with 5wt%Cr-0.5wt%Mo and 9wt%Cr-1wt%Mo are the most common metallurgies selected for improved corrosion resistance over carbon steel. Stainless steels, especially the 300 series austenitic stainless-steels (304SS, 310SS, 316SS, 317SS, 347SS) are employed as corrosive tendencies increase further. Titanium alloys and nickel alloys, amongst a few others are used in the most aggressive refining operations.[93] Stephenson et al.[21] demonstrated improved corrosion resistance of 316 stainless-steel versus pure iron. Wang and Watkinson[5] showed decreasing susceptibility to corrosion over a range of steels: carbon steel, 9wt%Cr steel, 317 stainless-steel and a nickel alloy, respectively. Kamel et al.,[94] demonstrated incremental resistance to sour corrosion with steels having increased chromium content, specifically carbon steel < Cr-Mo steel < stainless steel. Li and Chen[95,96] have studied the resistance of iron-nickel-chromium steels (austenitic steels), with silicon additions, to sulfidic corrosion in high temperature oxidizing and carburizing environments.

Chromium-molybdenum steels, containing less than 10wt% Cr, combine high creep strength, good ductility, moderate corrosion resistance, and good thermal cycling properties.[97] The 9wt% Cr-1wt% Mo steels are an important grade of steel in the refinery industry, due its mechanical properties at elevated temperatures combined with moderate resistance to high temperature sulfidic and naphthenic acid corrosion.[98] Moura explores the effect on corrosion resistance when manipulating Mo content of a Fe-9Cr-xMo steel.[99] Qu et al.,[48] demonstrated corrosion rates: carbon steel < 5wt% Cr-0.5wt% Mo steel in naphthenic acid; 5wt% Cr steel < carbon steel in reactive sulfide (DMDS); and 5wt% Cr steel < carbon steel mixed systems. It is interesting to note that the chromium-molybdenum steel was more susceptible to naphthenic acid corrosion than carbon steel. Sixian[100] investigated naphthenic acid corrosion of a carbon steel and a 5wt% Cr-0.5wt% Mo steel and highlight that increasing fluid velocity, increased corrosion rates.

Stainless steels have been defined as complex alloy steels containing a minimum of 10.5wt% Cr.[101] These materials derive enhanced passivation from a nano-meter sized layer of metallic oxide, high in chromium. Chromia-Cr_2O_3, spinel $(Fe,Mn)Cr_2O_4$ and $(Fe,Cr)_2O_3$ have been identified.[95,102,103] Ramachandran et al.,[104] have described 5.0–6.7 nm thick oxide layers: an outer layer rich in a mixture of $FeO.Fe_2O_3$, an intermediate layer rich in Cr_2O_3 with a mixture of $FeO.Fe_2O_3$ and an inner oxide layer rich in nickel, on 316 stainless-steel. Below, 10.5wt% Cr continuously passivating oxide layers are not expected, but corrosion resistance and mechanical properties are improved, none the less. Austenitic stainless steel have gained wide acceptance in high temperature applications because of their corrosion resistance, strength and toughness at both elevated and ambient temperature.[105] In general, they are Fe-C-Cr-Ni and Fe-C-Cr-Mn-Ni-N alloys containing 0.03–0.35 wt% C, 16–26 wt% Cr, 0.75–19.0 wt% Mn, 1–40 wt% Ni, and sufficient Ni to stabilize austenite at room and elevated temperatures.[101] The 300 series, Cr–Ni types contain higher amounts of Ni and up to 2wt% Mn, while Mo, Cu, and Si may be added to increase corrosion resistance. Type 316 contains Mo, which aids integrity of the passivating Fe,Cr-oxide, especially in the presence of chlorides.[106] It is well established that stainless steels are susceptible to chloride attack, especially when in a stressed state (SCC – stress corrosion cracking). Type 347 contains Nb and used when sensitization is a concern. Composition of 304SS, 316SS, and 347SS stainless steels is presented in Table 2.2.

Table 2.2 Composition of three austenitic stainless steels: 304, 316 and 347. Data from ASM Metals Reference Book, Third Edition, Michael Bauccio, Ed., ASM International, Materials Park, OH, p357-358, (1993).

Steel	Phase	C	Mn	Si	Cr	Ni	P	S	Other
		wt%	wt%	wt%	wt%	wt%	wt%	wt%	
304L	Austenitic	0.03	2	1	18-20	8-12	0.045	0.03	
316L	Austenitic	0.03	2	1	16-18	10-14	0.045	0.03	2.0-3.0 Mo
347	Austenitic	0.08	2	1	17-19	9-13	0.045	0.03	10x%C min Nb
410	Martensitic	0.15	1	1	11.5-13.5	-	.04	.03	

2.7.4 Coatings

Coatings have been utilized as a mitigation tool to hinder fouling and corrosion in petroleum and petrochemical processing. Broutin et al.[107] examine the effectiveness of a large number of coating materials and processes, utilized as an anti-fouling strategy in high temperature petroleum and petrochemical processes. They study plasma sprayed coatings, packed cementation coatings, and CVD coatings and find chromia packed cementation coatings, titanium carbide, and silicon carbide CVD samples were most effective. Titanium nitride coatings have also been applied successfully, as an anti-coking barrier for materials used in high temperature hydrocarbon cracking reactors.[108,109] Also titanium oxide.[110] Wang and Watkinson[5] observed that carbon steel coated with chrome reduced the inorganic(ash) portion of deposits, when compared with uncoated steels and stainless steels, suggesting improved corrosion resistance. Li and Yang[111] applied a sintered glass coating to heat resistant steel to reduce catalytic coking and carburization in 800 ºC and 85 0ºC coking experiments.

Fluid velocity can be increased to a threshold value where the shearing stress at a fouling interface will deter foulant accumulation. Threshold fouling models consider a point when fluid shearing stresses fully overcome adhesive forces, effectively stopping fouling. Equation 2-3 is a model for systems undergoing chemical reaction fouling, widely accepted, originally proposed by Ebert and Panchel.[112] It suggests a threshold condition, where material removal can balance deposition processes and fouling rates are forced to zero, or become negative. Experimentally, Crittenden et al.[15] have demonstrated both positive and negative fouling accumulation as a function of fluid velocity. Yeap et al.,[113] present how consideration of threshold fouling data and modelling can be introduced into heat exchanger design to reduce fouling.

2.8 Synergies Amongst Fouling

2.8.1 Surface Initiation

Fouling is an interfacial phenomenon. The fields of heterogeneous catalysis and high temperature, gas phase cracking demonstrate that specific chemical and physical properties of a surface can be important initiators for fouling reactions. Heterogeneous catalysis is used extensively

in refining and functions in two important catalytic processes: cracking and hydro-processing. Catalytic cracking reactions rely on acidic sites that enhance adsorption and provide a low energy pathway for breaking bonds in larger hydrocarbon molecules.[114] Moro-oka[115] has studied the acidity of various metal oxides, specifically low coordination iron. Hydrodesulfurization, a subset to hydro-processing, results when hydrogen becomes promoted to an active state, typically over a metallic sulfide, and reacts to replace sulfur in sulfur-bearing species, H2S for example, in a crude oil.[116] Catalyst fouling by coking and asphaltene adsorption is a severe encumbrance for refiners.[117,118]

High temperature ethane cracking has been shown to have a strong link to surface chemistry. Catalytic, filamentous growth of carbon by Fe and Ni and mitigation by metallic-chromium containing oxides is described by Liu et al.[119] Gandarillas et al.[120] studied coke formation during steam cracking of ethane at 1159 K, over nine metallic alloys. Initial and asymptotic coking rates, changed by more than 250%, with varying metallurgy. They highlight the surface oxide composition and not the bulk material as the prime influencer. Interestingly, aluminum-containing alloys were most effective, manganese chromite films inhibited coking to an extent, and Si additions were also beneficial. The aluminum-containing materials revealed a degree of susceptibility to internal oxidation and carburization, compromising resistance after cyclic coking-decoking. Additionally, uniform surface composition, spalling and fracture resistance were offered as important influencers. Jazayeri and Karimzadeh[121] evaluated coke production on Cr, Fe and stainless steel surfaces and a subset of pre-sulfided coupons, at temperatures in excess of 800 ºC, in mixed H_2S/Ethane/Nitrogen atmospheres. Their results convey that pre-sulfided coupons reduced coke formation for all samples, and Fe experienced the highest coking rates. The researchers hypothesize a competitive process involving H_2S promoted adsorption and active site blocking by sulfide corrosion product, to explain a reduction to the catalytic effect. An excellent overview on the effects of H_2S on coke formation for these high temperature, gas phase reactions is provided by Tan and Baker.[122] They found that catalytic coke formation was dependent on the concentration and type of sulfide species, and that H_2S was a strong promoter of carbon growth.

2.8.2 Sulfidic and Naphthenic Acid Corrosion

A complex relationship exists between sulfidic and naphthenic acid corrosion. These mechanisms exist simultaneously in almost all crude oils and are reactive in an overlapping temperature range (~220-400 °C), often one against the other.[45,46] Separately, both processes can lend a degree of passivity to a metallic, steel surface. Sulfidic corrosion forms pseudo-passivating layers of iron sulfide, often as pyrrhotite, in refinery conditions.[123] Naphthenic acids and naphthenates have been shown to form iron oxides, in some cases as magnetite, which can also be pseudo-passivating.[69] Sulfidic corrosion, resulting in a layer of iron sulfide, can resist naphthenic acid attack. Rebak[45], showed increased H_2S content, relative to a constant acid content, reduces corrosion of carbon steel. Slavcheva[46] states that in many cases, a refinery processing low sulfur crude is susceptible to naphthenic acid corrosion, and presents supportive information in his review. In contrast, naphthenic acids were shown to have deleterious effects on the passivation of iron sulfide layers, especially when fluid velocity is high. Huang et al.,[47] has demonstrated experimentally that below a certain concentration reactive sulfur content accelerated naphthenic acid corrosion, but prevented naphthenic above a threshold content. Zheng et al.,[48] presented an identical trend, then went on to trial the effect of constant sulfur and increasing TAN. He shows that corrosion rate rises, then decreases with increasing TAN, and the effect was more pronounced for carbon steel than a 5wt% Cr, 0.5wt% Mo steel.

2.8.3 Corrosion and Fouling

Undoubtedly, a complex synergy exists between surface condition and fouling / corrosion. Wang and Watkinson[5] have studied fouling from a sour crude fraction as function of corrosive resistance metallurgy and temperature. Five metals: 1018 carbon steel, 9-chrome steel, 317 stainless steel, Incoloy 825 and Cr-coated carbon steel were immersed, isothermally at 380-410°C, for up to 24 hours in an atmospheric reduced crude containing 4.1wt% sulfur and 710wppm dispersed iron. Analysis of the foulants revealed sour corrosion product at the initial interfaces of all metals, except the coated carbon steel. The content of organic carbonaceous foulant was more pronounced at

temperatures over 400 °C, due to coking reactions. In experiments run at a constant 390 °C, deposits were analyzed over the depth of the resultant foulant, from the initiating to terminal surfaces. On carbon steel and 9wt% Cr steel the foulant had the highest iron (sulfide) content, and iron sulfides comprised at least 50wt% of the foulant over its depth. Deposits on 317 stainless-steel had intermediate iron content, Incoloy 825, and Cr-coated carbon steel had the least. This is consistent with their expected corrosion resistance. Conversely, the foulant on Incoloy 825 and Cr-coated carbon steel contained much higher carbon content, nearly a constant 85wt%. Notably, on Cr-coated carbon steel the foulant had a constant iron content, throughout its depth, which suggests this is a baseline for iron sulfide deposition, due to the natural iron content in the oil. Largely, the observed foulants were comprised of carbonaceous material and iron sulfides. Iron sulfide content decreased with increasing corrosion resistance of the underlying metals and outward from the initial surface. Interestingly, good deposit adherence was associated to foulants with low iron sulfide content, ie the more corrosion resistant material, which links mechanical properties of the corroding interface to ultimate fouling thickness. The low corrosion-fouling rate on Cr-coated carbon steel reveals potential for coatings that resist corrosion.

Many of the observations of Wang and Watkinson have also been made by Stephenon et al.,[21,22] who tested fouling and corrosion tendency at above 500 °C on iron and 316 stainless-steel. Investigation of their experimentally derived foulants revealed similar deposits, where radially outwards: a corroded surface, of metallic sulfides, and carbonaceous material interspersed with iron sulfides. Significant study of the fouled wire surfaces, using techniques such as SEM and XPS (X-ray Photoelectron Spectroscopy), yielded new, albeit preliminary, insight: They observed that for heated metal surfaces immersed in hot oil, surface corrosion via sulfidation initiates in a matter of minutes and carbonaceous fouling occurs only subsequently. The corrosion process, driven by H_2S that is evolved at elevated temperatures, results in a weakly adhering pyrrhotite ($Fe_{1-x}S$) layer that cyclically undergoes surface growth and detachment. It was hypothesized that this iron sulfide layer catalyzes subsequent carbonaceous deposition, at high rates. Delaminated corrosion product is also

seen to attract carbonaceous material away from the immediate fouling surface inferring a role of particulate fouling. Delamination events were observed for both metallurgies, but severe material loss distinguished the iron substrate from the stainless steel. The high Cr alloy – 316 stainless-steel, reduces the rate of fouling considerably, versus pure iron. Presumably, the natural terminal metallic oxide(s) exists as a barrier to diffusion, inhibiting surface sulfide growth. Thus, metallurgy selection emerges as an obvious parameter to fouling mitigation, as does coating technology. A critical observation in Stephenson's second publication was that significant organic fouling did not initiate until the metal surface was fully covered by a microscopic layer of sulfide. Furthermore, a reduction in corrosion, demonstrated using thiophene as an inhibitor, drastically reduced overall carbonaceous fouling amount.

Delamination of corrosion films introduces particulates into the oil that can influence downstream fouling. Suspended corrosion residuals, such as iron sulfides and oxides, have been demonstrated to intensify fouling.[35] Rebak[45] presents data showing a decrease in corrosion scale delamination with increasing chromium content. This, in part, can be attributed to mechanical properties imparted by increased Cr content. Increasing naphthenic acid was also shown to enhance delamination of iron sulfide scale. Stephenson et al.[21]note improved foulant adherence to 316 stainless-steel versus pure iron wires, and iron sulfide particulates throughout carbonaceous foulant, were observed. Lepore[76] noted frequent delamination events of sulfide scales from carbon steel when higher reactivity sulfur species were used as corrodants / precursors for thermally generated H_2S. Further, it is demonstrated that these events occur more frequently with reactive sulfides and less corrosion resistant material (316SS, 410SS, P91, 5Cr, CS).

In summary, reaction products from corrosion buildup and deteriorate the surface of processing vessels, which has been demonstrated to have meaningful influence on subsequent fouling. The interactions between inorganic fouling, linked to corrosion, and organic, chemical reaction fouling is not well understood, but research is ongoing. Watkinson[8] notes contradicting results in literature regarding corrosion-influenced fouling and presents three, possibly temperature

dependent, mechanisms: FeS particulate fouling; FeS film formation and enhanced wetting of coking precursors; simultaneous FeS and coke formation. With each mechanism an associative catalytic effect of FeS towards organic, carbonaceous fouling is offered, supported by previous studies. Wiehe[37] has described the role of iron sulfide towards enhancing wetting behavior of fouling precursor phases on a metallic surface. Wang and Watkinson[5] propose enhanced adhesion and trapping of fouling precursors due to roughening of a corroding surface. Stephenson have noted all three catalytic effects in their works. At the very least, there exists a synergism that warrants further study.

2.9 References

(1) Speight, J. G. *Fouling in refineries*; Gulf Professional Publishing, 2015.

(2) Mozdianfard, M. R.; Behranvand, E. In *Applied Thermal Engineering*; 2013; Vol. 50, pp 908–917.

(3) Tay, F. H.; Kazarian, S. G. *Energy and Fuels* **2009**, *23* (8), 4059–4067.

(4) Deshannavar, U. B.; Rafeen, M. S.; Ramasamy, M.; Subbarao, D. *Journal of Applied Sciences*. 2010, pp 3167–3174.

(5) Wang, W.; Watkinson, a. P. *Heat Transf. Eng.* **2015**, *36* (7–8), 623–631.

(6) Ebrahimi, S.; Moghaddas, J. S.; Aghjeh, M. K. R. *Fuel* **2008**, *87* (8–9), 1623–1627.

(7) Gentzis, T.; Parker, R. J.; McFarlane, R. A. *Fuel* **2000**, *79* (10), 1173–1184.

(8) Wang, W.; Watkinson, A. P. *Proc. Int. Conf. Heat Exch. Fouling Clean. IX* **2011**, 23–30.

(9) Bennett, C. a.; Kistler, R. S.; Nangia, K.; Al-Ghawas, W.; Al-Hajji, N.; Al-Jemaz, A. *Heat Transf. Eng.* **2009**, *30* (10–11), 794–804.

(10) Morales-Fuentes, A.; Picón-Núñez, M.; Polley, G. T.; Méndez-Díaz, S. *Appl. Therm. Eng.* **2014**, *62* (2), 777–784.

(11) Coletti, F.; MacChietto, S. *Ind. Eng. Chem. Res.* **2011**, *50* (8), 4515–4533.

(12) Fan, Z.; Rahimi, P.; McGee, R.; Wen, Q.; Alem, T. *Energy and Fuels* **2010**, *24* (11), 6110–6118.

(13) Lestina, T. G.; Zettler, H. U. *Heat Transf. Eng.* **2014**, *35* (3), 217–223.

(14) P. Watkinson, A. In *Heat Exchanger Fouling and Cleaning: Fundamentals and Applications*; 2004.

(15) Yang, M.; Wood, Z.; Rickard, B.; Crittenden, B.; Gough, M.; Droegemueller, P.; Higley, T. *Appl. Therm. Eng.* **2013**, *54* (2), 516–520.

(16) Aminian, J.; Shahhosseini, S. *Int. Commun. Heat Mass Transf.* **2009**, *36* (5), 525–531.

(17) Polley, G. T.; Wilson, D. I.; Yeap, B. L.; Pugh, S. J. In *Applied Thermal Engineering*; 2002; Vol. 22, pp 777–788.

(18) Petkovic, B.; Watkinson, P. *Heat Transf. Eng.* **2013**, *35* (3), 302–310.

(19) Derakhshesh, M.; Eaton, P.; Newman, B.; Hoff, A.; Mitlin, D.; Gray, M. R. In *Energy and Fuels*; 2013; Vol. 27, pp 1856–1864.

(20) Derakhshesh, M. *ProQuest Diss. Theses Glob.* **2012**.

(21) Stephenson, T.; Kubis, A.; Derakhshesh, M.; Hazelton, M.; Holt, C.; Eaton, P.; Newman, B.; Hoff, A.; Gray, M.; Mitlin, D. *Energy and Fuels* **2011**, *25* (10), 4540–4551.

(22) Stephenson, T.; Hazelton, M.; Kupsta, M.; Lepore, J.; Andreassen, E. J.; Hoff, A.; Newman, B.; Eaton, P.; Gray, M.; Mitlin, D. *Fuel* **2015**, *139*, 411–424.

(23) Trejo, F.; Centeno, G.; Ancheyta, J. *Fuel* **2004**, *83* (16), 2169–2175.

(24) Ávila, B. M. F.; Pereira, V. B.; Gomes, A. O.; Azevedo, D. A. *Fuel* **2014**, *126*, 188–193.

(25) Rogel, E.; Ovalles, C.; Moir, M. In *Energy and Fuels*; 2012; Vol. 26, pp 2655–2662.

(26) Kekäläinen, T.; Pakarinen, J. M. H.; Wickström, K.; Lobodin, V. V.; McKenna, A. M.; Jänis, J. *Energy & Fuels* **2013**, *27* (4), 2002–2009.

(27) Ho, T. C. *Int. J. Heat Mass Transf.* **2016**, *95*, 62–68.

(28) Stratiev, D.; Shishkova, I.; Nedelchev, A.; Kirilov, K.; Nikolaychuk, E.; Ivanov, A.; Sharafutdinov, I.; Veli, A.; Mitkova, M.; Tsaneva, T.; Petkova, N.; Sharpe, R.; Yordanov, D.; Belchev, Z.; Nenov, S.; Rudnev, N.; Atanassova, V.; Sotirova, E.; Sotirov, S.; Atanassov, K. *Energy and Fuels* **2015**, *29* (12), 7836–7854.

(29) ASTM. *ASTM Stand.* **2016**, 1–43.

(30) ASTM. *Pet. Prod. Lubr. Foss. Fuels* **2013**, *05*, 1–6.

(31) Wang, J.; Buckley, J. S. *Energy and Fuels* **2003**, *17* (6), 1445–1451.

(32) Mousavi, M.; Abdollahi, T.; Pahlavan, F.; Fini, E. H. *Fuel* **2016**, *183*, 262–271.

(33) Ashoori, S.; Sharifi, M.; Masoumi, M.; Mohammad Salehi, M. *Egypt. J. Pet.* **2017**, *26* (1), 209–213.

(34) Somerscales, E. F. C. *Exp. Therm. Fluid Sci.* **1997**, *14* (4), 335–355.

(35) Watkinson, a. P. *Heat Transf. Eng.* **2007**, *28* (January 2015), 177–184.

(36) Watkinson, A. P.; Wilson, D. I. *Exp. Therm. Fluid Sci.* **1997**, *14* (4), 361–374.

(37) Wiehe, I. A. *Process Chemistry of Petroleum Macro Molecules*, Vol. 121.; CRC Press: Boca Raton, FL, 2008.

(38) Wiehe, I. A. In *Energy and Fuels*; 2012; Vol. 26, pp 4004–4016.

(39) Painter, P.; Veytsman, B.; Youtcheff, J. *Energy & Fuels* **2015**, *29* (5), 2951–2961.

(40) Forte, E.; Taylor, S. E. *Adv. Colloid Interface Sci.* **2015**, *217*, 1–12.

(41) Coletti, F.; Hewitt, G. F. *Crude Oil Fouling*; 2015.

(42) Schabron, J. F.; Pauli, A. T.; Rovani, J. F.; Miknis, F. P. *Fuel* **2001**, *80* (10), 1435–1446.

(43) Souza, B. A.; Matos, E. M.; Guirardello, R.; Nunhez, J. R. *J. Pet. Sci. Eng.* **2006**, *51* (1–2), 138–148.

(44) Wiehe, I. A. *Ind. Eng. Chem. Res* **1993**, *32*, 2447–2454.

(45) Rebak, R. B. *Corrosion Reviews*. 2011, pp 123–133.

(46) Slavcheva, E.; Shone, B.; Turnbull, A. *Br. Corros. J.* **1999**, *34* (2), 125–131.

(47) Huang, B. S.; Yin, W. F.; Sang, D. H.; Jiang, Z. Y. *Appl. Surf. Sci.* **2012**, *259*, 664–670.

(48) Qu, D. R.; Zheng, Y. G.; Jing, H. M.; Yao, Z. M.; Ke, W. *Corros. Sci.* **2006**, *48* (8), 1960–1985.

(49) Tavakkoli, M.; Panuganti, S. R.; Vargas, F. M.; Taghikhani, V.; Pishvaie, M. R.; Chapman, W. G. *Energy & Fuels* **2014**, *28* (3), 1617–1628.

(50) Tavakkoli, M.; Panuganti, S. R.; Taghikhani, V.; Pishvaie, M. R.; Chapman, W. G. *Energy and Fuels* **2014**, *28* (6), 3594–3603.

(51) Seifried, C. M.; Crawshaw, J.; Boek, E. S. In *Energy and Fuels*; 2013; Vol. 27, pp 1865–1872.

(52) Bennett, C. A. *Heat Transf. Eng.* **2012**, *33* (15), 1246–1250.

(53) Mullins, O. C. *Annu. Rev. Anal. Chem. (Palo Alto. Calif).* **2011**, *4*, 393–418.

(54) Adams, J. J. *Energy and Fuels*. 2014, pp 2831–2856.

(55) Leyva, C.; Ancheyta, J.; Berrueco, C.; Millán, M. *Fuel Process. Technol.* **2013**, *106*, 734–738.

(56) Gabrienko, A. A.; Lai, C. H.; Kazarian, S. G. *Energy and Fuels* **2014**, *28* (2), 964–971.

(57) Guisnet, M.; Magnoux, P. *Appl. Catal. A Gen.* **2001**, *212* (1–2), 83–96.

(58) Alvarez, E.; Marroquín, G.; Trejo, F.; Centeno, G.; Ancheyta, J.; Díaz, J. A. I. *Fuel* **2011**, *90* (12), 3602–3607.

(59) Hsieh, P. Y.; Bruno, T. J. In *Energy and Fuels*; 2014; Vol. 28, pp 1868–1883.

(60) Müller, A. L. H.; Picoloto, R. S.; Mello, P. D. A.; Ferrão, M. F.; Dos Santos, M. D. F. P.; Guimarães, R. C. L.; Müller, E. I.; Flores, E. M. M. *Spectrochim. Acta - Part A Mol. Biomol. Spectrosc.* **2012**, *89*, 82–87.

(61) Yépez, O. *Fuel* **2005**, *84* (1), 97–104.

(62) Qu, D. R.; Zheng, Y. G.; Jing, H. M.; Jiang, X.; Ke, W. *Mater. Corros.* **2005**, *56* (8), 533–541.

(63) Jin, P.; Robbins, W.; Bota, G. *Corros. Sci.* **2018**, *131*, 223–234.

(64) Groysman, A. *Top. Safety, Risk, Reliab. Qual.* **2017**, *32*, 37–99.

(65) Rowland, S. J.; Scarlett, A. G.; Jones, D.; West, C. E.; Frank, R. A. *Environ. Sci. Technol.* **2011**, *45* (7), 3154–3159.

(66) Parisotto, G.; Ferrão, M. F.; Müller, A. L. H.; Müller, E. I.; Santos, M. F. P.; Guimarães, R. C. L.; Dias, J. C. M.; Flores, È. M. M. *Energy and Fuels* **2010**, *24* (10), 5474–5478.

(67) Chakravarti, R.; Patrick, B. N.; Barney, M.; Kusinski, G.; Devine, T. M. *Energy & Fuels* **2013**, *27* (12), 7905–7914.

(68) Flego, C.; Galasso, L.; Montanari, L.; Gennaro, M. E. In *Energy and Fuels*; 2014; Vol. 28, pp 1701–1708.

(69) Jin, P.; Bota, G.; Robbins, W.; Nesic, S. *Energy and Fuels* **2016**, *30* (8), 6853–6862.

(70) Jin, P.; Nesic, S.; Wolf, H. A. *Surf. Interface Anal.* **2015**, *47* (4), 454–465.

(71) Xiaofei, Z.; Tao, M.; Xiaochun, H.; Jinde, Z.; Xiaoyi, W.; Sixian, R. *Eng. Fail. Anal.* **2020**, *117*, 104802.

(72) Bai, P.; Zheng, S.; Zhao, H.; Ding, Y.; Wu, J.; Chen, C. *Corros. Sci.* **2014**, *87*, 397–406.

(73) American Petroleum Institute. *API Recomm. Pract. 939* **2008**.

(74) Wang, H.; Salveson, I. *Phase Transitions* **2005**, *78* (7–8), 547–567.

(75) Gray, M. R.; Ayasse, A. R.; Chan, E. W.; Veljkovic, M. *Energy & Fuels* **1995**, *9* (7), 500–506.

(76) Lepore, J. The Role of Sulfur Species in Establishing the Corrosion Reactions in Refinery Metallurgies, University of Alberta, 2016.

(77) Mrowec, S.; Walec, T.; Werber, T. *Oxid. Met.* **1969**, *1* (1), 93–120.

(78) El Kamel, M.; Galtayries, A.; Vermaut, P.; Albinet, B.; Foulonneau, G.; Roumeau, X.; Roncin, B.; Marcus, P. *Surf. Interface Anal.* **2010**, *42* (6–7), 605–609.

(79) Bai, Z. S.; Wang, H. L. *Chem. Eng. Res. Des.* **2007**, *85* (12 A), 1586–1590.

(80) Vafajoo, L.; Ganjian, K.; Fattahi, M. *J. Pet. Sci. Eng.* **2012**, *90–91*, 107–111.

(81) Álvarez, P.; Menendez, J. L.; Berrueco, C.; Rostani, K.; Millan, M. *Fuel Process. Technol.* **2012**, *96*, 16–21.

(82) Mendoza De La Cruz, J. L.; Cedillo-Ramírez, J. C.; Aguirre-Gutiérrez, A. D. J.; García-Sánchez, F.; Aquino-Olivos, M. A. *Energy and Fuels* **2015**, *29* (2), 480–487.

(83) E, H.; Watkinson, A. P. *Heat Transf. Eng.* **2009**, *30* (10–11), 786–793.

(84) Mena-Cervantes, V. Y.; Hernández-Altamirano, R.; Buenrostro-González, E.; Beltrán, H. I.; Zamudio-Rivera, L. S. *Fuel* **2013**, *110*, 293–301.

(85) Mena-Cervantes, V. Y.; Hernández-Altamirano, R.; Buenrostro-González, E.; Beltrán, H. I.; Zamudio-Rivera, L. S. *Energy and Fuels* **2011**, *25* (1), 224–231.

(86) Rogel, E. *Energy and Fuels* **2011**, *25* (2), 472–481.

(87) Towfighi, J.; Sadrameli, M.; Niaei, A. *J. Chem. Eng. Japan* **2002**, *35* (10), 923–937.

(88) Wang, J.; Reyniers, M. F.; Van Geem, K. M.; Marin, G. B. *Ind. Eng. Chem. Res.* **2008**, *47* (5), 1468–1482.

(89) Wang, J.-Q.; Li, M.; Li, S.-F.; Li, C.; Que, G.-H. *Ranliao Huaxue Xuebao/Journal Fuel Chem. Technol.* **2006**, *34* (1).

(90) Russell, C. A.; Crozier, S.; Sharpe, R. *Energy and Fuels* **2010**, *24* (10), 5483–5492.

(91) Habib, F. K.; Diner, C.; Stryker, J. M.; Semagina, N.; Gray, M. R. *Energy and Fuels* **2013**, *27* (11), 6637–6645.

(92) Zachariah, A.; Wang, L.; Yang, S.; Prasad, V.; De Klerk, A. *Energy and Fuels* **2013**, *27* (6), 3061–3070.

(93) Speight, J. G. *Oil and Gas Corrosion Prevention*; 2014.

(94) El Kamel, M.; Galtayries, A.; Albinet, B.; Foulonneau, G.; Roumeau, X.; Roncin, B.; Marcus, P. In *European Corrosion Congress 2009, EUROCORR 2009*; 2009; Vol. 6, pp 3591–3608.

(95) Li, H.; Chen, W. *Oxid. Met.* **2012**, *78* (1–2), 103–122.

(96) Li, H.; Chen, W. *Oxid. Met.* **2012**, *77* (3–4), 107–127.

(97) Rojas, D.; Garcia, J.; Prat, O.; Sauthoff, G.; Kaysser-Pyzalla, A. R. *Mater. Sci. Eng. A* **2011**, *528* (15), 5164–5176.

(98) Hucin, J. *Mater. Corros.* **2000**, *176*, 173–176.

(99) Moura, L. B.; Guimarães, R. F.; Abreu, H. F. G. De; Miranda, H. C. De; Tavares, S. S. M. *Mater. Res.* **2012**, *15* (2), 277–284.

(100) Sixian, R.; Yu, Z.; Ziwei, P.; Yuwan, C.; Xuedong, C. *Mater. Corros.* **2014**, *65* (6), 619–625.

(101) ASM International. *ASM Metals Handbook Vol.01, Properties and Selection: Irons, Steels, and High-Performance Alloys*; 1991.

(102) Ohmi, T.; Nakagawa, Y.; Nakamura, M.; Ohki, A.; Koyama, T. *J. Vac. Sci. Technol. A* **1996**, *14* (4), 2505–2510.

(103) Young, D. *High Temperature Oxidation and Corrosion of Metals*; 2015; Vol. 1.

(104) Ramachandran, D.; Egoavil, R.; Crabbe, A.; Hauffman, T.; Abakumov, A.; Verbeeck, J.; Vandendael, I.; Terryn, H.; Schryvers, D. *J. Microsc.* **2016**, *264* (2), 207–214.

(105) Ramesh, M.; Leber, H. J.; Janssens, K. G. F.; Diener, M.; Spolenak, R. *Int. J. Fatigue* **2011**, *33* (5), 683–691.

(106) Tomio, A.; Sagara, M.; Doi, T.; Amaya, H.; Otsuka, N.; Kudo, T. *Corros. Sci.* **2015**, *98*, 391–398.

(107) Broutin, P.; Ropital, F.; Reyniers, M. F.; Froment, G. F. *Oil Gas Sci. Technol.* **1999**, *54* (3), 375–385.

(108) Tang, S.; Hu, S.; Zhang, Y.; Wang, J.; Zhu, Q.; Chen, Y.; Li, X. *J. Anal. Appl. Pyrolysis* **2014**, *107*, 197–203.

(109) Tang, S.; Gao, S.; Hu, S.; Wang, J.; Zhu, Q.; Chen, Y.; Li, X. *Ind. Eng. Chem. Res.* **2014**, *53* (13), 5432–5442.

(110) Tang, S.; Wang, J.; Zhu, Q.; Chen, Y.; Li, X. *ACS Appl. Mater. Interfaces* **2014**, *6* (19), 17157–17165.

(111) Li, C. S.; Yang, Y. S. *Surf. Coatings Technol.* **2004**, *185* (1), 68–73.

(112) Coletti, F.; Macchietto, S. *Ind. Eng. Chem. Res.* **2011**, *50* (8), 4515–4533.

(113) Polley, G. T.; Wilson, D. I.; Yeap, B. L.; Pugh, S. J. In *Applied Thermal Engineering*; 2002; Vol. 22, pp 763–776.

(114) Sadrameli, S. M. *Fuel*. 2016, pp 285–297.

(115) Moro-oka, Y. *Appl. Catal. A Gen.* **1999**, *181* (2), 323–329.

(116) Breysse, M.; Furimsky, E.; Kasztelan, S.; Lacroix, M.; Perot, G. *Catal. Rev.* **2002**, *44* (4), 651–735.

(117) Rana, M. S.; Ancheyta, J.; Sahoo, S. K.; Rayo, P. In *Catalysis Today*; 2014; Vol. 220–222, pp 97–105.

(118) Absi-Halabi, M.; Stanislaus, A.; Trimm, D. L. *Applied Catalysis*. 1991, pp 193–215.

(119) Bao, B.; Liu, J.; Xu, H.; Liu, B.; Zhang, W. *RSC Adv.* **2016**, *6* (73), 68934–68941.

(120) Mu??oz Gandarillas, A. E.; Van Geem, K. M.; Reyniers, M. F.; Marin, G. B. *Ind. Eng. Chem. Res.* **2014**, *53* (15), 6358–6371.

(121) Jazayeri, S. M.; Karimzadeh, R. *Energy and Fuels* **2011**, *25* (10), 4235–4247.

(122) Tan, C. D.; Baker, R. T. K. *Catal. Today* **2000**, *63* (1), 3–20.

(123) El Kamel, M.; Galtayries, A.; Vermaut, P.; Albinet, B.; Foulonneau, G.; Roumeau, X.; Roncin, B.; Marcus, P. In *Surface and Interface Analysis*; 2010; Vol. 42, pp 605–609.

CHAPTER 3

Experimental

3.1 Introduction

Fouling experiments were conducted in a broad range of crude and blended, with three substrate materials, several combinations of oil and substrate temperatures, and at constant pressure and flow. A goal of the experimentation was to document a broad interrelation between corrosion and organic fouling. To this end, a series of tests were designed to include contrasting conditions of wire and oil temperature, both above and below those required for thermal cracking. In the final stages of the research a chemical additive and several metallic surface coatings were employed to manipulate key aspects of the documented corrosion and fouling processes.

3.2 Experimental Conditions

Table 3.1 Experimental matrix of the testing conditions

Oil / Blend	Metallurgy	Oil Temperature	Wire Temperature	Time
		°C	°C	
Hight Temperature Conditions				
H:I	347SS	290	490	250 min.
*varied pressure				
*varied time				
B:C	carbon steel	290	490	60 min.
	P91	290	490	60 min.
	347SS	290	490	60 min.
Low Temperature Conditions				
B:D:H	Carbon steel	250	350	4, 8 hrs.
	P91	250	350	4, 8 hrs.
	347SS	250	350	4, 8 hrs.
B:C	Carbon steel	250	350	4, 8 hrs.
	P91	250	350	4, 8 hrs.
	347SS	250	350	4, 8 hrs.
H:I	Carbon steel	250	350	4, 8 hrs.
	P91	250	350	4, 8 hrs.
	347SS	250	350	4, 8 hrs.
Iron-Naphthenate Additive Study				
G	Carbon steel	290	490	4 hrs.
	P91	290	490	4 hrs.
	Carbon steel	150	350	*48 hrs.
	P91	150	350	*48 hrs.
Anti-Fouling Coatings Evaluation				
A	*Carbon steel	250	350	4, 8 hrs.
*Varied coating	*P91	250	350	4, 8 hrs.

Table 3.2 is a summary of the fouling tests conducted throughout this study, and their respective experimental parameters. These experiments were chosen to represent conditions encountered throughout the preheat train, including heat exchangers and fired furnaces, of a refinery. Nominal operating conditions and infrequent, extreme conditions, especially relative to temperature, were included within the test matrix. Pressure during the experiments – working pressure, varied between 285 psig and 800 psig, but was most often maintained at a constant 400 psig. Agitation, provided by a magnetically coupled stir bar, was held constant at 300 RPM throughout the testing series. Two operating environments were broadly utilized for comparing fouling above and below thermal cracking conditions. The high temperature scenarios consisted of a bulk oil temperature of 290 °C and a wire temperature of 490 °C. Low temperature conditions consisted of 250 °C bulk oil temperature and a wire temperature of 350 °C. These contrasting operating scenarios were expected to demonstrate fundamentally different fouling mechanisms and rates. Under the high temperature condition, organic fouling is expected to be dominated by coking reactions and aggressive sulfidic corrosion. At the lower temperature, the corrosion mechanism will remain, but will progress with reduced kinetics. Organic fouling from coking will be limited because tests are below cracking temperature and expected to be influenced by asphaltene stability and particulate/depositional fouling.

Importantly, it is not the intent of this research to establish a link between fouling behavior and stability of the blended oils, nor any link to asphaltene stability, but rather a focused effort on the role of the fouling surface. For a given oil combination there were not enough blends made/tested to probe into this aspect. Moreover, the phenomenological links between asphaltene incompatibility and fouling rates are well established by Wiehe[1] and others.[2] It was the core intent of this work to demonstrate a consistent link amongst sulfidic corrosion and organic fouling, while testing with blended oils of known and varying stability and operating above and below cracking temperature.

3.3 Fouling Reaction Vessel

A stirred, 2000 ml high pressure and temperature autoclave was utilized to conduct all fouling experiments in this work. It was equipped with a magnetically coupled stir bar to provide fluid agitation and a sparge system to introduce inert gas(es) that enabled removal of oxygen and atmospheric gases/vapors from the oil and vessel headspace. The vessel could sustain operating pressures up to 10 000 psig and temperatures up to 350 °C. Four, custom electrical feedthroughs (heated wire probes) were designed to facilitate resistive- (Joule-) heating of metallic wire or ribbon that would represent the heated fouling surface in a refinery. The probes were mounted through the vessel headplate, and up to four could be run in parallel or series. The entire assembly allows for the immersion and controlled heating of metallic samples in hot crude oil, under repeatable conditions. Figure 3.1 is a detailed schematic of the reactor and probes.

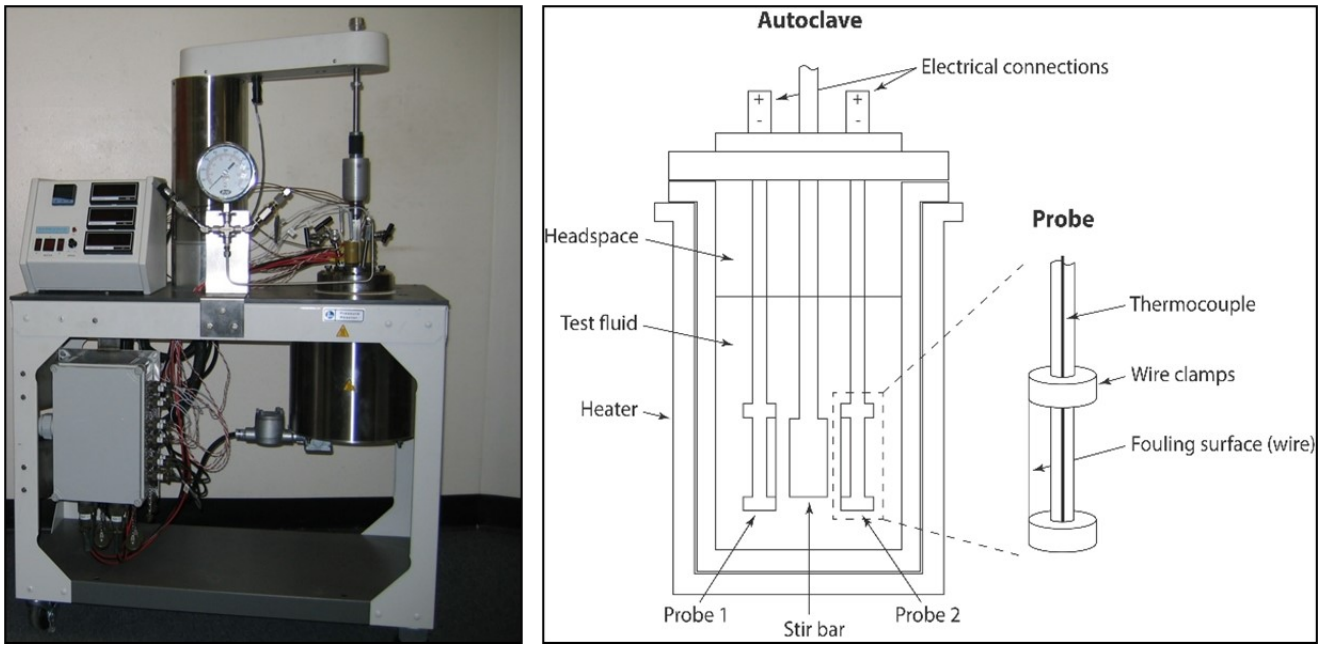

Figure 3.1 A photograph and a schematic of the fouling reactor cross-section.

Each fouling test was setup by installing a metallic wire in the heated wire probes, adding oil to the reactor and sparging the system. The system was then programmed for the desired initial oil bath temperature and pressure. Experiments were completed under controlled conditions of bulk oil temperature, wire temperature, stir rate, and pressure. Metallic wires were cleaned in an ultrasonic bath for one hour, using toluene and methanol, then mounted in a probe that was installed into the

reactor headplate. The reactor was charged with 1200 mL of crude oil, sealed, and sparged for 20 minutes with the stir bar set at 300 RPM. The reactor was then pressurized to 120 psig and heated to initial oil bath temperature. Pure nitrogen (99.999%) was used for sparging and pressurization.

Once the oil bath had reached its temperature set point, the pressure of the reactor was adjusted to achieve the desired working pressure for the fouling run. The crude oil bath was maintained at a constant temperature, using a PID (proportional-integral-derivative) controlled heating element and a thermocouple in a thermowell. The wires in the reactor probe were heated resistively to a desired temperature above the bulk oil temperature via a constant current input. The voltage (and thus power output) of the wires increased by approximately 10% from their initial values during the constant current tests, and, to a first approximation, the heat flux across the expanding foulant-oil interface remained constant. The temperature of the wire was determined by measuring voltage across the wire, in a four-wire setup, and calculating resistance. The wire resistance was compared with a calibration plot for each metallurgy. These were generated ex-situ in an inert atmosphere inside a quartz tube furnace. Resistively heated wire temperature was also verified using temperature indicating liquids purchased from Tempil and found to agree within 5-10% of the extrapolated values.

3.4 Crude Oils

Table 3.2 Selected properties of the crude oils used in this study.

Physical Properties	Crude B	Crude C	Crude D	Crude H	Crude I	Crude G	Crude A
Sulfur content (wt.%)	1.5	0.51	0.086	3.36	0.3	0.93	2.4
API (degrees)	32.2	43.3	45.2	21.9	42.1	32.1	24.7
TAN (mg KOH/g oil)	0.09	0.44	0.038	0.715	0.05	0.119	0.62
Fe (ppmw)	0.8	1.5	0.3	1.9	6.8	0.4	1.6
Asphaltene (wt.%)	1.1	0.2	0.11	6.7	0.23	1.65	6.2
Wax (wt.%)	6.5	6.75	3.7	2.9	6.5	4.0	3.5

Table 3.2 is a list of crude oils that were used in this study, with several relevant physical and chemical properties. Crude B is considered medium sulfur, low TAN, low asphaltene and high wax

content. Crude C is low sulfur, low TAN, low asphaltene, with high wax content. Crude D is a light, sweet crude. Crude H has a high sulfur content, low TAN, high asphaltene content, and low wax content. Crude I is a light, low sulfur and low asphaltene oil.

Blended systems were utilized for experimentation. Blend HI was 90 vol% H to 10 vol% I, Blend BC 40 vol% B to 60 vol% C, and Blend BDH as 25 vol% B 55 vol% D 20 vol% H. Crudes G and A were tested as received and are noted as low and medium fouling oils, respectively. Each blend offered a unique propensity for fouling and/or corrosion, and the combinations were important feedstocks for industrial application.

3.5 Metallurgy

Three metallurgies were tested as 0.2 mm diameter wires. Representative refinery metallurgies were selected. The first metallurgy was 347 austenitic stainless-steel (347SS) (max 0.08 wt.%C, 2 wt.%Mn, 0.045 wt.%P, 0.03 wt.%S, 0.75 wt.%Si, 17 – 19 wt.%Cr, 9 -13 wt.%Ni, 1 wt.% (Nb+Ta)) (ASTM A240, A580). Alloy 347 is a stabilized stainless-steel which offers an excellent resistance to intergranular corrosion, specifically in the range 800 to 1500°F (427 to 816°C).[3] Alloy 347 is stabilized by the addition of Nb and Ta and utilized in various high temperature refinery processes.[4,5]Additionally, this material possesses both good ambient and high temperature mechanical properties. The second metallurgy was a low-alloy, 9wt% Cr-1wt% Mo steel (P91). This material is a power industry standard in high temperature applications.[6,7] This ferritic alloy is known for its high temperature strength and creep resistance. The third metallurgy was conventional mild carbon steel with up to 0.25 wt.% C and 0.4 wt.% Mn (ASTM A179).

3.6 Fouling Factor

Fouling was monitored via fouling factors, which is a measured and calculated resistance to heat flow. They parameters were calculated and presented in two ways. An in-situ fouling factor (FF) measurement is obtained directly from wire resistivity data, while assuming a constant heat transfer surface area (Ac). In this case FF is expressed as the following formula:

$$FF = A_c\left[\left(\frac{\Delta T}{P}\right)_{fouled} - \left(\frac{\Delta T}{P}\right)_{clean}\right] \qquad \textbf{Equation 3.1}$$

Additionally, a final fouling factor (FFF) was calculated by considering the changing heat transfer surface area as the wire diameter grew with fouling or shrank with corrosion.

$$FFF = \left[A_f\left(\frac{\Delta T}{P}\right)_{fouled} - A_c\left(\frac{\Delta T}{P}\right)_{clean}\right] \qquad \textbf{Equation 3.2}$$

Where ΔT is (T_{wire}-T_{oil}) and P is the power output across the wire, due to Joule heating ($P = I^2R_{wire}$). The area A_c is the initial *clean* surface area of the wire. The *fouled* surface area (A_f) is calculated using the diameter of the fouled wires (i.e. the clean wire diameter and the observed foulant thickness). This diameter was obtained, post-fouling, using SEM analysis of the fouled cross sections. The foulant includes all inorganic and organic material remaining after cleaning the wires.

3.7 Wire Temperature and Resistivity

In the fouling experiments, 52.8 mm of wire sample was mounted into a custom electrical feedthrough and brought to temperature via an applied current. Under controlled conditions, Joule-Heating causes the small diameter wires to achieve the metal surface temperatures desired. Wire temperature was controlled by manipulating input current and monitoring wire resistance in a constant feedback loop. Resistance of the metal wires is a function of temperature and their geometry and thus

a good indicator of temperature. Resistance was calculated by measuring voltage drop across the wire, using a four-terminal (four-wire) setup, and multiplying by the input current.

Calibration plots of wire resistivity versus temperature were generated in two systems. First, wires were mounted in a four-wire configuration within a tube furnace and resistivity was calculated via an applied constant current of 50mA. This was conducted over the temperature range 100°C to 600°C. The second system utilized temperature indicating liquids, supplied from Tempil. These liquids were applied as small droplets at both ends of the wire and one midsection. Indicating liquids for 300°C through 550°C were used, which had a quoted accuracy of 3% (°C). Wires were resistively heated via increasing applied current until the indicator changed phase. Resistivity from each setup correlated well and was used to produce calibration plots for the fouling experiments.

3.8 Thin-Film Coatings

Various metallic coatings were applied to carbon steel and P91 wires to investigate their ability for mitigating fouling and corrosion. Nominally 50 nm coatings of pure Cr metal, Cr_2O_3-chromium oxide, TiO_2-titanium oxide, and Al_2O_3-aluminum oxide were applied to the wires using physical vapor deposition – sputtering. Thin films were deposited onto four-inch wire samples in a DC magnetron co-sputtering system (AJA International), using targets of pure Cr, Al, and Ti, in high vacuum at 200°C. Deposition was done in a sputter-up configuration with continuous substrate rotation to ensure film uniformity and the wires were rotated 180° between two separate sessions to coat their full circumference. Prior to sputtering the wires were cleaned in an ultrasonic bath and using acetone then IPA. They were dried with nitrogen and placed in a custom holder capable of being mounted in the sputtering system. Before sputtering, the chamber reached a base pressure below 5×10^{-8} Torr. Argon sputtering of the pure metals was maintained at 4.0 mTorr with a base pressure of approximately 4.0×10^{-8} Torr, while substrate temperature was maintained at 200 °C.

Oxides were deposited in a mixed argon-oxygen plasma, where the ratio of argon to oxygen was controlled by two mass-flow controllers. The total pressure in the sputtering chamber was

maintained at 10×10^{-3} Torr for these experiments, and the volume flow ratios of argon to oxygen ranged from 20:1 to 18:1 with a total flow rate of 10 sccm. Films were deposited in roughly 10 at.% intervals. After sputtering, the films were annealed at 200 °C for 2 hours in the deposition chamber under the same flow of argon and oxygen.

3.9 Post Fouling Analysis

After removal from the reactor, the wires were soaked in petroleum ether for five minutes, washed with fresh petroleum ether, and finally rinsed with isopropyl alcohol. This ensured that any pitch (toluene-solubles) remained adhered to the sample surface. Generally, petroleum pitch is the nonvolatile product obtained from thermal or catalytic cracking of heavy petroleum residua.[8] Washing and rinsing were done gently to retain the delicate surface deposits. After cleaning, the wires were dried in a vacuum oven at 90 ºC for 2 hours. All fouled wires were stored in 75 mm capped test tubes, at room temperature prior to subsequent analysis. All wires were catalogued with initial and final weights, optical images, and electron micrographs of their length prior to destructive analysis.

Detailed analysis of the wire samples included Scanning Electron Microscopy (SEM), Energy Dispersive X-ray Spectroscopy (EDXS), and X-ray Diffraction (XRD), and Transmission Electron Microscopy (TEM). SEM and EDXS analysis utilized a Hitachi S-3000N microscope with an Oxford INCA EDXS system. The SEM was operated at an accelerating voltage of 15 keV, and a working distance ranging from 7-15 mm, for optimum resolution. EDXS scans were completed at a 15 keV accelerating voltage and a working distance of 15 mm. XRD analysis was performed using a Bruker AXS D8 Discover diffractometer with a Histar GADDS area detector. TEM was completed using a JEOL JEM-2100. Selected area electron diffraction patterns were processed using an open-source software package that was developed in-house (Diffraction Ring Profiler version 1.7).[9]

Cross sections of the fouled wires were prepared by mounting a portion of each sample in a metallographic epoxy. The wires were cut at mid-length and immersed in a two-part epoxy resin to

which nickel powder was added to improved electrical conductivity and reduce charging during SEM and EDXS analysis. The epoxy mounts were left to cure in vacuum for at least 24 hours at room temperature. Final sample preparation included light grinding and polishing of the cured epoxy mounts. This exposed an undamaged portion of the wire cross section (see image) that was suitable for imaging, thickness measurements, and elemental analysis of the corroded and fouled surfaces.

Thickness measurements of the wire cross sections were conducted as follows: Using Quartz PCI software the foulant was measured radially at 8 places around the circumference of the wire cross section, in increments of 45°, starting at the 12 o'clock position. The thicknesses reported were the average of these values and utilized for calculation of the FFF data.

In the next chapter, fouling tests are conducted in high temperature scenarios with all three metallurgies. First, the fouling behavior of 347SS in Blend HI is documented, while altering exposure time and working pressure. Next, all three metallurgies are contrasted in high temperature fouling experiments with Blend BC. These tests were run for 60 minutes, with a constant oil bath temperature of 290°C, working pressure of 400 psig, and an initial wire temperature of 490°C.

Next, low temperature fouling tests were conducted as a function of oil and metallurgy. Carbon steel, P91, and 347SS wires were exposed to Blends HI, BC, and BDH to demonstrate the broadness of the interrelation between corrosion and fouling. These tests were conducted at a lower temperature, with the oil bath being 250°C and the initial wire temperature being 350°C. Experiments were run for four and eight hours.

In the final parts of this research, fouling behavior is manipulated with a chemical additive and thin-film coatings. An iron naphthenate is added to Oil G and tested at high and low temperature conditions, using carbon steel and P91. Coatings of Cr_2O_3, Al_2O_3, TiO_2, and Cr metal are applied to carbon steel and P91 wires and fouled in Oil A, under low temperature conditions.

3.10 References

(1) Wiehe, I. A. *Process Chemistry of Petroleum Macro Molecules*, Vol. 121.; CRC Press: Boca Raton, FL, 2008.

(2) Derakhshesh, M.; Eaton, P.; Newman, B.; Hoff, A.; Mitlin, D.; Gray, M. R. In *Energy and Fuels*; 2013; Vol. 27, pp 1856–1864.

(3) Chandra, K.; Kain, V.; Tewari, R. *Corros. Sci.* **2013**, *67*, 118–129.

(4) Wang, H.; Du, H.; Wei, Y.; Hou, L.; Liu, X.; Wei, H.; Liu, B.; Jia, J. *Steel Res. Int.* **2021**, *92* (2), 1–12.

(5) Zhou, Y.; Liu, Y.; Zhou, X.; Liu, C.; Yu, J.; Huang, Y.; Li, H.; Li, W. *J. Mater. Sci. Technol.* **2017**, *33* (12), 1448–1456.

(6) Rojas, D.; Garcia, J.; Prat, O.; Sauthoff, G.; Kaysser-Pyzalla, A. R. *Mater. Sci. Eng. A* **2011**, *528* (15), 5164–5176.

(7) Pandey, C.; Giri, A.; Mahapatra, M. M. *Mater. Sci. Eng. A* **2016**, *664*, 58–74.

(8) Eser, S.; Andrésen, J. M. In *Fuels and Lubricants Handbook: Technology, Properties, Performance, and Testing, 2nd Edition*; Totten, G., Shah, R., Forester, D., Eds.; ASTM International: West Conshohocken, PA, 2019; pp 1327–1361.

(9) Zhang, L.; Holt, C. M. B.; Luber, E. J.; Olsen, B. C.; Wang, H.; Danaie, M.; Cui, X.; Tan, X.; Lui, V. W.; Kalisvaart, W. P.; Mitlin, D. *J. Phys. Chem. C* **2011**, *115* (49), 24381–24393.

CHAPTER 4

Sulfide promoted chronic fouling in a refinery: A broad phenomenon spanning a range of heat transfer surfaces and oil types

Material in this chapter has been published in the journal article;

Sulfide Promoted Chronic Fouling in a Refinery: A Broad Phenomenon Spanning a Range of Heat Transfer Surfaces and Oil Types, Fuel, **2015**, 160, 479-489.

Composed by:

Mike Hazelton, Tyler Stephenson, Justin Lepore, Velu Subramani and David Mitlin

4.1 Abstract

Fouling of metal heat-transfer surfaces employed in crude oil refining operations, driven by inorganic corrosion products, is not well understood. Here we employ a range of advanced analytical techniques, including TEM, SEM, FIB and XRD to systematically document the interdependent corrosion – fouling processes of three refinery metallurgies: a carbon steel, a 9wt%Cr-1wt%Mo (P91) steel, and a 347 stainless steel (347SS). We utilize two representative crude oil blends, testing at a metal surface temperature of 490 °C and an oil bath temperature of 290 °C. For the three metallurgies there is a mechanistic similarity of the fouling phenomenon, which begins with sulfidic corrosion of the metal surface and progresses to coking. It is observed that after 1 hour of testing carbon steel samples fouled somewhat less than the P91, which was initially unexpected since the latter is considered a more sulfidic corrosion resistant alloy. TEM and SEM analyses demonstrate that there is poor adhesion of the sulfide layer on the carbon steel, which we hypothesize results in the metal surface effectively self-cleaning. Despite being the most resistant to sulfidic corrosion and to fouling, the stainless steel nevertheless forms a thin Fe-Cr-Mn rich inner sulfide and a thicker Fe-rich outer sulfide. We also examine the role of volatiles (reactor pressure) and demonstrate that fouling rates drop off with successive tests on the same oil batch. This is attributed to a gradual exhaustion of Sulfur-containing species that react at high temperature to sulfide the metal surface, which in turn catalyze the growth of the organic carbonaceous fouling.

4.2 Introduction

Complex deposits of organic and inorganic material build up and foul the surface of process vessels during crude oil refining operations.[1–4] Wholly described as crude oil fouling,[5] the encompassed phenomena distress operations by encumbering efficient heat transfer, increasing hydraulic resistance – reducing throughput, and compromising safety. Consequently, refinery units can realize millions of dollars in incremental expenses due to increased energy consumption and maintenance costs.[6] Opportunity oils are attractive inputs for a refiner, since they can be purchased at a discount, but require complex, deep refining processes to create on-specification products and

may present acute challenges related to fouling and corrosion.[7] Accordingly, fouling is an active field of scientific and engineering research,[8–11] and improving the quality and knowledge depth of feedstock chemistry is becoming increasingly essential.[12–16] Crude oil fouling has been described by distinct mechanistic scenarios such as chemical reaction fouling[17], corrosion fouling[18], and particulate fouling,[19] which do not manifest with exclusivity in real systems.

Above cracking temperatures or in cases where catastrophic asphaltene flocculation does not occur, chronic fouling has been linked to corrosion, especially from sulfur bearing species and naphthenic acids.[20–22] Wiehe[23] has described the role of iron sulfide towards enhancing wetting behavior of fouling precursor phases on a metallic surface. Furthermore, in catalysis, transition metal sulfides have specific surface chemistry which makes them important compounds for hydrodesulphurization.[24] Wang and Watkinson[8] proposed enhanced adhesion and trapping of fouling precursors due to roughening of a corroding interface. Particulate matter, suspended in crude oils, such as corrosion residuals (iron oxides and sulfides) and various formation minerals (clays and sands), are also contaminants that can influence fouling.[25] In their examination of deposits from an Australian light crude, authors Alem *et al*.[26] identified suspended particulates as a secondary causation for fouling. More directly, Watkinson *et al*.[27] have investigated particulate fouling in a batch stirred system using a heated carbon steel rod. The same group[28] have recently studied fouling from a sour crude fraction on corroding and non-corroding metallic surfaces, as a function of temperature and shear rate. Mitlin *et al*.[29] investigated fouling at delayed coking conditions, using 316 stainless steel and iron wires, and emphasized the role of the initiating surface in their analysis.

What remains poorly understood is the degree to which corrosion-fouling is a general phenomenon for different oil types. Moreover, the microstructural details of the hot oil-exposed metal surface for any metallurgy remains elusive, and there are few direct comparisons between different steels found in refining environments. This is the focus of the current study; to provide an in-depth analysis of the metallurgical changes at the wire surface for representative carbon steel, a representative Cr-Mo steel and a representative stainless steel. To make these findings more general,

two different oil blends are employed. By providing a detailed analysis on this relatively broad sampling, one can define both the essential commonalities for early-stage corrosion – fouling and highlight the key differences between the metallurgies. Table 4.1 is a subset of Table 3.1 and shows a summary of the experiments conducted for this study, and their respective experimental conditions.

Table 4.1 Summary of the experiments and test conditions

Oil	Metallurgy	T_{oil} (°C)	T_{wire} (°C)	Time (min)
HI	347SS	290	490	250
	347SS	290	490	30
	347SS	290	490	10
	347SS	290	490	5
BC	Carbon steel	290	490	60
	P91	290	490	60
	347SS	290	490	60

4.3 Results and Discussion

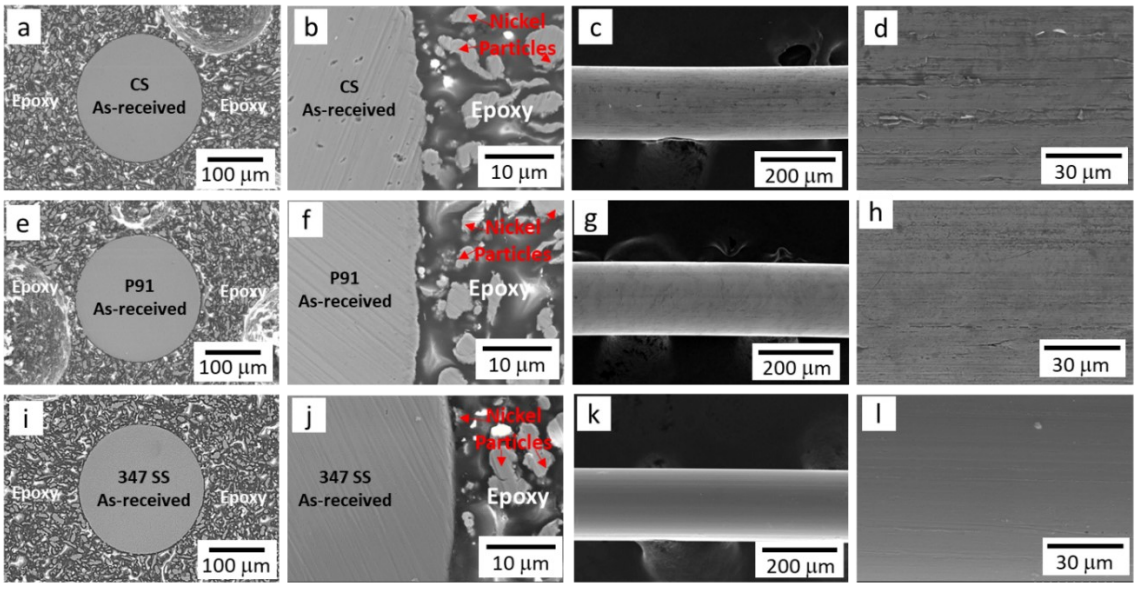

Figure 4.1 SEM micrographs of cross-sections and surfaces of as-received (a-d) carbon steel, (e-h) P91, and (i-l) 347SS wires.

Figure 4.1 shows SEM micrographs of the as-received wire cross-sections and surfaces, highlighting their morphology and surface finish. The cross-sectioned surface of the wires, along with the bulk epoxy and several nickel particles are identified in Figures 4.1(a,b), 4.1(e,f), and 4.1(i,j).

Figure 4.2 shows TEM bright- and dark- field micrographs of the as-received carbon steel and P91metallurgies, as well as an indexed SAD (selected area diffraction) pattern. The ferrite metallurgy is a standard rolled texture, highlighted in the dark field images. The dark field micrographs for P91 highlight not only the rolled texture of the ferrite, but also the fine Cr-based precipitates that give the material its strength. Figure 4.3 shows a TEM bright-field micrograph, an indexed SAD, and dark-field micrograph of cross-sections of the as-received 347SS, highlighting its austenitic structure. Figure 4.3(d,e) shows TEM bright field micrographs of an approximately 10 nm thick surface Cr - oxide (arrowed) on the as-received 347SS.

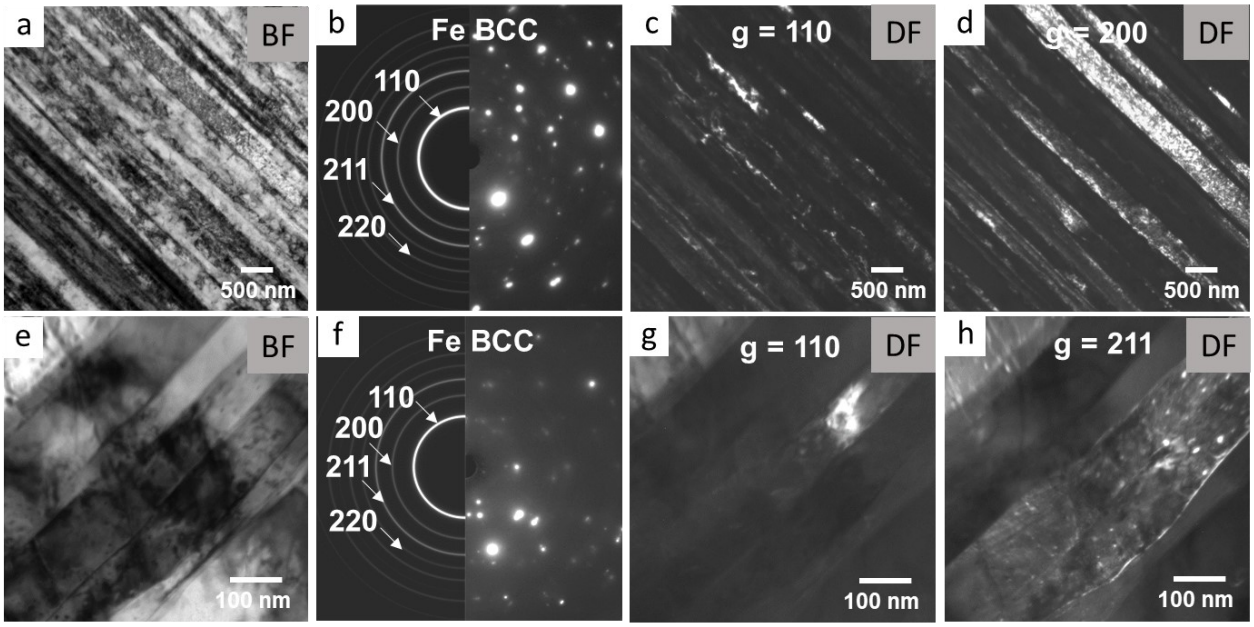

Figure 4.2 TEM bright field, indexed SAD, and dark field micrographs of cross sections of the as-received (a-d) carbon steel and (e-h) P91 steel

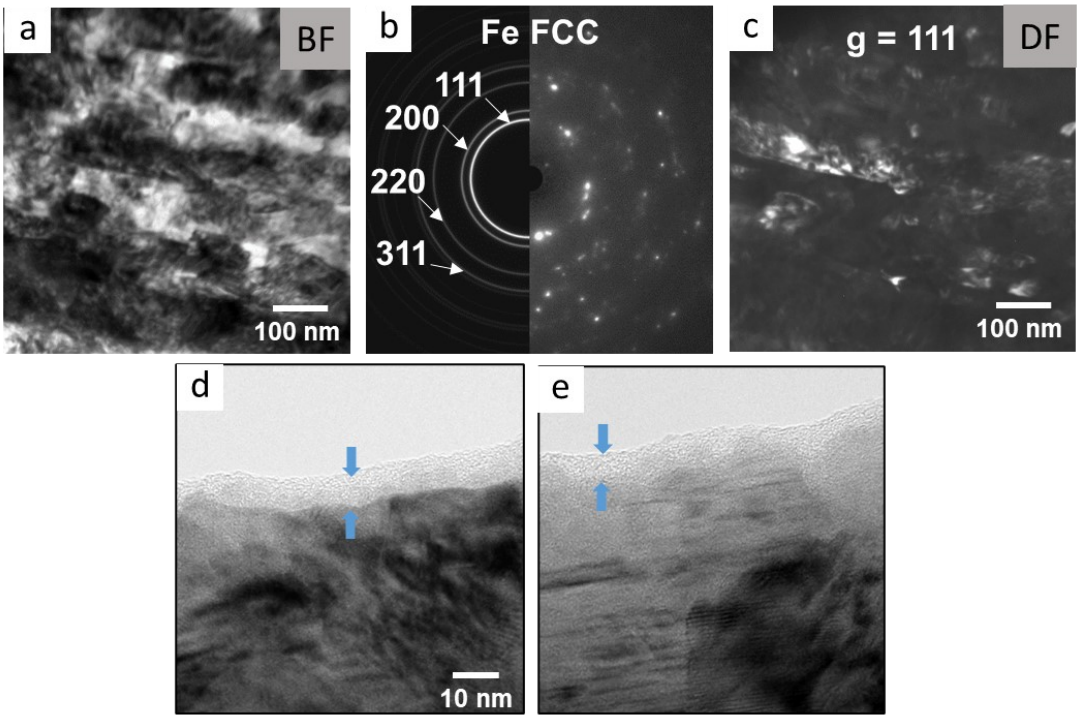

Figure 4.3 (a-c) TEM bright field, indexed SAD, and dark field micrographs of cross-sections of the as-received 347SS and (d-e) TEM bright field micrographs of the ~10 nm surface oxide (arrowed).

Initially, Blend HI was utilized to explore the role of bath ageing on fouling behavior. Figure 4.4(a) shows the in-situ fouling factor for each experiment. Figure 4.4(b) shows the final foulant thickness as a function of run number and indicated above each data point is the corresponding reactor working pressure. Figure 4.4(c) shows the corresponding *ex-situ* or final fouling factor values for these experiments. An important distinction regarding the experimental process should be noted: In this set of experiments the initial reactor pressure was set to 120 psig, this being done while the reactor was still at ambient temperature. The resultant pressure at the working oil bath temperature of 290 °C could be naturally established by the outgassing of the hot oil. For this set of runs we employed the same oil charge for consecutive experiments. In subsequent sections, a fresh oil charge was used for every run, while the pressure at 290 °C was set at 400 psig. A new wire sample was installed for every run, in all cases.

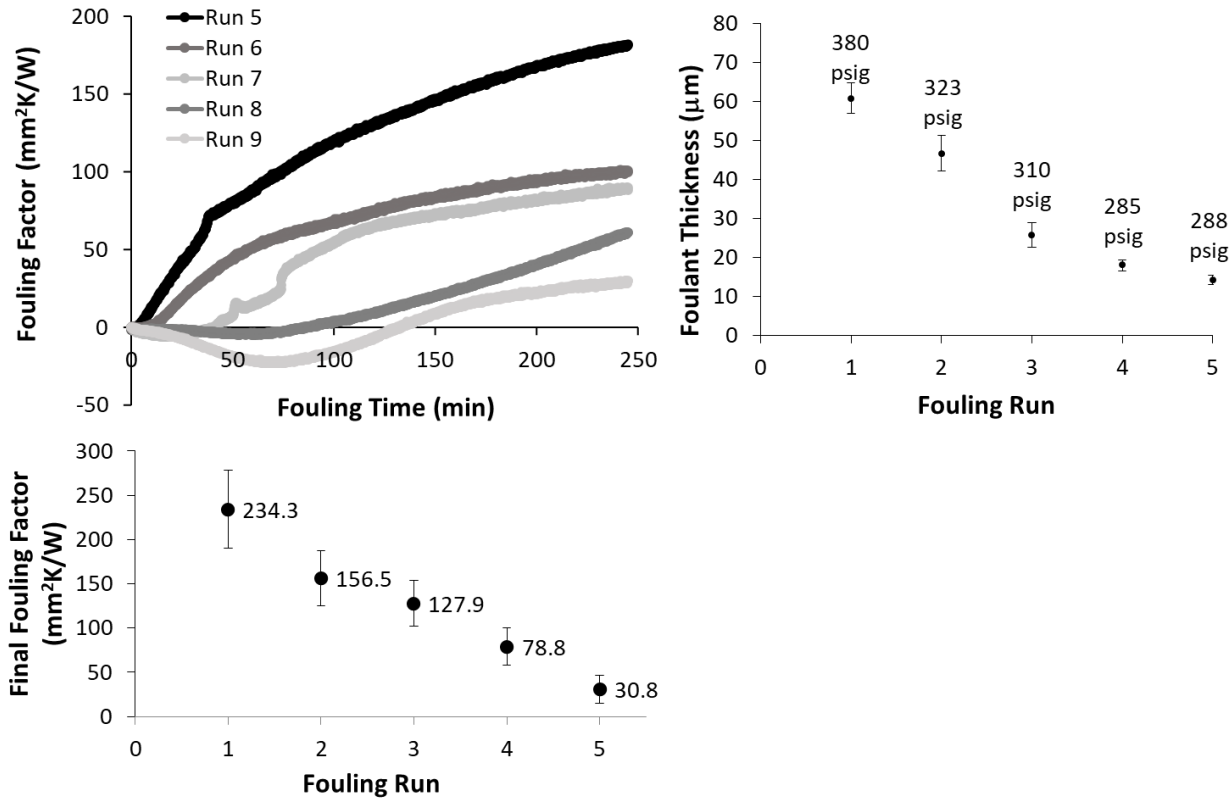

Figure 4.4 The role of bath ageing (using the same oil charge) on the fouling behavior of blend H-I. (a) In-situ fouling factors for runs 1–5. (b) Final foulant thickness (measured ex-situ from wire diameters) as a function of run number, with reactor pressure at temperature listed above each data point. (c) Plot of the final fouling factors (FFF) for each run. Negative fouling factor for run 5 is caused by a combination of a very low fouling rate and the annealing of the wire that reduces its resistivity with time. Blend H-I, metallurgy 347 SS, wire T = 490 °C, oil T = 290 °C, run time was 250 min.

The trend over runs 1 through 5 reveals decreasing foulant thickness and fouling rates, indicating a diminishing fouling propensity with high temperature aging of the oil bath. The decreasing fouling propensity with successive experiments can be linked to the depletion of fouling precursor material, both organic and inorganic and through a synergism of the two, which is discussed in detail in subsequent discussion. Considering Figure 4.4(a), the in-situ fouling rates in Runs 1 – 3 proceed initially at a nearly linear rate, followed by asymptotic behavior. Furthermore, a short induction period appears in Run 2 and extends in time with each consecutive test. The negative fouling factors in Runs 4 and 5 are caused by a combination of a very low fouling rates and the metallurgical annealing of the wire that reduces its resistivity with time. Specifically, the rapid resistive heating of the highly textured, as-drawn wire results in two phenomena: (1) The annealing of forming-induced dislocations; and (2) grain growth. Consequently, the electrical resistivity decreases with time, as does the derived wire temperature and the fouling factor. Separately, a

stainless-steel wire was subject to an ex-situ annealing heat treatment and an approximate 1% decrease in wire resistivity was measured. The treatment was carried out at the same temperature and time as the high temperature fouling experiments, under an inert atmosphere, in a quartz tube furnace. Propagating this result through our wire temperature equations would correspond to a virtual drop in temperature of ~50 °C. Researchers have also associated initially negative fouling rates with improved heat transfer across a roughening surface,[30] and with a change in the flow conditions around the wire surface where hydrodynamic forces become sufficient to remove the initially deposited material.[10,27,31] Certainly these additional effects will also factor into the negative *in-situ* fouling rates measured here. However, as may be seen from Figure 4.4(c), the *ex-situ* fouling factors are consistently positive for all runs and show the same decreasing trend with run number.

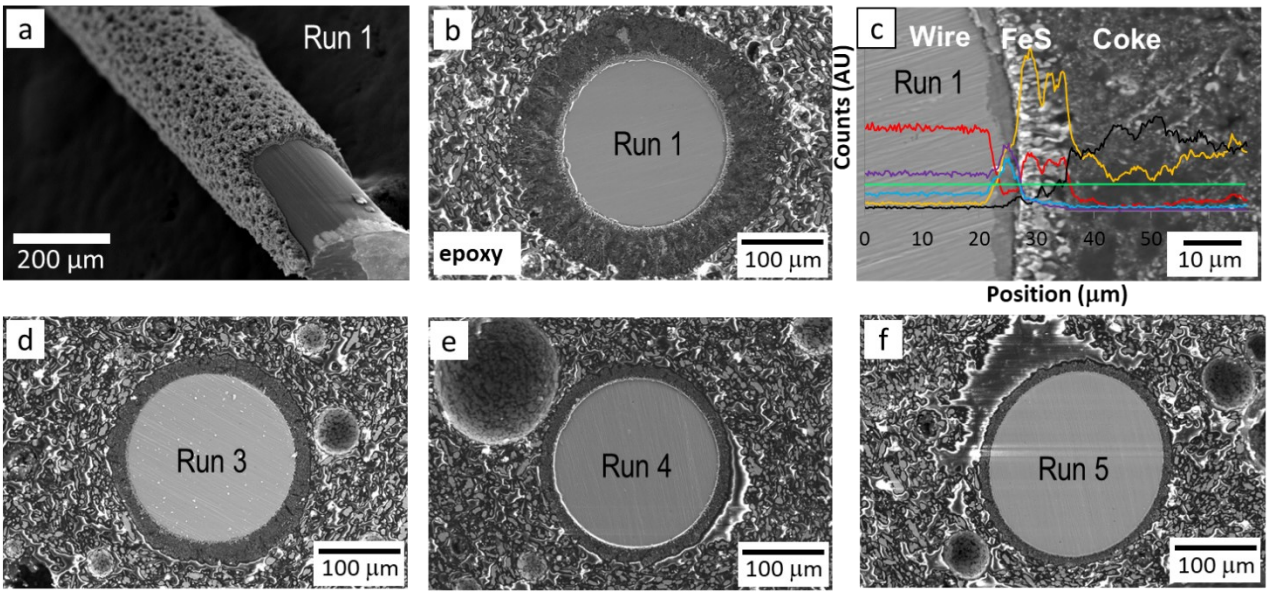

Figure 4.5 (a) SEM of the fouled wire from Run 1, (b and c) SEM and EDXS compositional scans of the fouled wire cross-sections in Run 1 (previous figure), highlighting the Fe, C, O, S and Cr distribution at the wire-foulant interface. Blend HI, metallurgy 347SS, wire T = 490°C, oil T = 290 °C, run time 250 mins. (d) Run 3 (310 psig). (e) Run 4 (285 psig). (f) Run 5 (288 psig).

Figure 4.5 presents SEM-EDXS results of the fouled 347 stainless steel wire after Run 1 (pressure = 80 psig) highlighting the iron (Fe), carbon (C), oxygen (O), sulfur (S) and chromium (Cr) distribution on the wire surface. The Figure also shows post-fouled wire cross sections after runs 3 (310 psig), 4 (285 psig) and 5 (288 psig). It may be observed that iron sulfide crystals extend from the wire surface and are densely interspersed within the coke. Figure 4.5(a) is a plan view of the wire

surface, taken near a cut end where the foulant flaked off during handling. Plan view and cross-sections of the post-fouled wires were prepared near mid length (unless otherwise specified). Figures 4.5(b and c) reveal the wire cross-section and a dense interspersion of iron sulfide (optically the light phase) throughout the surrounding organic foulant, i.e. coke/pitch (optically the dark phase). It should be noted that a carbon-based metallographic epoxy, filled with spherical and semi-spherical micron-scale nickel particles, surrounds the foulant. The nickel particles are added to reduce sample charging during SEM analysis. These rounded microparticles embedded in the epoxy (not in the foulant) are visible in all images and should not be confused with the acicular or otherwise highly crystallographic sulfide within the fouling layer. Figures 4.5(d-f) reveal diminishing foulant thickness with each consecutive run. Both the amount of organic foulant and of the sulfide decreases with each run.

It is important to make a distinction between the fouling mechanisms that occur above and below cracking temperature (i.e. ~ 350 °C)[32], since they are fundamentally different. The foulant structures we have observed, are a composite of organic and inorganic material; the inorganic material being primarily sulfidic corrosion products of the substrate material. Organic fouling below cracking temperatures is predominately related to asphaltene stability and precipitation tendency. In our experiments, at 490 ºC, there is more than enough thermal energy to induce cracking of hydrocarbon molecules and thereby induce the formation of new, reactive molecules at the heat transfer surface, which contributes to organic fouling, as coking. Asphaltene stability will play a role in coking reactions.[3334] Fouling rates of both coking and sulfidic corrosion increase as a function of increasing temperature, above ~350 °C. Additionally, we support a synergism between the organic and inorganic foulant, wherein the presence of metallic sulfide contributes to the amount of organic fouling. Consequently, at 490 ºC, we expect organic fouling as coking and inorganic fouling as metallic sulfides to proceed very rapidly, after a very short induction period that can be difficult to resolve.

Figure 4.5(c) demonstrates that the foulant immediately adjacent to the wire surface is primarily inorganic. It is composed of an approximately 10 μm thick layer of sulfides, with a coarse columnar grain structure. The SEM images in Figures 4.5(a-f) confirm the reduction in fouling behavior over Runs 1 through 5. While it is expected that total fouling will decrease with the exhaustion of organic fouling precursors, such as pericondensed aromatics, we propose that there is an additional effect, related to the amount of inorganic corrosion product - metallic sulfides. With each successive fouling run in the same oil batch, not only is the cumulative foulant thickness lowered, but so is the ratio of metallic sulfide to coke. This agrees with what might be expected if the total amount of reactive sulfur species in the oil decreased with each subsequent fouling run, i.e. the reactive volatiles are progressively exhausted. Agreeing with this scenario, we observed a progressively lowered working pressure for each fouling run (numbers above each foulant thickness data point in Figure 1(b)). From the results presented, a synergistic relationship between organic fouling and iron sulfide is highly probable.

The occurrence of iron sulfides in fouling deposits and a possible synergy with coke formation have been reported in literature.[8,29] The Blend HI contains a significant amount of sulfur, H_2S is a well-known decomposition product of high temperature cracking reactions, and sulfidic corrosion is therefore expected. Iron and nickel will rapidly sulfide in the presence of H_2S and/or other reactive sulfur species,[35] and hydrogen gas will be generated. An example of this is shown by the overall reaction described as $Fe + H_2S \Rightarrow Fe_xS + H_2$, where x may be less than 1 and depends on the partial pressure of the H_2S. Metal sulfides are good dehydrogenation catalysts,[36,37] and have been noted to increase wetting of fouling precursors,[23,38] especially asphaltenes.[39] Collectively, this might be expected to accelerate coking reactions, particularly over the metallic sulfide surfaces. Therefore, with less iron sulfide on the wire surface, one may expect less fouling to occur. As the oil bath is aged at 250 °C and is exposed to ambient atmosphere between runs (during insertion of new wires, with the system being extensively sparged with nitrogen, afterwards) fewer reactive sulfur species

would be liberated during the subsequent run. Collectively, this results in a fouling rate that attenuates with Run number.

Table 4.2 Summary of the Final Fouling Factor (FFF) for each experimental condition, where a new oil sample was employed for each experiment. σ represents the standard error, calculated for the corresponding FFF.

Oil	Metallurgy	T_{oil} (ºC)	T_{wire} (ºC)	Time (min)	FFF (mm^2*K/W)	± σ (mm^2*K/W)
HI	347SS	290	490	250	234	44
	347SS	290	490	30	55.6	18
	347SS	290	490	10	3.0	1
	347SS	290	490	5	0.9	0.5
BC	Carbon steel	290	490	60	130	37
	P91	290	490	60	139	26
	347SS	290	490	60	76	23

Table 4.2 shows a summary of experimental conditions, the corresponding final fouling factors (FFF) and the calculated standard error (σ) for each test. The final fouling factor takes into consideration the radius of the wire plus foulant thickness, in contrast to the in-situ fouling factor, and this can be seen if Equations 3.1 and 3.2 are compared: the difference being A_c vs A_f. A_f is the final heat transfer surface area, calculated from the average of eight measurements of the final foulant thickness around the wire circumference (ie $A_f = \pi(r_{foulant} + r_{wire})^2 L_{wire}$). Also worth noting, is that all results presented in this table employ a new oil sample for each experiment. Table 4.2 reveals that for each combination of oil blend - oil temperature - wire temperature, the 347SS was consistently the most resistant to fouling. A key, and initially unexpected finding, however, was that the P91 steel accumulates more fouling than the plain carbon steel. This was, originally, somewhat surprising since P91 is typically considered to be more corrosion resistant than the carbon steel in a sour environment.[40] The higher propensity of P91 to foul will be further detailed, later in the paper, and we also provide a hypothesis regarding this observation.

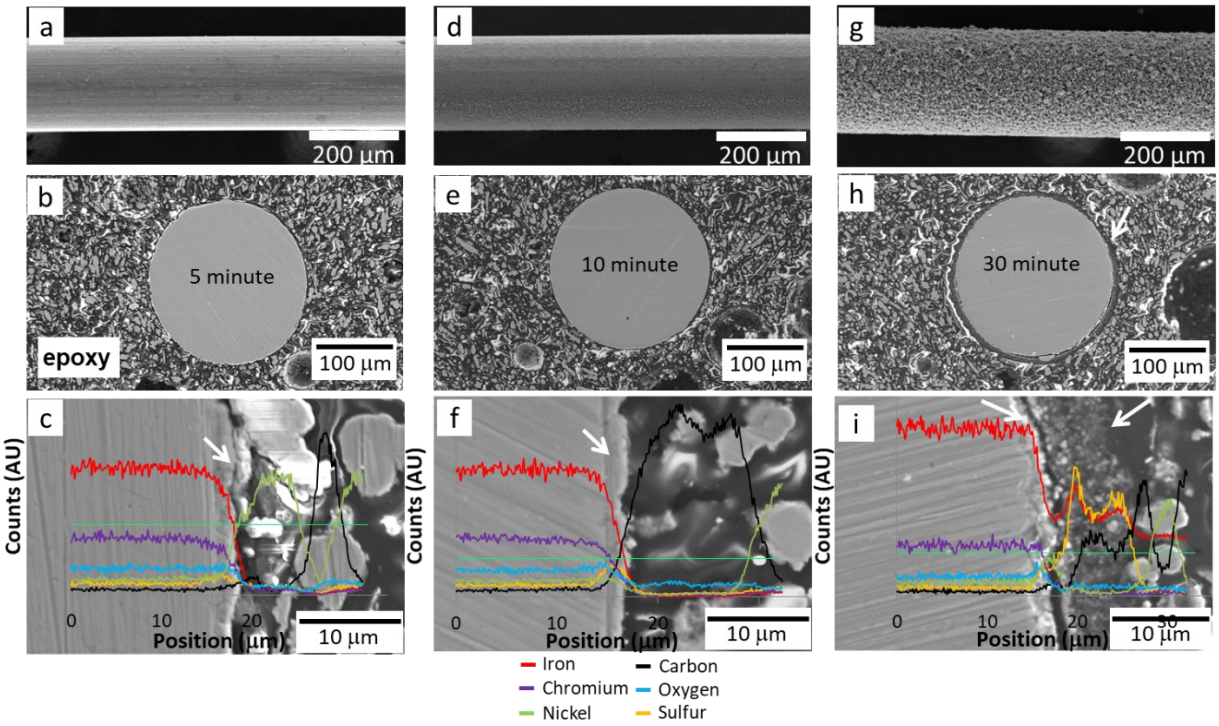

Figure 4.6 SEM and EDXS compositional scans of the fouled wire plan view and cross sections after (a-c) 5, (d-f) 10 and (g-i) 30 minutes at temperature. The arrow in (c) is a nickel microparticle at the wire interface, the arrow in (d) indicates a sulfide layer, and in (i) demarcates the foulant layer, which contains iron sulfide and carbon. Blend HI, metallurgy 347SS, wire T = 490 °C, oil T = 290 °C. For this and remaining experiments / figures a fresh oil charge was employed for every test.

Figure 4.6 details a series of experimental results that explored the foulant evolution with time in Blend HI. Here, 347SS wires, at initial surface temperature of 490 °C, were immersed for 5, 10 and 30 minutes in 290 °C oil. The figure presents SEM micrographs of the fouled wires from plan and cross-sectional vantages, with supporting EDXS elemental linescans across the wire-foulant interface in the cross-sectioned view. After 5 minutes of fouling (Figures 4.6(a and c)) there is minimal coke formation on the wire surface. The carbon signal in proximity of the wire surface originates from the surrounding epoxy (note the nickel microparticles in contact with the wire surface). The EDXS scans do detect an enrichment of sulfur at the wire surface (arrowed), accompanied by a slight surface roughening which may be the onset of sulfide growth. Figures 3(d-f) present the 10-minute fouled wire. At this point the sulfur (S) signal becomes more intense although there is still minimum detectable coke growth. Figure 3(g-i) demonstrates a much more significant degree of fouling has occurred after 30 minutes. The high magnification SEM micrograph and overlaid EDXS line scan reveal a layer of carbonaceous foulant intermixed with the sulfide, with that

layer being marked by the two opposing arrows at the top of the image. After 30 minutes the total foulant thickness is roughly 9 microns. At this point the nickel microparticles in the epoxy are no longer in contact with the wire surface, but rather impinge on the foulant layer. The FFFs were calculated as 0.9, 3.0 and 55.6 mm^2K/W, for the 5-, 10- and 30-minutes specimens. The FFFs for the 5- and 10- minute specimens presumably correspond to the growth of the sulfide layer, which would also provide a small impediment to heat transfer.

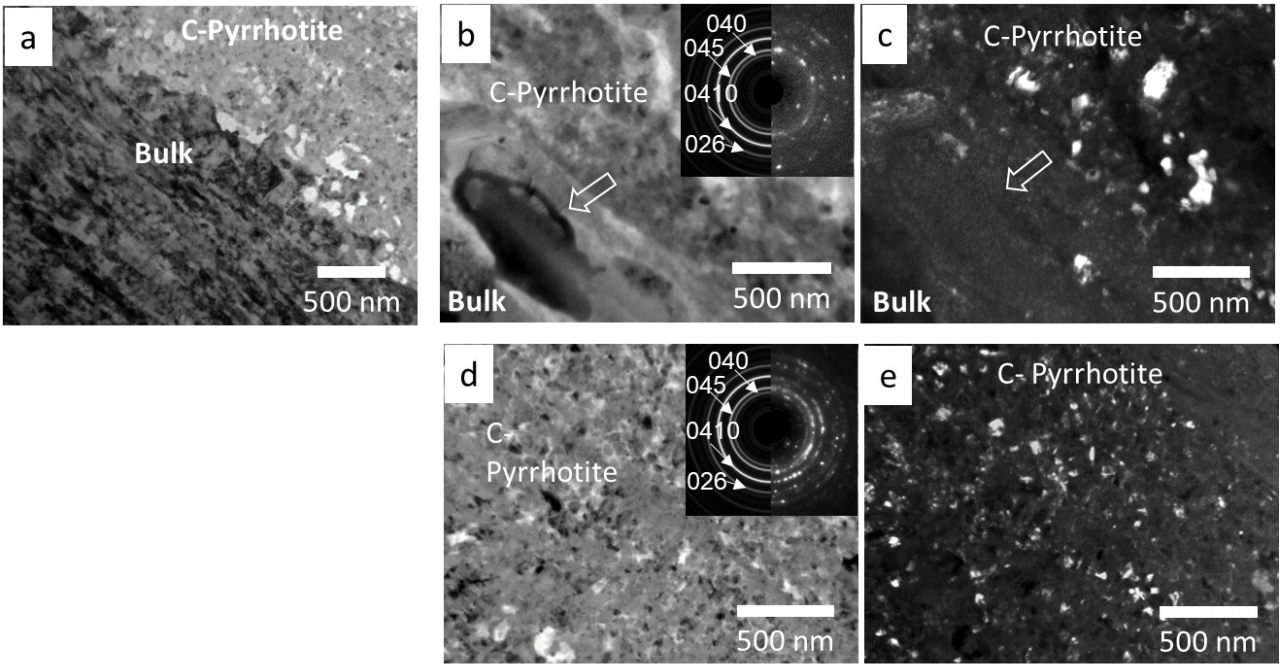

Figure 4.7 TEM bright field , indexed SAD, and dark field micrographs exploring the inner sulfide structure of fouled 347SS wire cross-sections. Fouled for 4 hours in Blend HI, wire T = 490 °C, oil T = 290 °C. (a) Micrograph highlighting the interface between the uncorroded bulk metallurgy and the inner sulfide. These inner sulfides were indexed as C-pyrrhotite (Cmca (No. 64)). (b – e) Micrographs highlighting the two general pyrrhotite morphologies encountered: larger irregular grains (arrowed in (b)) and fine equiaxed ones(arrowed in (c)), both interspersed with porosity (white regions in (a), (b) and (d)). (c and e) Dark field micrographs taken using a portion of the C-pyrrhotite ring patterns.

Figure 4.7 shows TEM bright field, indexed SAD, and dark field micrographs of cross-sections of 347SS, fouled for 4 hours in Blend HI, with the wire temperature at 490 °C and oil temperature at 290 °C. As the figures demonstrate, the wire surface is covered by an iron sulfide layer. This layer is relatively thin (2 - 3 μm), as compared to the inner sulfide that we observed for other metallurgies. This is the inner sulfidation layer, which is distinct from the outer sulfide imaged by SEM in the previous figures. The inner sulfide remains adhered to the wire surface after mechanical abrasion, which removes the much coarser outer sulfide and coke. The crystal structure

of the inner sulfide is also distinct from that of the outer sulfide (detailed in the next figure). Both phases are pyrrhotite, a sub-stoichiometric $Fe_{1-x}S$ sulfide commonly encountered during H_2S corrosion of steels.[41–45] However pyrrhotite exists as different polymorphs, with the inner sulfide being conclusively indexed as orthorhombic Cmca (No. 64), being subsequently labeled "C-pyrrhotite" in the figures. The inner sulfide is heterogeneous, generally possessing two morphologies. There are coarser sulfide crystallites (e.g. ~500 nm long) and finer sulfide nano-crystallites. In general, there are more of the coarser crystallites adjacent to the inner sulfide – metal interface. Both morphologies are interspersed with porosity, which shows up as white regions in the bright field micrographs (Figures 4.7(a, b, d)), but is practically invisible in the dark field images.

Researchers have argued that in sulfur and oxygen containing high temperature environments there will be an intermediate layer based on a mixture of chromium-rich oxides and inner sulfides,[46] the sulphides being created by the inward diffusion of H_2S gas through the thin oxide layer.[45] Chromium oxides are generally known to be a combination of Cr_3O_4 and corundum - Cr_2O_3, with both layers being heavily alloyed in elements such as nickel and iron.[47–51] Often for brevity a "Cr_2O_3/Cr_3O_4" designation is employed when referring to these oxide structures, with the understanding that both phases should be heavily doped with iron, nickel, manganese, etc. In the case of high chromium alloys where the oxygen/water vapor partial pressure is substantial, a partially porous chromium oxide layer is known to grow[47,50] It is feasible that despite extensive room temperature nitrogen sparging of the system, some oxygen and water vapor will be present in the test environment. For instance, tightly emulsified water[52,53] may remain in the crude oil despite extensive sparging. Thermally unstable naphthenic acids may decompose via a dehydration mechanism to generate water as a byproduct.[54] Roughly, 8 ppb by volume of water would be required to form a 500 nm Cr_2O_3 layer, although several orders of magnitude higher partial pressures may be needed in the presence of H_2S.[55] Overall, while some amorphous oxides could be stable in the inner layer during testing (they would not show up in the SAD patterns), the majority of the inner layer appears to be sulfide-based. This may be deduced from the indexed TEM SAD patterns and from the analytical

results shown later in the manuscript. The prevalence of sulfides is reasonable, considering that one would expect a much higher activity of reactive sulfur species versus of oxidizing species.

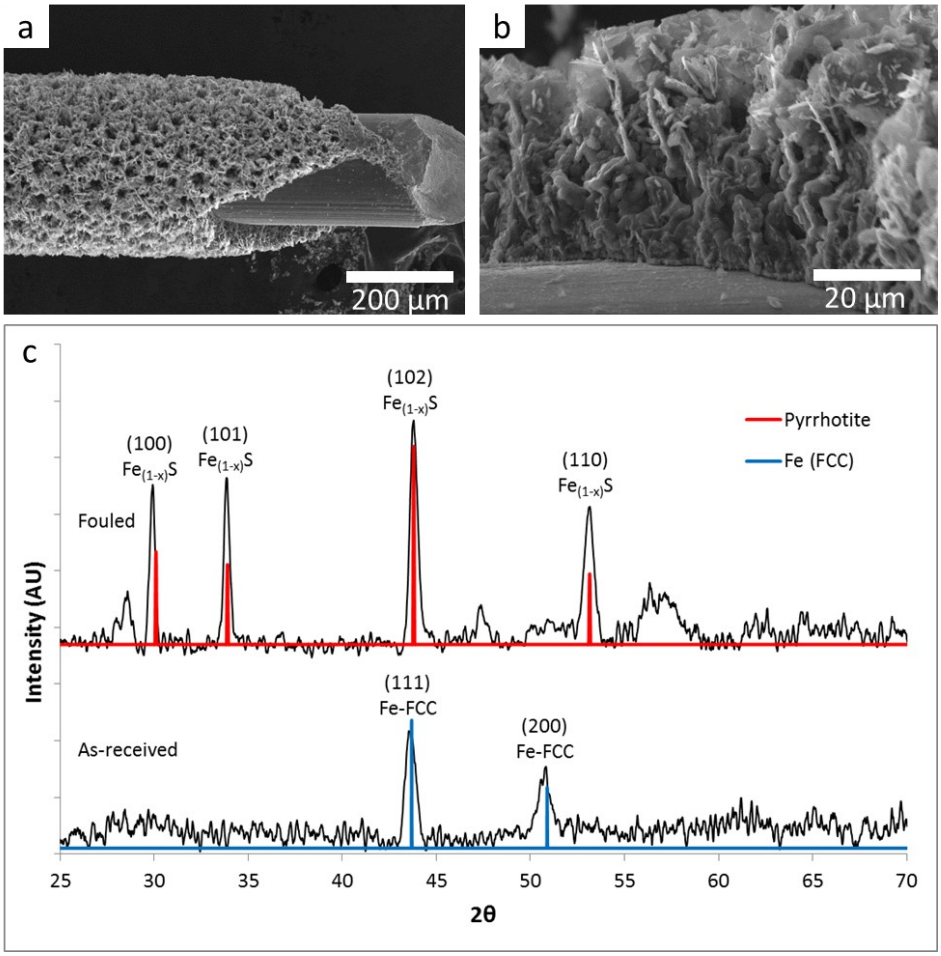

Figure 4.8 (a and b) SEM images of the 347SS surface after 4 h of fouling. (c) Indexed XRD pattern of the fouled and the as-received wire surfaces showing the growth of a thick outer sulfide P-pyrrhotite, (P6(3)/mmc, (No. 194)). Blend HI, wire T = 490 °C, oil T = 290 °C.

Figure 4.8 provides plan view SEM images of the 347 stainless steel surface after 4 hours of fouling in Blend HI (wire T = 490 °C, oil T = 290 °C). The figure also shows the associated, indexed XRD pattern of the fouled wire surface. The penetration depth of the X-rays primarily includes the outer sulfide and the coke layers only, with the underlying inner sulfide and base metal not showing up in the resultant patterns. The thick outer sulfide is indexed as another polymorph of pyrrhotite (P6(3)/mmc, (No. 194)), and is consequently labeled as "P-pyrrhotite". The morphology of the coke and of the sulfide is highly porous, with coarse P-pyrrhotite crystallites producing well-defined Bragg peaks in the XRD. Duplex corrosion film structures (e.g. fine layer of mixed inner sulphide/oxide + coarse outer sulphide) are expected when layer growth is primarily due to the outward diffusion of

metal ions.[46] Considering the 347SS, at high temperatures, both iron and nickel will readily move though the initially present ~ 10 nm surface chromium oxide (Figure 4.3(d,e)) via bulk and grain boundary cation diffusion.[41,56–58] Ionic diffusion of iron is known to be faster than that of nickel, and an enrichment of this element might be expected in the near-surface wire metallurgy after prolonged, high temperature exposure[59–61] All three elements (iron, nickel, chromium) will react with H_2S and other reactive sulfides to form mixed alloy iron-nickel-chromium sulfides that are iron rich.[62,63] These porous sulfide layers offer far less protection, and possess growth rates that are orders of magnitude higher than stable oxide layers.[55,64,65]

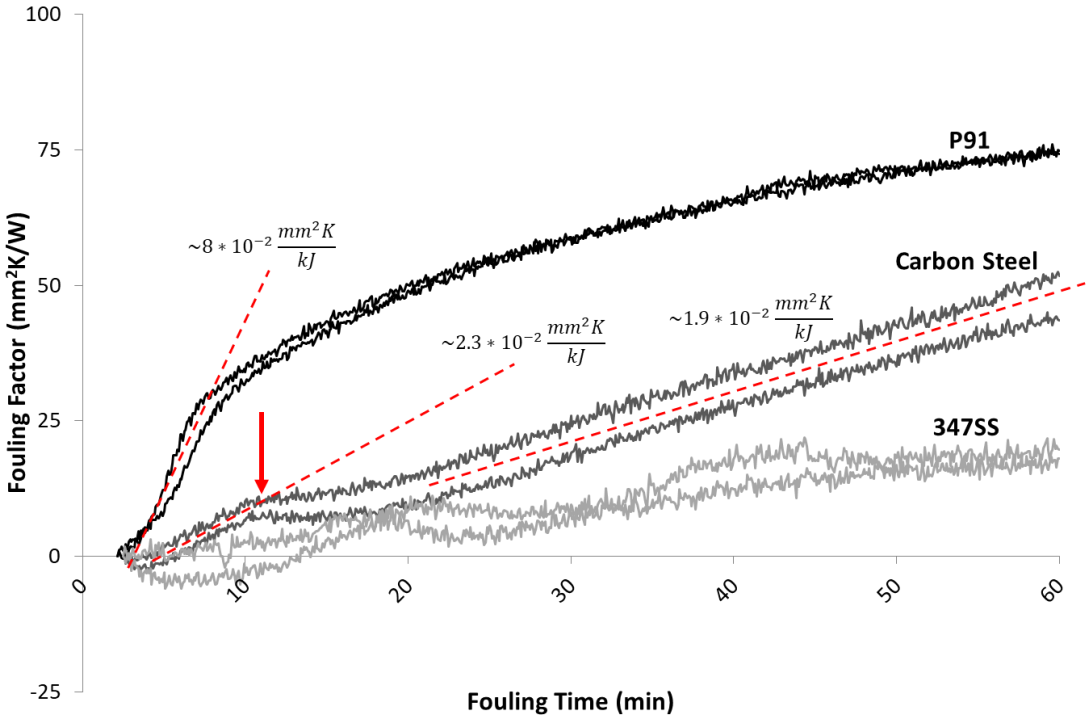

Figure 4.9 Effect of metallurgy on fouling behavior, showing in-situ fouling factor as a function of time for each metallurgy. A potential delamination event is arrowed in the carbon steel data. Approximate values for dRf/dt are provided for carbon steel, before and after delamination, and for P91. Blend BC, metallurgy 347SS, P91, carbon steel, wire T = 490 °C, oil T = 290 °C.

Figures 4.9 through 4.13 cover the effect of metallurgy on the high temperature fouling propensity of Blend BC. The other process parameters remained the same: 347SS, P91 and carbon steel, tested at wire temperature of 490 °C and oil temperature of 290 °C. The associated foulant thicknesses are presented in Table 4.3. Figure 4.9 shows the time evolution of the in-situ fouling factor, up to a 60-minute exposure, for the three wire metallurgies. Two separately obtained curves

are provided per metallurgy, highlighting the general reproducibility, not only in the degree of fouling, but also in the shape of the curves. The initial rate of change to the fouling factor was calculated and provided in the plots, for carbon steel and P91. The lowest fouling rate is achieved with 347SS, consistent with the FFF results. According to the *in-situ* FF plot, alloy P91 undergoes more fouling after one hour than the carbon steel. Notably, the carbon steel fouls at a nearly linear rate over the duration shown, while the rate of P91 asymptotes with time. Considering this, the fouling factors for carbon steel may ultimately surpass those of P91, although it is not possible to confirm this in our current experimental setup (the probes cannot withstand prolonged exposure at 290°C/490°C, in these whole crude oils). Additionally, the carbon steel suffers a discontinuity after 10 minutes of fouling, in both plots, which could discern a delamination event. The fouling factor rate of change was calculated for carbon steel before and after the event and is included along with extrapolation of the values indicated by the red dashed lines. According to the FFF data shown in Table 4.2, and on this time interval, P91 fouls more than the carbon steel, albeit with a smaller difference than observed in the *in-situ* FF plots.

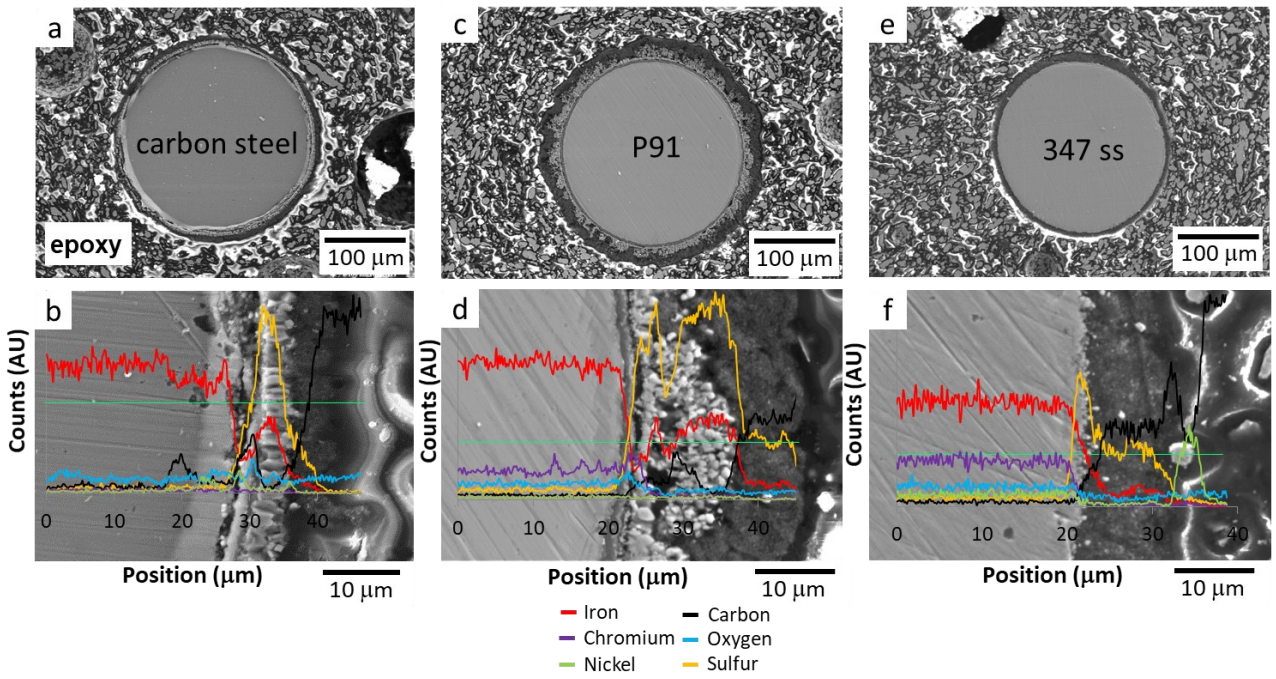

Figure 4.10 Effect of metallurgy in Blend BC. SEM micrographs and accompanying EDXS line scans of (a and b) 347SS, (c and d) P91, and (e and f) carbon steel. Fouling time = 1 h, wire T = 490 °C, oil T = 290 °C.

Figure 4.10 presents SEM micrographs and the accompanying EDXS linescans of fouled 347SS, P91 and carbon steel wires, which correlate with the data from Figure 4.9. The cross-sectional results support the fouling factor trends observed in Figure 4.9, and those listed in Table 4.2. The foulant on the P91 wire is the thickest, followed by carbon steel, and then 347SS, which exhibits a significantly thinner deposit. From the morphology and structure of the foulant, it can be inferred that the fouling mechanisms for the 347SS varies from that of carbon steel and P91. The carbon steel and P91 suffer from far more sulfidic corrosion, as evidenced by the significant iron sulfide formation on the immediate wire surface (sulfur and iron peaks in the EDXS linescans). The stainless-steel also sulfides on its surface, but to a much lesser extent. In all three materials, the foulant layer directly at the wire surface is an inorganic sulfide. The deposits become an intermixed bilayer comprised of metallic sulfide and coke as one moves radially outward, away from the base metal.

It may be seen from the cross-sectional SEM micrographs in Figure 4.10 that the foulant layers in all three metallurgies are non-uniform. Largely, the lack of uniformity stems from the plume-type sulfide structures, especially evident in Figure 4.10(c), which is the P91 cross-section. The P91 possesses the greatest concentration of these sulfide plumes, and more organic foulant, consistently. Compared to P91, the outer sulfide on the carbon steel is substantially thinner. It is also more interspersed with the coke layer; concluded because of the stronger sulfur signal in the mixed inorganic-organic layer.

An aspect when detailing the final foulant structure and thickness is how well the foulant remained adhered to the underlying material; be it the base metallurgy, or the rapidly formed metallic sulfide. Experience with these systems has demonstrated that the foulant on the stainless-steel samples adheres more tenaciously than on P91, and on P91 much more tenaciously than carbon steel. Much of this evidence comes from preparing samples for cross-sectional analysis and the effort required to retain the full amount of foulant produced on the wires. Furthermore, the thickness of the foulant on the stainless-steel suggests that no significant delamination events occurred. Additionally,

there has been very little solid material observed on the bottom of the fouling reactor, or suspended in the oils, after each experiment regardless of the alloy used.

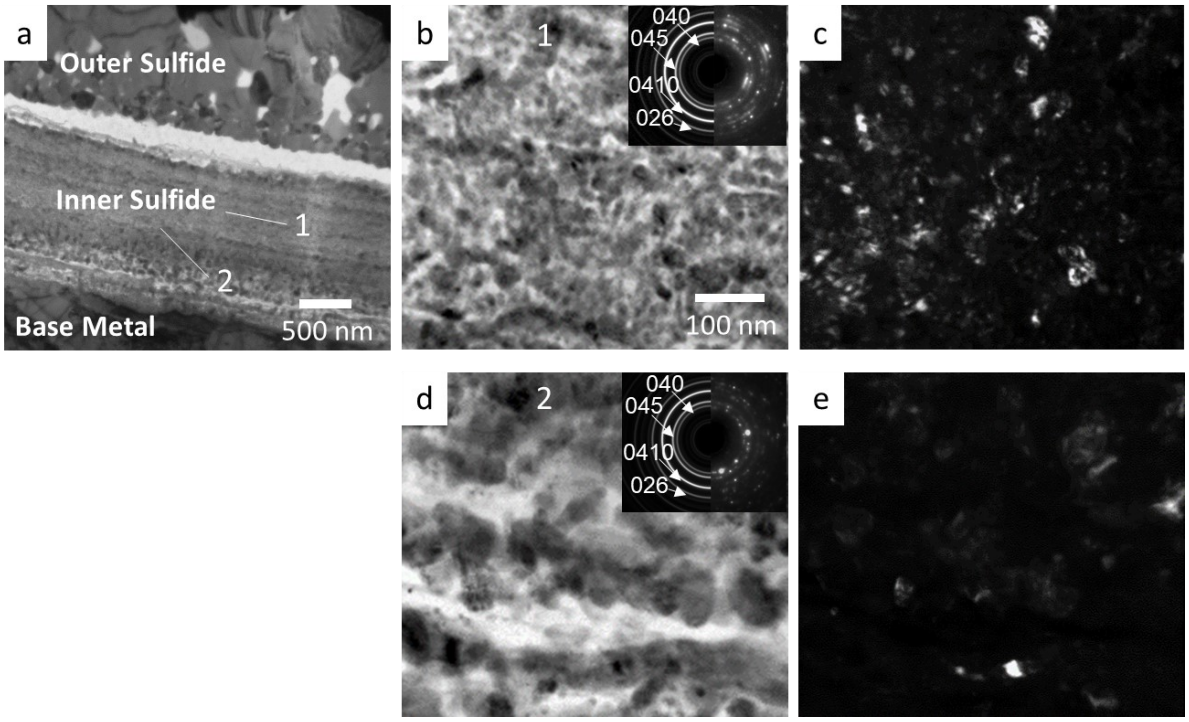

Figure 4.11 TEM bright field, indexed SAD, and dark field micrographs of cross-sectioned carbon steel wires fouled for 1 hour. Blend BC, wire T = 490 °C, oil T = 290 °C. Highlighted is the overall morphology of the inorganic foulant, showing the inner and outer sulfides. Numbers on the image correspond to regions of the inner sulfide, which were analyzed in greater detail. The dark field micrographs were taken using a portion of the C-pyrrhotite (Cmca (No. 64)) ring patterns.

Figure 4.11 shows a TEM bright field, indexed SAD, and dark field micrographs of cross sectioned samples of carbon steel wires fouled for 1 hour in Blend BC. Figure 4.11(a) highlights the overall morphology of the inorganic foulant, showing the inner and outer sulfides. The numbers on the image correspond to regions of the inner sulfide, which were analyzed in greater detail, and indexed as C-pyrrhotite (Cmca (No. 64)). Figures 4.11(b) and (d) are bright field micrographs of the inner sulfide, while Figures 4.11(c and e) are dark field micrographs taken using a portion of the pyrrhotite ring patterns. It should be noted that the crack (Figure 4.11(a)) between the inner and the outer sulfide was introduced during the FIB sectioning process of the specimen.

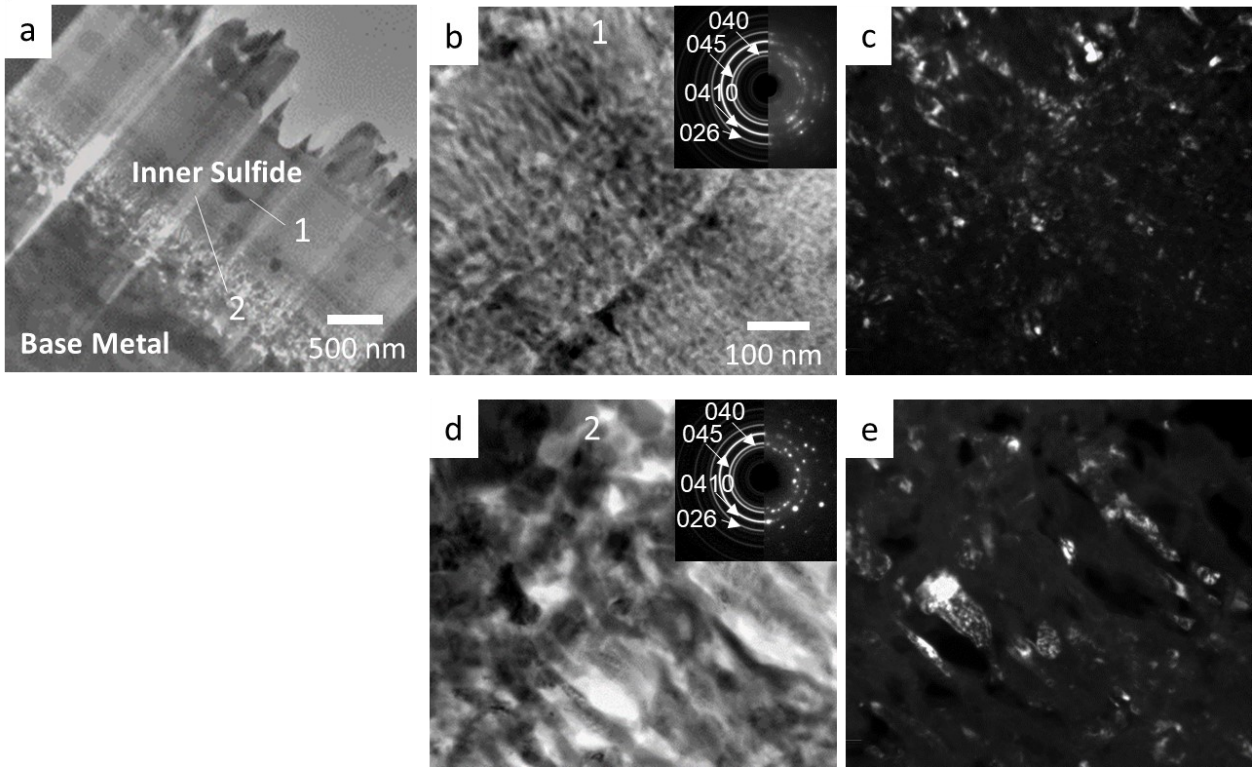

Figure 4.12 TEM bright field, indexed SAD, and dark field micrographs of P91 wire cross-sections, fouled for 1 hour. Blend B:C, wire T = 490 °C, oil T = 290 °C. Numbers on the image correspond to regions of the inner sulfide, which were analyzed in greater detail. The dark field micrographs taken using a portion of the C-pyrrhotite (Cmca (No. 64)) ring patterns.

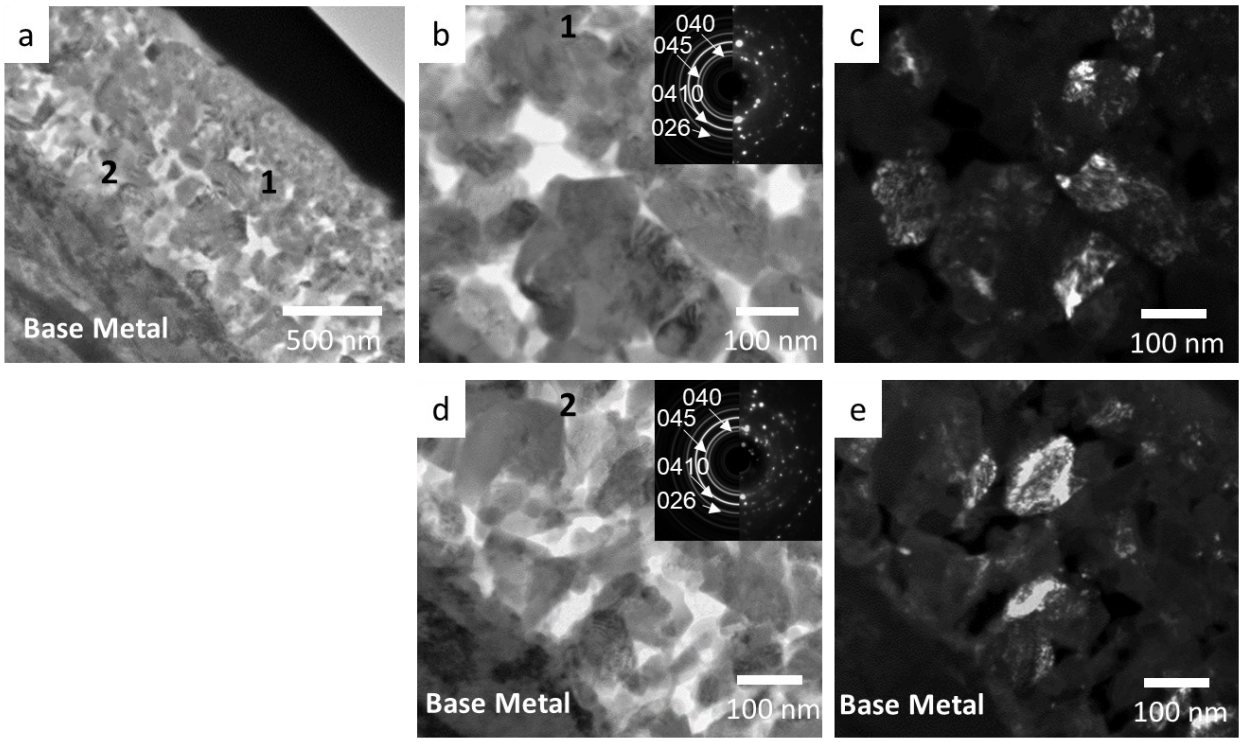

Figure 4.13 TEM bright field, indexed SAD, and dark field micrographs of cross sections of 347SS fouled for 1 hour. Blend BC, wire T = 490 °C, oil T = 290 °C. (a) Highlights the overall morphology of the inorganic foulant, showing a single sulfide layer that is C-pyrrhotite (Cmca (No. 64)). The outer sulfide was lost during the FIB process.

Figure 4.12 shows a TEM bright field, indexed SAD, and dark field micrographs of cross-sectioned P91 wires, highlighting the inner sulfide C-pyrrhotite (Cmca (No. 64)). The outer sulfide was lost during the FIB sectioning process. Figure 4.13 shows TEM bright field, indexed SAD, and dark field micrographs of cross-sectioned 347SS wires fouled for 1 hour, highlighting the inner sulfide, with the outer sulfide again being lost during the FIB milling procedure. It should be noted that the image magnification for the 347SS sample is higher than for the other two materials, and the scale marker is not the same size. A key observation is that the inner sulfide in the stainless-steel is substantially thinner, being in this case 1.5 μm, versus 5 μm for the carbon steel, and 6 μm for P91. This indicates that the inner sulfide in the stainless grows more slowly during high temperature exposure, for reasons that will be detailed shortly.

Figures 4.14, 4.15, and 4.16, show plan view SEM images and indexed XRD patterns of the fouled carbon steel, P91 and 347SS wire surfaces after 60 minutes at temperature, respectively. The results are fully consistent with what was identified after fouling in Blend HI, namely pyrrhotite ($Fe_{1-X}S$). Figure 4.17 shows field emission SEM - EDXS analysis of the inner corrosion layer of 347SS, fouled for 1 hour. The sulfide is not only iron rich, but contains significant amounts of chromium and manganese, but very little nickel. Based on the oxygen signal it is also possible that some chromium oxide coexists with the sulfide phase. It is reasonable to argue that the outward diffusion of iron in such a mixed alloy sulfide – oxide will be slower than in pure $Fe_{1-X}S$.[55] This helps to explain the lesser thickness of outer sulfide with the stainless-steel, as the alloy elements have to diffuse through the alloy sulfide (outwards) before becoming exposed to the reactive oil. While an alloyed sulfide should not affect the inward diffusion of H_2S though the pores and defects, it may make it more resistant to sulfidation, explaining the thinner inner sulfide. A competition between oxide (chromium-based) and sulfide formation would impede inner sulfide growth.

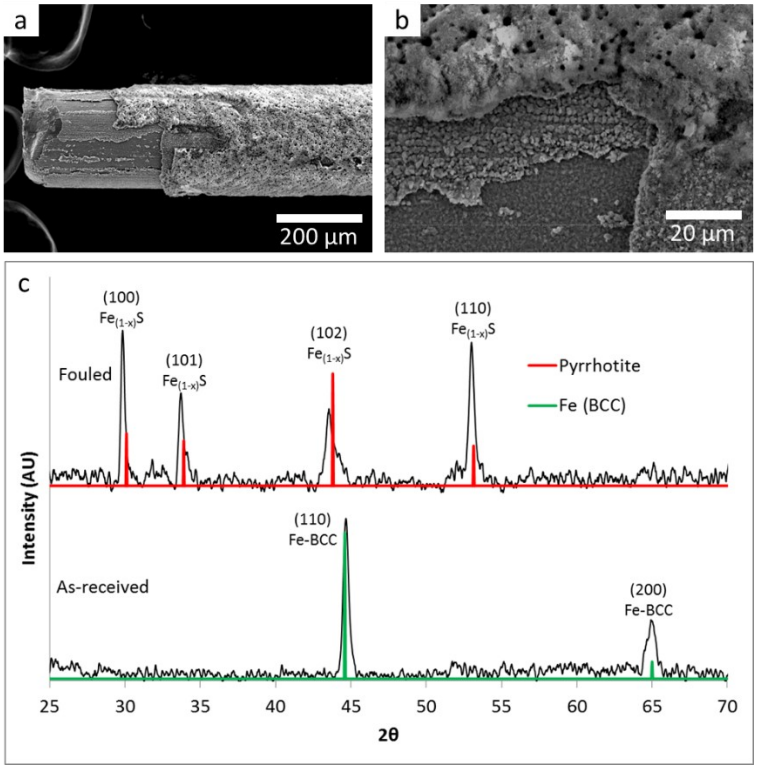

Figure 4.14 (a and b) SEM images of the carbon steel surface after 60 minutes at temperature. (c) Indexed XRD pattern of the fouled and the as-received wire surfaces showing the growth of a thick P-pyrrhotite iron sulfide phase. Blend BC, wire T = 490 °C, oil T = 290 °C.

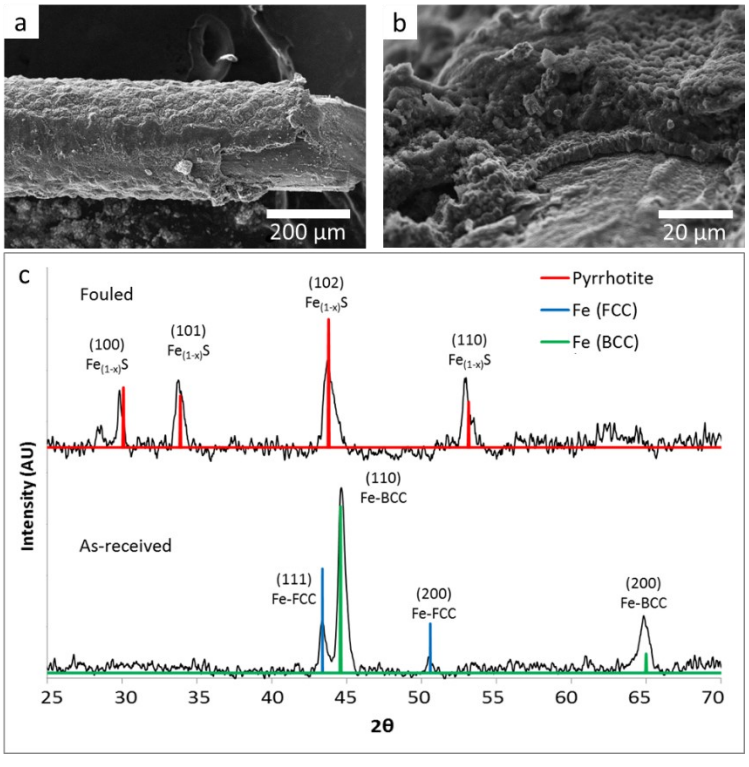

Figure 4.15 (a and b) SEM images of the P91 surface after 60 minutes at temperature. (c) Indexed XRD pattern of the fouled and the as-received wire surfaces showing the growth of a thick P-pyrrhotite iron sulfide phase. Blend BC, wire T = 490 °C, oil T = 290 °C.

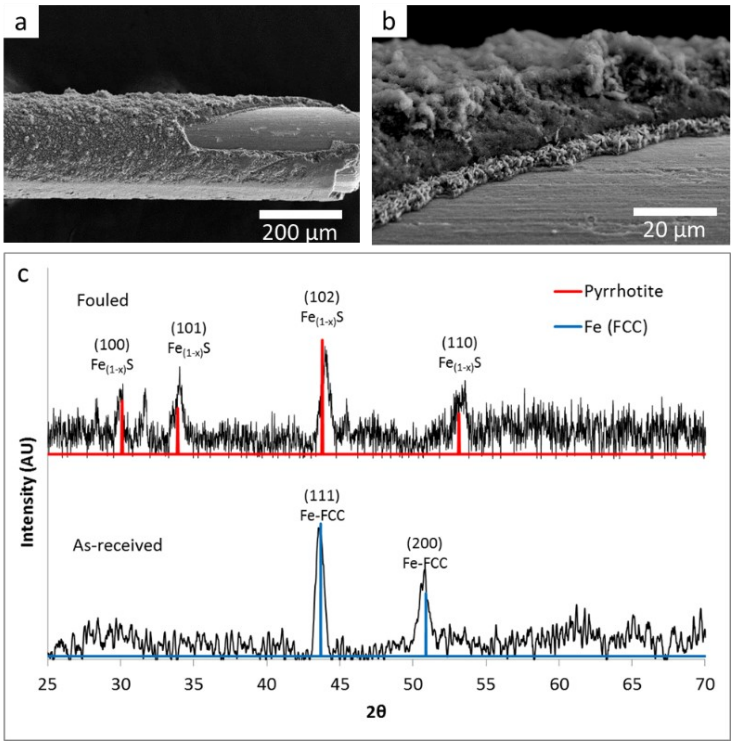

Figure 4.16 (a and b) SEM images of a 347SS wire surface after 60 minutes at temperature. (c) Indexed XRD pattern of the fouled and the as-received wire surfaces showing the growth of a thick P-pyrrhotite iron sulfide phase. Blend BC, wire T = 490 °C, oil T = 290 °C.

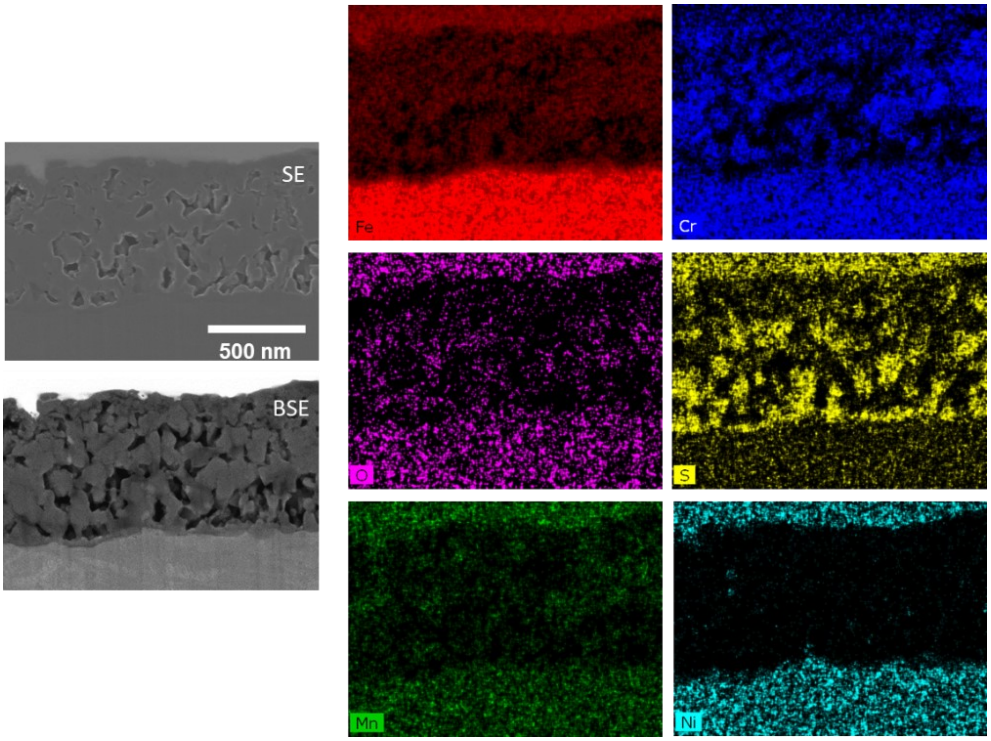

Figure 4.17 Field-Emission SEM and EDXS analysis of the inner corrosion layer of 347SS fouled for 60 minutes. Blend BC, wire T = 490 °C, oil T = 290 °C.

Table 4.3 Wire diameters pre- and post- fouling and foulant thickness.

Test	Metallurgy	Clean Wire Diameter	Corroded Wire Diameter	Δ wire diameter	Total Foulant Thickness
HI, 4 h	347SS	208.0 ± 1.7 μm	207.4 ± 1.1 μm	0.6 ± 2.0 μm	62.2 ± 6.0 μm
BC,1 h	Carbon Steel	233.7 ± 1.7 μm	229.7 ± 2.3 μm	4.0 ± 0.3 μm	13.7 ± 2.1 μm
BC, 1h	P91	233.4 ± 1.8 μm	232.8 ± 2.6 μm	0.6 ± 3.2 μm	28.1 ± 2.9 μm
BC, 1h	347SS	208.0 ± 1.7 μm	208.0 ± 1.7 μm	0	8.9 ± 2.2 μm

Since there is no reason why carbon steel should sulfide at a slower rate than alloy P91, we argue that the sulfide on the carbon steel forms, but continuously delaminates ("self – cleans") during the tests. To test this hypothesis, the diameter of the fouled wires was measured and compared against as-received geometry, looking for any meaningful changes in their cross-sections due to extensive spallation of the sulfide. These results are shown in Table 4.3. It may be seen that the carbon steel is indeed the only metallurgy with a statistically significant reduction in its cross section after the 1-hour test: ~4μm/hour, which is a 1.7% reduction to its original diameter. The mechanistic origin of the difference in the delamination behavior of the sulfide scales depends on where the actual fracture occurs, which at this point is not entirely known. For instance, if fracture and delamination occur through the bulk of the sulfide, the difference between P91 and carbon steel would presumably be due to the toughness of the sulfide. Even a marginally alloyed sulfide may be more resistant to fracture, requiring greater stresses to delaminate from the base metal. If fracture occurs in the actual base metal, but near the interface, the intrinsic high temperature toughness of the steels will be important. At 480°C the strength of a carbon steel is 148 MPa, while a P91 alloy maintains 457 MPa at 550 ºC.[66] The toughness of the metal – sulfide interface will be essential if that is where fracture occurs. Here a bond between two alloyed phases (metal and sulfide) may be stronger than between two almost pure ones.

The geometry of the wire surface will facilitate spallation due to the compressive film stress that scales logarithmically with the thickness of the growing film.[64,65] This stress would cause the growing films to buckle as they thickened, ultimately breaking them off into the surrounding viscous, but fluid, coke/pitch. Shearing stress imposed by the liquid oil, or vapors boiled of the hot wire

surface, will further accelerate this process. Any sulfide that becomes detached from the wire surface will naturally move away from the heated source due to thermophoretic motion. As it loses contact with the wire and drifts away, it will cool to the temperature of the surrounding fluid, therefore reducing any catalytic activity associated with thermal coking. An additional factor to consider is that the chromium and molybdenum present in P91 are actually catalytic towards coke growth, since both elements are known to promote surface growth of crystalline and organic carbon structures from the gas phase.[67,68] This may also drive accelerated sulfide formation in P91, which in turn leads to higher organic fouling rates.

4.4 Conclusions

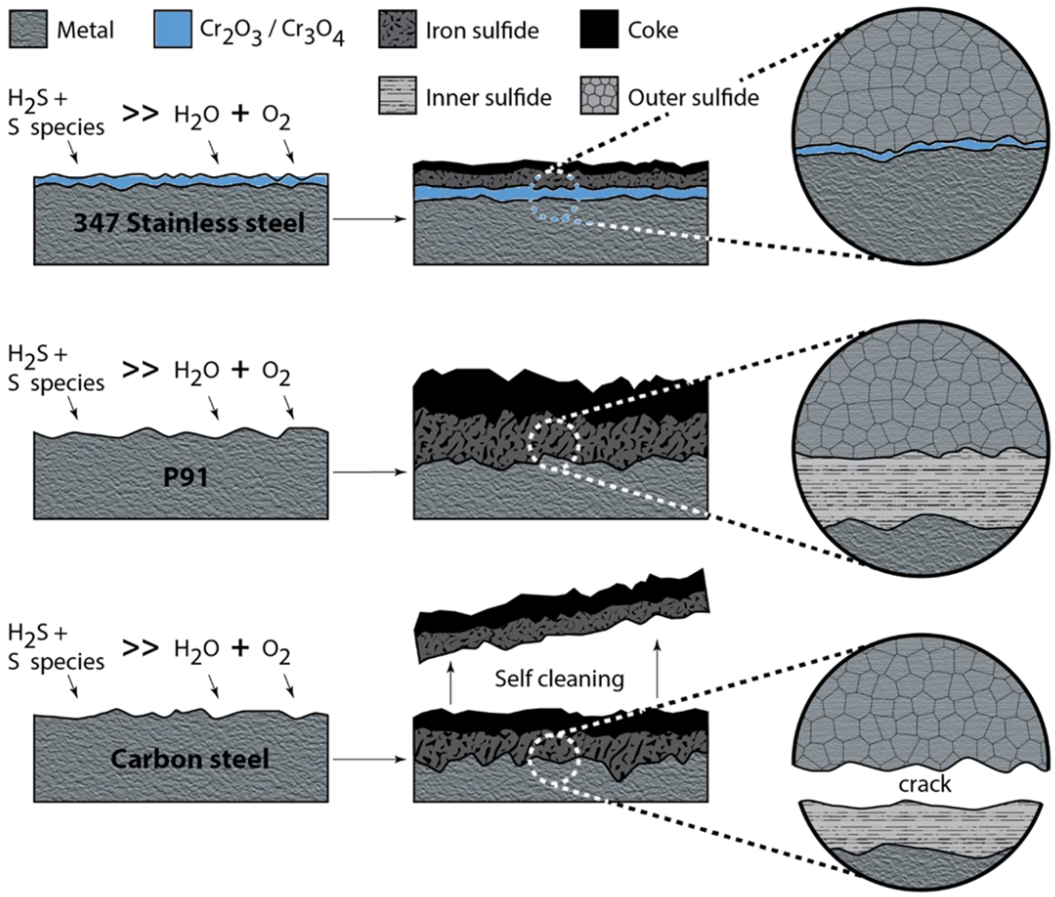

Figure 4.18 Schematic of the metallic-sulfide catalyzed fouling mechanism for the three metallurgies. At high temperatures the carbon steel is mechanically softer than P91 making the adherent FeS more susceptible to surface spallation due growth stresses, boiling, and fluid shearing forces. This results in "self-cleaning" of the carbon steel metal surface, and overall a reduced amount of FeS and coke.

To summarize, the steady-state fouling behavior of three representative refinery metallurgies (carbon steel, P91 alloy steel, and 347SS) was explored in two fundamentally different crude oil blends. A mechanistic description to elucidate the time-dependent mechanism of the interrelated carbonaceous and sulfidic build-up was put forth, explaining the essential role of surface metallurgy in establishing the fouling rates for a given feedstock. Figure 4.18 illustrates our hypotheses for each of the three metallurgies tested. The key and novel conclusion to come out of this study is a broad similarity of the fouling phenomena that begins with sulfidic corrosion of a metal surface and progresses to carbonaceous fouling. It was also surprising that the P91 metallurgy fouls more than the plain carbon steel but was explained in terms a "self-cleaning" behavior of the carbon steel surface which reduces the rate of sulfide / coke buildup over time, at the expense of significant material loss from the original wire diameter.

4.5 References

(1) Tay, F. H.; Kazarian, S. G. *Energy and Fuels* **2009**, *23* (8), 4059–4067.

(2) Gentzis, T.; Parker, R. J.; McFarlane, R. A. *Fuel* **2000**, *79* (10), 1173–1184.

(3) Mozdianfard, M. R.; Behranvand, E. **2013**, *50*, 908–917.

(4) de Oliveira Souza, M.; Ribeiro, M. A.; Carneiro, M. T. W. D.; Athayde, G. P. B.; de Castro, E. V. R.; da Silva, F. L. F.; Matos, W. O.; de Queiroz Ferreira, R. *Fuel* **2015**, *154*, 181–187.

(5) Deshannavar, U. B.; Rafeen, M. S.; Ramasamy, M.; Subbarao, D. *Journal of Applied Sciences*. 2010, pp 3167–3174.

(6) Coletti, F.; Macchietto, S. *Ind. Eng. Chem. Res.* **2011**, *50* (8), 4515–4533.

(7) Gary, J. H.; Handwerk, G. E.; Kaiser, M. J. *Petroleum Refining: Technology and Economics*, 5th ed.; CRC Press/Taylor and Francis: New York, NY, 2005.

(8) Wang, W.; Watkinson, A. P. *Proc. Int. Conf. Heat Exch. Fouling Clean. IX* **2011**, 23–30.

(9) Stephenson, T.; Hazelton, M.; Kupsta, M.; Lepore, J.; Andreassen, E. J.; Hoff, A.; Newman, B.; Eaton, P.; Gray, M.; Mitlin, D. *Fuel* **2015**, *139*, 411–424.

(10) Macchietto, S.; Hewitt, G. F.; Coletti, F.; Crittenden, B. D.; Dugwell, D. R.; Galindo, A.; Jackson, G.; Kandiyoti, R.; Kazarian, S. G.; Luckham, P. F.; Matar, O. K.; Millan-Agorio, M.; Müller, E. A.; Paterson, W.; Pugh, S. J.; Richardson, S. M.; Wilson, D. I. *Heat Transf. Eng.* **2011**, *32* (3–4), 197–215.

(11) Lestina, T. G.; Zettler, H. U. *Heat Transf. Eng.* **2014**, *35* (3), 217–223.

(12) Kim, D.; Jin, J. M.; Cho, Y.; Kim, E. H.; Cheong, H. K.; Kim, Y. H.; Kim, S. *Fuel* **2015**, *157*, 48–55.

(13) Niyonsaba, E.; Manheim, J. M.; Yerabolu, R.; Kenttämaa, H. I. *Anal. Chem.* **2019**, *91* (1), 156–177.

(14) Verşan Kök, M.; Varfolomeev, M. A.; Nurgaliev, D. K. *J. Pet. Sci. Eng.* **2019**, *179* (April), 1–6.

(15) Adams, J. J. *Energy and Fuels*. 2014, pp 2831–2856.

(16) Alshareef, A. H.; Tan, X.; Diner, C.; Zhao, J.; Scherer, A.; Azyat, K.; Stryker, J. M.; Tykwinski, R. R.; Gray, M. R. *Energy and Fuels* **2014**, *28* (3), 1692–1700.

(17) Watkinson, A. P.; Wilson, D. I. *Exp. Therm. Fluid Sci.* **1997**, *14* (4), 361–374.

(18) Somerscales, E. F. C. *Exp. Therm. Fluid Sci.* **1997**, *14* (4), 335–355.

(19) Watkinson, a. P. *Heat Transf. Eng.* **2007**, *28* (January 2015), 177–184.

(20) Rebak, R. B. *Corrosion Reviews*. 2011, pp 123–133.

(21) Slavcheva, E.; Shone, B.; Turnbull, A. *Br. Corros. J.* **1999**, *34* (2), 125–131.

(22) Hau, J. *Corrosion* **2009**, *65* (12), 831–843.

(23) Wiehe, I. A. *Process Chemistry of Petroleum Macro Molecules*, Vol. 121.; CRC Press: Boca Raton, FL, 2008.

(24) Liu, C.; Liu, H.; Yin, C.; Zhao, X.; Liu, B.; Li, X.; Li, Y.; Liu, Y. *Fuel* **2015**, *154*, 88–94.

(25) Coletti, F.; Hewitt, G. *Crude Oil Fouling: Deposit Characterization, Measurements, and Modeling*; Elsevier Science, 2014.

(26) Fan, Z.; Rahimi, P.; McGee, R.; Wen, Q.; Alem, T. *Energy and Fuels* **2010**, *24* (11), 6110–6118.

(27) Petkovic, B.; Watkinson, P. *Heat Transf. Eng.* **2013**, *35* (3), 302–310.

(28) Wang, W.; Watkinson, a. P. *Heat Transf. Eng.* **2015**, *36* (7–8), 623–631.

(29) Stephenson, T.; Kubis, A.; Derakhshesh, M.; Hazelton, M.; Holt, C.; Eaton, P.; Newman, B.; Hoff, A.; Gray, M.; Mitlin, D. *Energy and Fuels* **2011**, *25* (10), 4540–4551.

(30) Ogbonnaya, S. K.; Ajayi, O. O. *Front. Heat Mass Transf.* **2017**, *9*, 2007–2018.

(31) Yang, M.; Wood, Z.; Rickard, B.; Crittenden, B.; Gough, M.; Droegemueller, P.; Higley, T. *Appl. Therm. Eng.* **2013**, *54* (2), 516–520.

(32) Ebrahimi, S.; Moghaddas, J. S.; Aghjeh, M. K. R. *Fuel* **2008**, *87* (8–9), 1623–1627.

(33) Derakhshesh, M.; Eaton, P.; Newman, B.; Hoff, A.; Mitlin, D.; Gray, M. R. In *Energy and Fuels*; 2013; Vol. 27, pp 1856–1864.

(34) Wiehe, I. A. In *Energy and Fuels*; 2012; Vol. 26, pp 4004–4016.

(35) Ávila, B. M. F.; Pereira, V. B.; Gomes, A. O.; Azevedo, D. A. *Fuel* **2014**, *126*, 188–193.

(36) Connell, G.; Dumesic, J. A. *J. Catal.* **1986**, *102* (1), 216–233.

(37) Rana, M. S.; Ancheyta, J.; Sahoo, S. K.; Rayo, P. In *Catalysis Today*; 2014; Vol. 220–222, pp 97–105.

(38) Breysse, M.; Furimsky, E.; Kasztelan, S.; Lacroix, M.; Perot, G. *Catal. Rev.* **2002**, *44* (4), 651–735.

(39) Absi-Halabi, M.; Stanislaus, A.; Trimm, D. L. *Applied Catalysis*. 1991, pp 193–215.

(40) Schulte, M.; Rahmel, A.; Schutze, M. *Oxid. Met.* **1998**, *49* (1), 33–70.

(41) Baxter, D. J.; Natesan, K. *Oxid. Met.* **1989**, *31* (3), 305–323.

(42) Xiaofei, Z.; Tao, M.; Xiaochun, H.; Jinde, Z.; Xiaoyi, W.; Sixian, R. *Eng. Fail. Anal.* **2020**, *117* (January), 104802.

(43) Soltanattar, S.; Nowakowski, P.; Bonifacio, C. S.; Fischione, P.; Gleeson, B. *Oxid. Met.* **2019**, *91* (1–2), 11–31.

(44) Stephan-Scherb, C.; Nützmann, K.; Kranzmann, A.; Klaus, M.; Genzel, C. *Mater. Corros.* **2018**, *69* (6), 678–689.

(45) Lobnig, R. E.; Grabke, H. J. *Corros. Sci.* **1990**, *30* (10), 1045–1071.

(46) Atkinson, A. *Rev. Mod. Phys.* **1985**, *57* (2), 437–470.

(47) Saunders, S. R. J.; Monteiro, M.; Rizzo, F. *Progress in Materials Science*. Pergamon July 1, 2008, pp 775–837.

(48) Cheng, S. Y.; Kuan, S. L.; Tsai, W. T. *Corros. Sci.* **2006**, *48* (3), 634–649.

(49) Oh, K. N.; Ahn, S. H.; Eom, K. S.; Jung, K. M.; Kwon, H. S. *Corros. Sci.* **2014**, *79*, 34–40.

(50) Karimi, N.; Riffard, F.; Rabaste, F.; Perrier, S.; Cueff, R.; Issartel, C.; Buscail, H. *Appl. Surf. Sci.* **2008**, *254* (8), 2292–2299.

(51) Buscail, H.; Messki, S. El; Riffard, F.; Perrier, S.; Cueff, R.; Caudron, E.; Issartel, C. *Mater. Chem. Phys.* **2008**, *111* (2–3), 491–496.

(52) Kilpatrick, P. K. *Energy & Fuels* **2012**, *26* (7), 4017–4026.

(53) Perini, N.; Prado, A. R.; Sad, C. M. S.; Castro, E. V. R.; Freitas, M. B. J. G. *Fuel* **2012**, *91* (1), 224–228.

(54) Nguyen, M. T.; Sengupta, D.; Raspoet, G.; Vanquickenborne, L. G. *J. Phys. Chem.* **1995**, *99* (31), 11883–11888.

(55) Danielewski, M.; Natesan, K. *Oxid. Met.* **1978**, *12* (3), 227–245.

(56) Young, D. *High Temperature Oxidation and Corrosion of Metals*; 2015; Vol. 1.

(57) Kai, W.; Leu, C. T.; Lee, P. Y. *Oxid. Met.* **1996**, *46* (3), 185–211.

(58) Jacob, K. T.; Bhogeswara Rao, D.; Nelson, H. G. *Oxid. Met.* **1979**, *13* (1), 25–55.

(59) Hobby, M. G.; Wood, G. C. *Oxid. Met.* **1969**, *1* (1), 23–54.

(60) Sabioni, A. C. S.; Huntz, A. M.; Souza, J. N. V; Martins, M. D.; Jomard, F. *Philos. Mag.* **2008**, *88* (3), 391–405.

(61) Sabioni, A. C. S.; Huntz, A. M.; Silva, F.; Jomard, F. *Mater. Sci. Eng. A* **2005**, *392* (1–2), 254–261.

(62) Li, H.; Chen, W. *Oxid. Met.* **2012**, *78* (1–2), 103–122.

(63) Li, H.; Chen, W. *Oxid. Met.* **2012**, *77* (3–4), 107–127.

(64) Mitlin *, D.; Misra, A.; Mitchell, T. E.; Hirth, J. P.; Hoagland, R. G. *Philos. Mag.* **2005**, *85* (28), 3379–3392.

(65) Mitlin, D.; Misra, A.; Radmilovic, V.; Nastasi, M.; Hoagland, R.; Embury, D. J.; Hirth, J. P.; Mitchell, T. E. *Philos. Mag.* **2004**, *84* (7), 719–736.

(66) Shashank Dutt, B.; Nani Babu, M.; Venugopal, S.; Sasikala, G.; Bhaduri, A. K. *Mater. Sci. Technol.* **2011**, *27* (10), 1527–1533.

(67) Baker, R. T. K.; Yates, D. J. C.; Dumesic, J. A. *ACS Symp. Ser.* **1982**, 1–21.

(68) DE JONG, K. P.; GEUS, J. W. *Catal. Rev.* **2000**, *42* (4), 481–510.

CHAPTER 5

Low Temperature Fouling Experiments

5.1 Introduction

In high temperature fouling experiments, tests were conducted with wire temperatures of 490 °C. This is well above thermal cracking temperature for crude oils, which commonly becomes appreciable above 370-390 °C. Those tests demonstrated a consistent sequence of sulfidic corrosion, then organic fouling. Below thermal cracking temperatures, organic fouling is expected to be dominated by asphaltene instability and depositional fouling, wherein particles from the bulk oil migrate and attach to the surface of the heated wire.[1] The phenomenon of carbonaceous fouling because of thermal cracking of asphaltene is well documented.[2] A strong synergy between sulfidic corrosion product and the amount of organic, carbonaceous fouling has been identified amongst other researchers,[3,4] and confirmed in this work under high temperature conditions for a range of crude oils and metallurgies. Surface corrosion and associated roughening of the wires surface is expected to influence the rate of deposited material, but overall fouling rates are anticipated to be much lower. Sour corrosion (driven by H_2S) is expected to remain significant for the least corrosion resistant carbon steel and be minimized on the resilient 347SS, due stability of the iron-chromium surface oxide, highlighted by TEM analysis in Figure 4.3(d and e).

For direct comparison to high temperature results, the same three metallurgies – carbon steel, P91 and 347SS, were utilized. Low temperature experiments were conducted using wire temperature of (350 °C), oil temperature (250 °C), and pressure (400 psig). The wires were fouled for 4 hours and 8 hours, to demonstrate the effect of exposure time. Low fouling rates at these conditions meant that wire cross-sections were not as insightful as in high temperature experiments and the wire surfaces were also analyzed by SEM near their mid length. Some inconsistency of the foulant deposit was observed as a function of position along the wire length.

5.2 Low Temperature Metallurgy Study

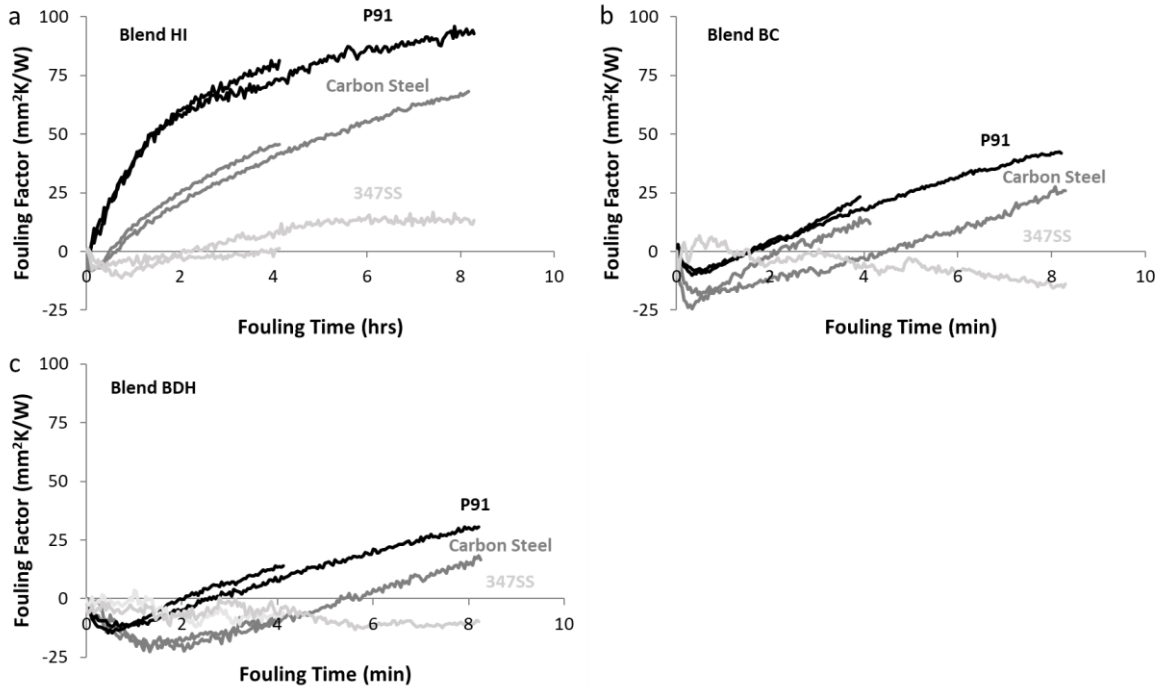

Figure 5.1 The effect of metallurgy on fouling at low temperature in (a) Blend HI, (b) Blend BC, and (C) Blend BDH. Twire = 350°C, Toil = 250°C, run time = 4 and 8 hours.

Figure 5.1 and Table 5.1 summarize fouling factor data for low temperature experiments in all three blended oils. Figures 5.1(a-c) pertain to Blends HI, BC, and BDH respectively. Interestingly, and consistent with the high temperature dataset, P91 is shown to reach larger peak fouling factors than carbon steel, in all three blends. The 347SS wire does not foul detectably in any of the three oils. From Table 5.1, the maximum fouling factor for P91 and carbon steel wires in Blends HI, BC, and BDH were 95.8, 42.0, and 30.1 mm^2K/W and 67.5, 27.5, and 16.6, mm^2*K/W, respectively. Final fouling factor data demonstrates an identical trend. In all cases except carbon steel in Blend HI, the final fouling factor is greater than the maximum fouling factor recorded during the live experiments. This observation is linked to the self-cleaning, delamination events that have been characteristic of this metallurgy. Notable, is the lack of correlation between the average foulant thickness ($R_{foulant}$) and either of the fouling factor datasets. This is because the fouling factors only represent a total resistance to heat transfer but provide no predictive ability as to the specific resistance to heat transfer for the foulant materials that have been observed. Iron sulfides, coke, and other carbonaceous/organic foulant will resist heat transfer to varying.[5]

Table 5.1 Summary of experimental conditions and fouling factors for low temperature tests in Blends HI, BC, and BDH.

Oil	Metallurgy	T_{oil} (°C)	T_{wire} (°C)	Time (h)	$R_{foulant}$ (µm)	FF, max. (mm^2*K/W)	FFF (mm^2*K/W)
HI	CS	250	350	4	2.9	81.4	27.7
				8	4.6	67.5	45.5
	P91	250	350	4	13.6	81.4	92.8
				8	16.3	95.8	102.5
	347SS	250	350	4	Ø	0.1	Ø
				8	Ø	13.2	Ø
BC	CS	250	350	4	12.8	14.1	56.7
				8	13.3	27.5	59.5
	P91	250	350	4	18.2	23.1	82.4
				8	22.6	42.0	98.0
	347SS	250	350	4	Ø	-2.3	Ø
				8	Ø	-15.6	Ø
BDH	CS	250	350	4	5.4	-6.4	3.5
				8	5.6	16.6	46.3
	P91	250	350	4	8.3	13.4	38.5
				8	12.9	30.1	90.0
	347SS	250	350	4	Ø	-6.4	Ø
				8	Ø	-9.7	Ø
BDH	CS	250	300	4 hrs.			
	P91	250	300	4 hrs.			

*CS – carbon steel

There is, as has been observed previously, negative portions to the fouling factor curves for all three metallurgies. The negative regions also extend for a larger percentage of the experiment duration than at higher temperature. Consistent with previous observation and discussion, is that the depth of the minimal values are greater for carbon steel than for P91 and for lower fouling oil. This has been attributed to a greater degree of microstructural stability in the P91 alloyed material versus the carbon steel, and a superior adherence of the corrosion/fouling layer onto P91 relative to carbon steel. A lower fouling oil means that there is relatively more effect from the microstructural change, which lowers the wire resistance and causes the fouling factor to drop, than there is from the thermally insulating foulant, which causes the fouling factor (resistance to heat dissipation) to rise. The fouling factor for 347SS was dominated by system noise. Some resistance to heat transfer was resolved in Blend HI, but the lack of foulant, will be presented throughout subsequent analysis. All fouling factor

data, in these low temperature experiments was more susceptible to various sources of system noise/scatter, several of which were well documented and will be discussed.

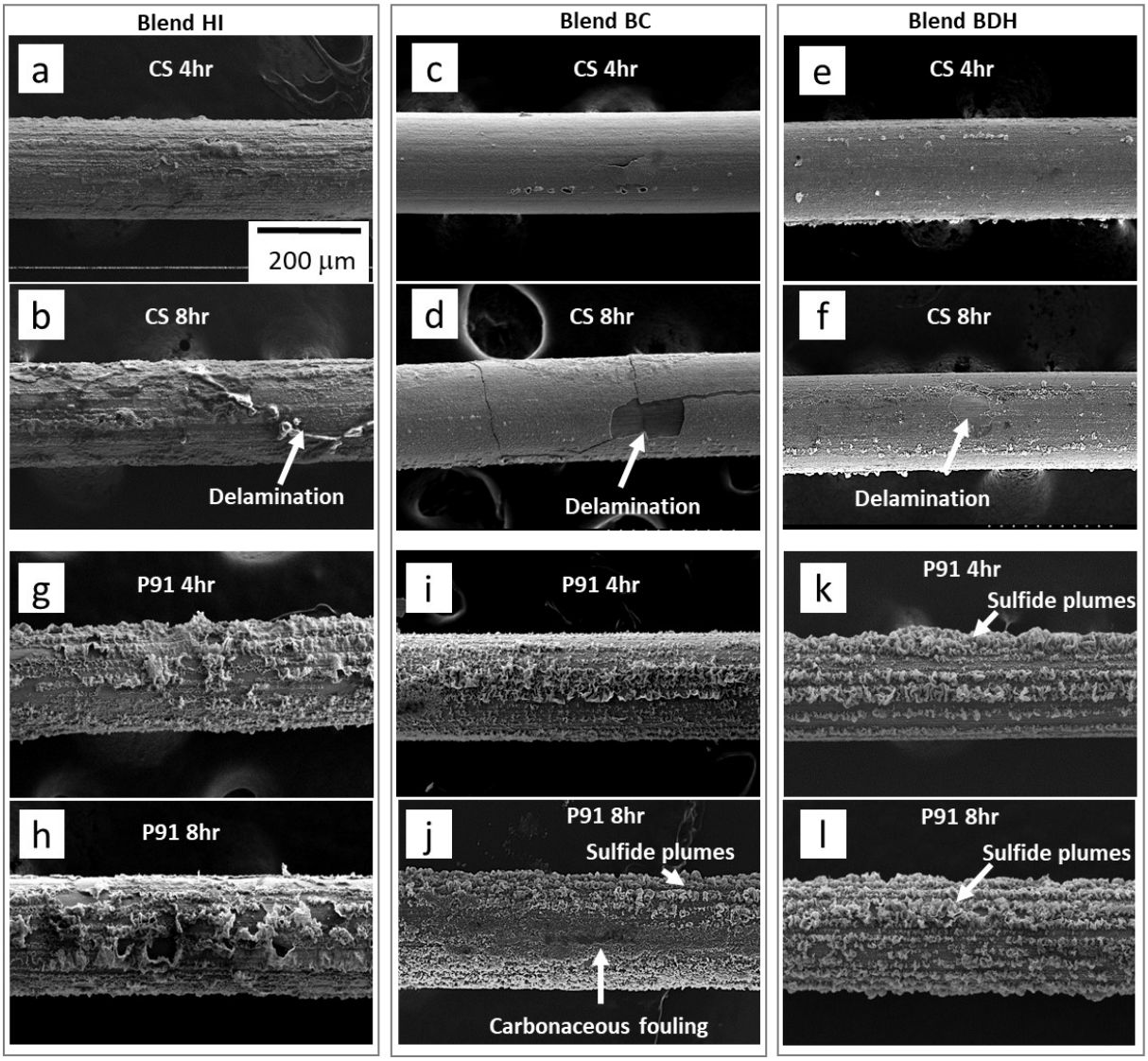

Figure 5.2 Low magnification SEM micrographs of fouled wire surfaces after 4- and 8-hour exposure in Blends HI, BC, and BDH. (a-f) Carbon steel and (g-l) P91 metallurgies.

Figure 5.2 contains low magnification SEM micrographs of fouled carbon steel and P91 wires as a function of oil and fouling time. Figures 5.2(a-f), the upper image set, are carbon steel wires, which exhibit relatively smooth surfaces and the appearance of only limited overall foulant. Blend HI has imparted the most foulant and Blend BDH the least. In Blend BC the foulant seems to be a dense sheath of corrosion product, especially considering Figure 5.2d which is the 8-hour test result. Figures 5.2(g-l) are P91 wires and in contrast to carbon steel, appear to have retained more foulant, although much less foulant is noticeable, and with significantly unique texture, versus P91 fouled

under the high temperature conditions. Blend HI is the highest fouling, but it is difficult to identify a clear relative distinction between the remaining two oils.

Overall, fouling morphologies are surprisingly unique amongst each combination of metallurgy and oil. This correlates with the (lack of) trend amongst the average foulant thickness and fouling factor data, presented in discussion regarding data from Figure 5.1 and Table 5.1. For both metallurgies, it appears the highest fouling oil is Blend HI, which is consistent with the fouling factor data. Beyond Blend HI, it is unclear from these images which of the remaining two combinations of oil and metallurgy has a higher fouling propensity, and further analysis will be presented.

A comparison of carbon steel versus P91 under identical test conditions reveals that the P91 metallurgy retains more foulant, consistent with the fouling factor data in Figure 5.1 and Table 5.1, and with observations throughout the high temperature experiments. Delamination of the fouling layer is observed with the carbon steel metallurgy, especially in the longer,8-hour experiments. The surface of the P91 wires exhibits much more structure and roughness, and several unique features are labelled as *sulfide plumes*, while the carbon steel surface is relatively smooth, but obviously different versus the as-received condition presented in Figure 4.1.

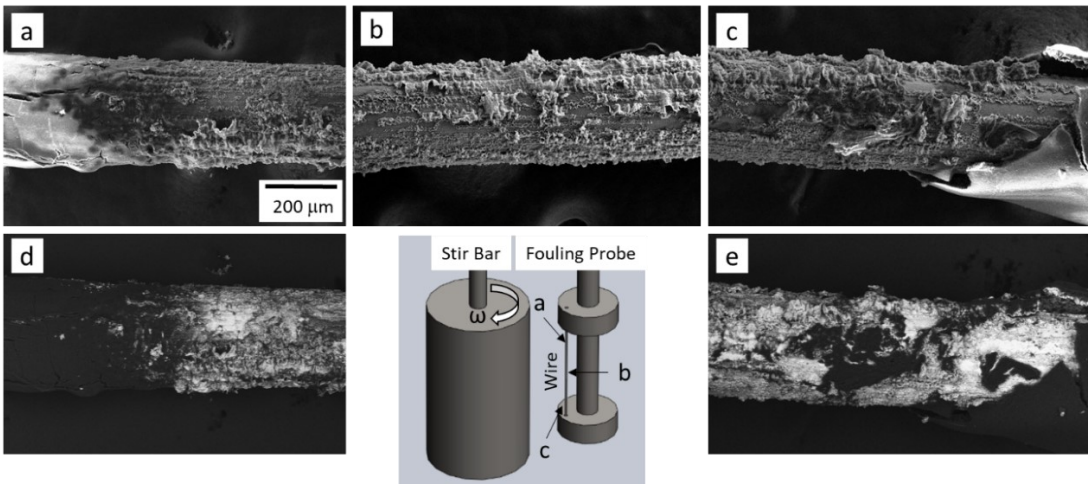

Figure 5.3 SEM micrographs of a fouled wire surface showing variability along its length. (a) Location "a", near the upper connection, (b) near the wire mid-length, and (C) at the lower connection with the probe. (c,d) BSE images of the wire surface demonstrating phase contrast of the deposited material. An inset image highlights the wire geometry within the fouling reactor. Blend BDH, Twire = 350°C, Toil = 250°C.

Figure 5.3 introduces a characteristic of the low temperature fouling experiments that was not observed under the high temperature conditions, and one of the sources of noise/scatter alluded to in previous discussion. Figures 5.3(a-c) are low magnification SEM micrographs of the wire surface at the upper probe connection, the wire mid-length, and the lower probe connection. An inset graphic of a fouling probe identifies the locations. Figures 5.3(d and e) are micrographs collected with a backscatter detector, which promotes atomic number contrast of the analyzed material. Contrast of the carbonaceous foulant appears darkest, carbon having a low (14) atomic number, versus the bulk of the wire (Fe) and corrosion product (FeS) which both produce relatively light contrast. Near the wire connections to the probe, where bulk flow of the oil is expected to be significantly disturbed, varying amounts of organic, carbonaceous foulant can be observed. This material is loosely adhered and easily dislodged from the wire surface when handled. Underneath the carbonaceous mass the fouling is relatively consistent with what was evident on the remaining length of wire. These organic deposits were largely toluene soluble, indicating that they are likely a result of unstable asphaltenes, asphaltene flocculation, and eventual deposition on the hot surface of the wire. Depositional or particulate fouling is promoted on the hot wire surface, roughened by sulfidic corrosion product, and where little or no flow exists. This foulant covered less than 15% of the wire length in the most extreme case. Wire cross-sections were prepared near mid-length and did not capture these deposits.

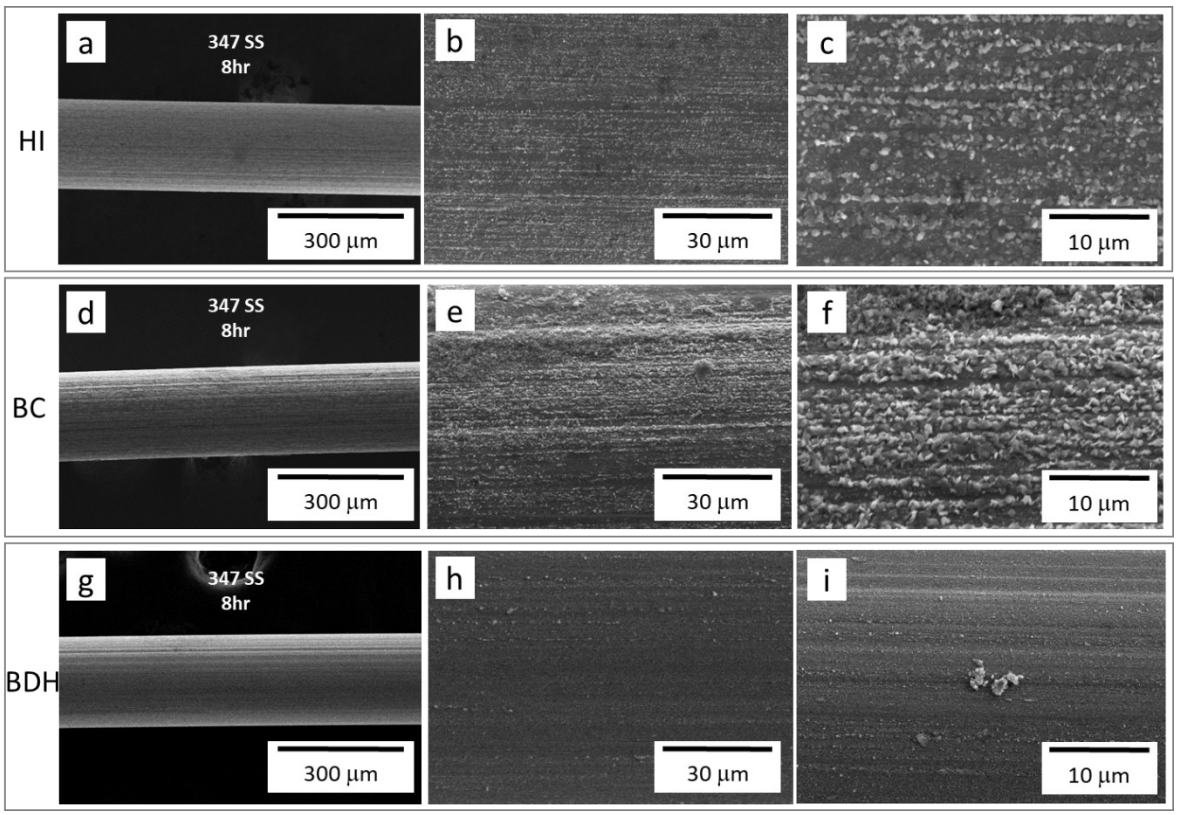

Figure 5.4 SEM micrographs of 347SS wire surfaces after 8 hours of fouling in each oil Blend. (a) Blend Hi, (b) Blend BC, and (c) Blend BDH.

Figure 5.4 through 5.6 explore the 347SS metallurgy after testing under the low temperature fouling conditions (350 °C wire temperature and 250 °C oil bath temperature). Figure 5.4 contains SEM micrographs of the 347SS wire surfaces near mid-length. Collectively, these images demonstrate the effectiveness of the anti-corrosion, anti-fouling ability of this metallurgy. Figures 5.4(c, f, and i) are high resolution micrographs and it is only here that some evidence of corrosion produced. In Figure 5.2, the wire surfaces were imaged at 150x magnification and here 3500x. At this resolution, small crystallizes are observed that have preferentially formed along the textured microstructure of the wire. The 347SS metallurgy exhibits the most foulant after exposure to Blend BC and least in Blend BDH. In fact, the wire removed from Blend BDH has experienced almost no change versus the as-received condition.

The small amount of foulant present on the 347SS metallurgy is analyzed in Figure 5.5, which includes a SEM micrograph and EDXS elemental maps for the outlined area. Elemental maps for iron (Fe), chromium (Cr), nickel (Ni), sulfur (S), oxygen (O), and carbon (C) are presented and

correlate spatially with the region outlined in Figure 5.5a. This compilation reveals that the surface features are iron sulfides, with a lesser amount of carbon, which may just be contamination. Figure 5.6 are wire cross-sections after 8 hours of fouling. No fouling or corrosion is evident in the low or higher resolution SEM micrographs displayed.

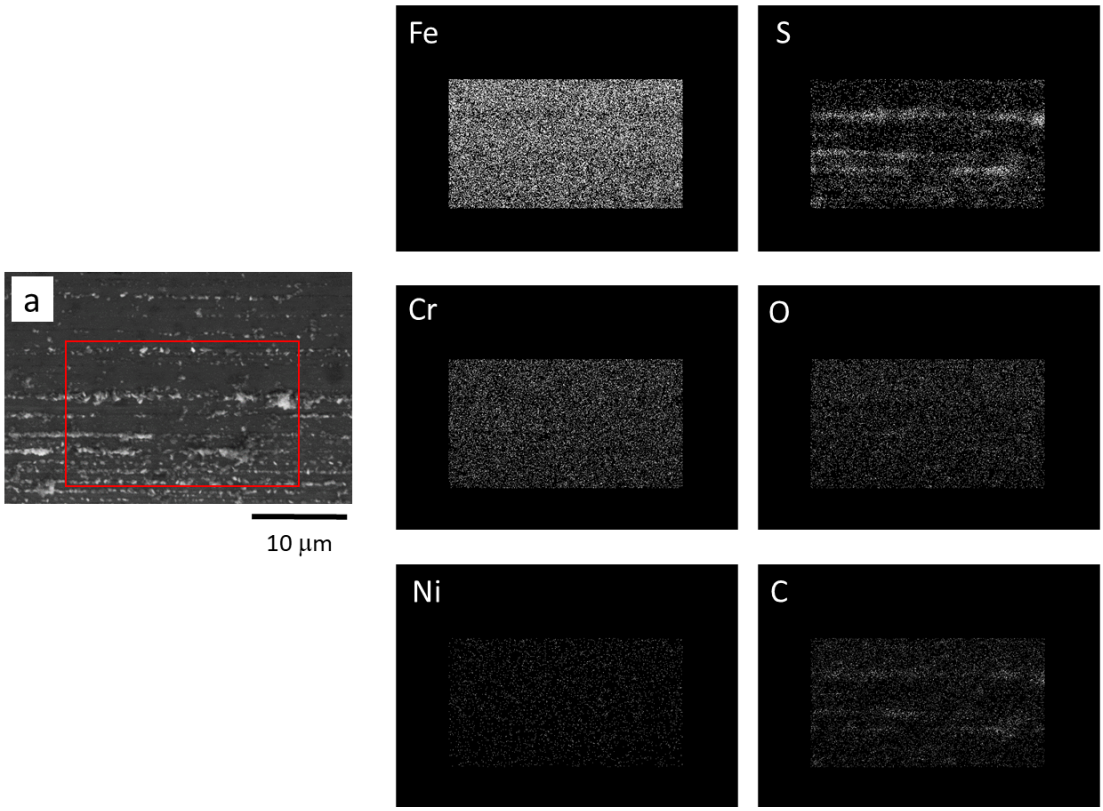

Figure 5.5 SEM micrograph and EDXS elemental maps of fouled 347SS wire surface.

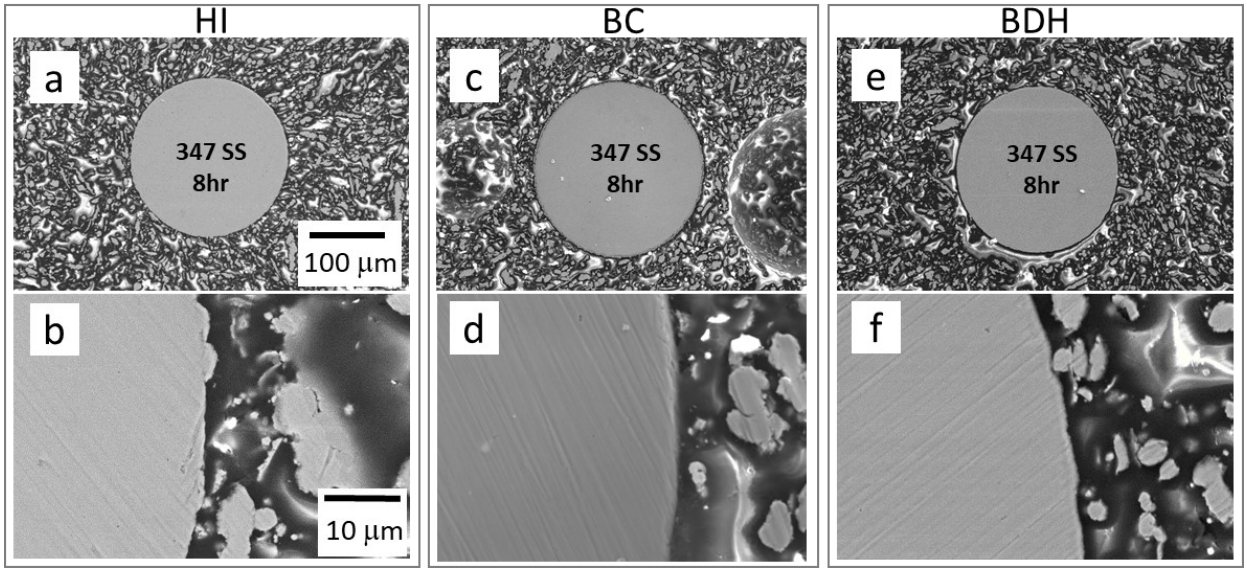

Figure 5.6 SEM micrographs of 347SS wire cross-sections after fouling for 8 hours in each oil blend.

From the fouling factor plots, it was anticipated that the wire exposed to Blend HI would exhibit the most fouling. However, the insignificant amount of fouling produced by these conditions of time, oil temperature, and wire temperature, on the 347SS wires make fouling factor data difficult to resolve and analyze. It is also worth noting that both carbon steel and 347SS seem to have experienced the most sulfidic corrosion with no associated organic/carbonaceous fouling in Blend BC, though carbon steel to a much greater extent. It seems that of the three oils used in these low temperature tests, Blend BC is the most prone to produce sulfidation. On P91 there is evidence of both organic fouling and sulfidic corrosion product in Blend BC, and all other oils. The remaining analysis within the low temperature study will be focused on the carbon steel and P91 metallurgies.

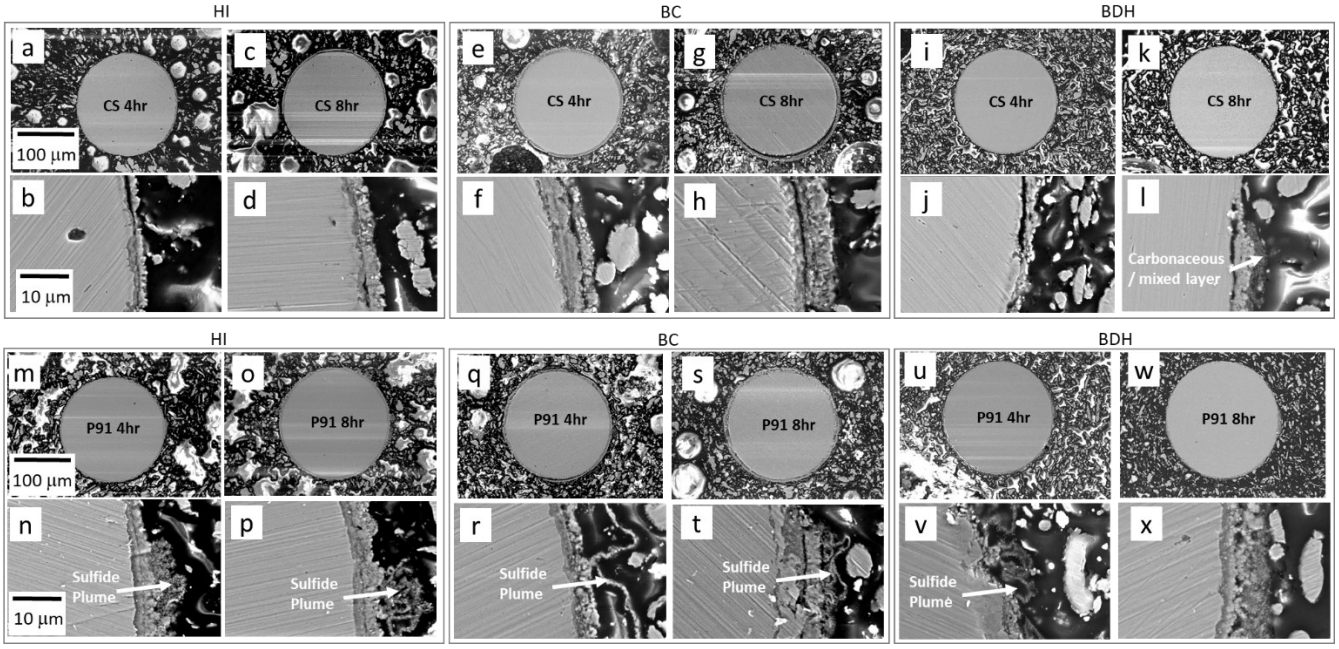

Figure 5.7 SEM micrographs of fouled wire cross-sections. (a-l) Carbon steel wires fouled 4 and 8 hours in each oil blend. (m-x) P91 wires fouled 4 and 8 hours in each oil blend. Twire = 350°C, Toil = 250°C.

Figure 5.7 is a survey of the fouled carbon steel and P91 wire cross-sections. Micrographs for each combination of oil, time, and metallurgy are presented at two magnifications and follows the layout in Figure 5.2, where results with carbon steel are shown throughout the uppermost images and P91 the lower. From left to right, the wires have been exposed to Blends HI, BC, and BDH, respectively. In this format, an obvious reduction of foulant thickness is observed, versus that produced under the high temperature conditions. A direct comparison can be made between the three

metallurgies fouled in Blend HI and Blend BC at low temperature, to those at high temperature. Blend BDH was not utilized in high temperature tests.

Several consistent observations about the fouling behavior can be made. On the carbon steel wires shown in Figures 5.7(a-l), the fouling layer appears to consist of corrosion product, except for Figure 5.6h where darker contrast material has collected on top of the presumed iron sulfide (arrowed). For all carbon steel samples, delamination of the foulant is observed. Figures 5.7(m-x) present P91 wires surfaces, after fouling in each oil blend. For each wire, the foulant possesses a similar, characteristic *corrosion-to-organic fouling* sequence, and is comprised of an inner and outer corrosion layer covered by a mixed (FeS and carbonaceous) foulant. In the higher magnification SEM micrographs of the P91 wire, there are unique features to the foulant, labelled as *sulfide plumes*, which were also pointed out in Figure 5.2(j,k,l). These morphologies are mixed FeS and carbon and are explored progressively throughout subsequent analyses.

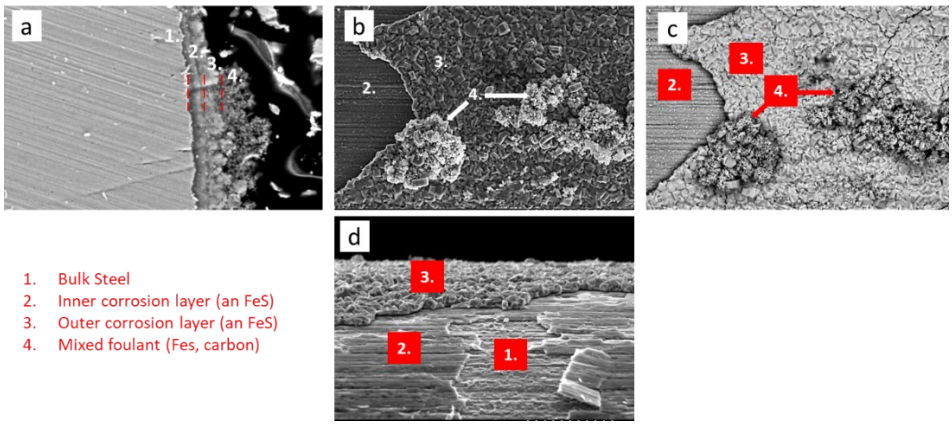

Figure 5.8 SE and BSE micrographs exploring the multilayer sulfidic corrosion of P91 metallurgy. (a) Wire cross-section with dashed lines indicating the interfaces between wire-inner sulfide, inner sulfide-outer sulfide, and deposited mixed layer. (b,c) SE and BSE micrographs of the wire surface highlighting the layers identified in (a). (d) Corrosion layers on exposed base steel on the P91 metallurgy.

Figure 5.8 contains four micrographs of the foulant on P91 after 4 hours of exposure in Blend HI. The collection of images highlights the inner and outer corrosion layers and mixed foulant alluded to previously. Figure 5.8a is a high magnification SEM micrograph of a P91 wire cross-section. Three dashed, red lines separate distinct layers of the corrosion and fouling phenomenon. Radially outwards from the bulk wire, one encounters first an interface between bulk steel and internal

corrosion, then a layer of external corrosion, and finally an agglomerate of mixed foulant. Figure 5.7b is an electron micrograph and 5.7c, a backscatter electron micrograph of the wire surface in plan view, on which the same layers are identified. The internal corrosion layer is dense and follows the textured microstructure of the drawn wire, while the outer corrosion layer has a blocky structure with no obvious preferential orientation. Sporadically, the outer corrosion layer is covered by a mixed foulant that contains both fine particles and the larger cubic crystals. Figure 5.7d shows another region of the corroded P91 wire surface, where both the outer and inner corrosion films have been removed and base steel is exposed. No mixed foulant was observed on the outer corrosion layer in this vicinity.

From this analysis it is clear the fouling occurs by inward diffusion of the corrodent – H_2S and outward diffusion of iron. This phenomenon was discussed in detail in the high temperature fouling, where diffusion rates are expected to be much greater. The inner corrosion product there was an iron rich, FeS (a pyrrhotite), while the outermost contained more sulfur, and an increasing gradient of iron existed radially outwards and sulfur, inwards. The mixed foulant may deposit from the oil and adhere to the wire surface because of the highly roughened/textured surface.

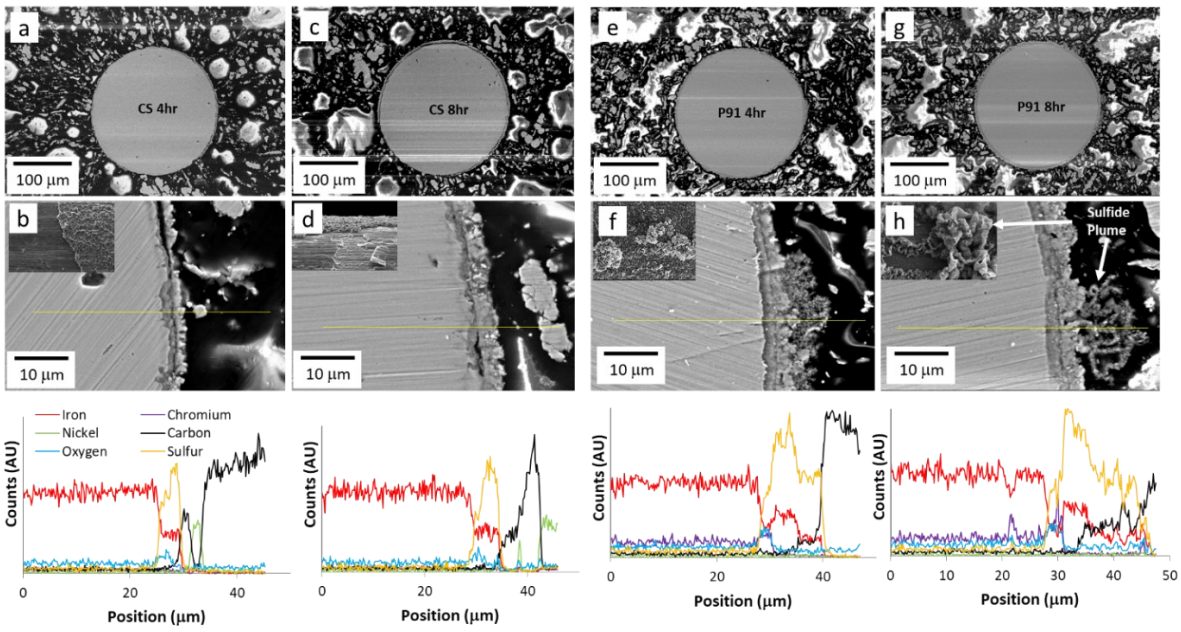

Figure 5.9 SEM and EDXS compositional scans of the fouled wire cross sections. (a-d) Carbon steel wires fouled 4 and 8 hours and (e-h) P91 wires fouled 4 and 8 hours. Blend HI, Twire = 350°C, Toil = 250°C.

Figure 5.9 contains SEM and EDXS linescans for the carbon steel and P91 wires fouled in Blend HI. The foulant appears with similar structure to the high temperature tests, where *corrosion-then-fouling* was observed consistently, but these layers are much thinner. The EDX plots follow the overlaid yellow lines, and reveal features previously observed. In particular, the FeS corrosion product and the detectable increase in oxygen near the internal corrosion-bulk wire interface, where the oxygen levels are more pronounced with the P91 metallurgy. Fouling on the carbon steel wire is predominately sulfidic corrosion product (FeS), with no visible carbonaceous material in or on the sulfide layer. This is consistent with the fouled wire surfaces presented in Figure 5.2. After 4 hours, the carbon steel has a distinct inner and outer corrosion layer that grows with time and, after 8 hours, becomes a thick layer of uniform morphology that has fully delaminated from the wire. Insets in the higher resolution micrographs show the wire surface near the location of the cross-section and assist with visualization of the corrosion scale, growth, and detachment. The P91 wires, fouled 4 and 8 hours, have an adherent corrosion film to which a mixed layer of foulant is attached. An internal corrosion layer can be resolved by observing the contrast differences under the outer layer of sulfidic corrosion product. This feature is much better defined on the P91 metallurgy. After 8 hours of fouling, the P91 wires reveal deeper internal corrosion and the surface features (plumes) extend further out from the wire surface. This can be observed in Figures 5.9(f and h).

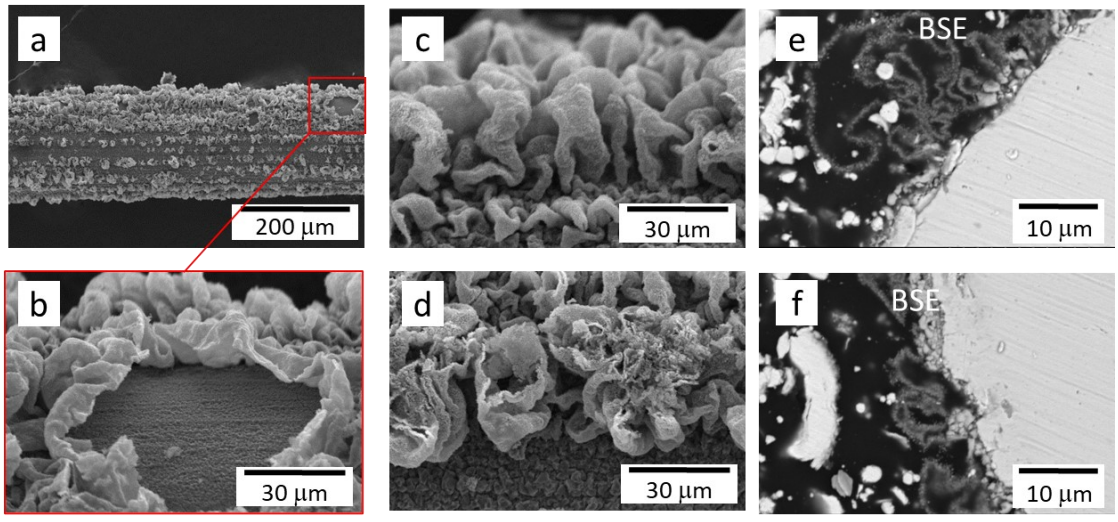

Figure 5.10 Low temperature metallurgy Study. SEM micrographs at various locations and magnifications, which explore the variety of surface features present on the P91 wire surface after fouling for 8 hours.

Figures 5.10 through 5.12 examine the unique foulant structures noted on the fouled P91 wires and their potential to influence subsequent fouling behavior. Figure 5.10a is a section of P91 wire fouled in Blend BC for 8 hours. It displays the distinctive fouling morphology identified (arrowed) and labelled as *sulfide plumes* throughout Figures 5.2 and 5.7. These structures emanate from the wire surface much beyond the nominal foulant thickness. Figure 5.10c is a high-resolution micrograph of several densely packed *plumes* that extend more than 30 µm. Figure 5.10d is a plan view of the P91 wire surface, where a cluster of these structures have trapped an agglomeration of distinct material/particles. Where these tortuous features exist, it seems reasonable that material suspended in the bulk oil would accumulate with higher probability versus onto a smooth surface, as in the case of the carbon steel wires. Figures 5.10e and 5.10f are BSE micrographs of two, fouled P91 wire cross-sections highlighting the plume structures from this vantage. It is interesting to note the absence of the typical bi-layered corrosion films where the plumes originate. Figures 5.10b highlights a feature whose circular shape seems to indicate a point where boiling was occurring at the hot wire surface.

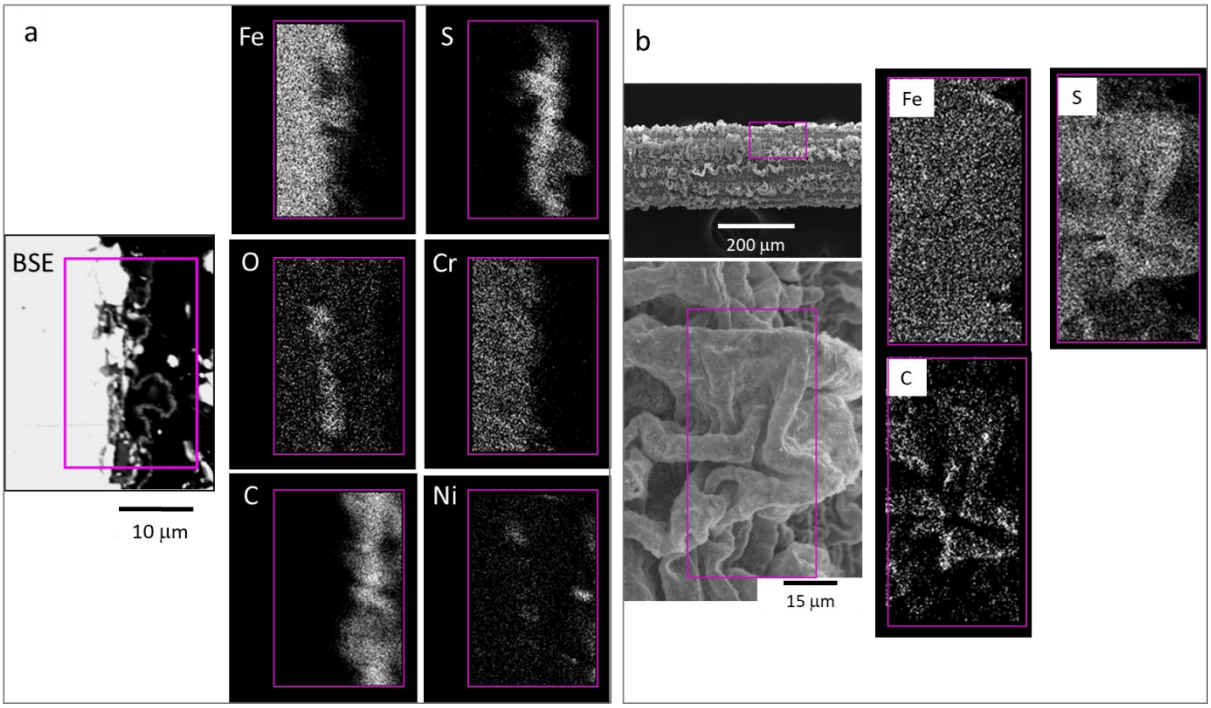

Figure 5.11 (a) BSE micrograph and associated EDXS maps for a sulfide plume on P91 metallurgy, after 4 hours of fouling in Blend BDH. (b) SE micrograph and associated EDX maps which explore a sulfide plume on P91 metallurgy, after 8 hours of fouling in Blend BDH

Figure 5.11 contains two datasets, comprised of electron micrographs and EDXS maps of sulfide plumes observed on the cross-section and surface of P91 wires fouled in Blend BDH. The data suggests the features are a mixture of iron sulfides and carbonaceous material, especially Figure 5.11b. Figure 5.9h is also supportive, as one follows the sulfur, iron, and carbon data through the layer of foulant. Iron drops from base levels in the bulk steel, with a simultaneous rise in sulfur, suggesting an iron sulfide throughout the internal and external corrosion layers. Continuing through the *plume*, sulfur and iron levels drop and carbon increases, until reaching the epoxy, where the carbon signal spikes.

In Figure 5.11a, a region enriched with oxygen is observed at the wire-foulant interface. Arrows identify the locations on iron (Fe) and oxygen (O) maps and suggest there is a relationship, wherein reduced Fe associates with enriched O. It is difficult to link with chromium (Cr) as this map demonstrates a consistent signal in the bulk wire metallurgy and lacks any distinguishing signal contrast at the corroded/fouled wire interface.

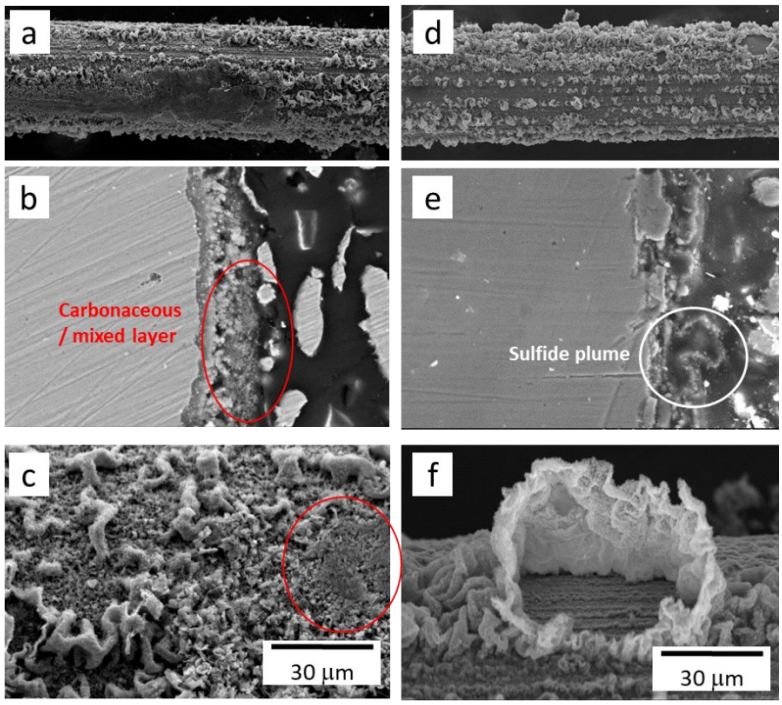

Figure 5.12 SEM micrographs of unique foulant texture on P91 metallurgy and deposition/trapping of mixed particulate foulants. (a) P91 wire surface with organic/mixed foulant over the highly texture sulfide. (b) P91 wire showing the highly textured sulfide without deposition. (b,e) Images of the wire cross-sections. (c,f) Unique foulant structure on the wire surface.

Figure 5.12 expands upon a proposed fouling mechanism influenced by the sulfide plumes. It was alluded to, in previous discussion, how suspended materials in the bulk oil may preferentially wet or entangle within a complex network of the plume structures. Figure 5.12(a and d) present two locations on a P91 wire fouled for 8 hours. In Figure 5.12a a layer of organic, carbonaceous material overlays a region dense with the sulfide plumes. A cross-section at this location is presented in Figure 5.12b and a multilayered foulant is observed. It contains the characteristic sulfidic corrosion and is covered with the carbonaceous material. Figure 5.12c is a higher resolution micrograph of the organic material that has accumulated on top of the sulfide plumes. In Figure 5.12(d-f), no such accumulation of organic material is observed.

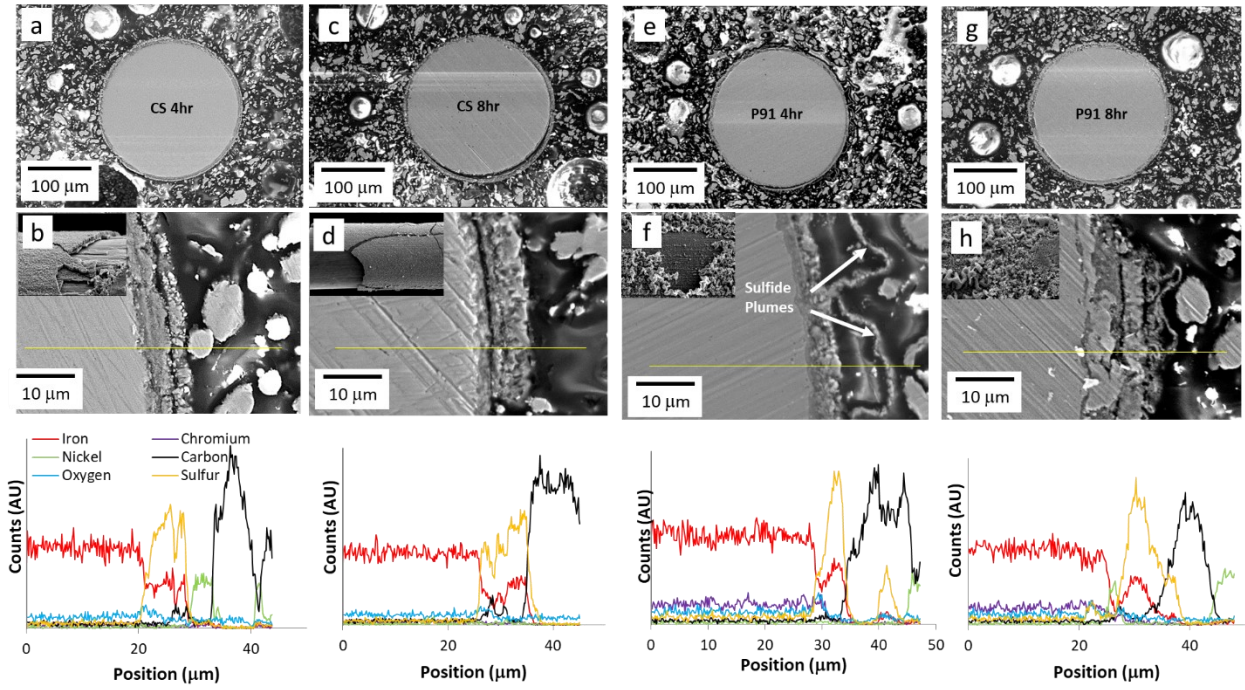

Figure 5.13 SEM micrographs and EDXS linescans of carbon steel wire cross-sections after being fouled for (a,b) 4 hours and (c,d) 8 hours. SEM micrographs and EDX linescans of P91 wire cross-sections after being fouled for (a,b) 4 hours and (c,d) 8 hours.

Figures 5.13 examines the carbon steel and P91 metallurgies fouled in Blend BC. It contains low and high magnification SEM micrograph of the wire cross-sections and EDXS linescans. The higher magnification images are inset with a micrograph of the wire surface near this location and overlaid with a yellow line, which indicates the path of an EDXS analysis. In this oil, versus Blend HI, more corrosion is evident for both metallurgies. For the carbon steel, a bi-layer corrosion layer

exists after 4 hours of fouling time, which becomes a thick uniform layer after 8 hours, and delaminates from the wire. The P91 wire exhibits sulfide plumes after 4 hours that are about 10 μm thick, then a very complex, multilayered foulant after 8 hours. A notable oxygen peak exists in the EDXS data for the wire fouled 4 hours, at the interface between the internal corrosion and bulk wire. This peak is absent in the 8-hour EDXS data, and for the carbon steel wires.

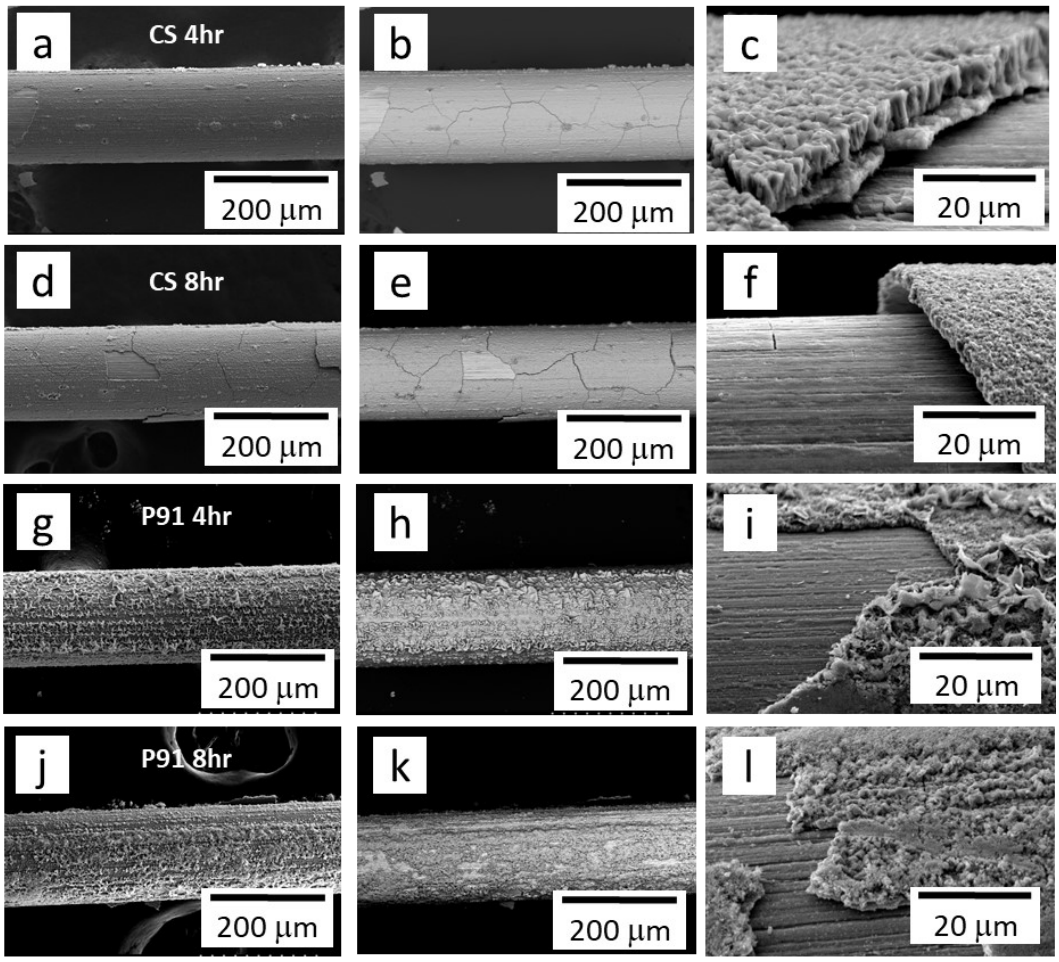

Figure 5.14 SE and BSE micrographs of fouled P91 and carbon steel wires, after exposure in Blend BC. Images contrast cracking of the sulfide layer on carbon steel versus P91.

Figures 5.14 through 5.16 examines and contrasts the facility of delamination events and condition of carbon steel and P91 wire surfaces after fouling tests at low temperature. Figure 5.14 contains a series of micrographs, generated by secondary electron and backscattered electron (SE- and BSE-) detection to contrast the structure of the fouled wire surfaces after 4- and 8-hour exposure in Blend BC. In each series is presented a secondary, then backscatter micrograph, and a higher magnification image of the wire surface near an area where the foulant had dislodged (naturally on

the carbon steel, and near the cut end of the wire in the case of P91). The imaging process to generate a BSE micrograph results in an alternative contrast and reveals significant breakup of the surface corrosion layer that was not obvious in the previously presented series of SE micrographs.

Figures 5.14(a-c) and 5.14(d-f) are carbon steel wires fouled in Blend BC for 4 and 8 hours. Figures 5.14(g-i) and 5.14(j-l) are P91 wires fouled in Blend BC for 4 and 8 hours. A comparison between 4- and 8-hour carbon steel samples highlights an increasing degree of fragmentation with time, of the surface sulfide layer. This is contrasted with the P91 wires, where no cracking is observed after either fouling duration. Furthermore, the sulfide layer on the carbon steel wire changes morphology with time, from a distinct multilayer (Figure 5.14c) and relatively thin delaminated layer in the 4-hour experiment, to a thick homogenous layer, fully delaminated after the 8-hour experiment, as seen in Figure 5.14f. The sulfide corrosion layer remained well-adhered to the P91 metallurgy, as evidenced in Figure 5.14(i and j).

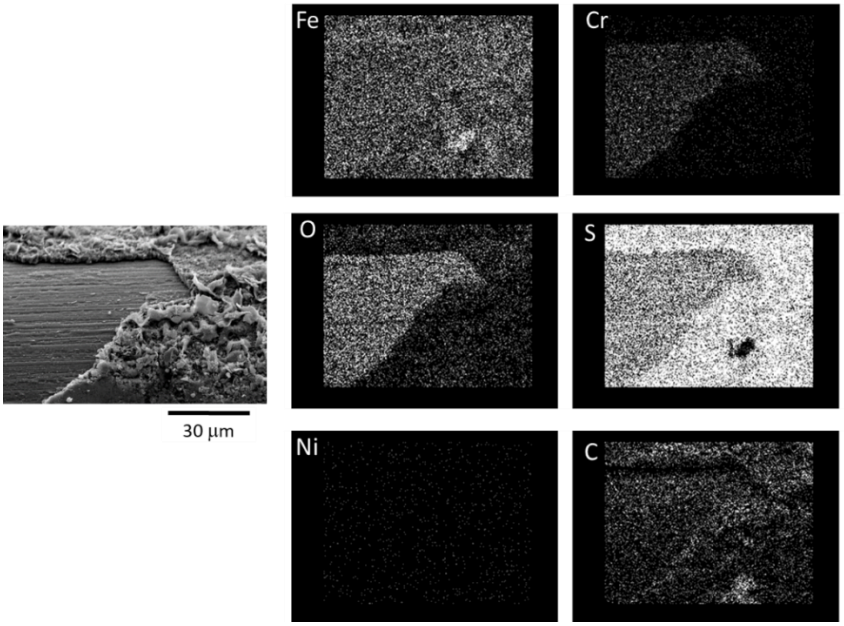

Figure 5.15 SEM micrograph and EDXS elemental maps of a P91 wire surface where the foulant layer has been mechanically removed.

Figure 5.15 presents an SEM micrograph and EDXS elemental maps of the P91 wire after 4 hours of fouling. Elemental data was acquired over a region where the outer sulfide / foulant layer had been removed while preparing the wire sample for analysis. The EDXS maps identify chromium and oxygen enrichment under the dislodged foulant, at the freshly exposed wire surface. This same

enrichment has been observed throughout many of the EDXS linescans for the wire cross-sections. There is very little distinction amongst iron signal between the outer sulfide layer and exposed surface. It is chromium content, for one, at the wire-foulant interface for P91 that contributes to the strength of the steel, tenacity of the foulant adhesion, and low rate of delamination versus carbon steel.

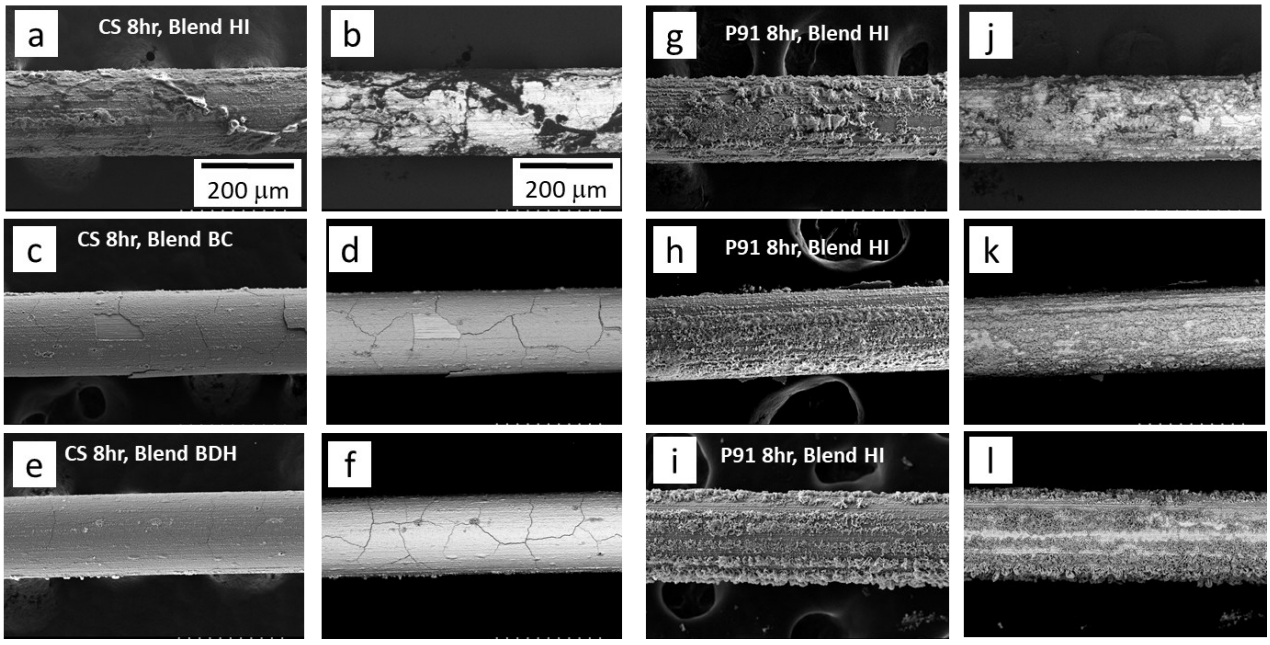

Figure 5.16 BSE and SE micrographs for carbon steel and P91 wires in Blends HI, BC, and BDH. Images compare the delicate nature of the corrosion product on carbon steel versus P91.

Figure 5.16 reiterates through each combination of oil with carbon steel and P91, presenting SE and BSE micrographs of the fouled wire surfaces. This image can be contrasted with Figure 5.2, which only presented SE micrographs and lacked evidence of the cracking presented here. Cracking and delamination of the sulfide sheath is observed for the carbon steel wires fouled in Blend BC and Blend BDH, but much less so in Blend HI. The trend, going from 4 to 8 hours of fouling with carbon steel is growth, cracking, and delamination of the sulfide layer. Comparing the P91 experiments, referring to Figures 5.16(g-l), it is observed that the sulfide layer grows thicker with time, and the unique structures on the surface also become larger and more densely distributed. No cracking is evident and the layers of sulfidic corrosion product at the corroding interface remained integral for each of the P91 wires analyzed. Also notable, and evident only with Blend HI for the carbon steel

metallurgy, is a dark contrast material overlaying the metallic sulfide. This is highlighted by the BSE micrograph in Figure 5.16b.

Distinguishing the foulant morphology on the two metallurgies is the lack of surface features on the carbon steel when compared to the P91 alloy and the delamination of the corrosion layers from the carbon steel. Relating this to heat transfer ability, it must be that the dense iron sulfide on carbon steel is much more conductive than the plumes on the P91. This because, there is much more surface area generated by the plumes, but the fouling factor (resistance to heat transfer) is consistently much greater for P91 versus carbon steel. The sulfide plumes have also been observed to improve trapping and accumulation of other fouling materials, but these would be much less dense than the plumes or the dense sulfides on carbon steel. It could be assumed that these plumes would add to heat transfer resistance (and fouling factor) from this *particulate-trapping* aspect as well. Some of the lacking correlation between foulant thickness and fouling factor data can be revisited with these observations and assumption.

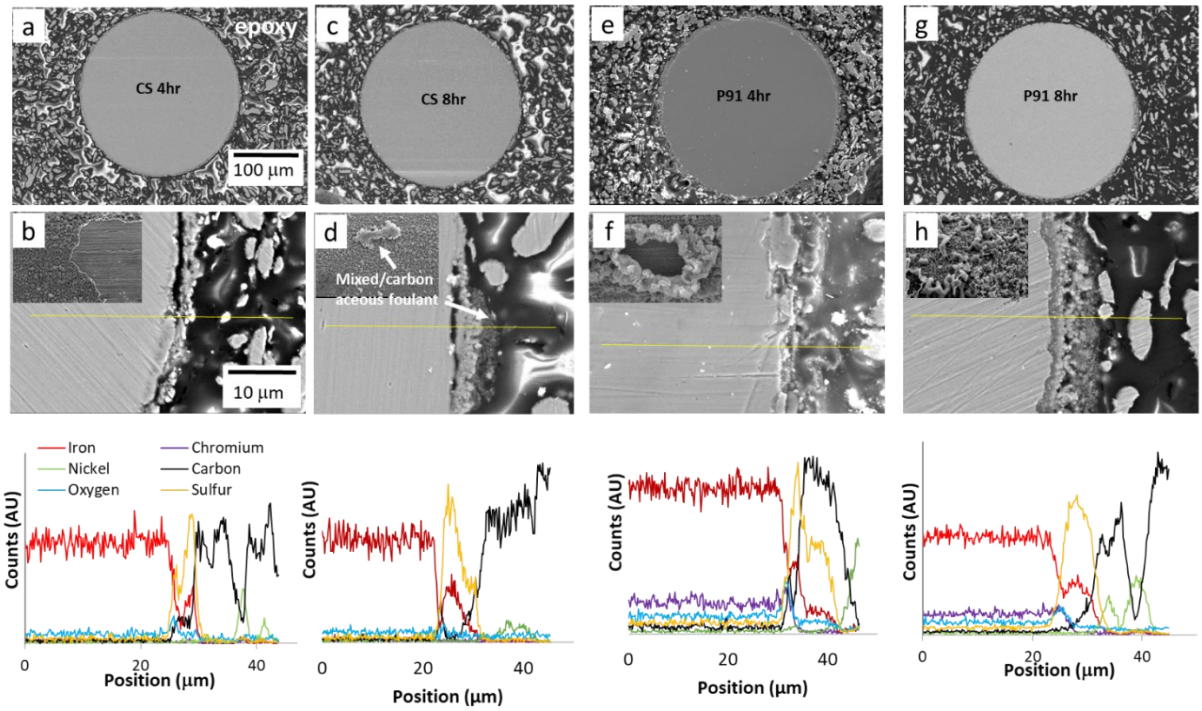

Figure 5.17 SEM micrographs and accompanying EDXS line scans of (a-d) carbon steel and (e-f) P91. Blend BDH, wire T = 350 °C, oil T = 250 °C, reactor pressure = 400 psig.

Figure 5.17 reveals SEM micrographs and EDXS linescans for carbon steel and P91 wires fouled in Blend BDH for 4 and 8 hours. Carbon steel wires are presented in Figures 5.17(a-d) and P91 wires in Figures 5.17(e-h). Elemental linescans are presented below the higher resolution micrographs and follow the overlaid, yellow lines. In Figure 5.17(b and d) a thin layer of sulfide has formed after 4 and 8 hours and has delaminated from the wire surface. No organic foulant is observed in the 4-hour dataset, and only a small deposit of mixed foulant is detected in the 8-hour data set. In Figure 5.17d, a small agglomeration of material is identified on the wire surface, via the inset micrograph, and in the cross-sectional image. The EDXS linescan identifies the layer as a mixed carbonaceous-FeS, due the drop in both iron and sulfur signal near the arrowed region, associated with a rise in carbon before reaching the epoxy. On the P91 metallurgy, referencing Figures 5.17(f and h), there is evidence for the consistent sulfide plume structure after 4 hours and the mixed layer foulant, assumed to be promoted by the same plumes features, after 8 hours. Specifically, in Figure 5.17h there is evidence of internal and external FeS, then an overlay of dense metallic sulfide mixed with a darker contrast material that consists of FeS and carbon. For both carbon steel and P91 there is evidence of a surface oxide (blue-oxygen line) that is more intense in the 4-hour data versus the 8-hour data, and greater for P91 versus carbon steel.

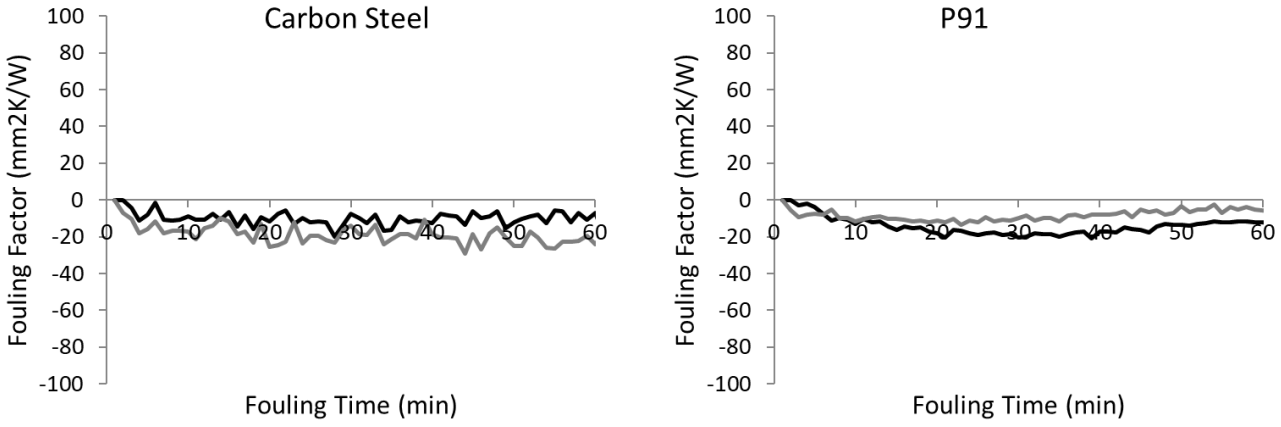

Figure 5.18 Fouling factor plots for carbon steel and P91 after fouling for 1 hour. Blend BDH, Twire = 300°C, Toil = 150°C

In a supplement to the data generated in this chapter, a series of experiments were conducted at 300°C, in Blend BDH. Fouling factor plots are presented in Figure 5.18. This was interesting data

to observe after consistently seeing the depth and prolonged interval of negative values in Figure 5.1, where wire temperature was only 50°C higher, at 350°C. It appears there is little of the annealing effect on fouling factor, as was observed and discussed earlier.

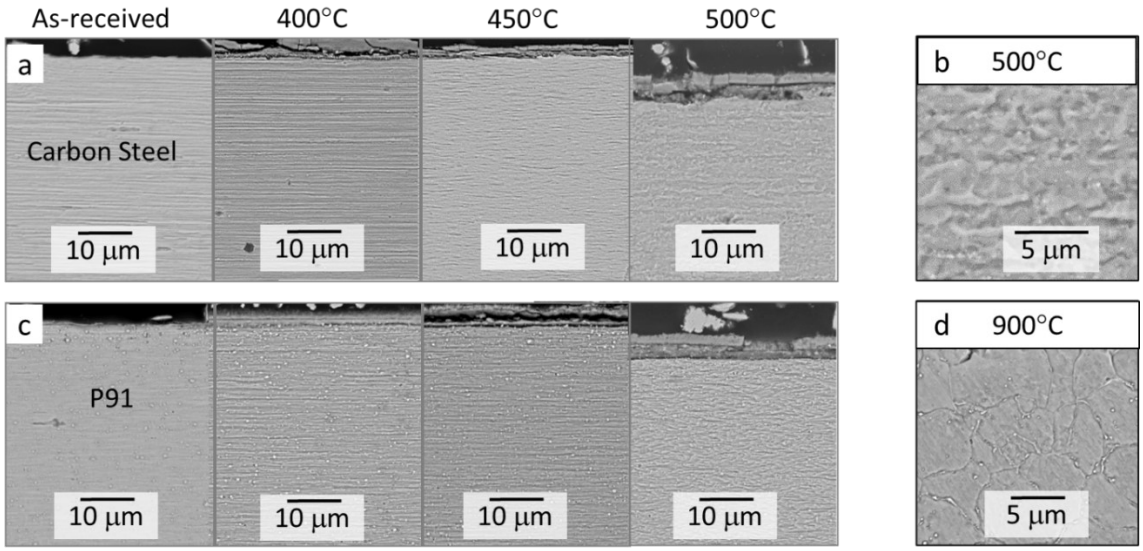

Figure 5.19 Microstructural analysis of (a and b) carbon steel and (c and d) P91 after 10-hour annealing treatments in inert atmosphere.

In support of this data, carbon steel and P91 wires were subjected to variable heat treatments and then their microstructures were compared. Heat treatments were conducted in a 3-zone tube furnace, under argon, and ramped/cooled at 5 °C/min. Carbon steel was etched with 3% Nital for 10 seconds and P91 with 4% Picral for 3 minutes. Figure 5.19 shows a series of micrographs corresponding to the microstructural analyses after annealing wires in inert (argon) atmosphere over the range of temperatures 400 °C to 500 °C, each for 10 hours. For carbon steel, some of the fibrous wire texture begins to anneal out after 450 °C, while P91 remains stable up to 500 °C and even then, there is only a small amount of grain growth. At 900 °C, considerable relaxation of the P91 microstructure was observed. Higher magnification images of the microstructures after the highest temperature treatment are presented in Figures 5.19(b and d).

5.3 Summary and Conclusions

A key feature across all three metallurgies is evidence of sulfidic corrosion, while the similarity ends with acknowledging existence. For carbon steel, corrosion by S-bearing species, causes the growth of both an internal and external metallic sulfide. It is assumed that the layer structures are similar to those generated in the high temperature experimentation, wherein an iron-rich pyrrhotite will exist internally and a more sulfur-rich, externally. This due, the relative rates of the inward diffusion of sulfur and outward diffusion of iron. Carbon steel experienced rapid growth of these layers and their delamination. The P91 metallurgy experienced similar bi-layer corrosion by S-bearing species, which remained well-adhered. Plumes of FeS grew from the surface of P91 and extended up to 50 μm from the wire surface. These structures trapped and mixed with carbon and suspended particles from the blended oils, promoting a similar sequence of corrosion-then-fouling as was seen at higher temperature. What was missing from the analyzed deposits was the significant fractions of carbonaceous material / coke / pitch that was observed at high temperature, but this was expected when operating below thermal cracking conditions. Figure 4.18 was proposed as a mechanistic depiction of the results and assumptions from the high temperature fouling tests. It is argued that the same explanations can be provided here, with only the lesser amounts of organic material observed. Iterating through the metallurgies portrayed: 347SS undergoes a small degree of initial sulfidic corrosion, but no organic fouling – this material has entered an integrity window of near immunity under the low temperature experimental conditions; P91 experiences less aggressive sulfidic corrosion, but this results in sulfide plumes that remain well-structured versus a burst of metallic sulfide at high temperature, and these structures trap and promote subsequent organic fouling; Carbon steel exhibits nearly identical behavior, under the low temperature conditions, wherein a film of sulfidic corrosion product grows rapidly, then delaminates, limiting the overall ability of the foulant layer to grow as thick as that observed on P91.

Beyond the mechanistic argument for inorganic-driven fouling, the fouling seemed to be greater on wires tested in Blend HI, and the structure of the foulant seemed different, as a *wavy, flakey*

deposit, versus a plumed structure in the remaining oils. Carbon steel retained a consistent amount of organic foulant, at the wire mid-length, in Blend HI, alone. Both carbon steel and P91 retained large masses of organic material near their connection to the electrical feedthroughs (probes), in all three oils, but this material was neither consistently deposited nor well-adhered and was due primarily to disturbed flow of the hot oil. This complicated fouling factor measurements and introduced a level on inconsistency in the fouling factor methodology. Low fouling rates and annealing of the wire microstructure meant deep and prolonged regions of negative fouling factor values, which also introduced a challenge for resolving fouling factor data.

5.4 References

(1) Wiehe, I. A. In *Energy and Fuels*; 2012; Vol. 26, pp 4004–4016.

(2) Wiehe, I. A. *Process Chemistry of Petroleum Macro Molecules*, Vol. 121.; CRC Press: Boca Raton, FL, 2008.

(3) Stephenson, T.; Hazelton, M.; Kupsta, M.; Lepore, J.; Andreassen, E. J.; Hoff, A.; Newman, B.; Eaton, P.; Gray, M.; Mitlin, D. *Fuel* **2015**, *139*, 411–424.

(4) Wang, W.; Watkinson, A. P. *Proc. Int. Conf. Heat Exch. Fouling Clean. IX* **2011**, 23–30.

(5) Diaz-Bejarano, E.; Behranvand, E.; Coletti, F.; Mozdianfard, M. R.; Macchietto, S. *Appl. Energy* **2017**, *206* (September), 1250–1266.

CHAPTER 6

Iron Naphthenate Additive in Crude G

6.1 Introduction

This section explores the effect of additive chemistry on fouling behavior above and below thermal cracking temperature. In previous work,[1,2] it was demonstrated that addition of thiophene to a heavy crude oil fraction significantly reduced fouling at delayed coking conditions (i.e. 550 °C). It was hypothesized that thiophene reduced sulfidic corrosion, which in turn reduced organic fouling, catalyzed by the presence of iron sulfides. The surface activity of the thiophene molecule allowed it to preferentially adsorb at the fouling/corroding surface and hinder corrosive and catalytic coking processes. Those results conceptualize that total sulfur content is less representative of fouling and corrosion propensity versus speciation of sulfur-bearing species. Following up, Lepore[3] tested several sulfur-bearing organic species in controlled corrosion experiments to correlate molecular structure, generation of H_2S, and resultant corrosion product on four different steels, in pure mineral oil. His results, coupled with knowledge of thiophene behavior, demonstrate important stages in understanding the *corrosion-then-fouling* behavior that has been broadly demonstrated in this current research.

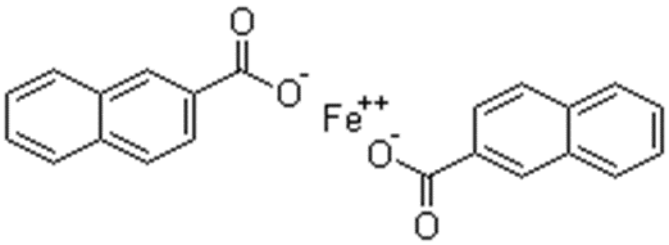

Figure 6.1 Iron naphthenate additive

Figure 6.1 presents the structure of an iron naphthenate additive that was selected for study. Naphthenic acids are generally understood to be corrosive species within a crude oil feedstock.[4] Metallic salts of these acids are well established foulants. Suspended iron will rapidly sulfide in a refinery environment which imparts particulate fouling. Equations 6.1, 6.2, and 6.3 represent a well-accepted mechanism that describes the competitive corrosion processes when both H_2S and naphthenic acids exist. Equation 6.1 indicates that naphthenic acids react with iron to form iron naphthenates, that are oil soluble, and hydrogen gas. Equation 6.2 broadly depicts sulfidation of steel

or suspended iron by H_2S or other S-bearing species. Equation 6.3 demonstrates a reversible reaction that suggests (re)generation of naphthenic acid, from a naphthenate salt, in an environment containing H_2S.

$$Fe + 2RCOOH \rightarrow Fe(RCOO)_2 + H_2 \quad \textbf{Equation 6.1}$$

$$Fe + H_2S \rightarrow FeS + H_2 \quad \textbf{Equation 6.2}$$

$$Fe(RCOO)_2 + H_2S \underset{rev}{\leftrightarrow} FeS + 2RCOOH \quad \textbf{Equation 6.3}$$

Naphthenates and Naphthenic acids are thermally labile species that typically start to decompose above 200 °C. Under such conditions stable, iron oxides such as magnetite have been observed on steels.[5] One group, has demonstrated the formation of magnetite from both model naphthenic acids and real crudes.[6] Equations 6.4 and 6.5 describe a proposed reaction pathway for this to occur.[7] Not straightforward, this mechanism is compromised by competitive sulfidation and naphthenic acid corrosion and dissolution of the pseudo-protective scales if sufficient naphthenic acid is available.

$$Fe(RCOO)_2 \rightarrow FeO + \mathrm{RCOR} \quad \textbf{Equation 6.4}$$

$$4FeO \rightarrow Fe_3O_4(magnetite) + \alpha Fe \quad \textbf{Equation 6.5}$$

Fouling behavior of carbon steel and P91 metallurgies were contrasted in experiments doped with 0 and 150 ppmw of Fe using an iron naphthenate (Fe-NA) additive with the chemical formula $(2(C_{11}H_7O_2)Fe$. The tests were conducted in Crude G, under both high and low temperature scenarios. Reactor pressure was constant at 400 psig during the experiments. Different from the low temperature conditions in the previous section, here the low temperature fouling tests were extended to 48 hours, due to the low fouling propensity of the oil. Also, the oil bath temperature was maintained at 150 °C, to prevent thermal decomposition of the additive in the bulk oil. The Fe-NA additive was supplied from Sigma-Aldrich as 12wt% iron in mineral spirits. Table 3.1 summarizes the experimental conditions for this section.

6.2 Results

6.2.1 High Temperature Experiments

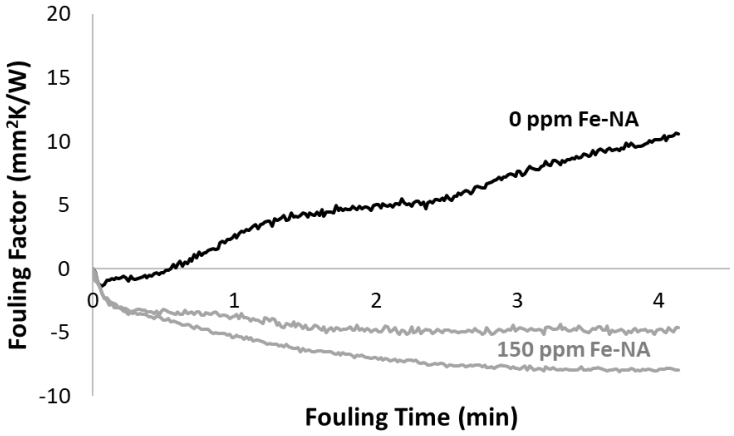

Figure 6.2 Fouling factor plots for carbon steel in Crude G with and without Fe-NA additive

Figure 6.2 shows fouling factor data for carbon steel in Crude G with and without Fe-NA, during exposure to the high temperature experimental conditions. Tests were run as a function of time, for 4 and 8 hours. Unexpectedly, the fouling factor curves show that the addition of Fe-NA caused a marked reduction in the fouling factor for carbon steel. This trend was demonstrated repeatably.

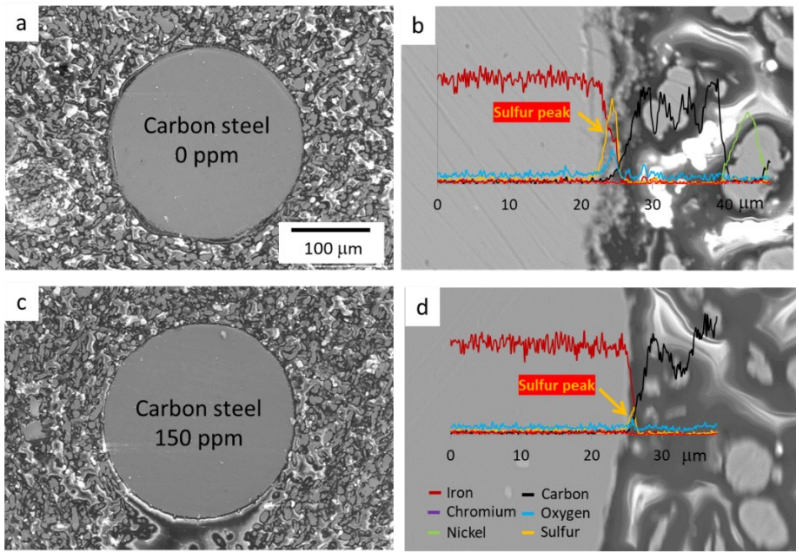

Figure 6.3 Effect of Fe-NA additive on fouling of carbon steel. (a,b) SEM and EDXS compositional scans of fouled wire cross-sections in Crude G without additive. (c,d) SEM and EDXS compositional scans of fouled wire cross-sections in Crude G with additive. Wire T = 490 °C, oil T = 290 °C, run time = 4 hours.

Figure 6.3 presents SEM micrographs and accompanying EDX line scans for carbon steel wires fouled in Crude G. Figures 6.3(a and c) are low magnification micrographs of the wires after 4 hours of fouling time, without and with Fe-NA, respectively. At this magnification, it is difficult to resolve a significant difference between fouling behavior of the systems, or the presence of any foulant at all. At higher magnification, the microscopy corroborates the fouling factor trends. Figures 6.3b is the wire taken from Crude G without Fe-NA additive and foulant is detectable on the interface. Figure 6.3c is the wire taken from tests in Crude G with Fe-NA additive and there is a complete absence of accumulated foulant or corrosion product. These figures and the overlaid EDX linescans suggests that the deposit is predominately iron sulfide, where present. Sulfur follows the yellow data series, and peaks are arrowed in Figure 6.3(b and d).

Very weak iron and sulfur signals are identifiable on the wire surface in tests with the Fe-NA additive. As has been demonstrated, there exists a direct link between the degree of sulfide formation and the overall levels of fouling in these systems. So, it is reasonable to connect the limited observed fouling with the lack of iron sulfide. Towards explaining the limited iron sulfide corrosion product, it is suggested that either the competitive naphthenic acid corrosion mechanism has taken over under these conditions, and sulfidic corrosion product is removed, or the additive has introduced and inhibitive effect by scavenging H_2S, according to equation 6.3, limiting sulfidic corrosion.

The existence of sulfur-bearing species and naphthenic acids, their total concentrations, and speciation are important factors in corrosivity of crude oils, especially at elevated temperature. Equation 6.1 identifies naphthenic acid attack and Equation 6.2 sulfidation, of a susceptible steel surface. Equation 6.3 is a reversible reaction balanced by a combination of Fe-NA and H_2S on the left side of equilibrium and a combination of iron sulfide corrosion product and naphthenic acid on the right. This suggests that the addition of Fe-NA, and the presence of H_2S, generated at the high temperature surface of the wire, would produce suspended iron sulfides and naphthenic acid. The organic acid would be corrosive and the carbon steel more susceptible versus the P91 metallurgy. Iron sulfide corrosion product would also be more susceptible to the naphthenic acids and as formed

it may be rapidly corroded away. An inhibitive pathway is also possible, through Equation 6.3, wherein the Fe-NA reacts with H_2S, producing particulate iron sulfides in the oil, consuming the corrosive species that would otherwise cause the ubiquitous sulfidic corrosion of the wire surfaces observed in all previous aspects of this study. This argument, however, leaves out the fact that there is a 1:1 production rate of iron sulfide and naphthenic acid in Equation 6.3, which will add to the acidity of the crude oil bath. Crude G has a nominal TAN value of 0.119 mg KOH/g of oil, reported in Table 3.1, in Chapter 3 (experimental section), which is intermediate amongst the oils utilized in this research. Naphthenic acids are notorious for their role in deteriorating pseudo-passivating iron sulfide scales,[8] and similar to sulfur-containing components, speciation is important to consider against total concentrations.[9] Above 230°C, chromium and molybdenum steels must be employed to resist competitive sulfidic and naphthenic acid attack.[10]

Another hypothesis for the reduction in foulant by Fe-NA at elevated temperature involves thermal decomposition of the naphthenate and competitive reactions of the products at the wire surface. This decomposition, in the presence of hydrogen, could yield a naphthenic acid which could further decompose and result in the release of water into the system.[11] The production of water in the vicinity of the hot wire surface could compete with the sulfidation reactions. However, iron oxide is not expected to be stable at elevated temperatures in an environment with high H_2S content. Furthermore, a comparison of the EDX line scans in Figure 6.3 demonstrate that there is a stronger oxygen signal at the surface of the specimen fouled in oil without the additive.

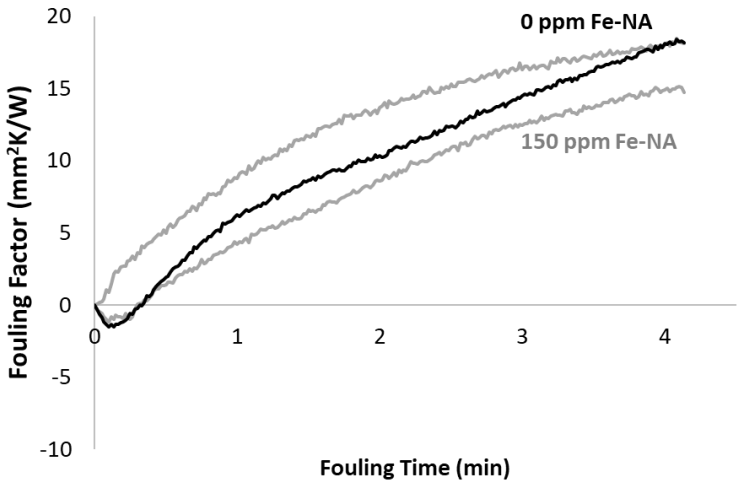

Figure 6.4 Fouling factor plots for P91 in Crude G with and without Fe-NA additive

Figure 6.4 presents fouling factor data for P91 wires in Crude G with and without Fe-NA, during exposure to the high temperature experimental conditions. In the case of P91, a trend related to the additive is quite weak, and even opposite that observed for carbon steel. The fouling factors for P91 are again higher, versus the carbon steel, and reach peak values of 18.2 and 17.7 mm^2K/W in tests without and with the Fe-NA additive, respectively.

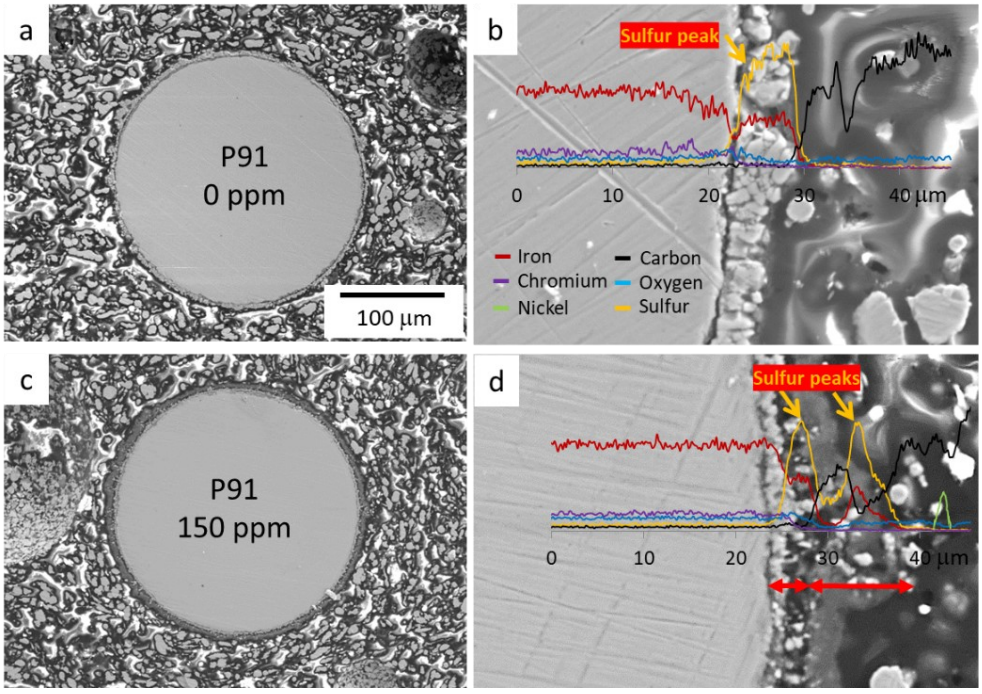

Figure 6.5 Effect of Fe-NA additive on fouling of P91. (a,b) SEM and EDXS compositional scans of fouled wire cross-sections in Crude G without additive. (c,d) SEM and EDXS compositional scans of fouled wire cross-sections in Crude G with additive. Wire T = 490 °C, oil T = 290 °C, run time = 4 hours.

Figure 6.5 includes SEM micrographs and accompanying EDX line scans of the P91 wires fouled in Crude G. Figures 6.5(a and c) are low magnification micrographs of the wires after 4 hours of fouling time, without and with Fe-NA, respectively. At this magnification, there is an obvious contrast to the foulant between tests. More material is observed on the wire taken from the test with additive, plus this foulant is visually much darker versus the wire taken from the test without additive. Figures 6.5(b and d) are micrographs at higher magnification, overlaid with data from EDXS linescans. Immediately apparent is confirmation that the thickness of foulant in the test with additive is thicker. The two wires also exhibit different foulant morphology and composition. In Figure 6b, foulant is predominately a thick layer of iron sulfide, while in Figure 6d a composite layer is observed, where each thickness is depicted by red arrows in the figure. The first layer seems consistent with the foulant morphologies observed previously. From the wire surface outwards, it is sulfidic corrosion product and very little organic material. In the second layer, there is a spike of carbon interspersed with iron sulfides, followed by another strong signal from iron and sulfur.

From these results, it seems likely that the Fe-NA scavenges H_2S from the systems, generating suspended iron sulfides, which then deposit onto the wire and trap and influence the accumulation carbonaceous fouling. In the system without additive, the surface of the wire corrodes, but lacks the organic/mixed particulate fouling. Furthermore, the increased deposit with the additive could be a result of a catalytic effect from the chromium and molybdenum present in the P91, the oxides and sulfides of which are known to be catalytic.[12] The discrepancy between P91 and carbon steel may again be an effect of the surface metallurgy and the differences in adhesion of the foulant to the wire surface for the two systems. More work is needed to conclusively establish the mechanisms for fouling in the presence of Fe-NA for these metallurgies, but discernable trends have emerged.

6.2.2 Low Temperature Experiments

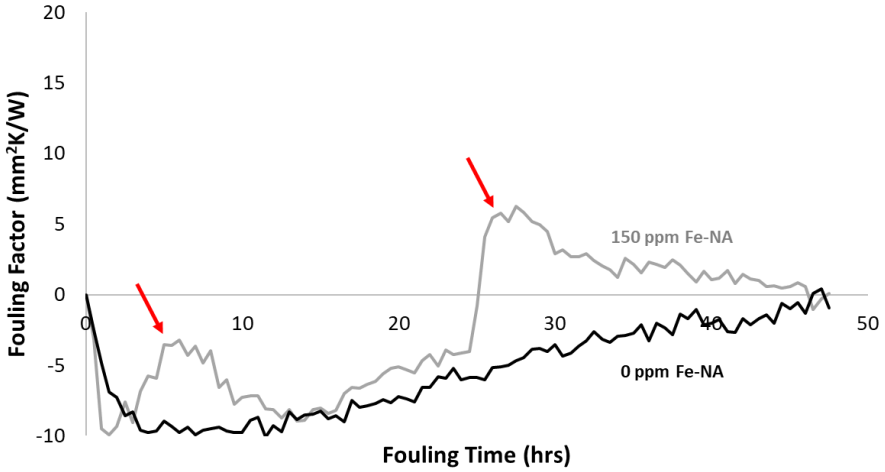

Figure 6.6 Fouling factor plots for carbon steel in Crude G with and without Fe-NA additive. Twire = 350°C, Toil = 150°C, run time = 48 hours.

Figure 6.6 presents fouling factor data for carbon steel wires in Crude G with and without Fe-NA. The fouling factors for both systems end at similar final values, but the shape of the two plots is different. In the test with additive, two events have caused the fouling factor to rise significantly above the otherwise linearly increasing trend. Two red arrows identify the two occurrences at approximately 5 hours and 25 hours. If particulate fouling is expected, this might have caused the jump and subsequent relaxation of the fouling factor. A loosely deposited aggregation of particles on the wire surface would certainly decrease heat transfer, increasing the fouling factor, and would be sensitive to removal as the accumulated mass grew and became sensitive to shear and gravity. It could be hypothesized that in the system with additive iron there would be an elevated probability for particulate formation (Equation 6.2) and their eventual deposition onto the wire surface. It should also be pointed out that the trend in the low temperature data, using carbon steel wires, is very different versus the high temperature data previously explored, in Figure 6.2. At any rate, the fouling factor data needs correlation with other supportive analysis for better explanation.

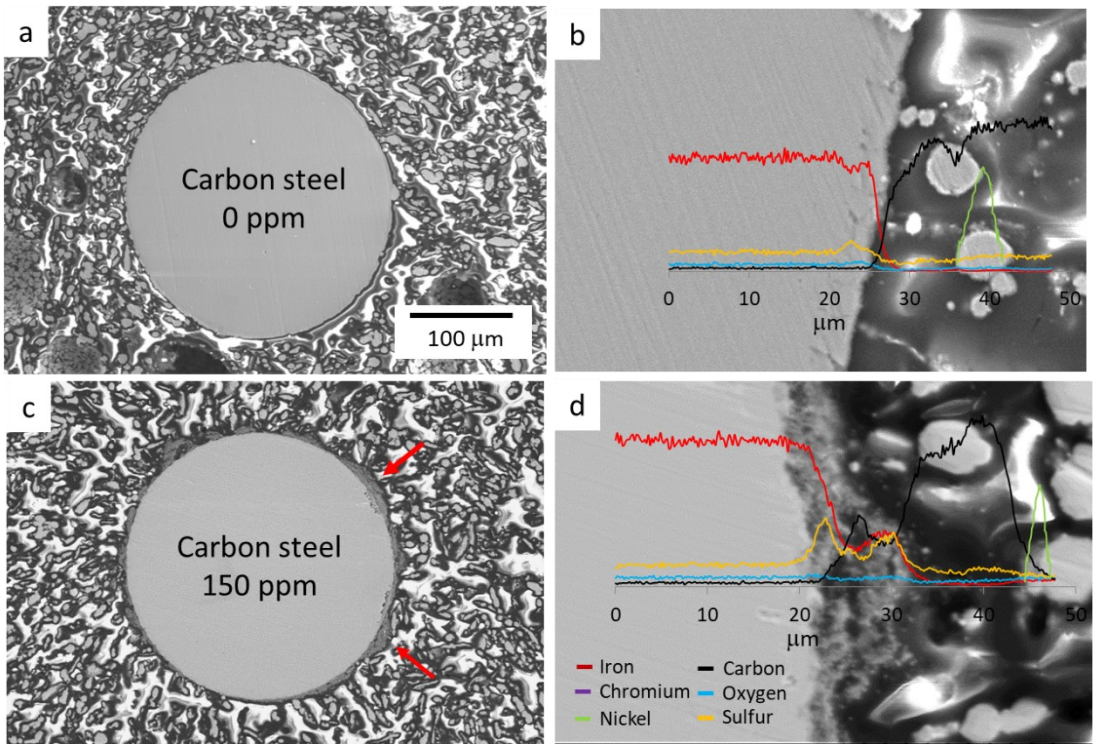

Figure 6.7 Effect of Fe-NA additive on fouling of carbon steel. (a,b) SEM and EDXS compositional scans of fouled wire cross-sections in Crude G without additive. (c,d) SEM and EDXS compositional scans of fouled wire cross-sections in Crude G with additive. Wire T = 350 °C, oil T = 150 °C, run time = 48 hours.

Figure 6.7 presents SEM micrographs and accompanying EDX line scans for carbon steel wires fouled in Crude G, at low temperature (350 °C wire temperature, 150 °C bulk oil temperature). Figure 6.7(a and c) are low magnification micrographs of the wires fouled without and with additive, respectively. The low ultimate fouling factors are supported by the very small amount of observed foulant. However, there is an apparent contrast between the two scenarios that is supportive of the events noted in the fouling factor data in Figure 6.6: There is little fouling when no additive was present in the oil and foulant when the Fe-NA was added. Furthermore, the foulant in Figure 6.7c is non-uniform around the circumference of the wire. Red arrows point at two of the largest accumulations.

Figures 6.7(b and d) are higher magnification SEM micrographs of the carbon steel wires, overlaid with EDXS linescans. In Figure 6.7b, from the system without additive, the resultant wire interface is nearly free of any fouling or corrosion. Only a very small sulfur peak is noted, aligned with a drop in iron signal, which suggests some sulfidic corrosion at the wire surface. Figures 6.7d

shows that with the addition of Fe-NA, an agglomeration of foulant is observed. The deposit is identified as a mixture of carbon and iron sulfide, evidenced by peaks in the EDXS line scan.

The observations amongst the fouling factor data and microscopy are consistent with a hypothesis that the Fe-NA contributes to particulate fouling in the system. Overall, fouling is very low in Crude G. Fouling factor data from the system with additive exhibits two distinct events where heat transfer from the wire is hindered, causing the fouling factor to increase. In both cases, the fouling values drop back to the linearly increasing trend established by both systems. Microscopy and EDXS data in Figure 6.7 is supportive. Without additive the carbon steel experiences very little fouling or corrosion. With additive, non-uniform deposits of carbon and iron sulfide are present around the circumference of the wire. Equation 6.2 states that the Fe-NA, originally soluble in the oil, may react with H_2S to form insoluble iron sulfides. These particles could migrate to the hot wire surface and attach, which would increase fouling factor, then after growing to a certain size they would dislodge, due to density, growth and shearing stress, and the fouling factor would return to base levels.

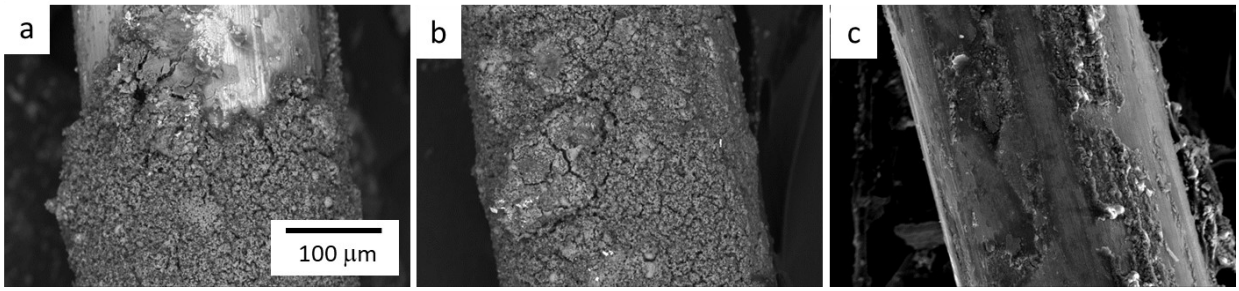

Figure 6.8 SEM micrographs of foulant along the surface of carbon steel wires from low temperature experiments in Crude G, with Fe-NA additive. (a) Was taken near the upper connection of wire to the probe, (b) towards the wire mid-section, and (c) at the wire mid-section.

Figure 6.8 contains additional microscopy of the carbon steel wire surface, from the low temperature system with additive. Figure 6.8a was taken from one of the clamped ends of the wires. Here, flow would be significantly reduced versus the wire midsection and an agglomeration of material is observed. Figure 6.8b is between the middle of the wire and the clamped end. Figure 6.8c is a portion of the wire near mid-length. At this point flow would be a maximum and much less material has been retained on the wire surface. The foulant that is observed is non-uniform around

the wire circumference, which was also observed in the cross-section image of the wire in Figure 6.7d. Even though an explanation has been put forth, such a small amount of foulant was observed on the carbon steel, there were a limited number of tests conducted, and only one oil was utilized. The effect of Fe-NA on carbon steel at low temperatures requires further study.

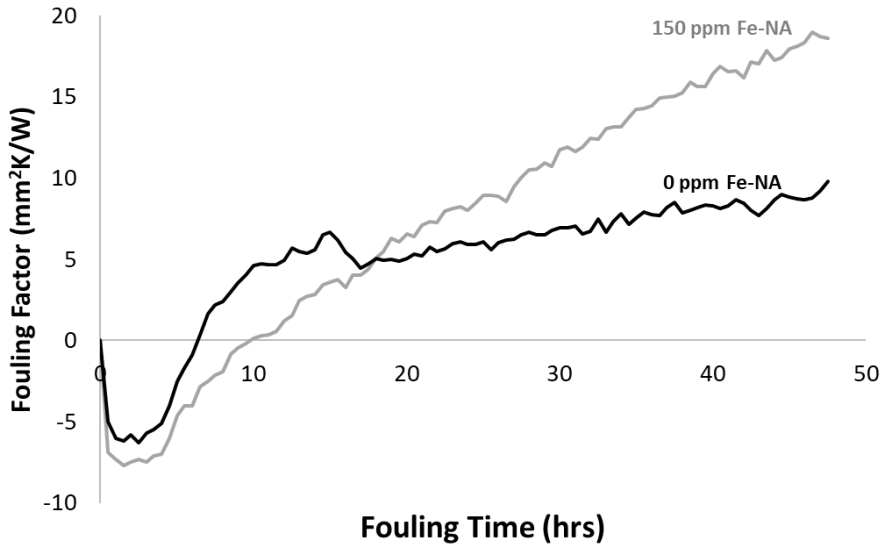

Figure 6.9 Fouling factor plots for P91 in Crude G with and without Fe-NA additive. Twire = 350°C, Toil = 150°C, run time = 48 hours.

Figure 6.9 presents fouling factor data for P91 wires in Crude G with and without Fe-NA, during exposure to the low temperature experimental conditions. A strong trend is observed compared with the data generated under the high temperature condition, in Figure 6.4. Ultimate fouling factors are 18.6 and 9.8 mm^2K/W for the system with and without additive, respectively. Fouling factors with Crude G and the additive are nearly identical in the high temperature experiment, after 4 hours, and here, in the low temperature condition after 48 hours. There appears to be a discontinuity in the fouling factor for the P91 wire in the system without additive.

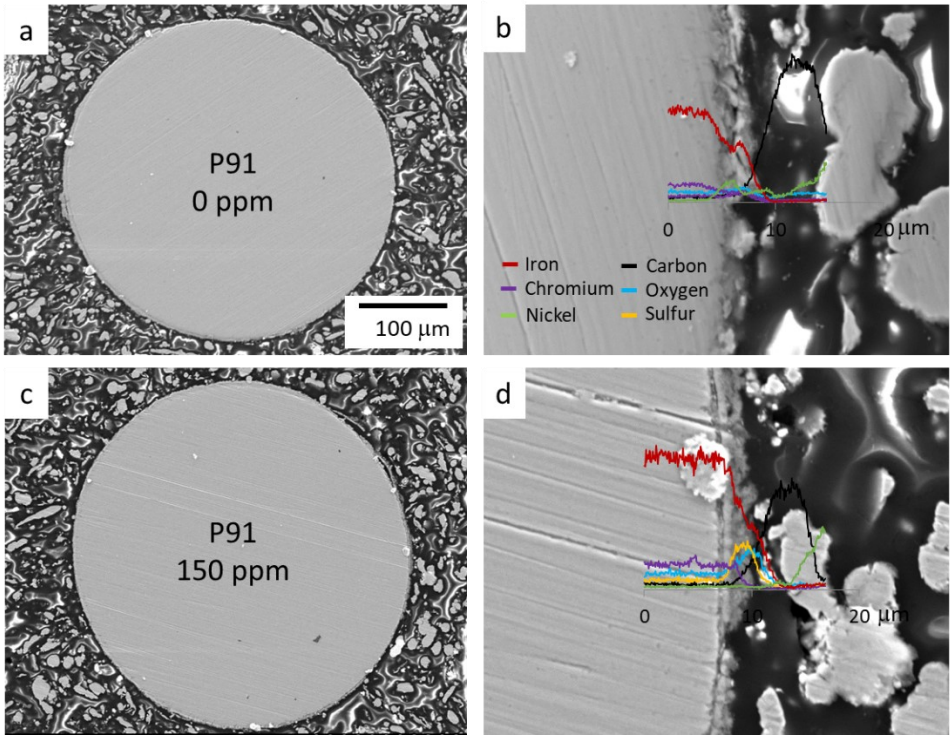

Figure 6.10 Effect of Fe-NA additive on fouling of carbon steel. (a,b) SEM and EDXS compositional scans of fouled wire cross-sections in Crude G without additive. (c,d) SEM and EDXS compositional scans of fouled wire cross-sections in Crude G with additive. Wire T = 350 °C, oil T = 150 °C, run time = 48 hours.

Figure 6.10 presents SEM micrographs and accompanying EDX line scans for P91 wires fouled in Crude G, at low temperature (350 °C wire temperature, 150 °C bulk oil temperature). Figure 6.10(a and c) are low magnification micrographs of the wires fouled without and with additive, respectively. Very little foulant is observed on either of the wires, which does not correlate well with the fouling factor data. Even in the higher magnification images, Figures 6.10(b and d), little fouling is evident. On the P91 wire taken from the system with additive, slightly more fouling is present. It is predominately iron sulfide, with some carbon observed radially outwards before transitioning to the epoxy. A strong peak for oxygen is evident through the layer of foulant, which could evidence of the original surface oxide, or a result of the additive. The same intensity of oxygen is not present in the system without additive. Previously, it was introduced and discussed that the thermal decomposition of the Fe-NA could result in the production of water at the surface of the hot wire and could compete with the sulfidation reactions.

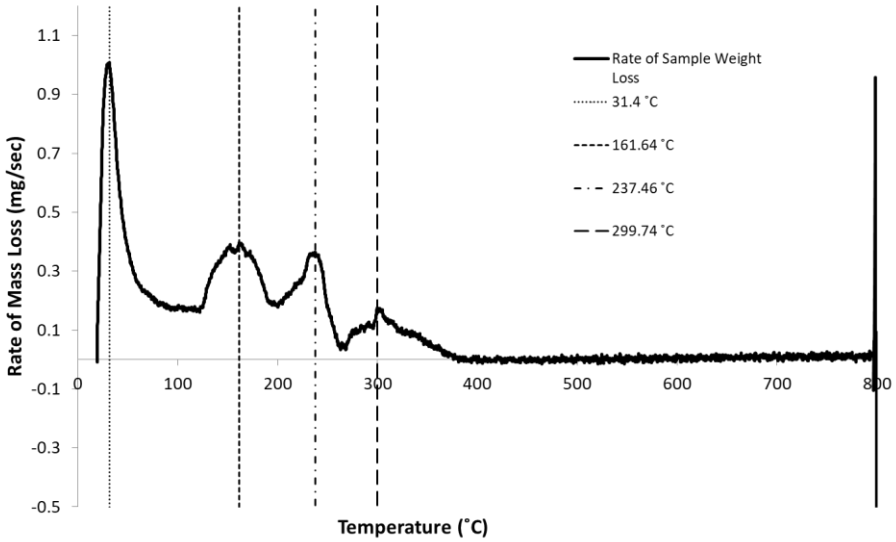

Figure 6.11 Thermogravimetric analysis of the Fe-NA used in this study. The graph shows mass loss due to evaporation of the mineral spirits in which the naphthenate was dissolved, up to about 30 °C, followed by three distinct decomposition events at 160, 240, and 300 °C.

Figure 6.11 is a plot from thermal analysis of the Fe-NA additive used in this study. Thermogravimetric analysis is plotted as mass loss rate versus temperature. This work was conducted to help characterize thermal behavior of the additive. A sample of the naphthenate was brought to 800°C in an inert argon atmosphere at a rate of 1 °C per minute. Clearly visible from the plot are an initial boiling event (from the mineral spirits solvent) at 30 °C, and three distinct decomposition events at approximately 160 °C, 240 °C, and 300 °C. This demonstrates that the Fe-NA is not expected to remain stable at the wire surface temperatures employed in both the high and low temperature conditions of this study. Furthermore, the additive will undergo a degree of decomposition even within the bulk oil in both scenarios at 250°C. This data Fe-NA is decomposed during fouling and is acting both at as H_2S scavenger at high temperature and a metal surface oxidant at low temperature.

6.3 Summary and Conclusions

High temperature fouling experiments were conducted in Crude G, with and without the Fe-NA additive. For carbon steel, addition of Fe-NA caused the fouling factor to drop significantly, to the point of no fouling. This was supported by SEM and EDXS data. For the P91 wire, there was no observable trend in the fouling factor data. In SEM and EDXS data, the P91 wire demonstrated very

different fouling morphology with and without additive. When the Fe-NA was present, fouling contained more carbonaceous deposit and particulate iron sulfide. In contrast, the foulant was predominately iron sulfide when no additive was present.

In low temperature scenario, trends were less evident. It seemed that for carbon steel the fouling factor plots detected deposition of particulate fouling that collected and then later dislodged, causing values to rise then return to trending levels. In SEM and EDXS irregular fouling was observed around the circumference of the wires, which supports a particulate deposition mode. Along the length of the fouled wires deposits increased where flow limited and the irregularity of the foulant was confirmed.

Addition of the Fe-NA additive has introduced resolvable tendencies to the fouling data generated in fouling factor plots and SEM and EDXS. However, a consistent mechanistic description requires more study. Several hypotheses have been put forth to explain the observations. One is that the additive decomposes and introduces iron to the system that subsequently sulfides and exists as an insoluble particulate in the oil. This suspension of iron sulfides adds to particulate fouling of the hot wire surface. This theory is supported by evidence of inconsistent fouling presented by microscopy. A second theory follows thermal decomposition of the naphthenate, generation of an oxidant such as H_2O or O_2, and a competitive mechanism of sulfidation and oxidation at the wire surface. There is supportive evidence for this explanation in reduced fouling and metallic oxide at the fouled wire surfaces.

6.4 References

(1) Stephenson, T.; Hazelton, M.; Kupsta, M.; Lepore, J.; Andreassen, E. J.; Hoff, A.; Newman, B.; Eaton, P.; Gray, M.; Mitlin, D. *Fuel* **2015**, *139*, 411–424.

(2) Stephenson, T.; Kubis, A.; Derakhshesh, M.; Hazelton, M.; Holt, C.; Eaton, P.; Newman, B.; Hoff, A.; Gray, M.; Mitlin, D. *Energy and Fuels* **2011**, *25* (10), 4540–4551.

(3) Lepore, J. The Role of Sulfur Species in Establishing the Corrosion Reactions in Refinery Metallurgies, University of Alberta, 2016.

(4) Xiaofei, Z.; Tao, M.; Xiaochun, H.; Jinde, Z.; Xiaoyi, W.; Sixian, R. *Eng. Fail. Anal.* **2020**, *117* (January), 104802.

(5) Jin, P.; Nesic, S.; Wolf, H. A. *Surf. Interface Anal.* **2015**, *47* (4), 454–465.

(6) Jin, P.; Nesic, S. *Corros. Sci.* **2017**, *115*, 93–105.

(7) Jin, P.; Bota, G.; Robbins, W.; Nesic, S. *Energy and Fuels* **2016**, *30* (8), 6853–6862.

(8) Yépez, O. *Fuel* **2005**, *84* (1), 97–104.

(9) Flego, C.; Galasso, L.; Montanari, L.; Gennaro, M. E. In *Energy and Fuels*; 2014; Vol. 28, pp 1701–1708.

(10) Rebak, R. B. *Corrosion Reviews*. 2011, pp 123–133.

(11) Qu, D. R.; Zheng, Y. G.; Jing, H. M.; Jiang, X.; Ke, W. *Mater. Corros.* **2005**, *56* (8), 533–541.

(12) Diaz, Y.; Sevilla, A.; Mónaco, A.; Méndez, F. J.; Rosales, P.; Garc\'\ia, L.; Brito, J. L. *Fuel* **2013**, *110*, 235-248.

CHAPTER 7

Preliminary Design and Initial Evaluation of Anti-fouling Coatings

7.1 Introduction

In this portion of the study, a series of surface coatings were introduced to the wires as a mitigative approach to reduce fouling. A variety of coatings have been utilized throughout the oil and gas industry to reduce fouling and corrosion of susceptible of metallic components.[1–5] Several initial coating designs were selected for their known protectiveness, thermodynamic stability, and slow growth rates in the process environment. A refinery is a particularly challenging environment for many materials, due to extreme temperatures and low oxygen/water vapor content, which many metals rely on to form a stable, protective oxide. Thermally stable oxides with demonstrated efficacy in high-temperature, corrosive environments include those of Cr, Al, and Si.[6] Intermetallics, such as those formed between Al and Ti,[7] as well as their oxides,[8] have also shown efficacy for reducing high temperature corrosion.

The initial coatings included Cr_2O_3, Al_2O_3, TiO_2 and Cr metal. Cr metal was selected because it was expected to bond better with the underlying metallurgies and would form the basis of an interlayer in later work. They were deposited onto wires to a nominal thickness of 50 nm, using physical vapor deposition (magnetron sputtering), in high vacuum, at 200 °C. Oxide coatings were deposited by reactive sputtering in a mixed argon and oxygen environment, while the Cr metal was deposited by conventional sputtering and no additive partial pressure of oxygen. The coatings were applied to carbon steel and P91 wires and tested for their efficacy towards reducing fouling and corrosion under the low temperature experimental conditions (i.e. 350 °C wire temperature and 250 °C oil temperature). Table 7.1 presents the list of coatings and experiments conducted for this section of study.

Table 7.1 Initial experimental evaluation of coated P91 and carbon steel wires.

	Duration	Metallurgy	Coating	T_{oil} (°C)	T_{wire} (°C)
1	4	P91	Cr2O3	250	350
2	8	P91	Cr2O3	250	350
3	4	CS	Cr2O3	250	350
4	8	CS	Cr2O3	250	350
5	4	P91	Cr	250	350
6	8	P91	Cr	250	350
7	4	P91	TiO2	250	350
8	8	P91	TiO2	250	350
9	4	CS	TiO2	250	350
10	8	CS	TiO2	250	350
11	4	P91	Al2O3	250	350
12	8	P91	Al2O3	250	350
13	4	CS	Al2O3	250	350
14	8	CS	Al2O3	250	350
15	4	CS	Cr	250	350
16	8	CS	Cr	250	350

7.2 Results and Discussion

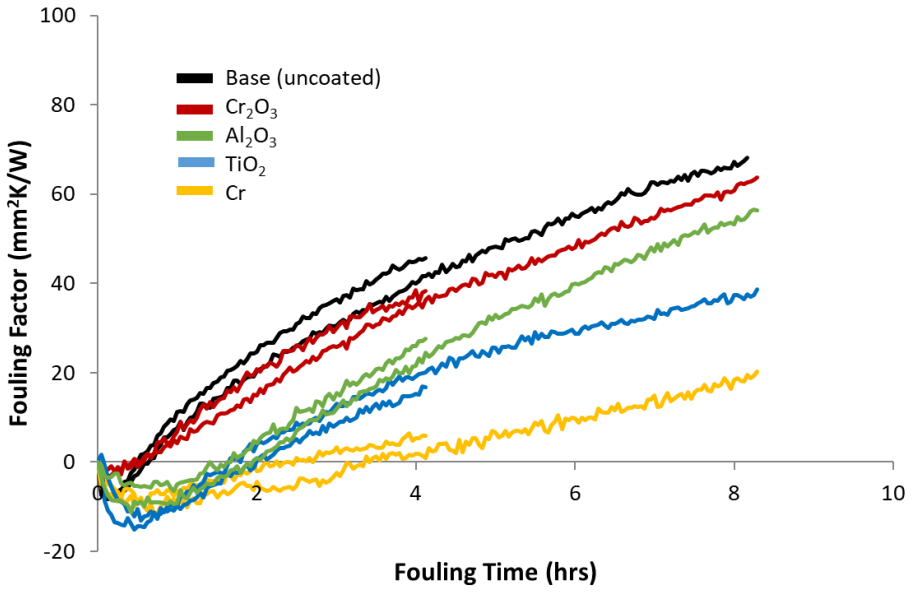

Figure 7.1 Fouling factor for P91 and P91 coated with 50 nm of Cr_2O_3, Al_2O_3, TiO_2 and Cr. Oil A, Twire = 350°C, Toil = 250°C, run time = 4 and 8 hours.

Figures 7.1 shows fouling factor plots of P91 and coated P91 wires after 4 and 8 hours of exposure to Crude A. This data demonstrates an initial efficacy of the coatings as the uncoated wire samples achieve larger fouling factors versus those with a coating. The uncoated wire sample has maximal fouling factors of 45.7 and 60.8 mm^2K/W after being fouled for 4 and 8 hours, respectively. This suggests Crude A has a lower fouling propensity than Blend HI, but greater than Blend BC, and Blend BDH under identical experimental conditions.

Immediately apparent is the stratified efficacy of the coatings compared to the uncoated wire. From the plots in Figure 7.1, the coating of pure Cr metal appears the most effective. The effectiveness of Cr at reducing catalytic coke formation in high temperature coking has been demonstrated.**Error! Bookmark not defined.** The Cr_2O_3 coating appears least effective towards reducing the fouling factor, and Al_2O_3 performs similarly. The TiO_2 layer appears to have some effectiveness towards reducing the fouling factor on P91 in this oil.

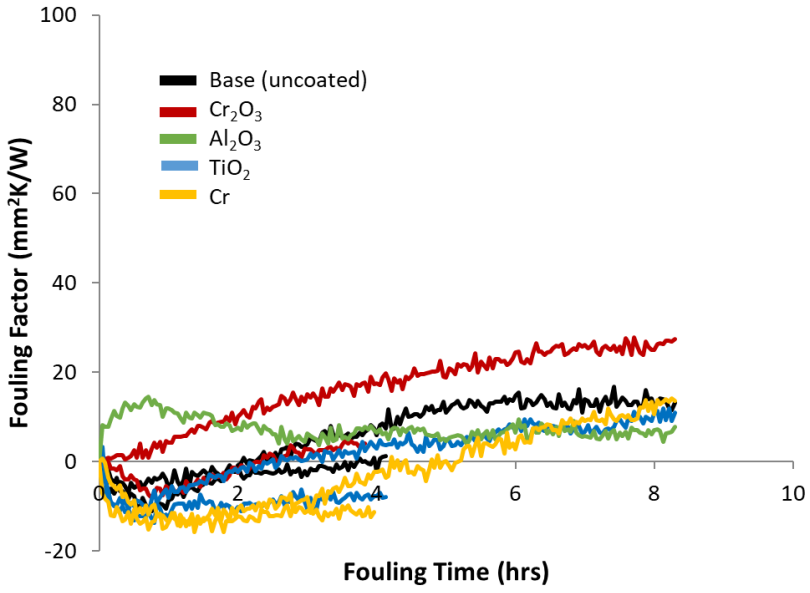

Figure 7.2 Fouling factor for carbon steel and carbon steel coated with 50 nm of Cr_2O_3, Al_2O_3, TiO_2 and Cr. Oil A, Twire = 350°C, Toil = 250°C, run time = 4 and 8 hours.

Figure 7.2 shows fouling factor plots for carbon steel wires with and without the respective coatings. The uncoated wire fouls to a maximal value of 16.1 mm^2K/W in the 8-hour tests, and only 1.1 mm^2K/W after 4 hours. There is much less repeatability with the carbon steel wires versus the

P91 wires presented in Figure 1. A similar trend to emerge is that the Cr_2O_3 coating is least effective. It could be reasonable to assume the most benefit comes from the chromium metal, but more work and analysis is required. If positive results are identified amongst the microscopy, the Cr metal could establish a basis as an interlayer for more complex, multilayer systems that may include Cr-CrN, Cr-Cr_2O_3, Cr-Al_2O_3, or combinations thereof.

Comparing the fouling factor plots, no meaningful trends regarding the reduction of the fouling factor by applying coatings to carbon steel emerge, while the P91 demonstrates noticeable advantages with all coated wires. In this initial application of the sputtered coatings, very little effort was afforded to enhancing the bonding of the materials. This could and will include pre-deposition surface conditioning, such as plasma cleaning or sputtering, interlayer or diffusion barrier coatings, and post-deposition heat treatments. These aspects can be completed within the sputter systems and have demonstrated effectiveness amongst other research and application[9,10] Without these improvements, it is reasonable to assume that these mitigative coatings on the carbon steel wire are suffering from similar effects that lead to the repeatedly observed delamination events seen throughout the fouling scenarios covered by this study. Continuous corrosion reactions occurring at the wire surface are producing corrosion products such as iron sulfide and hydrogen gas. The volume expansion associated with the production of irons sulfide facilitates delamination of the surface layers (corrosion product or the sputtered coatings), while the production of hydrogen gas within the metal matrix creates internal pressure, with similar effect. It is obvious that under the current design, the coatings are much less effective when applied to the carbon steel metallurgy.

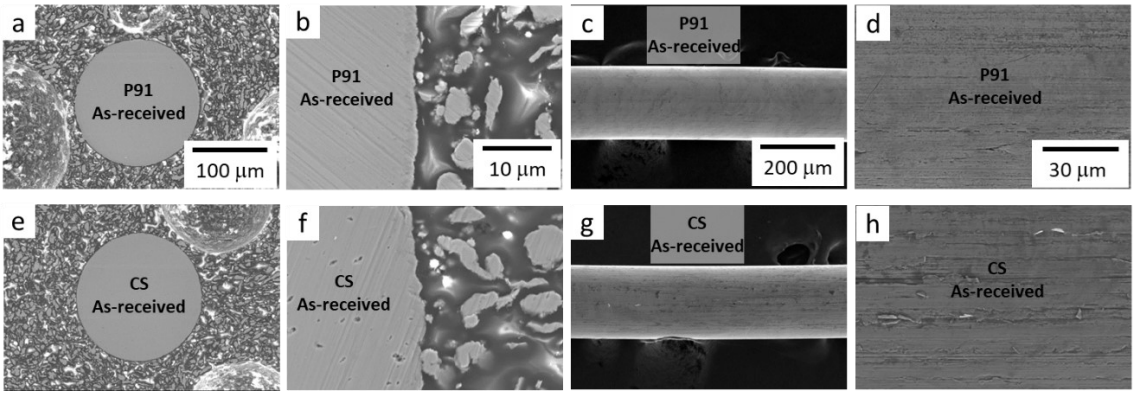

Figure 7.3 SEM micrographs of cross sections and surfaces of as-received P91 and carbon steel wires.

Figure 7.3 shows a series of SEM micrographs of the as-received P91 and carbon steel wires used for this study. Figures 7.3(a and e) are cross-sections of the P91 and carbon steel wires, respectively. Figures 7.3(b and f) are portions of the wire cross-sections at higher magnification. Figures 7.3(c and d) are micrographs of the P91 wire surface at low and high magnification, while Figures 7.3(g and h) show the surface of the carbon steel wire at the two magnifications. A comparison of the morphologies of P91 and carbon steel reveals some interesting results. Comparing Figures 7.3(b and f), one can see that the bulk of the carbon steel wire appears to contain numerous small voids, while the P91 lacks the same features, at this magnification. Such metallurgical defects can be introduced during the manufacturing process and can promote localized corrosion attack when the metal is exposed to a corrosive environment such as that employed in the fouling studies. Furthermore, a comparison of Figures 7.3(d and h) demonstrates that the outer surface of the P91 appears to be smoother and more defect-free than the carbon steel. While this could be an effect of differing manufacturing techniques, the surface of the P91 could also be a result of the alloying elements chromium and molybdenum that render the alloy less susceptible to shear-induced defects that would be encouraged by the drawing processes utilized to produce the wire.

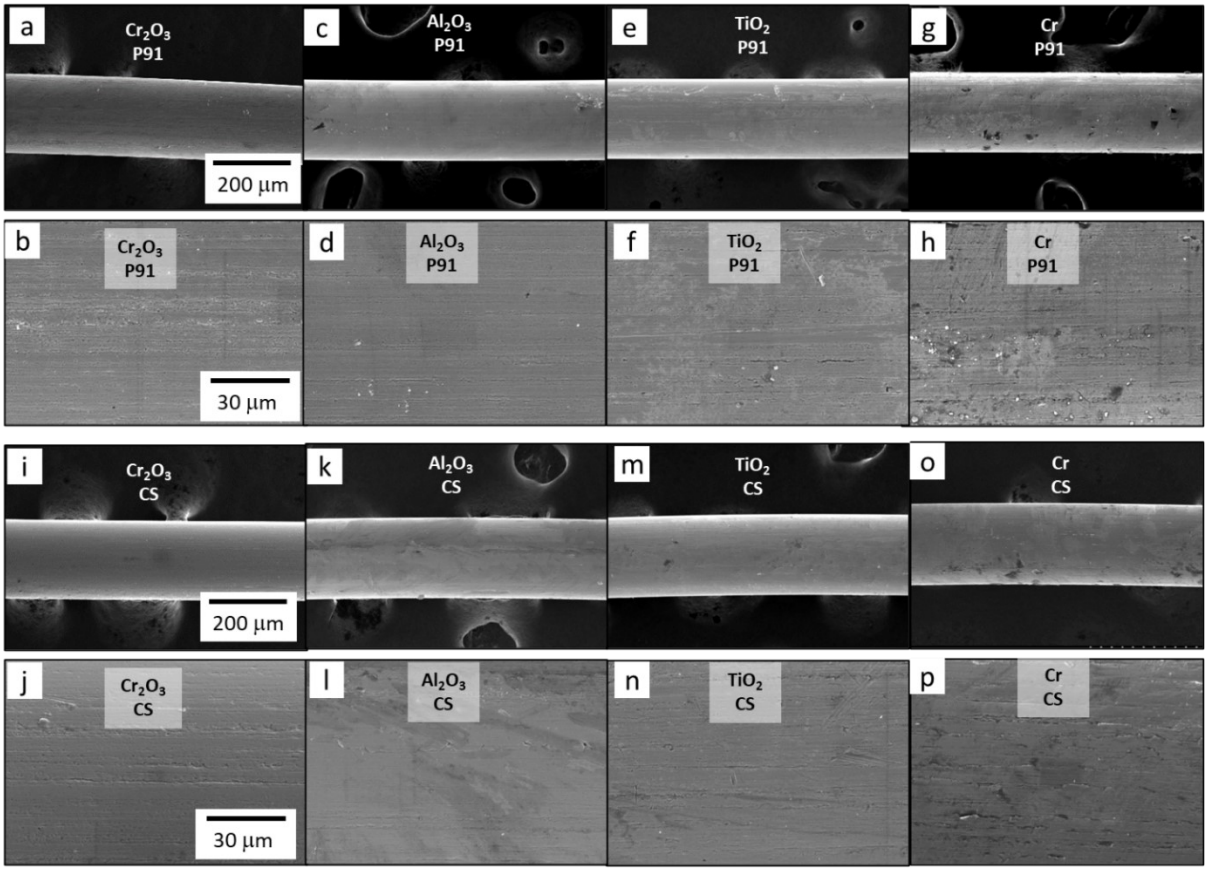

Figure 7.4 SEM micrographs of (a-h) P91 and (i-p) carbon steel wire surfaces after the indicated 50 nm coatings were applied.

Figure 7.4 presents SEM micrographs of the P91 and carbon steel wire surfaces after the 50 nm coatings were applied, but before use in a fouling experiment. For each coating, the wire surface is presented in a pair of images at low and higher magnifications. Figures 7.4(a and b) are the surface of a P91 wire after depositing 50 nm of Cr_2O_3. Figures 7.4(i and j) are the surface of a carbon steel wire after depositing 50 nm of Cr_2O_3. Figures 7.4(c - h) and Figures 7.4(k – p) present the remaining coatings - Al_2O_3, TiO_2, and pure Cr on P91 and carbon steel, respectively. Surface striations, running longitudinally are a remnant of the wire drawing process and are evident in the higher magnification micrographs.

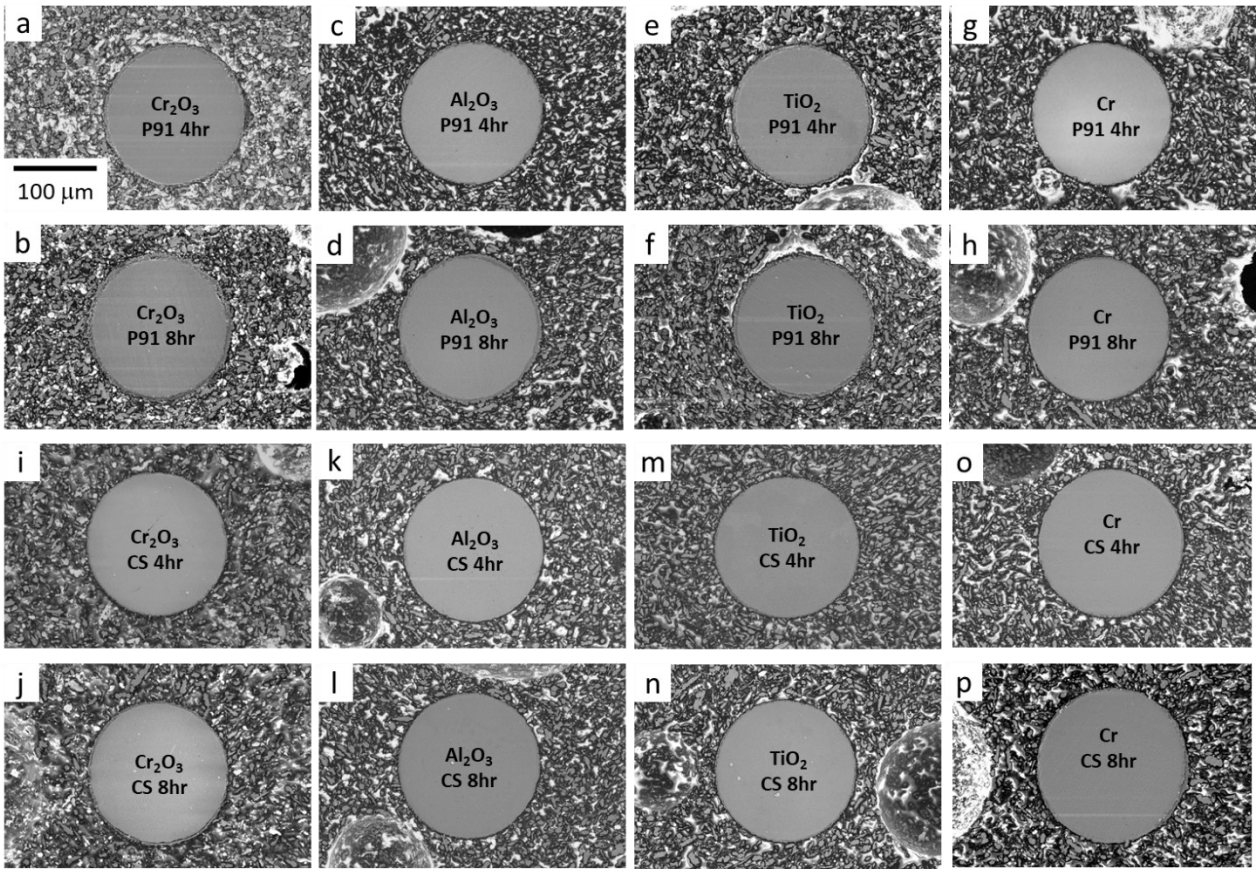

Figure 7.5 Low magnification SEM micrographs of coated (a-h) P91 and (i-p) carbon steel wire cross sections after 4 and 8 hours of fouling in Crude A.

Figure 7.5 is a series of SEM micrographs which show the cross sections of the coated P91 and carbon steel wires after exposure in 4- and 8- hour fouling experiments. At this magnification, only a small amount of foulant is observed, which is consistent with results from previous fouling experiments under these lower temperature conditions. The trends observed in the fouling factor plots (Figures 7.1 and 7.2) are reflected in these cross-sectional micrographs. For the P91 metallurgy, a comparison of the respective 4- and 8- hour tests reveal more fouling on wires with longer exposure time, as expected. This same trend is not immediately evident on the carbon steel wires. The amount of fouling and corrosion on each, coated P91 wire is also relatively consistent with the fouling factor plots, wherein the Cr metal coating demonstrates the least foulant and those with the Cr_2O_3 coating, the most. The P91 wires coated with TiO2 also appear to have a slight reduction in the amount of surface deposits relative to the Al_2O_3. In the carbon steel series, it appears the Cr_2O_3 was least effective – has the most foulant, and this is consistent with the fouling factor plots. For the remaining

carbon steel wires, there is very little to observe at this magnification, no consistent trends are obvious, and this coincides with the fouling factor plots.

Since these fouling runs were conducted under the low temperature test conditions (wire temperature 350 °C and oil temperature 250 °C), the surface deposits are extremely thin after 4- and 8- hour run times. The wire surface temperature is below cracking temperature of the oil (generally, thermal cracking will become appreciable only above 370 - 390 °C), which considerably reduces the amount of organic fouling. In this temperature regime, the fouling mechanism is expected to be dominated by sulfidic corrosion and the adhesion of particulates from the crude oil. Similar foulant morphology to the previous low temperature experiments suggest the corrosion product on these wires will be iron sulfides, and the efficacy of these initial coating designs is limited.

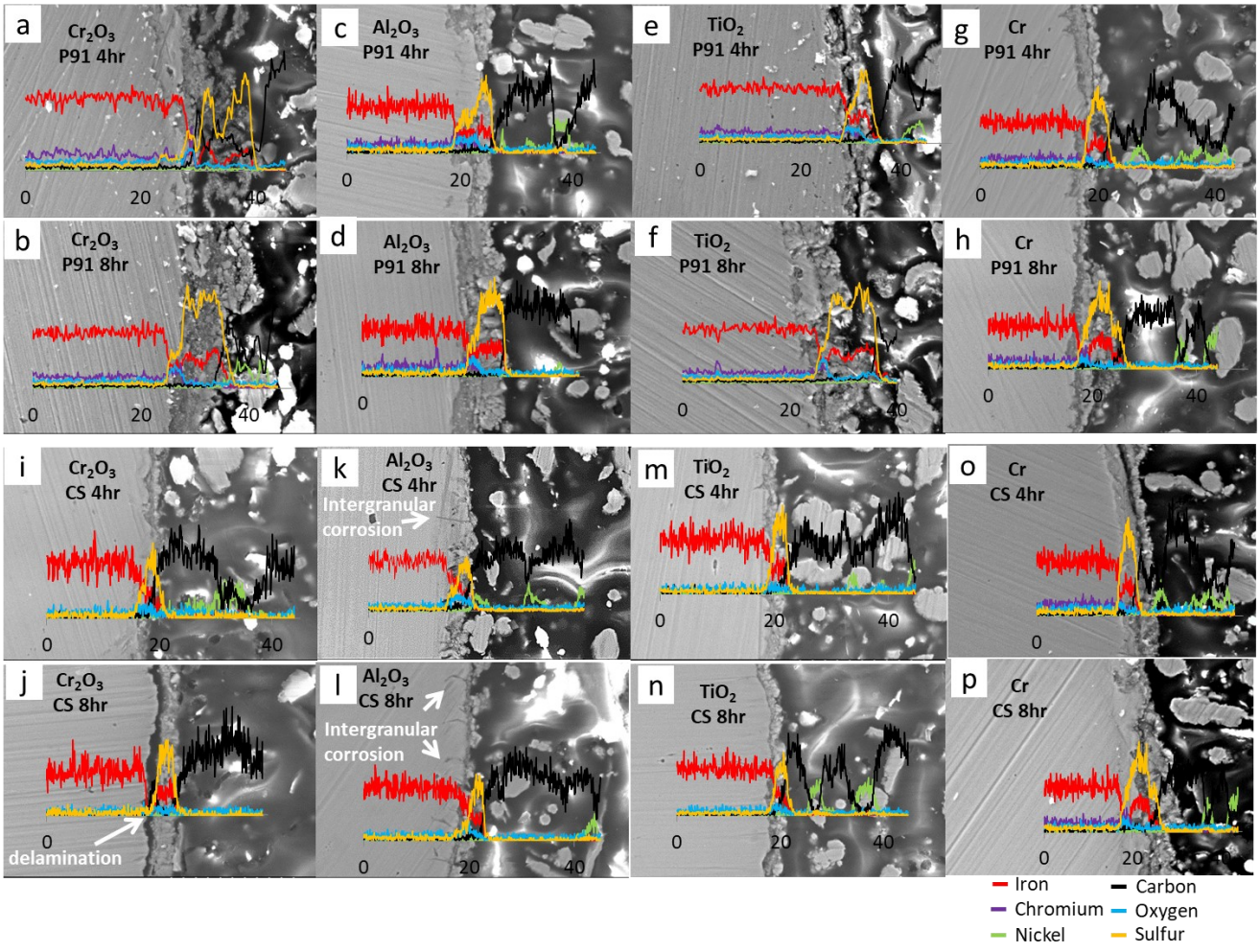

Figure 7.6 High magnification SEM micrographs and EDXS compositional linescans for coated (a-h) P91 and (i-p) carbon steel wire cross sections after 4 and 8 hours of fouling in Crude A.

Figure 7.6 is a series of SEM micrographs, taken at higher magnification, of the coated wire surfaces presented in Figure 7.5. Each image is overlaid with a plot generated from an EDXS linescan. These plots provide elemental information along the path of their x-axis. Figures 7.6(a-h) correspond to the coated P91 wires and Figures 7.6(i-p), the coated carbon steel wires. For each metallurgy, data from 4- and 8- hour experiments are included. The coatings are presented in order of Cr_2O_3, Al_2O_3, TiO_2, and finally the pure Cr metal. Each micrograph is labelled with corresponding coating, metallurgy, and fouling time.

At this magnification, the SEM micrographs resolve the foulant layer morphology, and similar structure is observed to previous, low temperature experimental results without coatings. They reveal that more fouling accumulates on the coated P91 wires, which conforms to this well-established trend. The linescans demonstrate that the foulant is predominantly iron sulfide: The now well-established, ubiquitous sulfidic corrosion product was detected on the surface of all samples. Delamination of the foulant layer is observed for the carbon steel wire coated with Cr_2O_3, after 8 hours of fouling (Figure 7.6j), and for the carbon steel wire coated with Cr metal, after 4 hours of fouling (Figure 7.6o). Note the carbon signal spike, detected at the break between the bulk wire and corrosion layer (arrowed in Figure 7.6j). No separation is observed in the micrographs presented for the P91 wires. This delamination is indicative of a compromised bond between the carbon steel wire and its respective corrosion products, which could also be pertinent to the tenacity of the sputtered coating. Across the combinations of wires and coatings there exists distinguishable evidence of metallic oxide at the foulant-wire interface. The blue plotted lines represent oxygen in each overlay. There are spikes, of varying degree, against the background oxygen levels at the interface for each wire. The spikes are more pronounced for P91 versus carbon steel, and for the Al_2O_3 coating amongst the carbon steel samples.

Figures 7.6(a, b and i, j) pertain to P91 and carbon steel wires, coated with 50nm of Cr_2O_3, respectively. Resolving the coating material from the EDX linescans was difficult due to both the geometry of the scan and the thinness of the coating. In Figure 7.6(a and b), evidence for a chromium

oxide layer at the P91 wire surfaces is possible, but this same feature was noted on uncoated wires in previous parts of the study, and it is unclear if this is the sputtered coating. Both the P91 and carbon steel wires coated with Cr_2O_3 exhibited the most fouling, versus the other coated wires, which is consistent with the fouling factor data in Figure 1.

Figures 7.6(c, d and k, l) present SEM and EDX data for the Al_2O_3 coating on P91 and carbon steel wires, respectively. This coating does not appear to have much effectiveness towards reducing the fouling and corrosion of P91, consistent with the fouling factor data. The trend for carbon steel appears slightly more positive. There is no obvious delamination of the sulfide, and the sulfide layer is thinner than was observed on the carbon steel wires coated with Cr_2O_3. Figures 7.6(i and j) contrast the foulant thicknesses after 8 hours of fouling for wires with the Al_2O3 coating versus Cr_2O_3. Interestingly, evidence of intergranular attack is made obvious (arrowed) in the figures where carbon steel wires were coated with Al_2O_3. This is not observed with the other wires or in previous aspects of this study. This damage mechanism would further compromise the ability of the mitigative coatings and the bond of the corrosion product.

Figures 7.6(e, f and m, n) present images of P91 and carbon steel wire cross sections, fouled 4 and 8 hours, that were coated with TiO_2. For P91, it is observed that the TiO_2 coating functioned similarly to the Al_2O_3 coated samples but outperformed those coated with Cr_2O_3. Figures 7.6(f, d, and b) compare the P91 wires coated with TiO_2, Al_2O_3, and Cr_2O_3 after 8 hours of fouling time, respectively. In the 8-hour fouling factor data from Figure 7.1, TiO2 demonstrates a slightly lower value versus the Al_2O_3, specifically 39.2 versus 56.3 mm_2K/W. Thermal conductivity of the foulants on both wires should be similar, but small differences to such physical properties could account for these contrasting results. The carbon steel wires present a weaker, but similar trend to the P91 wires, however much less iron sulfide and other foulant is observed on the surfaces of these samples. The sulfide corrosion layer that is present, appears much more dense and well-adhered versus foulant on the other carbon steel wires.

Figures 7.6.(g, h and o, p) present images of P91 and carbon steel wire cross sections, fouled 4 and 8 hours, that were coated with Cr metal. In Figure 7.1, this coating demonstrated the highest efficacy towards reducing the fouling factor for both wire metallurgies. Figures 7.6(g and h) corroborate this trend for P91. Compared against the other coatings the Cr metal has reduced the amount of surface corrosion and the overall thickness of the foulant layer on the P91 wires, especially when the 8-hour results are considered. This could be due the formation of a well-bonded and continuous diffusion barrier, provided by the Cr metal. For carbon steel the trend is not obvious, or absent in the micrographs. Comparing the 8-hour, carbon steel tests, demonstrates that those with the Cr metal coating may have accumulated more foulant. This conclusion needs to be considered against the delamination events established for carbon steel and the non-uniformity of the foulants that have been observed under the low temperature conditions. For example, it may be that the Cr metal increases the bonding of the foulant.

The corrosion products and general foulant adhere better to the surface of the P91 wire, and ultimately more buildup is observed, compared to the carbon steel. The corrosion products that form on the carbon steel bond poorly to the underlying surface, which leads to continuous delamination events during a fouling run, and ultimately thinner foulant. The enhanced bonding of corrosion products to the P91 surface is attributable to effects from the additional alloying elements, which, give it greater microstructural stability at temperature, than the carbon steel.[11] Furthermore, it appears that intergranular corrosion is introduced as a mechanism which contributes to the surface degradation of carbon steel, with the Al_2O_3 coating applied. In Figure 7.6(j and l), white arrows identify dark lines penetrating the sub-surface of the wire. These are presumably grain boundaries that have suffered preferential corrosion by H_2S, where the coating broke down. Localized failure of protective coatings on steels and stainless steels is known to produce this type of concentrated, intergranular attack.[12] Such a corrosion mechanism would cause delamination events as the corrosion products build stresses between the grains and work to push them out of the metal surface.

In Figure 7.6, the dominant efficacy of the chromium metal coating on P91 is revealed, particularly at the longer exposure time. The samples coated with Cr metal appear to have suffered less corrosion and overall accumulation of foulant, when compared to all other coated samples. This is most likely due to the excellent adherence of the chromium metal coating. Strong bonding characteristics of this metal during physical vapor deposition, on various materials, is well documented.[13,14] Furthermore, thermodynamic calculations which are presented in Table 4, along with evidence presented by EDX maps in Figure 7.12, suggests that the coating likely oxidized at the reactor conditions to Cr_2O_3, which is recognized as one of the most thermodynamically stable oxides, and can resist sulfidation at temperatures in excess of 550 °C.[6] A naturally occurring nanometer scale Cr_2O_3 layer is what facilitates passivation on the 347SS wire surface. It is the increased ability of the Cr metal to bond with the native wire surface, relative to the reactively sputtered Cr_2O_3, which improves coating performance.[9]

Table 7.2 Thermodynamic calculations for the coating materials.[15,16]

Reaction	ΔG_{rxn} at 350 °C (J/mol)
$2Cr_{(s)} + 3H_2O_{(g)} \leftrightarrow Cr_2O3_{(s)} + 3H_{2(g)}$	-422,000
$TiO_{2(s)} + 2H_2S_{(g)} \leftrightarrow TiS_{2(S)} + 2H_2O_{(g)}$	-13,500
$Al_2O_{3(S)} + 3H_2S_{(g)} \leftrightarrow Al_2S_{3(s)} + 3H_2O_{(g)}$	274,600
$Cr_2O_{3(S)} + 3H_2S_{(g)} \leftrightarrow Cr_2S_{3(s)} + 3H_2O_{(g)}$	NA
$Fe_2O_{3(S)} + 3H_2S_{(g)} \leftrightarrow Fe_2S_{3(s)} + 3H_2O_{(g)}$	-48,200
$Fe_{(S)} + H_2S_{(g)} \leftrightarrow FeS_{(s)} + H_{2(g)}$	-53,200
$Fe_{(s)} + H_2O_{(g)} \leftrightarrow Fe_2O_{3(s)} + 3H_{2(g)}$	-10,600

A well adhered layer of Cr metal and its subsequent oxidation to Cr_2O_3 would have been sufficient to facilitate a strong diffusion barrier on the P91 wire surface. This barrier would be stable at the wire surface temperature of 350 °C and would provide substantial mitigation against the outward diffusion of iron, and in the ingress of H_2S – the mechanisms behind the observable sulfidic corrosion process. Reducing the rate of corrosion, and thus minimizing the production of iron

sulfides, reduces the overall amount of foulant. The iron sulfides roughen the wire surface, which promotes wetting of fouling precursors and suspended particulate in the oil. They are also a known catalyst for coke formation in the absence of a high partial pressure of hydrogen.

From an examination of the ΔG_{rxn} for the various reactions, that the Cr_2O_3 and Al_2O_3 are expected to remain stable at the reactor conditions, while the TiO_2 coating is expected to form a sulfide. It is difficult to find thermodynamic and experimental evidence for of Cr_2O_3 forming a sulfide, and little data for Cr_2S_3 could be found.[17,18] Furthermore, we can see from Table 7.4 that the oxidation of iron to Fe_2O_3 is still thermodynamically favorable at 350 °C. However, it is not expected that this reaction will progress significantly in the environment of the reactor. The higher partial pressure of H_2S in the vessel and limited content of O_2 and H_2O will preferentially drive the sulfidation of any oxide that was present or that does form in the reactor.

Figures 7.7 through 7.12 present SEM and EDX elemental analysis of the coated wire surfaces pre- and post- fouling. Figures 7.7(a-h) are micrographs of P91 wires, coated with Cr_2O_3 (Figures 7.7a-7.7d) in and Al_2O_3 (Figures 7.7e-7.7h), after 4- and 8- hour fouling experiments. Each surface coating is presented in two images, at low and higher magnifications. Figures 7.7i through 7.7p are micrographs of coated carbon steel wires, after 4- and 8- hour experiments, in identical format. Figure 7.8 presents the P91 and carbon steel wires, coated with TiO_2 and Cr metal. Figures 7.9 through 7.12 are micrographs and elemental maps of the wire surfaces, both in their original coated condition and after 4- and 8- hour fouling tests. Figures 7.9(a-c) highlight P91 wires, coated with Cr_2O_3, before fouling (Figure 7.9a), after 4 hours of fouling (Figure 7.9b), and after 8 hours of fouling (Figure 7.9c). Figures 7.9(d-f) are carbon steel wires with Cr_2O_3 coating, as deposited, and after 4 and 8 hours of fouling, respectively. Figure 7.10 is in identical format but pertains to P91 and carbon steel wires coated with Al_2O_3. Figure 7.11 and Figure 7.12 follow with results from wires coated with TiO_2 and Cr metal, respectively.

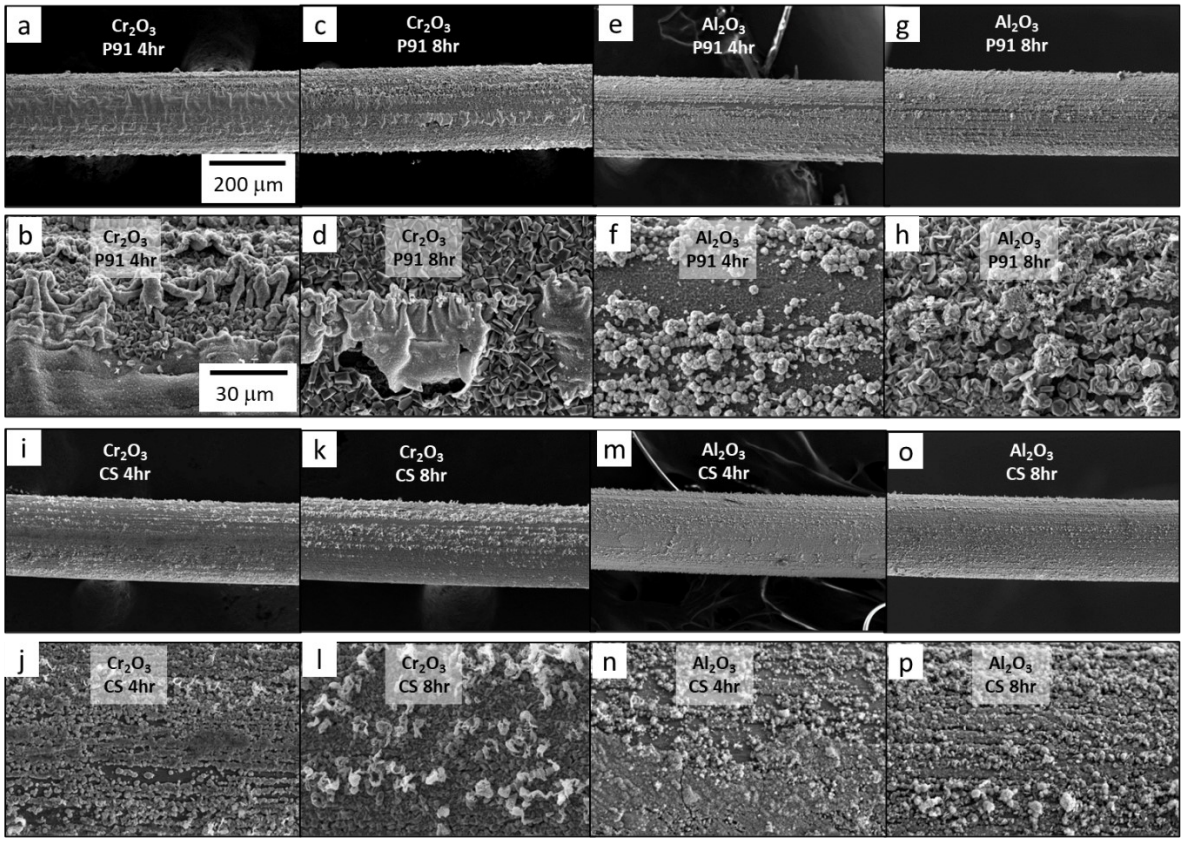

Figure 7.7 SEM micrographs of (a-h) P91 and (i-p) carbon steel wire surfaces with 50 nm of Cr2O3 and Al2O3 after 4 and 8 hours of fouling, as indicated.

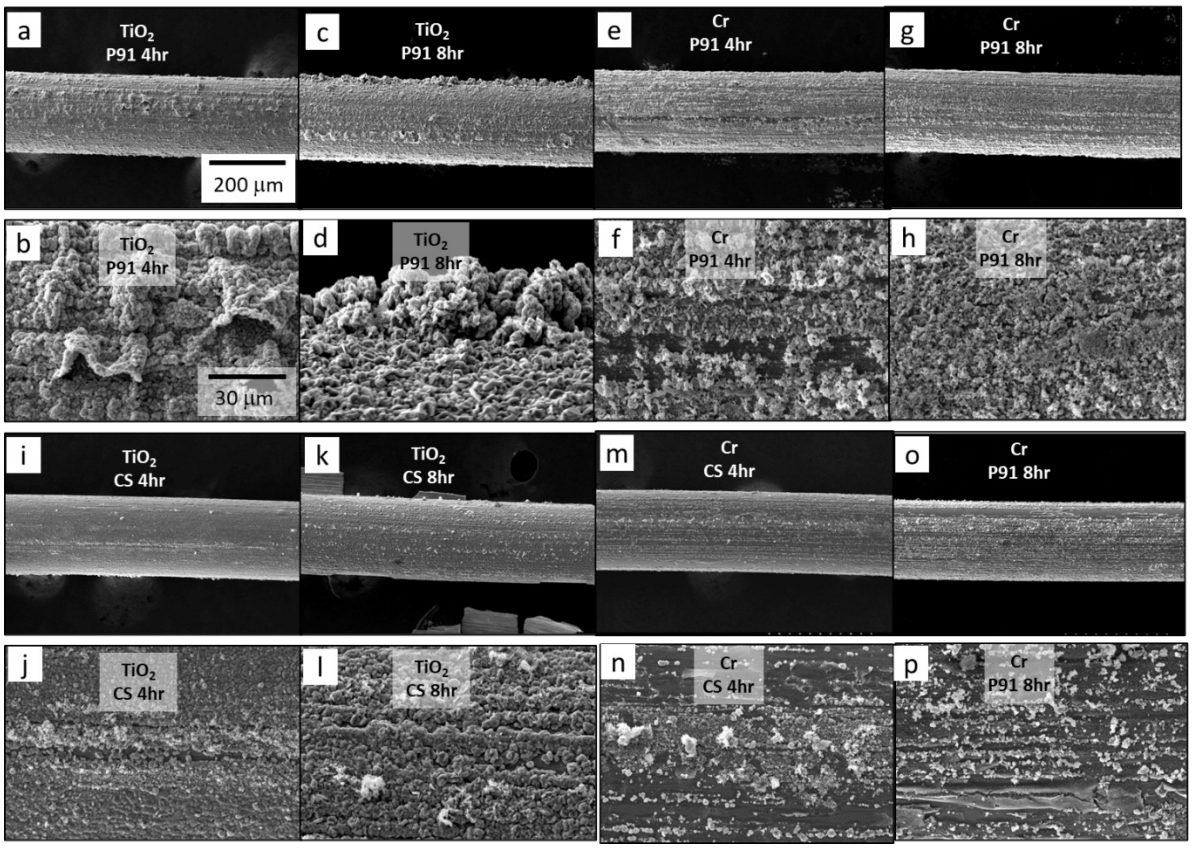

Figure 7.8 SEM micrographs of (a-h) P91 and (i-p) carbon steel wire surfaces with 50 nm of TiO2 and Cr after 4 and 8 hours of fouling, as indicated.

The data agrees with the trends that have been discussed thus far, however some additional and interesting phenomena emerge. The morphology of the sulfide corrosion product becomes a function of the coating material. Examining the P91 wires in Figures 7.7 and 7.8, we can see marked differences in the morphology of the surface sulfide crystals. These differences suggest different phases of iron sulfide. Of the many forms of iron sulfide, the two most commonly observed at these conditions are pyrite (FeS_2) and pyrrhotite ($Fe_{(1-x)}S$). Pyrite has a cubic crystal structure, while pyrrhotite is hexagonal. Pyrrhotite formation often dominants when strong interactions of the sulfide with coke forming molecules, and sulfur heteroatoms are present. Also, the interdiffusion of iron and H_2S, and the addition and removal of sulfur to the iron sulfide lattice results in a sub-stoichiometric sulfide with a high defect density (pyrrhotite).

Considering the samples that were fouled for 8 hours, the crystals that form on the Cr_2O_3 and TiO_2 coated wires appear to be blockier, while those that form on the Al_2O_3 and chromium coated wires appear more spherical or hexagonal. Similar results are observed on the carbon steel wires, although the particle size of the iron sulfide appears to be slightly smaller. Cr_2O_3 and Al_2O_3 share a corundum structure, which is described as a hexagonal close packed array of oxygen anions with 2/3 of the octahedral holes filled by the respective metal cations. The most common forms of TiO_2, rutile and anatase, share a tetragonal structure. However, the changing sulfide morphology does not appear to correlate with the changing crystal structure of the coating since blocky sulfide is observed on the corundum and tetragonal phases. The identity of the coating does seem to have some effect on the phase of the iron sulfide that forms, although the mechanism remains to be conclusively revealed.

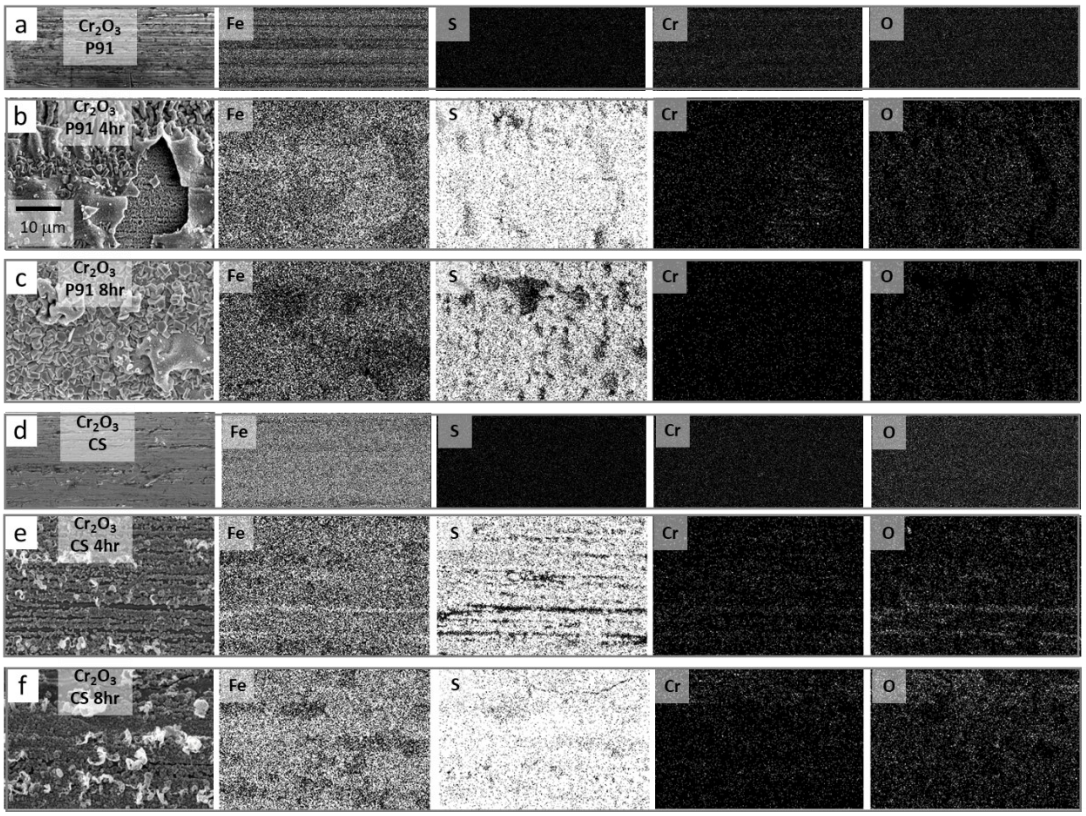

Figure 7.9 SEM micrographs and EDX elemental maps of (a-c) P91 and (d-f) carbon steel surfaces with 50 nm of Cr2O3. Figures (a,d) are coated wires, prior to fouling, and (b,e) are wires after 4 hours fouling, and (c,f) after 8 hours of fouling.

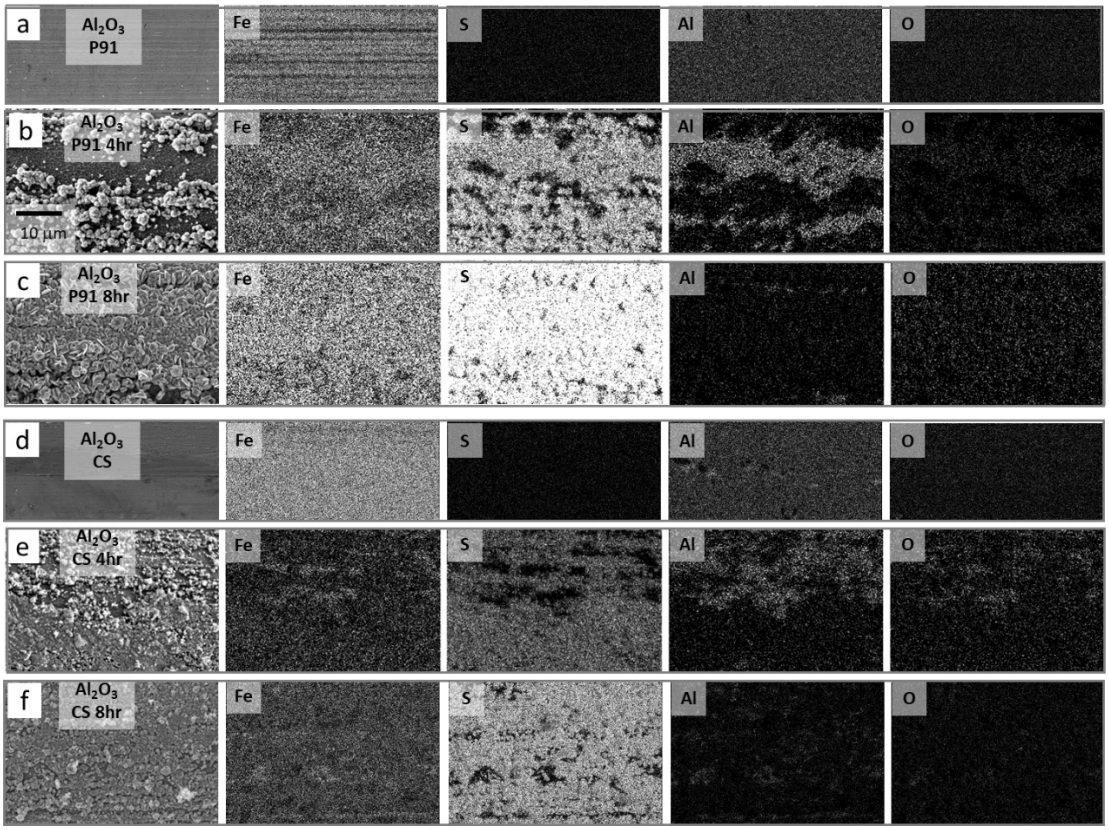

Figure 7.10 SEM micrographs and EDX elemental maps of P91 and carbon steel surfaces with 50 nm of Al2O3. Figures (a,d) are coated wires, prior to fouling, and (b,e) are wires after 4 hours fouling, and (c,f) after 8 hours of fouling.

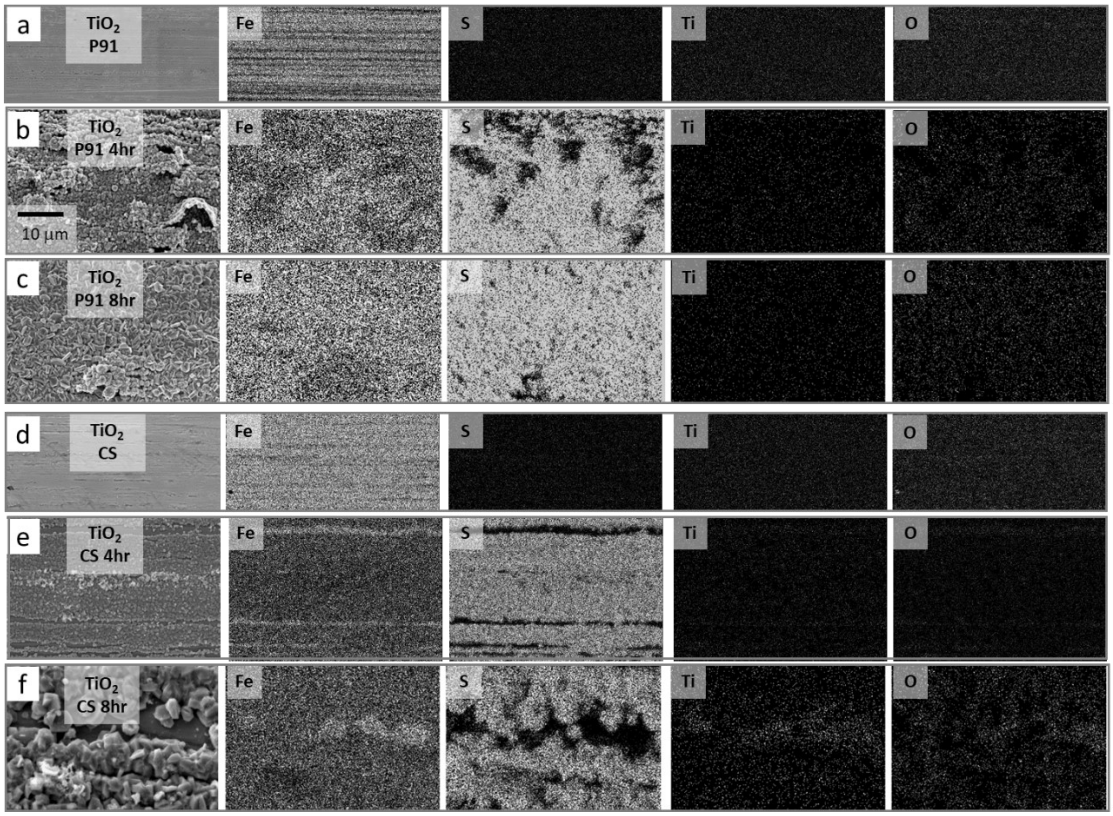

Figure 7.11 SEM micrographs and EDX elemental maps of P91 and carbon steel surfaces with 50 nm of TiO2. Figures (a,d) are coated wires, prior to fouling, and (b,e) are wires after 4 hours fouling, and (c,f) after 8 hours of fouling.

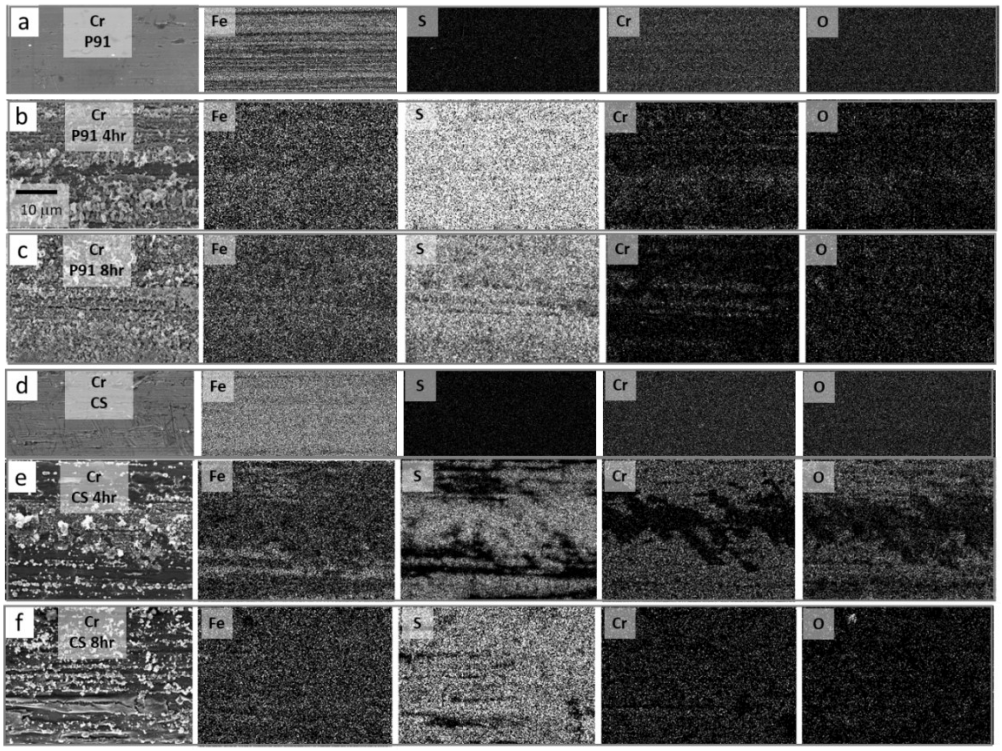

Figure 7.12 SEM micrographs and EDX elemental maps of P91 and carbon steel surfaces with 50 nm of Cr. Figures (a,d) are coated wires, prior to fouling, and (b,e) are wires after 4 hours fouling, and (c,f) after 8 hours of fouling.

In Figures 7.9-7.12, EDX elemental maps of un-fouled wire samples are presented above their fouled counterparts, for comparison. Consistent with previous observations, the P91 wires coated with Cr metal appear to have developed the least amount of surface foulant, with the smallest particle size. Referring to the EDX elemental maps for P91 and carbon steel, we can see that evidence of the respective coating was detected prior to fouling, and that iron sulfide was detected on the surface of all fouled samples. From a comparison of the 4- and 8-hour samples, we can see that the amount of surface sulfide continuously develops as expected. For many of the coated samples (and particularly for the carbon steel samples fouled for 4 hours), we can see a semi-continuous layer of sulfide, and areas that appear not to have sulfided. In these areas, EDX elemental maps reveal evidence of oxide, and these oxidized regions commonly correlate with surface striations on the wire left over from wire drawing. Gibbs free energy calculations from Table 4 reveal that the oxidation of iron to Fe_2O_3 is still favorable at the reactor conditions. However, these oxide regions are likely remnants of the original surface oxide that have not undergone conversion to a sulfide, whose stability would have been promoted by the presence of water in the reactor. While there is a strong driving force for the sulfidation of iron oxide, we expect this to be a secondary reaction relative to the sulfidation of iron metal, which is more favorable in the reactor environment.

7.3 Summary and Conclusions

Three metallic oxides and pure Cr metal were deposited to 50 nm thickness on P91 and carbon steel wires. Their effectiveness towards reducing fouling and corrosion was limited in this initial design and screenings. It is expected that the ineffectiveness of the reactively sputtered oxide coatings is a function of their poor adhesion to the substrates they were deposited on. The pure Cr metal performed better and was not reactively sputtered. This observation is meaningful as it suggests that the sophistication of the coating process is essential to its success as an anti-fouling mechanism. Quality coatings have been deposited by magnetron sputtering, but unfortunately, they are typically highly stressed. Thin ceramic coatings often retain a columnar grain structure with resulting high residual stresses, micro cracks, transient grain boundaries, and through-coating porosity, which all

lead to accelerated corrosion and failure at the coating/substrate interface, especially in hostile environments.[9] The microstructural stability and recrystallization of the underlying, highly textured wire substrates will further stress the overlying coating, causing bonding issues, while at temperature, during fouling experiments.

Progressive improvements to this research should include both analytical work, to understand the coating chemistry and stress states, and apply that knowledge effectively to coating design. Progressive analytical work will include XRD to identify phases and stresses amongst the coatings pre- and post- fouling, as well as nano-indentation for measuring toughness. Preparation of the wires prior to sputtering will include plasma cleaning and systematic pre-coating heat treatment to relax the substrate microstructure. The application of multilayer films, especially using Cr metal as an interlayer between the base metal and the oxides will be employed. This will help with bonding, for one, by relaxing coating stress. Reactively sputtered nitride coatings and intermetallics of Al and Ti will also be explored.

7.4 References

(1) Symoens, S. H.; Olahova, N.; Munoz Gandarillas, A. E.; Karimi, H.; Djokic, M. R.; Reyniers, M. F.; Marin, G. B.; Van Geem, K. M. *Ind. Eng. Chem. Res.* **2018**, *57* (48), 16117–16136.

(2) Xu, X. Q.; Miao, J.; Bai, Z. Q.; Feng, Y. R.; Ma, Q. R.; Zhao, W. Z. *Appl. Surf. Sci.* **2012**, *258* (22), 8802–8806.

(3) Rocha, A. da C.; Rizzo, F.; Zeng, C.; Paes, M. P. *Mater. Res.* **2004**, *7* (1), 189–194.

(4) Bischoff, C.; Poulsen, T.; Losada, R.; Mortensen, J. O.; Jackowski, L.; Taylor, S. T. *Int. Conf. Heat Exch. Fouling Clean.* **2015**, *2015*, 325–327.

(5) Santos, O.; Anehamre, J.; Wictor, C.; Tornqvist, A.; Nilsson, M. *Int. Conf. Heat Exch. Fouling Clean.* **2013**, *2013* (Dlc), 79–84.

(6) Schütze, M.; Malessa, M.; Rohr, V.; Weber, T. *Surf. Coatings Technol.* **2006**, *201* (7 SPEC. ISS.), 3872–3879.

(7) Schütze, M. *Corrosion* **2007**, *63* (1), 4–18.

(8) Pinzón, A. V.; Urrego, K. J.; González-Hernández, A.; Rincón Ortiz, M.; Vargas Galvis, F. *Ceram. Int.* **2018**, *44* (17), 21765–21773.

(9) Pang, X.; Gao, K.; Yang, H.; Qiao, L.; Wang, Y.; Volinsky, A. A. *Adv. Eng. Mater.* **2007**, *9* (7), 594–599.

(10) Medvedovski, E.; Mendoza, G. L.; Rzad, E.; Solecka, M.; Dudziak, T. P. *Surf. Coatings Technol.* **2020**, *403* (September), 126430.

(11) Pandey, C.; Giri, A.; Mahapatra, M. M. *Mater. Sci. Eng. A* **2016**, *664*, 58–74.

(12) Lazar, A. M.; Yespica, W. P.; Marcelin, S.; Pébère, N.; Samélor, D.; Tendero, C.; Vahlas, C. *Corros. Sci.* **2014**, *81*, 125–131.

(13) Pang, X.; Gao, K.; Luo, F.; Emirov, Y.; Levin, A. A.; Volinsky, A. A. *Thin Solid Films* **2009**, *517* (6), 1922–1927.

(14) Teng, Y.; Guo, Y. Y.; Zhang, M.; Yang, Y. J.; Huang, Z.; Zhou, Y. W.; Wu, F. Y.; Liang, Y. S. *Surf. Coatings Technol.* **2019**, *367* (March), 100–107.

(15) P, D. *CRC Handbook of Chemistry and Physics*; CRC press, 1992; Vol. 268.

(16) O'Hare, P. A. G.; Johnson, G. K. *J. Chem. Thermodyn.* **1986**, *18* (2), 189–199.

(17) Oikawa, K.; Mitsui, H.; Ohtani, H.; Ishida, K. *ISIJ Int.* **2000**, *40* (2), 182–190.

(18) Narita, T.; Ishikawa, T.; Nishida, K. *Oxid. Met.* **1987**, *27* (3–4), 221–237.

CONCLUDING REMARKS

In this research, a temporal sequence of corrosion then fouling was comprehensively documented by applying detailed analysis of the fouling surface over time and throughout a broad range of test conditions.

Experiments were conducted with five diverse crude oil feedstocks, important within industrial applications and with three representative metallurgies: carbon steel, P91 (a 9wt% Cr – 1wt% Mo) alloy steel, and 347SS (347 stainless-steel). The steels were immersed in 150°C to 290°C oil, with their surface temperatures spanning 300°C up to 490°C. Largely, two combinations of temperatures were utilized to contrast fouling behavior above and below thermal cracking. Low temperature fouling was conducted with wire and oil temperatures of 350°C and 250°C, and high temperature conditions consisted of 490°C wire temperature and 290°C oil temperature.

In all cases, fouling followed an identical sequence of events, beginning with sulfidation at the wire-oil interface, then forming or attracting organic, carbonaceous foulant. An iron sulfide (pyrrhotite Fe(1-x)S) corrosion product formed almost instantaneously at the metal surfaces. This initial sulfidation event was followed, by varying degree with accumulation of organic or mixed-layer foulant. Fouling rates and retention were a strong function of metallurgy. The P91 wire fouled more versus carbon steel in all cases, which was attributed to strength and toughness of the fouling interface and consistent delamination ("self-cleaning") of the carbon steel. In all scenarios the 347SS wire fouled and corroded less than the other metallurgies and was virtually immune in the low temperature environments.

In high temperature experiments metallic sulfides were aggressively ejected from the fouling surface and were interspersed with coke and pitch in 9 to 30 μm thick layers after only 60 minutes of exposure. In low temperature experiments the sulfidation was less aggressive and different for each metallurgy: (1) 347SS was nearly immune, up to 8 hours of exposure; (2) carbon steel developed a bilayer corrosion film that extended internally and externally from the original wire surface, then

delaminated and formed a dense uniform layer; and (3) P91 developed plume-structured metallic sulfides that considerably roughened the wire surface and promoted wetting and trapping of particulates from the surrounding oil. Also identified at low temperature was that the wire fouled non-uniformly along its length, exhibiting large deposits of carbonaceous foulant near ends connected to the probes, where flow was disturbed/stagnant. These were easily removed and largely soluble in toluene.

The addition of iron-napthenate introduced trends to the fouling behavior, but a full mechanistic understanding requires further investigation. Under high temperature conditions, carbon steel fouled without additive and was completely free of any resolvable foulant when the additive was present. P91 fouled to similar thickness with and without the additive, but with marked different morphology. With additive, fouling was predominately organic / mixed particulate fouling, while without additive, the foulant was completely comprised of FeS corrosion product. This suggests a corrosive mechanism at the wire surface by naphthenic acid, which would compete and dissolve the FeS corrosion product. In low temperature experiments, trends were very weak, and experiments had to run for up to 48 hours to detect even small amounts of fouling. Depositional fouling was observed on the carbon steel wire when additive was present, and no trend was discernable with P91.

REFERENCES

Chapter 1

(1) Petroleum, B. *BP Stat. Rev. World Energy* **2016**, No. June, 1–48.

(2) Papavinasam, S. *Corrosion Control in the Oil and Gas Industry*; 2014.

(3) Bott, T. R. *Fouling of Heat Exchangers*; Elsevier B.V.: Amsterdam, The Netherlands, 2005.

(4) Coletti, F.; Hewitt, G. F. *Crude Oil Fouling*; 2015.

(5) Diaz-Bejarano, E.; Behranvand, E.; Coletti, F.; Mozdianfard, M. R.; Macchietto, S. *Appl. Energy* **2017**, *206* (September), 1250–1266.

(6) Statista 2017. https://www.statista.com/statistics/273579/countries-with-the-largest-oil-refinery-capacity/.

(7) Gary, J. H.; Handwerk, G. E.; Kaiser, M. J. *Petroleum Refining: Technology and Economics*, 5th ed.; CRC Press/Taylor and Francis: New York, NY, 2005.

(8) Deshannavar, U. B.; Rafeen, M. S.; Ramasamy, M.; Subbarao, D. *Journal of Applied Sciences*. 2010, pp 3167–3174.

(9) Macchietto, S.; Hewitt, G. F.; Coletti, F.; Crittenden, B. D.; Dugwell, D. R.; Galindo, A.; Jackson, G.; Kandiyoti, R.; Kazarian, S. G.; Luckham, P. F.; Matar, O. K.; Millan-Agorio, M.; Müller, E. A.; Paterson, W.; Pugh, S. J.; Richardson, S. M.; Wilson, D. I. *Heat Transf. Eng.* **2011**, *32* (3–4), 197–215.

(10) Coletti, F.; MacChietto, S. *Ind. Eng. Chem. Res.* **2011**, *50* (8), 4515–4533.

(11) Kekäläinen, T.; Pakarinen, J. M. H.; Wickström, K.; Lobodin, V. V.; McKenna, A. M.; Jänis, J. *Energy & Fuels* **2013**, *27* (4), 2002–2009.

(12) Ho, T. C. *Int. J. Heat Mass Transf.* **2016**, *95*, 62–68.

(13) Coletti, F.; Hewitt, G. *Crude Oil Fouling: Deposit Characterization, Measurements, and Modeling*; Elsevier Science, 2014.

(14) Epstein, N. *Heat Transf. Eng.* **1983**, *4* (1), 43–56.

(15) Wiehe, I. A. *Process Chemistry of Petroleum Macro Molecules*, Vol. 121.; CRC Press: Boca Raton, FL, 2008.

(16) Wang, W.; Watkinson, A. P. *Proc. Int. Conf. Heat Exch. Fouling Clean. IX* **2011**, 23–30.

(17) Stephenson, T.; Kubis, A.; Derakhshesh, M.; Hazelton, M.; Holt, C.; Eaton, P.; Newman, B.; Hoff, A.; Gray, M.; Mitlin, D. *Energy and Fuels* **2011**, *25* (10).

(18) Stephenson, T.; Hazelton, M.; Kupsta, M.; Lepore, J.; Andreassen, E. J.; Hoff, A.; Newman, B.; Eaton, P.; Gray, M.; Mitlin, D. *Fuel* **2015**, *139*.

Chapter 2

(1) Speight, J. G. *Fouling in refineries*; Gulf Professional Publishing, 2015.

(2) Mozdianfard, M. R.; Behranvand, E. In *Applied Thermal Engineering*; 2013; Vol. 50, pp 908–917.

(3) Tay, F. H.; Kazarian, S. G. *Energy and Fuels* **2009**, *23* (8), 4059–4067.

(4) Deshannavar, U. B.; Rafeen, M. S.; Ramasamy, M.; Subbarao, D. *Journal of Applied Sciences*. 2010, pp 3167–3174.

(5) Wang, W.; Watkinson, a. P. *Heat Transf. Eng.* **2015**, *36* (7–8), 623–631.

(6) Ebrahimi, S.; Moghaddas, J. S.; Aghjeh, M. K. R. *Fuel* **2008**, *87* (8–9), 1623–1627.

(7) Gentzis, T.; Parker, R. J.; McFarlane, R. A. *Fuel* **2000**, *79* (10), 1173–1184.

(8) Wang, W.; Watkinson, A. P. *Proc. Int. Conf. Heat Exch. Fouling Clean. IX* **2011**, 23–30.

(9) Bennett, C. a.; Kistler, R. S.; Nangia, K.; Al-Ghawas, W.; Al-Hajji, N.; Al-Jemaz, A. *Heat Transf. Eng.* **2009**, *30* (10–11), 794–804.

(10) Morales-Fuentes, A.; Picón-Núñez, M.; Polley, G. T.; Méndez-Díaz, S. *Appl. Therm. Eng.* **2014**, *62* (2), 777–784.

(11) Coletti, F.; MacChietto, S. *Ind. Eng. Chem. Res.* **2011**, *50* (8), 4515–4533.

(12) Fan, Z.; Rahimi, P.; McGee, R.; Wen, Q.; Alem, T. *Energy and Fuels* **2010**, *24* (11), 6110–6118.

(13) Lestina, T. G.; Zettler, H. U. *Heat Transf. Eng.* **2014**, *35* (3), 217–223.

(14) P. Watkinson, A. In *Heat Exchanger Fouling and Cleaning: Fundamentals and Applications*; 2004.

(15) Yang, M.; Wood, Z.; Rickard, B.; Crittenden, B.; Gough, M.; Droegemueller, P.; Higley, T. *Appl. Therm. Eng.* **2013**, *54* (2), 516–520.

(16) Aminian, J.; Shahhosseini, S. *Int. Commun. Heat Mass Transf.* **2009**, *36* (5), 525–531.

(17) Polley, G. T.; Wilson, D. I.; Yeap, B. L.; Pugh, S. J. In *Applied Thermal Engineering*; 2002; Vol. 22, pp 777–788.

(18) Petkovic, B.; Watkinson, P. *Heat Transf. Eng.* **2013**, *35* (3), 302–310.

(19) Derakhshesh, M.; Eaton, P.; Newman, B.; Hoff, A.; Mitlin, D.; Gray, M. R. In *Energy and Fuels*; 2013; Vol. 27, pp 1856–1864.

(20) Derakhshesh, M. *ProQuest Diss. Theses Glob.* **2012**.

(21) Stephenson, T.; Kubis, A.; Derakhshesh, M.; Hazelton, M.; Holt, C.; Eaton, P.; Newman, B.; Hoff, A.; Gray, M.; Mitlin, D. *Energy and Fuels* **2011**, *25* (10), 4540–4551.

(22) Stephenson, T.; Hazelton, M.; Kupsta, M.; Lepore, J.; Andreassen, E. J.; Hoff, A.; Newman, B.; Eaton, P.; Gray, M.; Mitlin, D. *Fuel* **2015**, *139*, 411–424.

(23) Trejo, F.; Centeno, G.; Ancheyta, J. *Fuel* **2004**, *83* (16), 2169–2175.

(24) Ávila, B. M. F.; Pereira, V. B.; Gomes, A. O.; Azevedo, D. A. *Fuel* **2014**, *126*, 188–193.

(25) Rogel, E.; Ovalles, C.; Moir, M. In *Energy and Fuels*; 2012; Vol. 26, pp 2655–2662.

(26) Kekäläinen, T.; Pakarinen, J. M. H.; Wickström, K.; Lobodin, V. V.; McKenna, A. M.; Jänis, J. *Energy & Fuels* **2013**, *27* (4), 2002–2009.

(27) Ho, T. C. *Int. J. Heat Mass Transf.* **2016**, *95*, 62–68.

(28) Stratiev, D.; Shishkova, I.; Nedelchev, A.; Kirilov, K.; Nikolaychuk, E.; Ivanov, A.; Sharafutdinov, I.; Veli, A.; Mitkova, M.; Tsaneva, T.; Petkova, N.; Sharpe, R.; Yordanov, D.; Belchev, Z.; Nenov, S.; Rudnev, N.; Atanassova, V.; Sotirova, E.; Sotirov, S.; Atanassov, K. *Energy and Fuels* **2015**, *29* (12), 7836–7854.

(29) ASTM. *ASTM Stand.* **2016**, 1–43.

(30) ASTM. *Pet. Prod. Lubr. Foss. Fuels* **2013**, *05*, 1–6.

(31) Wang, J.; Buckley, J. S. *Energy and Fuels* **2003**, *17* (6), 1445–1451.

(32) Mousavi, M.; Abdollahi, T.; Pahlavan, F.; Fini, E. H. *Fuel* **2016**, *183*, 262–271.

(33) Ashoori, S.; Sharifi, M.; Masoumi, M.; Mohammad Salehi, M. *Egypt. J. Pet.* **2017**, *26* (1), 209–213.

(34) Somerscales, E. F. C. *Exp. Therm. Fluid Sci.* **1997**, *14* (4), 335–355.

(35) Watkinson, a. P. *Heat Transf. Eng.* **2007**, *28* (January 2015), 177–184.

(36) Watkinson, A. P.; Wilson, D. I. *Exp. Therm. Fluid Sci.* **1997**, *14* (4), 361–374.

(37) Wiehe, I. A. *Process Chemistry of Petroleum Macro Molecules*, Vol. 121.; CRC Press: Boca Raton, FL, 2008.

(38) Wiehe, I. A. In *Energy and Fuels*; 2012; Vol. 26, pp 4004–4016.

(39) Painter, P.; Veytsman, B.; Youtcheff, J. *Energy & Fuels* **2015**, *29* (5), 2951–2961.

(40) Forte, E.; Taylor, S. E. *Adv. Colloid Interface Sci.* **2015**, *217*, 1–12.

(41) Coletti, F.; Hewitt, G. F. *Crude Oil Fouling*; 2015.

(42) Schabron, J. F.; Pauli, A. T.; Rovani, J. F.; Miknis, F. P. *Fuel* **2001**, *80* (10), 1435–1446.

(43) Souza, B. A.; Matos, E. M.; Guirardello, R.; Nunhez, J. R. *J. Pet. Sci. Eng.* **2006**, *51* (1–2), 138–148.

(44) Wiehe, I. A. *Ind. Eng. Chem. Res* **1993**, *32*, 2447–2454.

(45) Rebak, R. B. *Corrosion Reviews*. 2011, pp 123–133.

(46) Slavcheva, E.; Shone, B.; Turnbull, A. *Br. Corros. J.* **1999**, *34* (2), 125–131.

(47) Huang, B. S.; Yin, W. F.; Sang, D. H.; Jiang, Z. Y. *Appl. Surf. Sci.* **2012**, *259*, 664–670.

(48) Qu, D. R.; Zheng, Y. G.; Jing, H. M.; Yao, Z. M.; Ke, W. *Corros. Sci.* **2006**, *48* (8), 1960–1985.

(49) Tavakkoli, M.; Panuganti, S. R.; Vargas, F. M.; Taghikhani, V.; Pishvaie, M. R.; Chapman, W. G. *Energy & Fuels* **2014**, *28* (3), 1617–1628.

(50) Tavakkoli, M.; Panuganti, S. R.; Taghikhani, V.; Pishvaie, M. R.; Chapman, W. G. *Energy and Fuels* **2014**, *28* (6), 3594–3603.

(51) Seifried, C. M.; Crawshaw, J.; Boek, E. S. In *Energy and Fuels*; 2013; Vol. 27, pp 1865–1872.

(52) Bennett, C. A. *Heat Transf. Eng.* **2012**, *33* (15), 1246–1250.

(53) Mullins, O. C. *Annu. Rev. Anal. Chem. (Palo Alto. Calif).* **2011**, *4*, 393–418.

(54) Adams, J. J. *Energy and Fuels*. 2014, pp 2831–2856.

(55) Leyva, C.; Ancheyta, J.; Berrueco, C.; Millán, M. *Fuel Process. Technol.* **2013**, *106*, 734–738.

(56) Gabrienko, A. A.; Lai, C. H.; Kazarian, S. G. *Energy and Fuels* **2014**, *28* (2), 964–971.

(57) Guisnet, M.; Magnoux, P. *Appl. Catal. A Gen.* **2001**, *212* (1–2), 83–96.

(58) Alvarez, E.; Marroquín, G.; Trejo, F.; Centeno, G.; Ancheyta, J.; Díaz, J. A. I. *Fuel* **2011**, *90* (12), 3602–3607.

(59) Hsieh, P. Y.; Bruno, T. J. In *Energy and Fuels*; 2014; Vol. 28, pp 1868–1883.

(60) Müller, A. L. H.; Picoloto, R. S.; Mello, P. D. A.; Ferrão, M. F.; Dos Santos, M. D. F. P.; Guimarães, R. C. L.; Müller, E. I.; Flores, E. M. M. *Spectrochim. Acta - Part A Mol. Biomol. Spectrosc.* **2012**, *89*, 82–87.

(61) Yépez, O. *Fuel* **2005**, *84* (1), 97–104.

(62) Qu, D. R.; Zheng, Y. G.; Jing, H. M.; Jiang, X.; Ke, W. *Mater. Corros.* **2005**, *56* (8), 533–541.

(63) Jin, P.; Robbins, W.; Bota, G. *Corros. Sci.* **2018**, *131*, 223–234.

(64) Groysman, A. *Top. Safety, Risk, Reliab. Qual.* **2017**, *32*, 37–99.

(65) Rowland, S. J.; Scarlett, A. G.; Jones, D.; West, C. E.; Frank, R. A. *Environ. Sci. Technol.* **2011**, *45* (7), 3154–3159.

(66) Parisotto, G.; Ferrão, M. F.; Müller, A. L. H.; Müller, E. I.; Santos, M. F. P.; Guimarães, R. C. L.; Dias, J. C. M.; Flores, È. M. M. *Energy and Fuels* **2010**, *24* (10), 5474–5478.

(67) Chakravarti, R.; Patrick, B. N.; Barney, M.; Kusinski, G.; Devine, T. M. *Energy & Fuels* **2013**, *27* (12), 7905–7914.

(68) Flego, C.; Galasso, L.; Montanari, L.; Gennaro, M. E. In *Energy and Fuels*; 2014; Vol. 28, pp 1701–1708.

(69) Jin, P.; Bota, G.; Robbins, W.; Nesic, S. *Energy and Fuels* **2016**, *30* (8), 6853–6862.

(70) Jin, P.; Nesic, S.; Wolf, H. A. *Surf. Interface Anal.* **2015**, *47* (4), 454–465.

(71) Xiaofei, Z.; Tao, M.; Xiaochun, H.; Jinde, Z.; Xiaoyi, W.; Sixian, R. *Eng. Fail. Anal.* **2020**, *117*, 104802.

(72) Bai, P.; Zheng, S.; Zhao, H.; Ding, Y.; Wu, J.; Chen, C. *Corros. Sci.* **2014**, *87*, 397–406.

(73) American Petroleum Institute. *API Recomm. Pract. 939* **2008**.

(74) Wang, H.; Salveson, I. *Phase Transitions* **2005**, *78* (7–8), 547–567.

(75) Gray, M. R.; Ayasse, A. R.; Chan, E. W.; Veljkovic, M. *Energy & Fuels* **1995**, *9* (7), 500–506.

(76) Lepore, J. The Role of Sulfur Species in Establishing the Corrosion Reactions in Refinery Metallurgies, University of Alberta, 2016.

(77) Mrowec, S.; Walec, T.; Werber, T. *Oxid. Met.* **1969**, *1* (1), 93–120.

(78) El Kamel, M.; Galtayries, A.; Vermaut, P.; Albinet, B.; Foulonneau, G.; Roumeau, X.; Roncin, B.; Marcus, P. *Surf. Interface Anal.* **2010**, *42* (6–7), 605–609.

(79) Bai, Z. S.; Wang, H. L. *Chem. Eng. Res. Des.* **2007**, *85* (12 A), 1586–1590.

(80) Vafajoo, L.; Ganjian, K.; Fattahi, M. *J. Pet. Sci. Eng.* **2012**, *90–91*, 107–111.

(81) Álvarez, P.; Menendez, J. L.; Berrueco, C.; Rostani, K.; Millan, M. *Fuel Process. Technol.* **2012**, *96*, 16–21.

(82) Mendoza De La Cruz, J. L.; Cedillo-Ramírez, J. C.; Aguirre-Gutiérrez, A. D. J.; García-Sánchez, F.; Aquino-Olivos, M. A. *Energy and Fuels* **2015**, *29* (2), 480–487.

(83) E, H.; Watkinson, A. P. *Heat Transf. Eng.* **2009**, *30* (10–11), 786–793.

(84) Mena-Cervantes, V. Y.; Hernández-Altamirano, R.; Buenrostro-González, E.; Beltrán, H. I.; Zamudio-Rivera, L. S. *Fuel* **2013**, *110*, 293–301.

(85) Mena-Cervantes, V. Y.; Hernández-Altamirano, R.; Buenrostro-González, E.; Beltrán, H. I.; Zamudio-Rivera, L. S. *Energy and Fuels* **2011**, *25* (1), 224–231.

(86) Rogel, E. *Energy and Fuels* **2011**, *25* (2), 472–481.

(87) Towfighi, J.; Sadrameli, M.; Niaei, A. *J. Chem. Eng. Japan* **2002**, *35* (10), 923–937.

(88) Wang, J.; Reyniers, M. F.; Van Geem, K. M.; Marin, G. B. *Ind. Eng. Chem. Res.* **2008**, *47* (5), 1468–1482.

(89) Wang, J.-Q.; Li, M.; Li, S.-F.; Li, C.; Que, G.-H. *Ranliao Huaxue Xuebao/Journal Fuel Chem. Technol.* **2006**, *34* (1).

(90) Russell, C. A.; Crozier, S.; Sharpe, R. *Energy and Fuels* **2010**, *24* (10), 5483–5492.

(91) Habib, F. K.; Diner, C.; Stryker, J. M.; Semagina, N.; Gray, M. R. *Energy and Fuels* **2013**, *27* (11), 6637–6645.

(92) Zachariah, A.; Wang, L.; Yang, S.; Prasad, V.; De Klerk, A. *Energy and Fuels* **2013**, *27* (6), 3061–3070.

(93) Speight, J. G. *Oil and Gas Corrosion Prevention*; 2014.

(94) El Kamel, M.; Galtayries, A.; Albinet, B.; Foulonneau, G.; Roumeau, X.; Roncin, B.; Marcus, P. In *European Corrosion Congress 2009, EUROCORR 2009*; 2009; Vol. 6, pp 3591–3608.

(95) Li, H.; Chen, W. *Oxid. Met.* **2012**, *78* (1–2), 103–122.

(96) Li, H.; Chen, W. *Oxid. Met.* **2012**, *77* (3–4), 107–127.

(97) Rojas, D.; Garcia, J.; Prat, O.; Sauthoff, G.; Kaysser-Pyzalla, A. R. *Mater. Sci. Eng. A* **2011**, *528* (15), 5164–5176.

(98) Hucin, J. *Mater. Corros.* **2000**, *176*, 173–176.

(99) Moura, L. B.; Guimarães, R. F.; Abreu, H. F. G. De; Miranda, H. C. De; Tavares, S. S. M. *Mater. Res.* **2012**, *15* (2), 277–284.

(100) Sixian, R.; Yu, Z.; Ziwei, P.; Yuwan, C.; Xuedong, C. *Mater. Corros.* **2014**, *65* (6), 619–625.

(101) ASM International. *ASM Metals Handbook Vol.01, Properties and Selection: Irons, Steels, and High-Performance Alloys*; 1991.

(102) Ohmi, T.; Nakagawa, Y.; Nakamura, M.; Ohki, A.; Koyama, T. *J. Vac. Sci. Technol. A* **1996**, *14* (4), 2505–2510.

(103) Young, D. *High Temperature Oxidation and Corrosion of Metals*; 2015; Vol. 1.

(104) Ramachandran, D.; Egoavil, R.; Crabbe, A.; Hauffman, T.; Abakumov, A.; Verbeeck, J.; Vandendael, I.; Terryn, H.; Schryvers, D. *J. Microsc.* **2016**, *264* (2), 207–214.

(105) Ramesh, M.; Leber, H. J.; Janssens, K. G. F.; Diener, M.; Spolenak, R. *Int. J. Fatigue* **2011**, *33* (5), 683–691.

(106) Tomio, A.; Sagara, M.; Doi, T.; Amaya, H.; Otsuka, N.; Kudo, T. *Corros. Sci.* **2015**, *98*, 391–398.

(107) Broutin, P.; Ropital, F.; Reyniers, M. F.; Froment, G. F. *Oil Gas Sci. Technol.* **1999**, *54* (3), 375–385.

(108) Tang, S.; Hu, S.; Zhang, Y.; Wang, J.; Zhu, Q.; Chen, Y.; Li, X. *J. Anal. Appl. Pyrolysis* **2014**, *107*, 197–203.

(109) Tang, S.; Gao, S.; Hu, S.; Wang, J.; Zhu, Q.; Chen, Y.; Li, X. *Ind. Eng. Chem. Res.* **2014**, *53* (13), 5432–5442.

(110) Tang, S.; Wang, J.; Zhu, Q.; Chen, Y.; Li, X. *ACS Appl. Mater. Interfaces* **2014**, *6* (19), 17157–17165.

(111) Li, C. S.; Yang, Y. S. *Surf. Coatings Technol.* **2004**, *185* (1), 68–73.

(112) Coletti, F.; Macchietto, S. *Ind. Eng. Chem. Res.* **2011**, *50* (8), 4515–4533.

(113) Polley, G. T.; Wilson, D. I.; Yeap, B. L.; Pugh, S. J. In *Applied Thermal Engineering*; 2002; Vol. 22, pp 763–776.

(114) Sadrameli, S. M. *Fuel*. 2016, pp 285–297.

(115) Moro-oka, Y. *Appl. Catal. A Gen.* **1999**, *181* (2), 323–329.

(116) Breysse, M.; Furimsky, E.; Kasztelan, S.; Lacroix, M.; Perot, G. *Catal. Rev.* **2002**, *44* (4), 651–735.

(117) Rana, M. S.; Ancheyta, J.; Sahoo, S. K.; Rayo, P. In *Catalysis Today*; 2014; Vol. 220–222, pp 97–105.

(118) Absi-Halabi, M.; Stanislaus, A.; Trimm, D. L. *Applied Catalysis*. 1991, pp 193–215.

(119) Bao, B.; Liu, J.; Xu, H.; Liu, B.; Zhang, W. *RSC Adv.* **2016**, *6* (73), 68934–68941.

(120) Mu??oz Gandarillas, A. E.; Van Geem, K. M.; Reyniers, M. F.; Marin, G. B. *Ind. Eng. Chem. Res.* **2014**, *53* (15), 6358–6371.

(121) Jazayeri, S. M.; Karimzadeh, R. *Energy and Fuels* **2011**, *25* (10), 4235–4247.

(122) Tan, C. D.; Baker, R. T. K. *Catal. Today* **2000**, *63* (1), 3–20.

(123) El Kamel, M.; Galtayries, A.; Vermaut, P.; Albinet, B.; Foulonneau, G.; Roumeau, X.; Roncin, B.; Marcus, P. In *Surface and Interface Analysis*; 2010; Vol. 42, pp 605–609.

Chapter 3

(1) Wiehe, I. A. *Process Chemistry of Petroleum Macro Molecules*, Vol. 121.; CRC Press: Boca Raton, FL, 2008.

(2) Derakhshesh, M.; Eaton, P.; Newman, B.; Hoff, A.; Mitlin, D.; Gray, M. R. In *Energy and Fuels*; 2013; Vol. 27, pp 1856–1864.

(3) Chandra, K.; Kain, V.; Tewari, R. *Corros. Sci.* **2013**, *67*, 118–129.

(4) Wang, H.; Du, H.; Wei, Y.; Hou, L.; Liu, X.; Wei, H.; Liu, B.; Jia, J. *Steel Res. Int.* **2021**, *92* (2), 1–12.

(5) Zhou, Y.; Liu, Y.; Zhou, X.; Liu, C.; Yu, J.; Huang, Y.; Li, H.; Li, W. *J. Mater. Sci. Technol.* **2017**, *33* (12), 1448–1456.

(6) Rojas, D.; Garcia, J.; Prat, O.; Sauthoff, G.; Kaysser-Pyzalla, A. R. *Mater. Sci. Eng. A* **2011**, *528* (15), 5164–5176.

(7) Pandey, C.; Giri, A.; Mahapatra, M. M. *Mater. Sci. Eng. A* **2016**, *664*, 58–74.

(8) Eser, S.; Andrésen, J. M. In *Fuels and Lubricants Handbook: Technology, Properties, Performance, and Testing, 2nd Edition*; Totten, G., Shah, R., Forester, D., Eds.; ASTM International: West Conshohocken, PA, 2019; pp 1327–1361.

(9) Zhang, L.; Holt, C. M. B.; Luber, E. J.; Olsen, B. C.; Wang, H.; Danaie, M.; Cui, X.; Tan, X.; Lui, V. W.; Kalisvaart, W. P.; Mitlin, D. *J. Phys. Chem. C* **2011**, *115* (49), 24381–24393.

Chapter 4

(1) Tay, F. H.; Kazarian, S. G. *Energy and Fuels* **2009**, *23* (8), 4059–4067.

(2) Gentzis, T.; Parker, R. J.; McFarlane, R. A. *Fuel* **2000**, *79* (10), 1173–1184.

(3) Mozdianfard, M. R.; Behranvand, E. **2013**, *50*, 908–917.

(4) de Oliveira Souza, M.; Ribeiro, M. A.; Carneiro, M. T. W. D.; Athayde, G. P. B.; de Castro, E. V. R.; da Silva, F. L. F.; Matos, W. O.; de Queiroz Ferreira, R. *Fuel* **2015**, *154*, 181–187.

(5) Deshannavar, U. B.; Rafeen, M. S.; Ramasamy, M.; Subbarao, D. *Journal of Applied Sciences*. 2010, pp 3167–3174.

(6) Coletti, F.; Macchietto, S. *Ind. Eng. Chem. Res.* **2011**, *50* (8), 4515–4533.

(7) Gary, J. H.; Handwerk, G. E.; Kaiser, M. J. *Petroleum Refining: Technology and Economics*, 5th ed.; CRC Press/Taylor and Francis: New York, NY, 2005.

(8) Wang, W.; Watkinson, A. P. *Proc. Int. Conf. Heat Exch. Fouling Clean. IX* **2011**, 23–30.

(9) Stephenson, T.; Hazelton, M.; Kupsta, M.; Lepore, J.; Andreassen, E. J.; Hoff, A.; Newman, B.; Eaton, P.; Gray, M.; Mitlin, D. *Fuel* **2015**, *139*, 411–424.

(10) Macchietto, S.; Hewitt, G. F.; Coletti, F.; Crittenden, B. D.; Dugwell, D. R.; Galindo, A.; Jackson, G.; Kandiyoti, R.; Kazarian, S. G.; Luckham, P. F.; Matar, O. K.; Millan-Agorio, M.; Müller, E. A.; Paterson, W.; Pugh, S. J.; Richardson, S. M.; Wilson, D. I. *Heat Transf. Eng.* **2011**, *32* (3–4), 197–215.

(11) Lestina, T. G.; Zettler, H. U. *Heat Transf. Eng.* **2014**, *35* (3), 217–223.

(12) Kim, D.; Jin, J. M.; Cho, Y.; Kim, E. H.; Cheong, H. K.; Kim, Y. H.; Kim, S. *Fuel* **2015**, *157*, 48–55.

(13) Niyonsaba, E.; Manheim, J. M.; Yerabolu, R.; Kenttämaa, H. I. *Anal. Chem.* **2019**, *91* (1), 156–177.

(14) Verşan Kök, M.; Varfolomeev, M. A.; Nurgaliev, D. K. *J. Pet. Sci. Eng.* **2019**, *179* (April), 1–6.

(15) Adams, J. J. *Energy and Fuels*. 2014, pp 2831–2856.

(16) Alshareef, A. H.; Tan, X.; Diner, C.; Zhao, J.; Scherer, A.; Azyat, K.; Stryker, J. M.; Tykwinski, R. R.; Gray, M. R. *Energy and Fuels* **2014**, *28* (3), 1692–1700.

(17) Watkinson, A. P.; Wilson, D. I. *Exp. Therm. Fluid Sci.* **1997**, *14* (4), 361–374.

(18) Somerscales, E. F. C. *Exp. Therm. Fluid Sci.* **1997**, *14* (4), 335–355.

(19) Watkinson, a. P. *Heat Transf. Eng.* **2007**, *28* (January 2015), 177–184.

(20) Rebak, R. B. *Corrosion Reviews*. 2011, pp 123–133.

(21) Slavcheva, E.; Shone, B.; Turnbull, A. *Br. Corros. J.* **1999**, *34* (2), 125–131.

(22) Hau, J. *Corrosion* **2009**, *65* (12), 831–843.

(23) Wiehe, I. A. *Process Chemistry of Petroleum Macro Molecules*, Vol. 121.; CRC Press: Boca Raton, FL, 2008.

(24) Liu, C.; Liu, H.; Yin, C.; Zhao, X.; Liu, B.; Li, X.; Li, Y.; Liu, Y. *Fuel* **2015**, *154*, 88–94.

(25) Coletti, F.; Hewitt, G. *Crude Oil Fouling: Deposit Characterization, Measurements, and Modeling*; Elsevier Science, 2014.

(26) Fan, Z.; Rahimi, P.; McGee, R.; Wen, Q.; Alem, T. *Energy and Fuels* **2010**, *24* (11), 6110–6118.

(27) Petkovic, B.; Watkinson, P. *Heat Transf. Eng.* **2013**, *35* (3), 302–310.

(28) Wang, W.; Watkinson, a. P. *Heat Transf. Eng.* **2015**, *36* (7–8), 623–631.

(29) Stephenson, T.; Kubis, A.; Derakhshesh, M.; Hazelton, M.; Holt, C.; Eaton, P.; Newman, B.; Hoff, A.; Gray, M.; Mitlin, D. *Energy and Fuels* **2011**, *25* (10), 4540–4551.

(30) Ogbonnaya, S. K.; Ajayi, O. O. *Front. Heat Mass Transf.* **2017**, *9*, 2007–2018.

(31) Yang, M.; Wood, Z.; Rickard, B.; Crittenden, B.; Gough, M.; Droegemueller, P.; Higley, T. *Appl. Therm. Eng.* **2013**, *54* (2), 516–520.

(32) Ebrahimi, S.; Moghaddas, J. S.; Aghjeh, M. K. R. *Fuel* **2008**, *87* (8–9), 1623–1627.

(33) Derakhshesh, M.; Eaton, P.; Newman, B.; Hoff, A.; Mitlin, D.; Gray, M. R. In *Energy and Fuels*; 2013; Vol. 27, pp 1856–1864.

(34) Wiehe, I. A. In *Energy and Fuels*; 2012; Vol. 26, pp 4004–4016.

(35) Ávila, B. M. F.; Pereira, V. B.; Gomes, A. O.; Azevedo, D. A. *Fuel* **2014**, *126*, 188–193.

(36) Connell, G.; Dumesic, J. A. *J. Catal.* **1986**, *102* (1), 216–233.

(37) Rana, M. S.; Ancheyta, J.; Sahoo, S. K.; Rayo, P. In *Catalysis Today*; 2014; Vol. 220–222, pp 97–105.

(38) Breysse, M.; Furimsky, E.; Kasztelan, S.; Lacroix, M.; Perot, G. *Catal. Rev.* **2002**, *44* (4), 651–735.

(39) Absi-Halabi, M.; Stanislaus, A.; Trimm, D. L. *Applied Catalysis*. 1991, pp 193–215.

(40) Schulte, M.; Rahmel, A.; Schutze, M. *Oxid. Met.* **1998**, *49* (1), 33–70.

(41) Baxter, D. J.; Natesan, K. *Oxid. Met.* **1989**, *31* (3), 305–323.

(42) Xiaofei, Z.; Tao, M.; Xiaochun, H.; Jinde, Z.; Xiaoyi, W.; Sixian, R. *Eng. Fail. Anal.* **2020**, *117* (January), 104802.

(43) Soltanattar, S.; Nowakowski, P.; Bonifacio, C. S.; Fischione, P.; Gleeson, B. *Oxid. Met.* **2019**, *91* (1–2), 11–31.

(44) Stephan-Scherb, C.; Nützmann, K.; Kranzmann, A.; Klaus, M.; Genzel, C. *Mater. Corros.* **2018**, *69* (6), 678–689.

(45) Lobnig, R. E.; Grabke, H. J. *Corros. Sci.* **1990**, *30* (10), 1045–1071.

(46) Atkinson, A. *Rev. Mod. Phys.* **1985**, *57* (2), 437–470.

(47) Saunders, S. R. J.; Monteiro, M.; Rizzo, F. *Progress in Materials Science*. Pergamon July 1, 2008, pp 775–837.

(48) Cheng, S. Y.; Kuan, S. L.; Tsai, W. T. *Corros. Sci.* **2006**, *48* (3), 634–649.

(49) Oh, K. N.; Ahn, S. H.; Eom, K. S.; Jung, K. M.; Kwon, H. S. *Corros. Sci.* **2014**, *79*, 34–40.

(50) Karimi, N.; Riffard, F.; Rabaste, F.; Perrier, S.; Cueff, R.; Issartel, C.; Buscail, H. *Appl. Surf. Sci.* **2008**, *254* (8), 2292–2299.

(51) Buscail, H.; Messki, S. El; Riffard, F.; Perrier, S.; Cueff, R.; Caudron, E.; Issartel, C. *Mater. Chem. Phys.* **2008**, *111* (2–3), 491–496.

(52) Kilpatrick, P. K. *Energy & Fuels* **2012**, *26* (7), 4017–4026.

(53) Perini, N.; Prado, A. R.; Sad, C. M. S.; Castro, E. V. R.; Freitas, M. B. J. G. *Fuel* **2012**, *91* (1), 224–228.

(54) Nguyen, M. T.; Sengupta, D.; Raspoet, G.; Vanquickenborne, L. G. *J. Phys. Chem.* **1995**, *99* (31), 11883–11888.

(55) Danielewski, M.; Natesan, K. *Oxid. Met.* **1978**, *12* (3), 227–245.

(56) Young, D. *High Temperature Oxidation and Corrosion of Metals*; 2015; Vol. 1.

(57) Kai, W.; Leu, C. T.; Lee, P. Y. *Oxid. Met.* **1996**, *46* (3), 185–211.

(58) Jacob, K. T.; Bhogeswara Rao, D.; Nelson, H. G. *Oxid. Met.* **1979**, *13* (1), 25–55.

(59) Hobby, M. G.; Wood, G. C. *Oxid. Met.* **1969**, *1* (1), 23–54.

(60) Sabioni, A. C. S.; Huntz, A. M.; Souza, J. N. V; Martins, M. D.; Jomard, F. *Philos. Mag.* **2008**, *88* (3), 391–405.

(61) Sabioni, A. C. S.; Huntz, A. M.; Silva, F.; Jomard, F. *Mater. Sci. Eng. A* **2005**, *392* (1–2), 254–261.

(62) Li, H.; Chen, W. *Oxid. Met.* **2012**, *78* (1–2), 103–122.

(63) Li, H.; Chen, W. *Oxid. Met.* **2012**, *77* (3–4), 107–127.

(64) Mitlin *, D.; Misra, A.; Mitchell, T. E.; Hirth, J. P.; Hoagland, R. G. *Philos. Mag.* **2005**, *85* (28), 3379–3392.

(65) Mitlin, D.; Misra, A.; Radmilovic, V.; Nastasi, M.; Hoagland, R.; Embury, D. J.; Hirth, J. P.; Mitchell, T. E. *Philos. Mag.* **2004**, *84* (7), 719–736.

(66) Shashank Dutt, B.; Nani Babu, M.; Venugopal, S.; Sasikala, G.; Bhaduri, A. K. *Mater. Sci. Technol.* **2011**, *27* (10), 1527–1533.

(67) Baker, R. T. K.; Yates, D. J. C.; Dumesic, J. A. *ACS Symp. Ser.* **1982**, 1–21.

(68) DE JONG, K. P.; GEUS, J. W. *Catal. Rev.* **2000**, *42* (4), 481–510.

Chapter 5

(1) Wiehe, I. A. In *Energy and Fuels*; 2012; Vol. 26, pp 4004–4016.

(2) Wiehe, I. A. *Process Chemistry of Petroleum Macro Molecules*, Vol. 121.; CRC Press: Boca Raton, FL, 2008.

(3) Stephenson, T.; Hazelton, M.; Kupsta, M.; Lepore, J.; Andreassen, E. J.; Hoff, A.; Newman, B.; Eaton, P.; Gray, M.; Mitlin, D. *Fuel* **2015**, *139*, 411–424.

(4) Wang, W.; Watkinson, A. P. *Proc. Int. Conf. Heat Exch. Fouling Clean. IX* **2011**, 23–30.

(5) Diaz-Bejarano, E.; Behranvand, E.; Coletti, F.; Mozdianfard, M. R.; Macchietto, S. *Appl. Energy* **2017**, *206* (September), 1250–1266.

Chapter 6

(1) Stephenson, T.; Hazelton, M.; Kupsta, M.; Lepore, J.; Andreassen, E. J.; Hoff, A.; Newman, B.; Eaton, P.; Gray, M.; Mitlin, D. *Fuel* **2015**, *139*, 411–424.

(2) Stephenson, T.; Kubis, A.; Derakhshesh, M.; Hazelton, M.; Holt, C.; Eaton, P.; Newman, B.; Hoff, A.; Gray, M.; Mitlin, D. *Energy and Fuels* **2011**, *25* (10), 4540–4551.

(3) Lepore, J. The Role of Sulfur Species in Establishing the Corrosion Reactions in Refinery Metallurgies, University of Alberta, 2016.

(4) Xiaofei, Z.; Tao, M.; Xiaochun, H.; Jinde, Z.; Xiaoyi, W.; Sixian, R. *Eng. Fail. Anal.* **2020**, *117* (January), 104802.

(5) Jin, P.; Nesic, S.; Wolf, H. A. *Surf. Interface Anal.* **2015**, *47* (4), 454–465.

(6) Jin, P.; Nesic, S. *Corros. Sci.* **2017**, *115*, 93–105.

(7) Jin, P.; Bota, G.; Robbins, W.; Nesic, S. *Energy and Fuels* **2016**, *30* (8), 6853–6862.

(8) Yépez, O. *Fuel* **2005**, *84* (1), 97–104.

(9) Flego, C.; Galasso, L.; Montanari, L.; Gennaro, M. E. In *Energy and Fuels*; 2014; Vol. 28, pp 1701–1708.

(10) Rebak, R. B. *Corrosion Reviews*. 2011, pp 123–133.

(11) Qu, D. R.; Zheng, Y. G.; Jing, H. M.; Jiang, X.; Ke, W. *Mater. Corros.* **2005**, *56* (8), 533–541.

(12) Diaz, Y.; Sevilla, A.; Mónaco, A.; Méndez, F. J.; Rosales, P.; Garc\'\ia, L.; Brito, J. L. *Fuel* **2013**, *110*, 235–248.

Chapter 7

(1) Symoens, S. H.; Olahova, N.; Munoz Gandarillas, A. E.; Karimi, H.; Djokic, M. R.; Reyniers, M. F.; Marin, G. B.; Van Geem, K. M. *Ind. Eng. Chem. Res.* **2018**, *57* (48), 16117–16136.

(2) Xu, X. Q.; Miao, J.; Bai, Z. Q.; Feng, Y. R.; Ma, Q. R.; Zhao, W. Z. *Appl. Surf. Sci.* **2012**, *258* (22), 8802–8806.

(3) Rocha, A. da C.; Rizzo, F.; Zeng, C.; Paes, M. P. *Mater. Res.* **2004**, *7* (1), 189–194.

(4) Bischoff, C.; Poulsen, T.; Losada, R.; Mortensen, J. O.; Jackowski, L.; Taylor, S. T. *Int. Conf. Heat Exch. Fouling Clean.* **2015**, *2015*, 325–327.

(5) Santos, O.; Anehamre, J.; Wictor, C.; Tornqvist, A.; Nilsson, M. *Int. Conf. Heat Exch. Fouling Clean.* **2013**, *2013* (Dlc), 79–84.

(6) Schütze, M.; Malessa, M.; Rohr, V.; Weber, T. *Surf. Coatings Technol.* **2006**, *201* (7 SPEC. ISS.), 3872–3879.

(7) Schütze, M. *Corrosion* **2007**, *63* (1), 4–18.

(8) Pinzón, A. V.; Urrego, K. J.; González-Hernández, A.; Rincón Ortiz, M.; Vargas Galvis, F. *Ceram. Int.* **2018**, *44* (17), 21765–21773.

(9) Pang, X.; Gao, K.; Yang, H.; Qiao, L.; Wang, Y.; Volinsky, A. A. *Adv. Eng. Mater.* **2007**, *9* (7), 594–599.

(10) Medvedovski, E.; Mendoza, G. L.; Rzad, E.; Solecka, M.; Dudziak, T. P. *Surf. Coatings Technol.* **2020**, *403* (September), 126430.

(11) Pandey, C.; Giri, A.; Mahapatra, M. M. *Mater. Sci. Eng. A* **2016**, *664*, 58–74.

(12) Lazar, A. M.; Yespica, W. P.; Marcelin, S.; Pébère, N.; Samélor, D.; Tendero, C.; Vahlas, C. *Corros. Sci.* **2014**, *81*, 125–131.

(13) Pang, X.; Gao, K.; Luo, F.; Emirov, Y.; Levin, A. A.; Volinsky, A. A. *Thin Solid Films* **2009**, *517* (6), 1922–1927.

(14) Teng, Y.; Guo, Y. Y.; Zhang, M.; Yang, Y. J.; Huang, Z.; Zhou, Y. W.; Wu, F. Y.; Liang, Y. S. *Surf. Coatings Technol.* **2019**, *367* (March), 100–107.

(15) P, D. *CRC Handbook of Chemistry and Physics*; CRC press, 1992; Vol. 268.

(16) O'Hare, P. A. G.; Johnson, G. K. *J. Chem. Thermodyn.* **1986**, *18* (2), 189–199.

(17) Oikawa, K.; Mitsui, H.; Ohtani, H.; Ishida, K. *ISIJ Int.* **2000**, *40* (2), 182–190.

(18) Narita, T.; Ishikawa, T.; Nishida, K. *Oxid. Met.* **1987**, *27* (3–4), 221–237.